Delft University of Technology

Directed Energy Deposition: an Additive Manufacturing Technology for Large High-Temperature Compact Heat Exchangers
Process characterization and fluid dynamic performance

Gradl, P.R.

DOI
10.4233/uuid:5e09e72b-457f-4aec-8b3f-b30426adcb11

Publication date
2025

Document Version
Final published version

Citation (APA)
Gradl, P. R. (2025). *Directed Energy Deposition: an Additive Manufacturing Technology for Large High-Temperature Compact Heat Exchangers: Process characterization and fluid dynamic performance*. [Dissertation (TU Delft), Delft University of Technology]. https://doi.org/10.4233/uuid:5e09e72b-457f-4aec-8b3f-b30426adcb11

Directed Energy Deposition: an Additive Manufacturing Technology for Large High-Temperature Compact Heat Exchangers

Process characterization and fluid dynamic performance

Paul R. Gradl

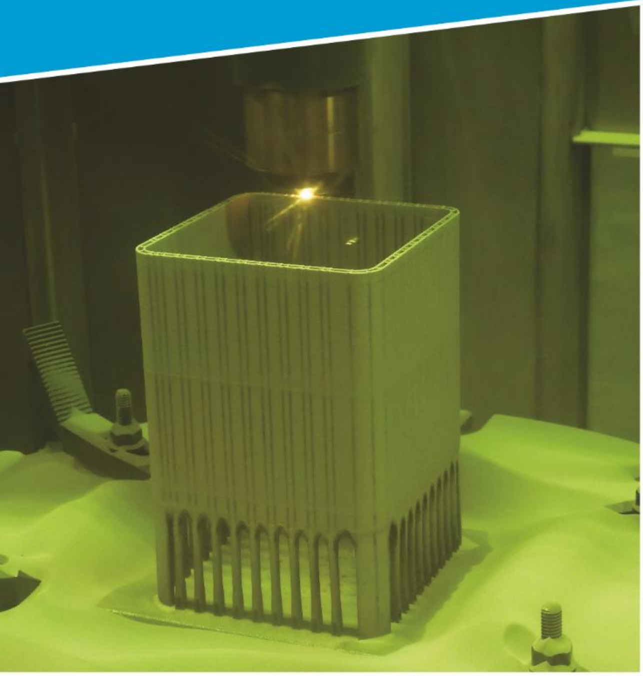

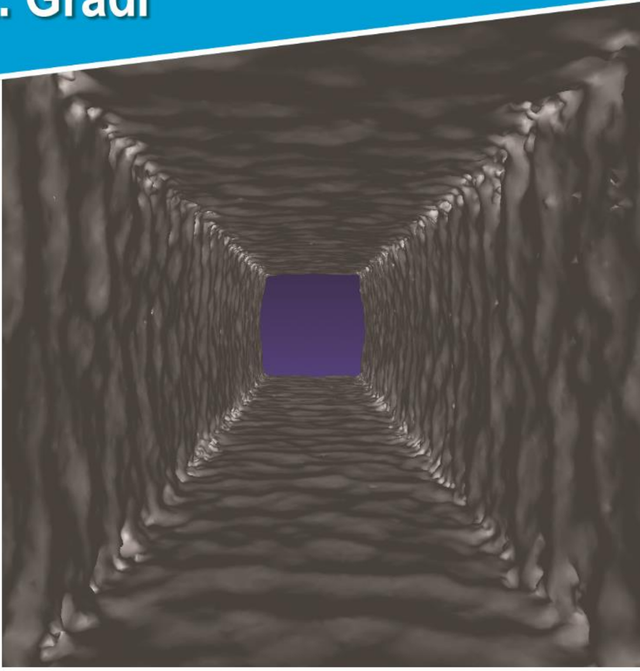

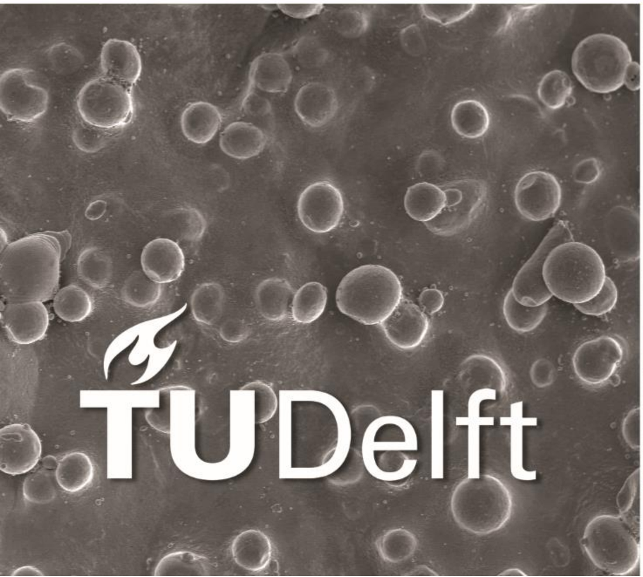

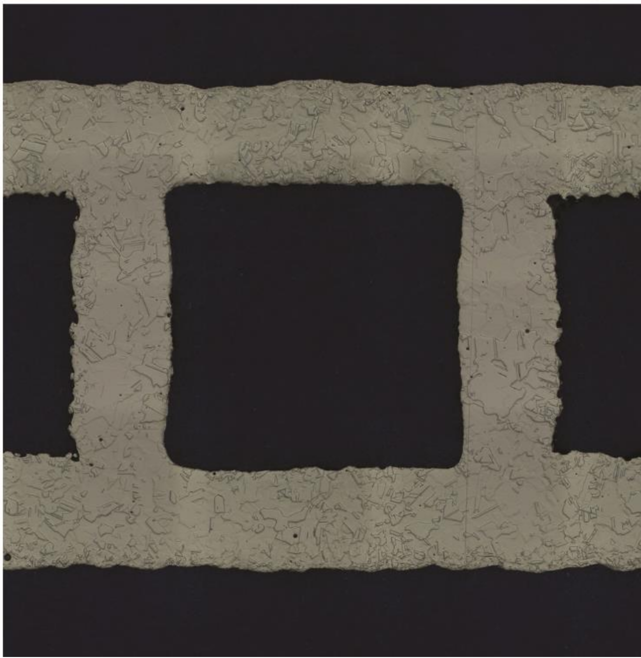

Directed Energy Deposition: an Additive Manufacturing Technology for Large High-Temperature Compact Heat Exchangers

Process characterization and fluid dynamic performance

Dissertation

for the purpose of obtaining the degree of doctor
at Delft University of Technology
by the authority of the Rector Magnificus Prof.dr.ir. T.H.J.J. van der Hagen
chair of the Board for Doctorates
to be defended publicly on
Wednesday 12 March 2025 at 10:00 o'clock

By

Paul Richard GRADL

This dissertation has been approved by the promotors.

Promotor: Prof.dr.ir. P. Colonna di Paliano
Promotor: Dr. A. Cervone

Composition of the doctoral committee:

Rector Magnificus,	chairperson
Dr. A. Cervone	Delft University of Technology, promotor
Prof.dr.ir. P. Colonna di Paliano	Delft University of Technology, promotor

Independent Members:

Prof. dr. ir. P. Breedveld	Delft University of Technology
Dr. C. Dordlofva	Luleå University of Technology/GKN, Sweden
Dr. F.K. Leverone	Dawn Aerospace
Dr. V.A. Popovich	Delft University of Technology
Dr. H. Yamaguchi	University of Florida, USA
Prof.dr.ir. P.N.A.M Visser	Delft University of Technology (reserve member)

Keywords: Additive Manufacturing, Microchannels, Heat Exchanger, Directed Energy Deposition, Surface Enhancements, Polishing, Friction Factors

Cover Art: Lynn Machamer

Contents

Figures VII
Tables X
1 Introduction and Background .... 1—1
  1.1 Background .... 1—1
  1.2 Traditional Manufacturing Methods .... 1—3
  1.3 Additive Manufacturing for Heat Exchangers .... 1—6
  1.4 The LP-DED process .... 1—13
  1.5 Potential and Challenges of LP-DED .... 1—14
  1.6 Surface Texture and Enhancements for LP-DED .... 1—16
  1.7 Aim of the Research .... 1—20
  1.8 Thesis Content .... 1—22
2 Research Questions and Methodology .... 2—24
  2.1 Gaps in Knowledge .... 2—24
  2.2 Surface texture as a systems engineering challenge .... 2—28
  2.3 Research Questions .... 2—29
  2.4 Innovations from the research and methodology .... 2—33
3 Process Overview and In-process Surface Evaluation .... 3—35
  3.1 Abstract .... 3—35
  3.2 Background .... 3—35
  3.3 Methodology .... 3—38
    3.3.1 LP-DED Experiment Parameters .... 3—40
    3.3.2 NASA HR-1 Material .... 3—43
    3.3.3 Design of Experiment (DOE) Samples .... 3—44
    3.3.4 Roughness Measurements and Microscopy .... 3—46
  3.4 Experimental Results .... 3—47
    3.4.1 Visual and SEM .... 3—47
    3.4.2 Microstructure .... 3—48
    3.4.3 Areal Measurements .... 3—50
    3.4.4 Directional Profile Measurements .... 3—52
    3.4.5 Waviness .... 3—53
    3.4.6 DOE Results .... 3—54
    3.4.7 Porosity .... 3—55
    3.4.8 Sample Wall Thickness .... 3—56
  3.5 Discussion .... 3—59
  3.6 Conclusions .... 3—62
4 Chapter 4 – Influence of Angles on Surface Texture and Geometry .... 4—65
  4.1 Abstract .... 4—65
  4.2 Background .... 4—65
  4.3 Methodology .... 4—67
    4.3.1 DED System and Samples .... 4—67
    4.3.2 Deposition Parameters .... 4—69
    4.3.3 NASA HR-1 Alloy .... 4—69
    4.3.4 Surface Metrology and Imaging .... 4—70

4.4 Results and Discussion .... 4—73
4.4.1 SEM Image Analysis .... 4—74
4.4.2 Optical Image Analysis .... 4—75
4.4.3 Surface Texture Characterization .... 4—80
4.5 Conclusions .... 4—86
5 Development and Characterization of Microchannels .... 5—88
5.1 Abstract .... 5—88
5.2 Introduction .... 5—88
5.3 Channel Process Development and Characterization .... 5—89
5.3.1 Microchannel Deposition .... 5—89
5.3.2 Channel Geometry .... 5—90
5.3.3 Characterization Methods .... 5—92
5.4 Microchannel Cross-Sectional Area and Perimeter .... 5—94
5.5 Surface Texture .... 5—97
5.6 Wall Thickness .... 5—101
5.7 Summary and Conclusions .... 5—102
6 Post-process Surface Enhancement and Characterization .... 6—104
6.1 Abstract .... 6—104
6.2 Introduction .... 6—104
6.3 Methodology .... 6—105
6.3.1 Fabrication of DED Samples and Processing .... 6—105
6.3.2 Surface Enhancement Processes .... 6—108
6.3.3 Test Configuration and Procedures .... 6—110
6.3.4 Sectioning and Imaging .... 6—112
6.4 Results and Discussion .... 6—114
6.4.1 Image Analysis .... 6—114
6.5 Flow Testing .... 6—121
6.6 Conclusions .... 6—129
7 Friction Factor of Channels with Improved Surface Finishing .... 7—131
7.1 Abstract .... 7—131
7.2 Introduction .... 7—132
7.3 Methodology .... 7—134
7.3.1 Fabrication of DED Samples and Processing .... 7—134
7.3.2 Surface Enhancements of 600 mm Length Channels .... 7—137
7.3.3 Test Configuration and Procedures .... 7—139
7.3.4 Post-test Channel Measurements .... 7—143
7.4 Results and Discussion .... 7—146
7.4.1 Channel Geometry Characterization .... 7—146
7.4.2 Surface Texture Characterization .... 7—154
7.4.3 Discharge Coefficient .... 7—157
7.4.4 Differential Pressure and Friction Factor .... 7—161
7.4.5 Sand Grain Roughness .... 7—171
7.4.6 Friction Factor Correlation and Mechanism .... 7—178
7.5 Conclusions .... 7—184
8 Summary and Recommendations .... 8—187
8.1 Main Findings and Conclusions .... 8—187

- 8.2 Key Innovations .... 8—193
- 8.3 Future Applications and Research Areas .... 8—195
  - 8.3.1 Initial Application Cases .... 8—195
  - 8.3.2 Future Applications .... 8—197
- 8.4 Recommendations .... 8—197
  - 8.4.1 Design and Analysis .... 8—197
  - 8.4.2 Process Specific .... 8—198
  - 8.4.3 Production and Operation .... 8—198
- 8.5 Reflections .... 8—199

9 References .... 9—201

10 Acknowledgements .... 10—224

11 Published Research Related to this Dissertation .... 11—226

12 Appendix .... 12—228

Figures

Figure 1.1. Examples of LP-DED manufacturing demonstrator........................ 1—2
Figure 1.2. Schematic cross-section of cooling channels .... 1—4
Figure 1.3. Process steps and fabrication options for channel wall nozzles .... 1—5
Figure 1.4. Schematic representation of a Laser Powder Bed Fusion .... 1—8
Figure 1.5. Examples of various integral channel chambers and nozzles.......... 1—10
Figure 1.6. Comparison of AM processes considering feature size.................. 1—12
Figure 1.7. Laser Powder DED System. .... 1—14
Figure 1.8. Example of laser polishing applied to a Stainless 316L .... 1—18
Figure 1.9. Indicative comparison between the idealized and typical design .... 1—21
Figure 1.10. Sequential phases of the LP-DED microchannel fabrication .... 1—22
Figure 2.1. Schematic visualization of the attributes of surface texture .... 2—26
Figure 2.2. Example of typical channel .... 2—27
Figure 2.3. A holistic view of surface texture throughout the AM lifecycle. .... 2—29
Figure 2.4. Chapter outline and associated publications.................................. 2—31
Figure 2.5. Relationship diagram of research gaps and research questions. ...... 2—32
Figure 3.1. Overview of LP-DED Process Parameters. .... 3—40
Figure 3.2. LP-DED parameter inputs that can impact surface texture. .... 3—41
Figure 3.3. Fabricated experimental select samples. .... 3—42
Figure 3.4. SEM Images of the NASA HR-1 Powder. .... 3—44
Figure 3.5. Nomenclature and measurement locations .... 3—47
Figure 3.6. SEM images of select samples. .... 3—48
Figure 3.7. Sectioned and etched samples with inner and outer surfaces .... 3—50
Figure 3.8. Areal texture measurements for all samples. .... 3—51
Figure 3.9. Directional vertical texture per sample. .... 3—54
Figure 3.11. Porosity measurements in samples compared to inner .... 3—56
Figure 3.12. Sample cross-sectional thickness compared to powder PSD .... 3—57
Figure 3.13. Comparison of average profile height (Pa) to average .... 3—58
Figure 3.14. Comparison of vertical and horizontal average profile height....... 3—59
Figure 3.15. Comparison of areal surface roughness map .... 3—61
Figure 3.16. Contour plot for average areal surface roughness with powder .... 3—62
Figure 4.1. As-built NASA HR-1 alloy angled specimens .... 4—68
Figure 4.2. SEM image of NASA HR-1 (55-105 µm) powder morphology. .... 4—70
Figure 4.3. Terminology for sample measurement. .... 4—72
Figure 4.4. SEM images of the normal surface for upskin and downskin .... 4—74
Figure 4.5. Example of powder impingement for vertical and angled sample. . 4—74
Figure 4.6. Wall thickness and melt pool visualized on angled wall samples. .. 4—76
Figure 4.7. Partially melted and adhered powder shown for the upskin .... 4—77
Figure 4.8. Measured and adjusted wall thickness of the angled samples. .... 4—79
Figure 4.9. Perpendicular melt pool height and adjusted height .... 4—80
Figure 4.10. Primary texture of areal surface .... 4—82
Figure 4.11. Roughness compared to particle count from SEM. .... 4—83
Figure 4.12. a) Directional vertical roughness and waviness. .... 4—85
Figure 4.13. Directional waviness and normal wall thickness. .... 4—86

Figure 5.1. Aspects affecting the LP-DED process that need to be studied ...... 5—89
Figure 5.2. Various types of small channels built with LP-DED .... 5—91
Figure 5.3. Tool path strategy and general order of operations .... 5—91
Figure 5.4. Various sized channel samples .... 5—92
Figure 5.5. Sectioning plan for microchannel samples .... 5—93
Figure 5.6. Reproducibility results of channel cross-sectional area .... 5—94
Figure 5.7. Difference of cross-sectional area (compared to as-designed area). 5—95
Figure 5.8. Adjusted cross-sectional channel areas .... 5—96
Figure 5.9. Measured perimeter and Differences .... 5—97
Figure 5.10. Average surface texture (Sa) of various sized channel samples. ... 5—98
Figure 5.11. Optical micrographs of selected channel samples .... 5—99
Figure 5.12. SEM Images of Internal Channels at the bottom. .... 5—100
Figure 5.13. Summary of rib and outer wall thickness for channel samples. .. 5—102
Figure 6.1. Channel specimen fabrication .... 6—107
Figure 6.2. Overview of surface enhancement processes .... 6—110
Figure 6.3. Flow test configuration. .... 6—111
Figure 6.4. Sectioning of channels post-flow testing. .... 6—112
Figure 6.5. Polished cross section of channel samples .... 6—116
Figure 6.6. SEM 50x magnification images of the surface of each channel. .. 6—118
Figure 6.7. SEM 500x magnification images of the surface of each channel .. 6—119
Figure 6.8. Micro-CT Scanning images related to various surface .... 6—120
Figure 6.9. Summary of *Cd* and comparison .... 6—123
Figure 6.10. Discharge coefficient in relation to core roughness and peak. ..... 6—125
Figure 6.11. Average areal texture compared to material removal per side. ... 6—126
Figure 6.12. Channel cross sectional area compared .... 6—127
Figure 6.13. Ratio of roughness peaks to density (Spk/Spd) .... 6—128
Figure 7.1. Channel sample fabrication. .... 7—136
Figure 7.2. Channel fabrication of inlet/outlet ports and instrumentation .... 7—137
Figure 7.3. Schematic of the experimental setup realized to test 600 mm ...... 7—139
Figure 7.4. Holding fixture for channels with a groove .... 7—140
Figure 7.5. Test facility with channel sample and holding fixture installed ... 7—141
Figure 7.6. Example of raw data set for channel AB-B1 with venturi .... 7—142
Figure 7.7. Caliper measurements to determine exact distance between ports 7—144
Figure 7.8. Location of the sectioning of the 600 mm length channels. .... 7—145
Figure 7.9. SEM images of the inner surfaces of the 600 mm length .... 7—148
Figure 7.10. Micrographs of the cross-sections of the square 600 mm .... 7—149
Figure 7.11. Micrographs of the etched square channel cross-sections. .... 7—150
Figure 7.12. Measurements characterizing the inner surface of channels. ..... 7—153
Figure 7.13. Surface texture maps overlayed on the optical+laser images. .... 7—156
Figure 7.14. 3D Contour Plot of as-built sample AB-B1 on VHX-1100 .... 7—157
Figure 7.15. Relationship of the estimated *Cd* .... 7—158
Figure 7.16. *Sk* and *Spk* as a function of *Cd*. .... 7—159
Figure 7.17. Flow resistance dependence for roughness and waviness .... 7—160
Figure 7.18. Relationship between material removal per side .... 7—161
Figure 7.19. Hydraulic Diameter based on various definitions .... 7—163
Figure 7.20. Reynolds number as a function of mass flow rate .... 7—164

Figure 7.21. Pressure difference of the measured m, processing method .... 7—165
Figure 7.22. Pressure difference of the measured m, surface texture .... 7—166
Figure 7.23. Darcy friction factor as a function of mass flow rate .... 7—169
Figure 7.24. Comparison of the friction factor determined experimentally..... 7—170
Figure 7.25. Reynolds number as a function of the differential pressure .... 7—171
Figure 7.26. Schematic representation of sand grains .... 7—172
Figure 7.27. Percent deviation between the experimentally determined f_D .... 7—173
Figure 7.28. Sand grain roughness (K_S/D_{h2}) as a function of the surface......... 7—175
Figure 7.29. Values of sand grain roughness factor based on Equation 7.18 .. 7—177
Figure 7.30. Correlation of f_M using the K_S/D_{h2} and Ra/D_{h2} linear fit .... 7—179
Figure 7.31. Maximum Peak Height (Rp) compared with waviness .... 7—180
Figure 7.32. Maximum peak height (Rp) compared to the dale void volume . 7—181
Figure 7.33. Surface attributes affecting reduction of the friction factor......... 7—183
Figure 7.34. Material removal per side and dale void volume......................... 7—184
Figure 8.1. Examples of LP-DED nozzles during hot-fire testing .... 8—196
Figure 12.1. Relationship of perimeter to cross-sectional area coefficient ... 12—228
Figure 12.2. Prediction of f_M using the K_S/D_{h2} and Ra/D_{h2} method .... 12—229
Figure 12.3. Average Darcy friction factor and standard deviation .... 12—230
Figure 12.4. Etched micrographs of the mid-section of round tubes............. 12—230

Tables

Table 1.1. Overview of various surface enhancement techniques ....1—17
Table 3.1. Chemistry for NASA HR-1 powder used in this study....................3—43
Table 3.2. Selected Parameters and Powder for DOE runs...............................3—45
Table 3.3. ANOVA for average inner surface roughness. ....3—55
Table 4.1. Parameters used for angled racetrack sample deposition.................4—69
Table 4.2. Chemical composition of NASA HR-1 alloy powder. ....4—69
Table 4.3. Description of surface parameters and definition. ....4—70
Table 4.4. Data from SEM and Optical Image Measurements. ....4—75
Table 5.1. Chemical composition of NASA HR-1 alloy powder. ....5—90
Table 6.1. Chemical composition of NASA HR-1 alloy powder. ....6—107
Table 6.2. Optical and SEM image geometric measurement and *Cd* ....6—121
Table 6.3. Summary of Surface Texture Measurements.................................6—124
Table 7.1. Chemical composition of the NASA HR-1 powder........................7—135
Table 7.2. Characteristics and nomenclature of the tested channels. ....7—138
Table 7.3. Identifiers of the 600 mm channel samples. ....7—139
Table 7.4. Instrumentation log for the testing of 600 mm length channels......7—142
Table 7.5. Summary of the geometric data of channels..................................7—151
Table 7.6. Summary of the measured values of parameters ....7—154
Table 7.7. Summary of the linear fit of K_S/D_{h2} for texture parameters ....7—178

Summary

Heat exchangers are essential for temperature regulation across various industries, from everyday applications to space exploration. Over time, these devices have evolved from simple clay vessels to complex structures made from advanced metal alloys and ceramics. In modern engineering, additive manufacturing (AM) has revolutionized heat exchanger production, enabling the creation of thin-walled structures with complex internal channels designed for efficient fluid flow. This is particularly critical in industries such as aerospace, power generation, and manufacturing, where components must be compact, lightweight, and capable of withstanding extreme temperatures and pressures. However, traditional AM methods like laser powder bed fusion (L-PBF) are constrained by size limitations, necessitating new manufacturing techniques to meet industry demands for compact large scale heat exchangers.

This research addresses the challenges of developing the Laser Powder Directed Energy Deposition (LP-DED) process for extreme-environment heat exchangers. Process and flow test experiments were conducted, along with comprehensive characterization of LP-DED-fabricated microchannels, which are thin-walled (1 mm) and capable of containing cryogenic or high-temperature pressurized fluids. The results from the research establishes LP-DED as a viable technology for heat exchanger fabrication by addressing challenges related to geometry, wall thickness, surface texture, and the fluid dynamics of these unique AM surfaces. Three key research questions guide the study:

1. How is the surface texture of heat exchanger microchannels affected by the LP-DED fabrication process?
2. What are the geometrical relationships and sensitivities affecting fluid flow performance if heat exchanger channels are manufactured with the LP-DED process?
3. What improvements can be made to control the surface texture of thin-wall LP-DED internal microchannels?

A detailed literature review identifies significant gaps in current thin-wall LP-DED manufacturing and internal surface enhancement techniques. An experimental study examines LP-DED process mechanics and build parameters, focusing on their influence of the thin-wall surface texture and the effect of build angles on both open and closed structures. This research establishes guidelines for Design for Additive Manufacturing (DfAM), addressing process limitations, surface texture, and wall thickness metrics for the LP-DED process.

This research introduces microchannels fabricated using LP-DED in various sizes, with their internal and external surface textures, wall thicknesses, and repeatability characterized. These microchannels are then processed internally using various surface enhancement techniques to provide variations of the surface finish. Two experimental studies were conducted, with comprehensive characterization performed of the internal channel surfaces to evaluate the variations in surface texture resulting from the enhancement processes and their relationship to flow resistance and friction factors.

Key innovations include the characterization of a new hydrogen-resistant alloy (NASA HR-1), which provides foundational data for heat exchanger design. The study also identifies surface texture mechanisms that affect fluid friction factors, resulting from distinct enhancement techniques such as peak smoothing, roughness minimization, waviness, and valley reduction. Additionally, friction factors and differential pressure in LP-DED-fabricated microchannels, both in as-built and surface-enhanced conditions, were investigated. Surface treatments such as abrasive flow machining, chemical milling, and chemical mechanical polishing were evaluated. The experimental results and comprehensive surface texture characterization led to the development of new correlations for calculating the hydraulic diameter of square channels and predicting sand grain roughness and friction factors. These correlations resulted in pressure drop predictions with deviations of less than 20% from experimental data, offering a 50% improvement over previous models.

Samenvatting (Dutch)

Warmtewisselaars zijn essentieel voor temperatuurregeling in verschillende industrieën, van alledaagse toepassingen tot ruimteverkenning. In de loop van de tijd zijn deze apparaten geëvolueerd van eenvoudige kleivaten tot complexe structuren gemaakt van geavanceerde metaallegeringen en keramiek. In de moderne techniek heeft additieve fabricage (AM) de productie van warmtewisselaars getransformeerd, waardoor de creatie van dunwandige structuren met complexe interne kanalen mogelijk is gemaakt, die zijn ontworpen voor efficiënte vloeistofstroming. Dit is vooral cruciaal in sectoren zoals de lucht- en ruimtevaart, energieopwekking en productie, waar onderdelen compact, licht en bestand tegen extreme temperaturen en drukken moeten zijn. Traditionele AM-methoden, zoals laserpoederbedfusie (L-PBF), hebben echter beperkingen in grootte, waardoor nieuwe productietechnieken nodig zijn om te voldoen aan de industriële vraag naar compacte grootschalige warmtewisselaars.

Dit onderzoek richt zich op de ontwikkeling van het Laser Powder Directed Energy Deposition (LP-DED) proces voor warmtewisselaars die geschikt zijn voor extreme omgevingen. Proces- en stromingstests zijn uitgevoerd, samen met uitgebreide karakterisering van LP-DED-gefabriceerde microkanalen, die dunwandig zijn (1 mm) en in staat zijn cryogene of hoog-temperatuur-geperste vloeistoffen te bevatten. De onderzoeksresultaten tonen aan dat LP-DED een levensvatbare technologie is voor de fabricage van warmtewisselaars, door uitdagingen aan te pakken met betrekking tot geometrie, wanddikte, oppervlaktetextuur en de vloeistofdynamica van deze unieke AM-oppervlakken. Drie belangrijke onderzoeksvragen sturen de studie:

1. Hoe wordt de oppervlakteafwerking van warmtewisselermicrokanalen beïnvloed door het LP-DED-fabricageproces?
2. Wat zijn de geometrische relaties en gevoeligheden die de prestatie van de vloeistofstroom beïnvloeden als warmtewisselarkanalen worden vervaardigd met het LP-DED-proces?
3. Welke verbeteringen kunnen worden doorgevoerd om de oppervlakteafwerking van dunwandige LP-DED interne microkanalen te beheersen?

Een gedetailleerd literatuuronderzoek identificeert significante hiaten in de huidige dunwandige LP-DED-productie en technieken voor interne oppervlakteverbetering. Een experimenteel onderzoek onderzoekt de mechanica van het LP-DED-proces en bouwparameters, met de nadruk op hun invloed op de oppervlaktetextuur van dunne wanden en het effect van bouwhoeken op zowel open als gesloten structuren. Dit onderzoek stelt richtlijnen op voor Design for Additive Manufacturing (DfAM), waarin proceslimieten, oppervlaktetextuur en wanddiktecriteria voor het LP-DED-proces worden behandeld.

Dit onderzoek introduceert microkanalen, vervaardigd met LP-DED in verschillende afmetingen, met hun interne en externe oppervlaktetexturen,

wanddiktes en herhaalbaarheid gekarakteriseerd. Deze microkanalen worden vervolgens intern verwerkt met verschillende oppervlakteverbeteringstechnieken om variaties in de afwerking te bieden. Twee experimentele studies zijn uitgevoerd, met een uitgebreide karakterisering van de interne kanaaloppervlakken om de variaties in oppervlaktetextuur als gevolg van de verbeteringstechnieken te evalueren en hun relatie tot stromingsweerstand en wrijvingsfactoren.

Belangrijke innovaties zijn onder andere de karakterisering van een nieuwe waterstofbestendige legering (NASA HR-1), die fundamentele gegevens voor warmtewisselaarontwerp biedt. De studie identificeert ook oppervlaktetextuurmechanismen die invloed hebben op wrijvingsfactoren van vloeistoffen, resulterend uit specifieke verbeteringstechnieken zoals piekafvlakking, ruwheidsminimalisatie, golving en dalreductie. Bovendien zijn wrijvingsfactoren en drukverschillen in LP-DED-gefabriceerde microkanalen onderzocht, zowel in de oorspronkelijke staat als na oppervlakteverbetering. Oppervlaktebehandelingen zoals abrasieve stroombewerking, chemisch frezen en chemisch mechanisch polijsten zijn geëvalueerd. De experimentele resultaten en uitgebreide oppervlaktetextuurkarakterisering hebben geleid tot de ontwikkeling van nieuwe correlaties voor het berekenen van de hydraulische diameter van vierkante kanalen en het voorspellen van zandkorrelruwheid en wrijvingsfactoren. Deze correlaties resulteerden in drukvalvoorspellingen met afwijkingen van minder dan 20% van experimentele gegevens, wat een verbetering van 50% biedt ten opzichte van eerdere modellen.

Nomenclature

α = angle of wall in degrees
A = area (mm^2)
A_{AB} = Average area of as-built channels
A_{Ch} = Area of channel being measured
AB = As-built
AFM = Abrasive flow machining
AM = Additive Manufacturing
ANOVA = Analysis of Variance
BD = Build direction
Cd = Discharge coefficient
CM = Chemical milling
CMP = Chemical mechanical polishing
CV = Coefficient of variation
ΔP = differential pressure (bar)
DED = directed energy deposition
DfAM = Design for additive manufacturing
D_h = Hydraulic diameter
D_{h1} = Hydraulic diameter, based on $\sqrt{A_{\mathrm{meas}}}$
D_{h2} = Adjusted hydraulic diameter for texture
DOE = Design of Experiments
HEE = Hydrogen Environment Embrittlement
F = powder feedrate, in grams/min
f_A = Friction Factor, Avci and Kargoz
f_B = Friction Factor, Brkic and Cojbasic
f_C = Friction Factor, Colebrook-White
f_D = Friction Factor, Darcy
f_M = Friction Factor, based on Moody
f_s = Friction Factor, Swamee and Jain
f_T = *Friction Factor,* Mileikovskyi and Tkachenko
FP = Fine powder
g_c = gravitational constant
K’ = Proportionality constant (2.35)
K_s = Sand grain roughness
λc = large-scale band pass filter (also Lc)
λs = small-scale (noise) filter (also Ls)
L = length (mm)
L-PBF = Laser Powder Bed Fusion
LP-DED = Laser Powder Directed Energy Deposition
MSFC = Marshall Space Flight Center
$\dot{m}$ = mass flow rate (kg/sec)
MR = material removal (um)
n = Exponent (0.005)
NASA HR-1 = Fe-Ni-Cr Hydrogen Resistant superalloy
P = Power, in watts
P = perimeter (mm)
[P] = Primary filtering (waviness and roughness)
Pa = Directional 2D profile average height
PBF = powder bed fusion

PECM = Pulsed electrochemical machining
Pku = 2D Profile Kurtosis
Pp = 2D Profile Peak Height
Ppm = part per million
PSD = Particle Size Distribution
Psk = 2D Profile Skewness
PT = pressure transducer
Pv = 2D Profile Valley depth
Pz = Average Maximum Profile Height
[R] = Roughness filtered
Re = Reynolds number
ρ = density of water (grams/cm^3)
Ra = Arithmetic mean directional roughness (λc at 0.8 mm)
Rk = 2D directional core roughness (λc at 0.8 mm)
Rz = Average directional maximum profile height (λc at 0.8 mm)
S_T = measured surface texture/roughness
Sa = Average texture
Sdr = Developed interfacial area ratio
SEM = Scanning Electron Microscope
Sk = Core texture depth
Sku = Kurtosis
Sp = Maximum peak height
Spd = Roughness Peak Density
Spk = reduced peak height
Sq = Root mean square (RMS) height
Ssk = Skewness
Sv = Maximum valley depth
Svk = Reduced valley depth
Sz = Maximum surface height
TC = thermocouple
TEM = Thermal energy method
u = dynamic viscosity (Pa-s)
V = Traverse scan speed of deposition head, in mm/min
v = kinematic viscosity (m^2/sec)
Vvv = dale void volume ($\mu m^3/\mu m^2$)
W = Watts
Wa = Arithmetic mean directional waviness (λc at 0.8 mm)
Wp = Waviness peak height (λc at 0.8 mm)
WPc = Waviness peak density (λc at 0.8 mm)
Wt = Wall thickness, in mm

Chapter 1

Introduction and Background

1.1 BACKGROUND

Heat exchangers surround us in our daily lives, finding application in our homes, offices, transportation systems, and various industrial sectors responsible for producing the goods and energy we consume. These devices play a crucial role in the efficient management and regulation of temperatures. In our homes, miniature heat sinks dissipate the heat generated by processing chips in our computers, while in vehicles, radiators circulate cooling fluids, maintaining engine temperatures and transferring energy to the surrounding air. Even the climate within buildings is regulated by heat exchangers, with plate heat exchangers and earth tubes enabling environmentally friendly heating and cooling systems. In contrast, the colossal shell and tube heat exchangers, resembling buildings in size, are integral to processes in petroleum refineries, chemical and steel industries, and power generation, facilitating efficient heat transfer between fluid mediums [1].

The comprehension of the physics underlying the functioning of heat exchangers and their critical role in our world has matured over decades, if not centuries, of practical application. The evolution of heat exchanger complexity is evident, progressing from rudimentary clay pots to high-tech ceramics and advanced metal alloys featuring intricate internal design features and channels. Today, the ability to manufacture thin-walled heat exchanger structures using high-temperature metal alloys, while actively flowing fluids through labyrinthine channels, has propelled modern advancements in industrial, power, and aerospace sectors. The demanding environments of aviation and space flight necessitate materials characterized by high strength, resistance to elevated temperatures, and high strength-to-weight ratio. The aerospace sector is often the first to adopt these advanced materials and processing thereof. These advancements in aerospace materials, design optimization methods, and specialized manufacturing processes often infuse into various industries including power and energy, oil and gas, industrial manufacturing, and many others, resulting in far-reaching societal impacts beyond aerospace applications.

Heat exchangers for use in aerospace applications are critical components because they must be efficient, compact, and low mass and often operate with working fluids at extreme temperatures or pressures or both. Various components and systems use heat exchangers such as power plants, chemical processing plants, gas turbines, hypersonic leading edges and control surfaces, fuel cells (air supply and thermal management), electric batteries and avionics cooling (thermal management), evaporators and recuperators of waste-heat-to-power systems, and rocket engines [2,3]. Ultra-compact and ultra-efficient heat exchangers are enablers of new propulsion systems, such as rotating detonation rocket engines [4].

The focus of the work documented in this thesis is on a novel manufacturing technology for extreme environment heat exchangers, namely Directed Energy Deposition (DED), and on the characterization of the achievable fluid dynamic performance if this technology is applied to these heat exchangers. These components are thin-walled (< 2 mm) and contain pressurized working fluids at cryogenic (-253 °C) or extreme temperatures (> 3300 °C) and high pressures (> 400 bar), or both [5]. Currently, a prominent application for this type of heat exchangers is their use for the regenerative cooling of liquid fuel rocket engine nozzles. They can also be used for the cooling of the combustion chambers of these rockets, and for the repressurization systems of launch vehicles. Examples of demonstrator parts fabricated in parallel with this research are shown in Figure 1.1.

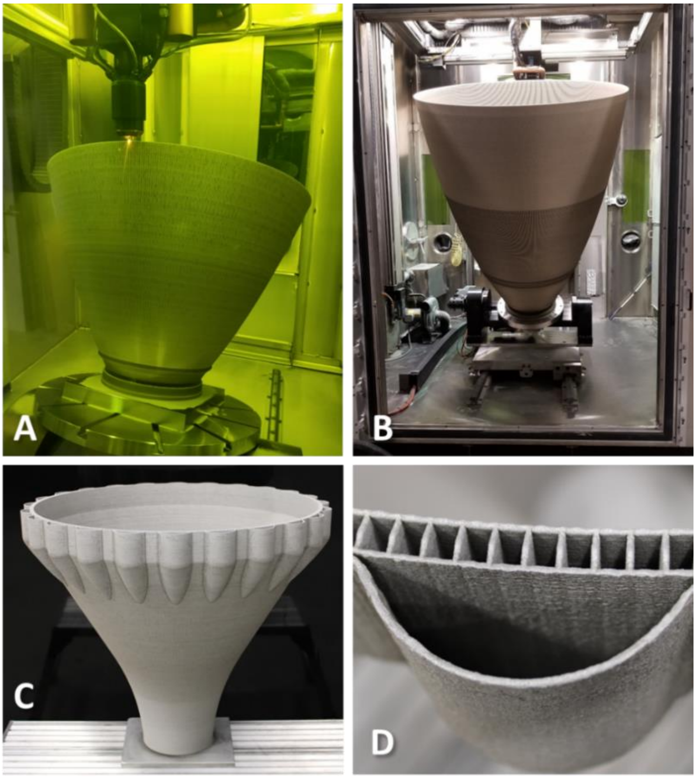

Figure 1.1. Examples of LP-DED manufacturing demonstrator heat exchangers built. A) LP-DED process shown depositing integral channels, B) Integral channel nozzle shown in LP-DED machine at 1.52 m diameter and 1.78 m height, C) Example of complex geometry using LP-DED aluminum 6061-RAM2, D) Examples of channels with 1.5 mm wall thickness in A6061-RAM2. From Ref. [6,7]

While there are many applications of heat exchangers, one of the most extreme environments they are used within is liquid rocket engines. In a liquid rocket engine system, the functionality of the overall system relies critically on heat exchanger components, specifically, the regeneratively-cooled or channel-cooled combustion chamber and nozzle. These system considerations involve a complex balance between component pressure drop, temperature rise, mass, cost, and reliability, in addition to other technical and programmatic metrics [8,9]. While the combustion chamber and nozzle direct the hot combustion products to create thrust, they incorporate integral channels to allow for active cooling of the internal surface to maintain adequate structural margins to prevent failure [10]. These internal channels act as a heat exchanger between the hot combustion gases and propellant being used for active cooling to increase the performance of the thermodynamic cycle. Heat exchangers allow for performance optimization through increases or decreases in fluid temperature, or through the reduction of structural wall temperatures through active cooling for high heat flux environments [1].

1.2 TRADITIONAL MANUFACTURING METHODS

Compact heat exchangers are designed and realized using tubes, micro-channels, passages of various shapes, or fins to increase the surface area and require thin-walls (< 2 mm) and compact form factors to minimize overall mass. While complex designs can be conceptualized and analyzed, the heat exchanger must be manufacturable with tight tolerances to contain high pressure fluids, which often limit the design space. In addition to meeting technical performance and manufacturing requirements, programmatic requirements (cost, schedule, reliability, maintainability, risk tolerance) must also be considered to ensure that a part is optimized for integration and use in the overall system. Given that the environments that these propulsion components must endure can be challenging or even extreme, the manufacturing to meet these specifications often require long lead times due to specialty processes and unique tooling associated with the combined thin-wall integral channel and large-scale structures.

Traditional manufacturing technologies for actively-cooled combustion chambers and nozzle heat exchangers include either tube-wall fabrication or channel-wall fabrication methods [11]. Tube-wall regeneratively-cooled components use a series of individual tubes that are bonded together by brazing or other joining methods in order to form the complete structure (Figure 1.2) [12]. Channel-wall manufacturing methods use an internal liner with slotted channels that are closed out using plating, brazing, laser welding or other bonding methods [13]. This forms the channels that contain the high pressure fluid [14]. With either of the fabrication methods, a series of manifolds distributes the fluid (fuel or oxidizer) to the individual channels or tubes. Alternate methods of cooling include film cooling through slots or transpiration cooling, but dependent on the engine cycle selected [12].

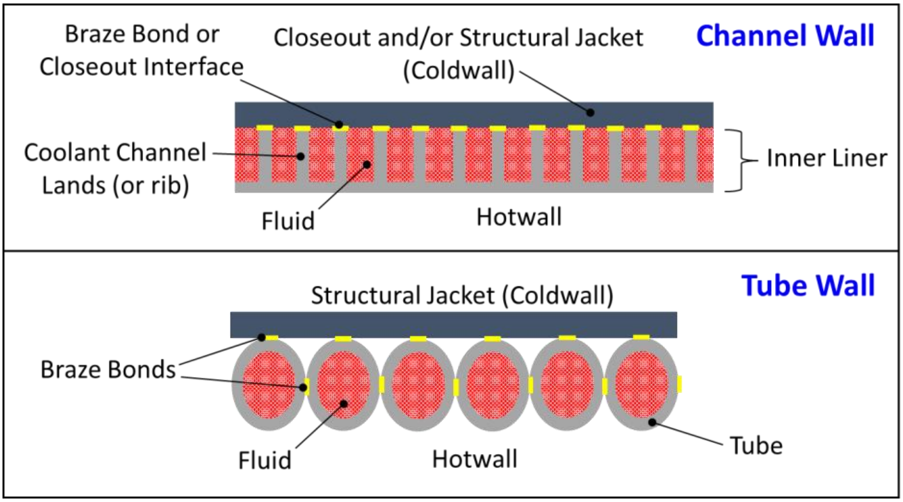

Figure 1.2. Schematic cross-section of cooling channels for actively-cooled chambers or nozzles which are different, depending on the adopted manufacturing method. From Ref. [15].

Various manufacturing techniques for fabrication of combustion chambers and nozzles have been evaluated and matured. An overview of the various steps to produce a traditional channel-wall component, including the liner perform, formation of the coolant channels, closeout of the coolant channels, and assembly of the manifolds, are illustrated in Figure 1.3 [13]. The traditional manufacturing process includes brazing, joining (welding), and plating. These techniques are actively used for production of flight components and can produce cooling channels capable of containing the high pressure propellants [16–18]. Several advanced techniques, some of which achieved flight maturity, include pressure-assisted hot isostatic pressing (HIP) bonding, vacuum plasma spraying (VPS), and laser welding of sandwich wall nozzles [19,20]. These novel techniques have proven advantageous over the more traditional brazing and plating processes.

Pressure-assisted HIP bonding has been used to improve bonding between the liner and structural jacket. This process uses pressure to deform the liner into close contact with the jacket and the brazing foil is melted to create the bond [21]. This approach has successfully reduced the amount of scrapped units and established a robust metallurgical bond. However, its limitations include the need for significant tooling, experimental development for heating and cooling rates of the HIP cycle, and detailed models to predict liner deformation for determining appropriate brazing gaps. VPS has been utilized for the closeout of chambers and nozzles by depositing material onto a slotted liner forming the closeout of the channels which must resist to the pressure of the propellant. This method improved the strength of the bond between the liner and jacket, but the channels must be filled with a sacrificial material, which is later removed. Challenges arise as the filler material needs to be compatible with the elevated temperatures of the deposition, leading to common blockages within channels.

The laser-welded sandwich nozzle process employs a laser welding technique to weld each channel rib/land between the internal liner and closeout jacket. This process actively tracks each rib seam in real-time using X-ray technology, followed by the laser weld bead [22]. While this process automates the closeout process, it still requires the initial forming and slotting of the inner and outer cones to ensure proper gaps for welding. The overall process involves multiple pieces and post-processing steps to complete a nozzle.

These traditional manufacturing techniques and their associated lifecycles involve sequential steps and potential long-lead times for materials or processing (*e.g.*, forging, liner machining, slotting, closeout, etc.), which in turn introduce the possibility of issues [15,23]. Despite advancements, these methods still necessitate sheet forming or forgings, tight-tolerance machining, slotting of coolant channels, and assembly operations to ensure leak-free joints. The extensive tooling required for these processes often causes higher costs than the actual components being built.

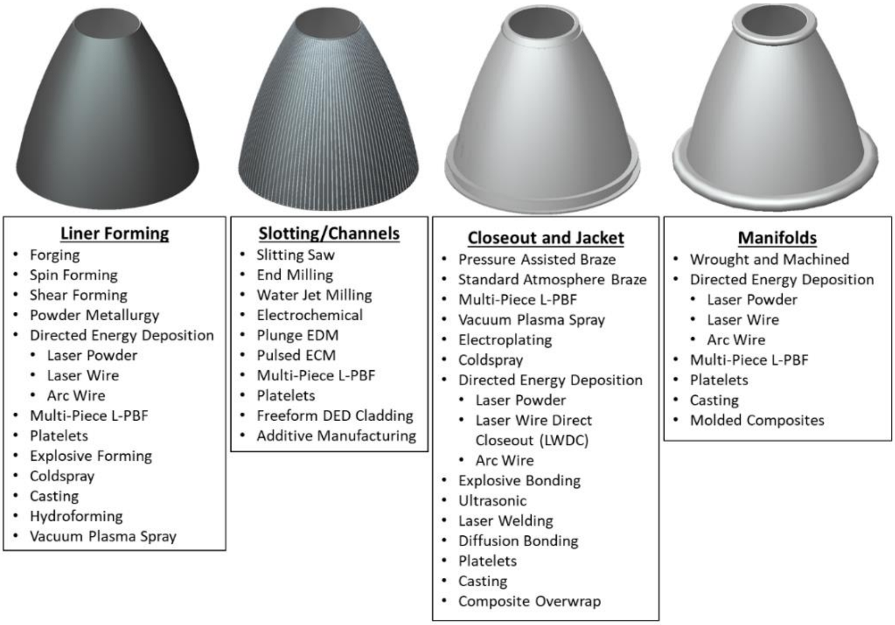

Figure 1.3. Process steps and fabrication options for channel wall nozzles and combustion chambers of rocket engines [13].

Manufacturing technologies are continually being developed to meet the need for higher performance components in terms of increased efficiency and reliability, decreased cost, decreased mass, or increased production rates [17,24,25]. Several designs have been conceived, only to discover that certain parts cannot be fabricated, that manufacturing limitations result in unintended performance consequences, or that the manufacturing cost is prohibitively high. All manufacturing processes are affected by limitations which in turn have repercussions on the entire lifecycle, therefore they must be well understood and solutions for these limitations must be incorporated into the design at an early stage [26]. Therefore, when a manufacturing process is being industrialized, it must be fully characterized to determine limits, tolerances, repeatability, and reproducibility to allow designers to achieve optimal solutions [27]. Once a manufacturing process has been baselined, adjustments or improvements can be pursued to further optimize it, like, for example, the inclusion of secondary process steps, if gaps were identified.

These manufacturing methods are complex because of the extremely tight tolerances required to form fluid passages that are leak-free. The surface texture inside these small cross-sectional area channels is extremely critical as it is directly related to the heat transfer and fluid dynamic performance of the component [28]. Traditional manufacturing methods, such as milling, allow for a roughness of the channels surfaces that is typically less than 3.2 μm [29]. All these system and component level considerations must be accounted for in the design and then translated into manufacturing requirements that can meet the design intent once fabrication is completed. The fabrication and manufacturing of the complex features in these components is extremely challenging and as complexity increases so does cost [30]. These consideration put into evidence an opportunity to develop and advance new manufacturing techniques for extreme-environment heat exchangers aimed at improving the following attributes [13]:

- Thinner hotwalls and ribs for effective cooling in a high heat flux environment.
- Complex internal features, or channels, to allow for increased fluid dynamic and heat transfer performance.
- Tailoring the surface texture (roughness) and optimized channel geometry to balance pressure drop and heat transfer effectiveness.
- Ability to eliminate joints or produce robust joints at increased bond temperatures.
- Ability to inspect the internal channel features and quality of the material.
- Reduction or elimination of non-recurring tooling.
- Reduction in assembly build hours and elimination of manual processing.
- Reduction in lead time for materials or processes.
- Provide new options for materials and material combinations (i.e. monolithic, bimetallic and multi-metallic).
- Direct build and/or simplified attachment of fluid distribution manifolds.
- Increased system performance through component mass reduction or hydraulic performance.
- Scalable to large scale components (>1 m diameter).

1.3 ADDITIVE MANUFACTURING FOR HEAT EXCHANGERS

Additive manufacturing (AM) is gaining recognition as a viable production technology in the aerospace industry, and particularly for thermal equipment of propulsion systems, transitioning from a mere prototyping tool to a full flight-qualified production of end-use parts and subsystems [31]. The key advantages of AM distinguishing it from conventional manufacturing methods include the ability to make very complex geometries, cost reduction, reduction of processing time, and elimination of joints and consolidation of parts. AM allows for the realization of complex part features that would be unattainable through traditional or emerging manufacturing techniques, even more so if novel metal alloys must be employed. Metal AM encompasses a myriad of processes, with unique benefits and disadvantages affecting different build sizes, microstructures arising from various melting or solid-state bonding methods, and geometries, ranging from coarse to finely detailed [32–35]. These high-level metal AM categories include:

- powder bed fusion (PBF),
- directed energy deposition (DED), and
- solid-state (cold spray, ultrasonic additive manufacturing, additive friction stir deposition, and binder jetting) [36].

These metal AM processes are being developed and actively used in aerospace, medical, and industrial applications [37]. As each AM process evolves, it becomes imperative to comprehensively characterize the achievable geometries (features and resolution), feedstock, microstructure, resulting properties, part size, deposition rates, industrial maturity, post-processing requirements, and lifecycle economics associated with each specific technology and the corresponding metal alloys [36,38–40]. Design for additive manufacturing (DfAM) guidelines are unique for each AM process and cannot be applied more broadly therefore using a DfAM guideline specific for one process for another. Without a proper application of specific guidelines, an end-use AM component may not meet the intended structural, thermal, dynamic, fluid flow, or life requirements [41]. Although AM offers significant design complexity, certain guidelines must still be followed to ensure that parts are correctly built and processed for their final application. Most AM research on PBF and DED processes focuses on microstructure and related mechanical and thermophysical properties. There is limited research on the development of DfAM guidelines for these processes, therefore on how these processes relate to geometry capabilities and limitations along with their impact on component and system performance [42–45].

Laser Powder Bed Fusion (L-PBF) is one of the most widely adopted AM processes, providing the ability to fabricate thin-walls (0.2 to 0.4 mm), small passages and channels (0.2 mm diameter), and complex shapes [46–48]. L-PBF is conducted within an inert *build box*, initiated with the uniform distribution of powder feedstock on a *build plate* (Figure 1.4). The laser melts the material within a layer whose thickness ranges from 30 to 100 µm, following a specified scan path derived from the CAD model geometry sliced into layers. Inert gas is blown from the side of the build plate to remove particle ejecta, minimizing the contamination of the material forming the part being built. Subsequently, the recoater arm disperses a fresh layer of powder, and this cyclic process is repeated numerous times (*i.e.*, hundreds or thousands) until completion of the part.

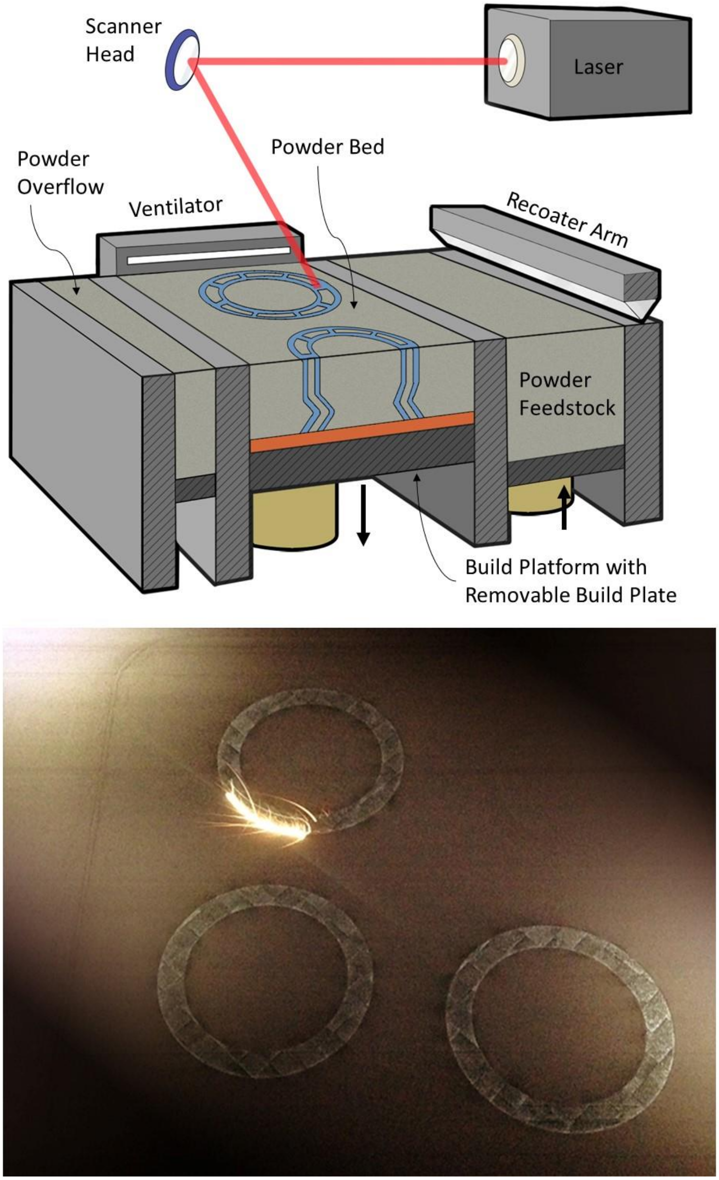

Figure 1.4. Schematic representation of a Laser Powder Bed Fusion (L-PBF) System (from Ref. [49]) and exemplary photograph of a part being built with L-PBF (image courtesy of NASA).

The ability to manufacture very complexity parts makes L-PBF an ideal manufacturing process for the production of heat exchangers used in aerospace vehicles, power plants and energy storage systems, electronics cooling systems, chemical plants, and oil and gas plants [50]. L-PBF has reached a good state of maturity (*i.e.*, high technology readiness level) and is widely available and actively employed in commercial and military aviation and spaceflight. Several integral-channel combustion chambers manufactured with L-PBF equipping propulsion systems from Rocket Lab, SpaceX, Relativity Space, ABL Space Systems, Ursa Major, and Aerojet Rocketdyne have successfully flown [26,51]. Commercial space companies worldwide, the National Aeronautics and Space Administration (NASA), European Space Agency (ESA), Japanese Aerospace Exploration Agency (JAXA) and several other organizations and academic institutions have tested combustion chambers and nozzles made with L-PBF on the ground [51–54]. Figure 1.5 shows several examples of L-PBF combustion chambers.

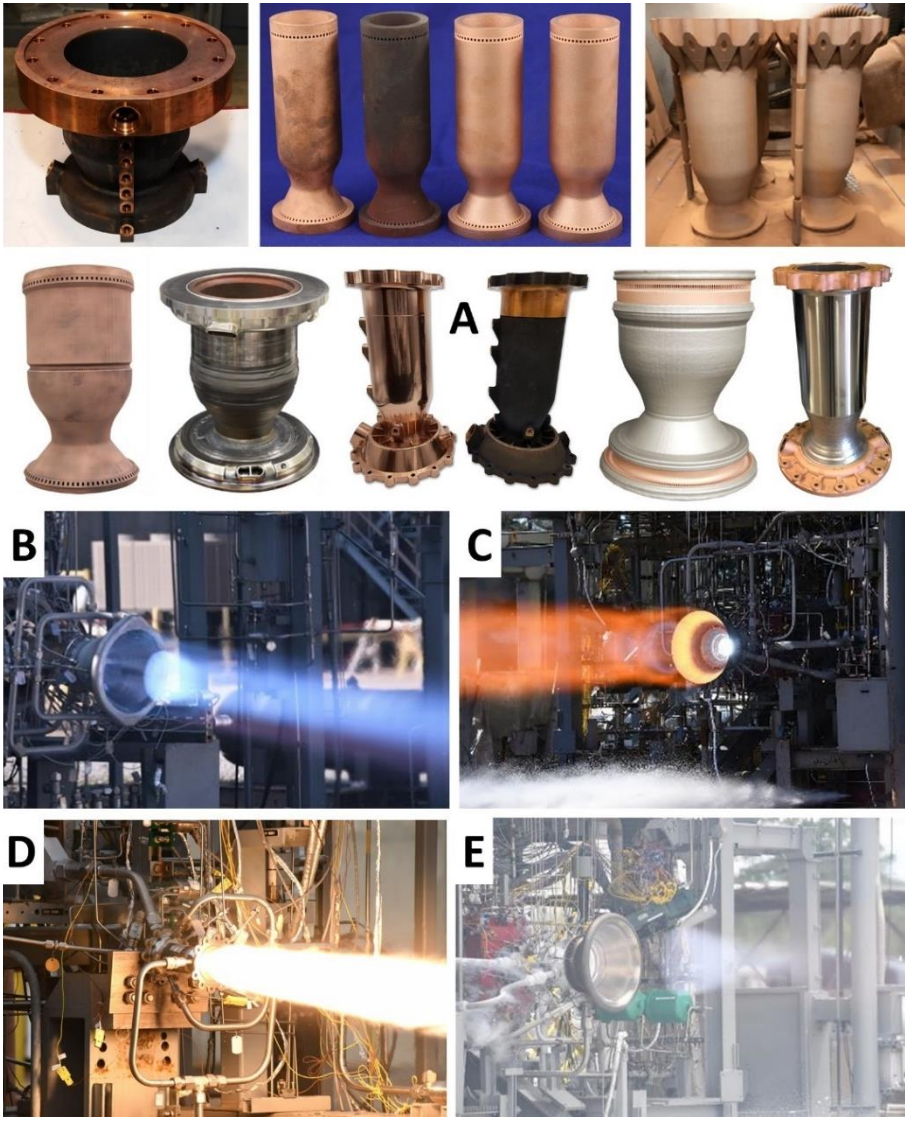

Figure 1.5. Examples of various integral channel combustion chambers and nozzles manufactured with L-PBF and tested by NASA. A) Various thrust-class GRCop-42 and bimetallic AM combustion chambers, B) Liquid Oxygen (LOX)/Liquid Methane (LCH4) Testing of 31 kN GRCop-42 Chamber and LP-DED nozzle, C) LOX/Liquid Hydrogen (LH2) Testing of 111 kN L-PBF/DED Bimetallic Chamber, D) LOX/RP-1 10kN Bimetallic L-PBF Chamber, E) LOX/LH2 150 kN Testing of Bimetallic L-PBF/DED Chamber and LP-DED nozzle (Courtesy: NASA) [26,52,55–57]

Research related to additive manufacturing for heat exchangers has grown significantly starting from 2006. In an initial study conducted in 2006, L-PBF was employed with a primary focus on the manufacturing of cooling systems for electronic components [58]. Research continued in diverse areas, and a notable study by Lu et al. documents the evaluation of the flow performance of micro-scale coolant channels with a 2:1 aspect ratio made with L-PBF and metal micromolding [28]. The predominate use of AM microchannels (< 3 mm) has focused on the L-PBF process [59–62].

While L-PBF has been shown to be of great benefit for the fine feature manufacturing of ultra-compact heat exchangers, its main limitation is the maximum volume of the component that can be built [63,64]. This size limitation is due to maximum dimensions of the (powder filled) build box, which typically must be less than 400 mm in each direction (X, Y, Z) and to the maximum build diameter which is 600 mm [26,36]. Custom machines capable of dealing with up to 1 m build diameter and 1.2 m in height have been developed, but they are not readily available in industry. The manufacturing of compact heat exchangers for aerospace propulsion systems and especially those of large rocket engines requires the capability to handle large volumes, given the growing need to fulfill ever increasing thrust requirements and therefore larger dimensions. For engines and combustion chambers produced using L-PBF, the thrust class is generally limited to 1,100 kN. For components, such as regeneratively-cooled nozzles, which are inherently larger (600 mm diameter), directed energy deposition (DED) is a suitable manufacturing technology [5,36]. Figure 1.6 shows a comparison of various AM processes in terms of build volumes and minimum feature sizes. Heat exchangers for power and propulsion applications require obtaining thin metal walls for the flow channels (typically below 1.5 mm).

Zhang et al. provided a comprehensive report on emerging AM processes for heat exchangers but did not acknowledge the possibility of employing directed energy deposition (DED) techniques [65]. Despite several authors have published extensive review papers on the potential of AM for heat exchangers, none of them has identified the DED process as suitable for this purpose [63,64,66–69]. Careri et al., in a review article on heat exchangers [70], explicitly state that DED is not suitable due to the poor surface finishing that can be obtained, its inability to make thin features, and its low dimensional accuracy.

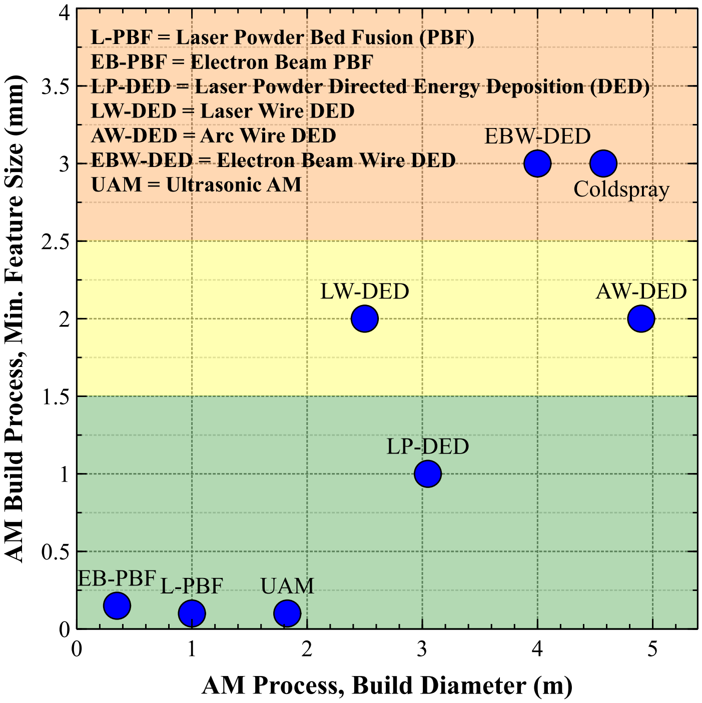

Figure 1.6. Comparison of AM processes considering feature size and build diameter. The green band groups AM processes that can produce wall thicknesses below 1.5 mm, while the yellow and orange bands indicate AM techniques that may require additional processing.

While AM offers numerous technical and programmatic advantages, it also presents several challenges that necessitate further research. Technical challenges include high surface texture, distortion, residual stresses, mechanical and geometric variations across different AM processes and machines, alloy weldability issues, limited process capability data, and insufficient mechanical and flow performance data [71]. Programmatic challenges encompass limited production volumes, potential risks associated with new technology, the need for training and education throughout the AM lifecycle, significant capital investments, and the cultural shift required for industry adoption of the technology.

To mature AM, it is essential to characterize each of the AM processes and the specific alloys of interest to generate data relevant to industrial applications. Unlike traditional manufacturing technologies, which have benefited from decades and centuries of experience, AM is relatively new, resulting in limited materials and process data. While thousands of metal alloys have been optimized for traditional manufacturing techniques, fewer than 100 alloys have been refined for AM processes and less than 10 qualified for flight applications [72]. This challenge is further compounded by the unique microstructures and properties produced by each AM process, as well as the process limitations related to specific alloys and geometries required for end-use parts [36].

1.4 THE LP-DED PROCESS

LP-DED (Figure 1.7) is a process in which a laser beam is directed to a powder stream which is blown in its focus forming a melt pool which subsequently solidifies thus forming the part by deposition of successive layers [73]. The blown powder deposition head and the laser beam optics are mounted on a gantry (or robot) to allow for the precise motion control needed to manufacture thin-wall features [74]. The laser is typically central to the integrated deposition head and the powder being blown is concentric with the laser. The blown powder deposition nozzles can be located in a coaxial annular ring or they are separate nozzles, typically 3 or 4, spaced equally around the laser beam [75].

The LP-DED process allows large scale fabrication (>3 meters) using metal powder feedstock, only limited by the robotic or Cartesian gantry system [76]. Freeform structures are fabricated based on toolpaths generated from CAD models. The size of the powder particles and particle size distributions (PSD) can vary from coarse (45 – 105 µm) to fine (15 – 45 µm) [75]. Examples of LP-DED applications include casting and forging replacements, cladding and repair, fabrication of primary structures, as well as thin-wall large diameter structures such as heat exchangers and rocket nozzles with integral channels [5,77]. However, the manufacturing of thin-wall components with integral channels with LP-DED is at a low maturity level: the characterization of the process is limited and DfAM practices are not established.

As indicated in Figure 1.6, Laser Powder DED (LP-DED) can overcome the limitation regarding overall object size affecting L-PBF, while still allowing to incorporate thin-wall (1 mm) internal flow passages or microchannels into the part [13,78].

The work reported in this dissertation provides design engineers with information about process limitations, design guidelines, post-processing requirements, and experimental test data related to the manufacturing of microchannels with LP-DED.

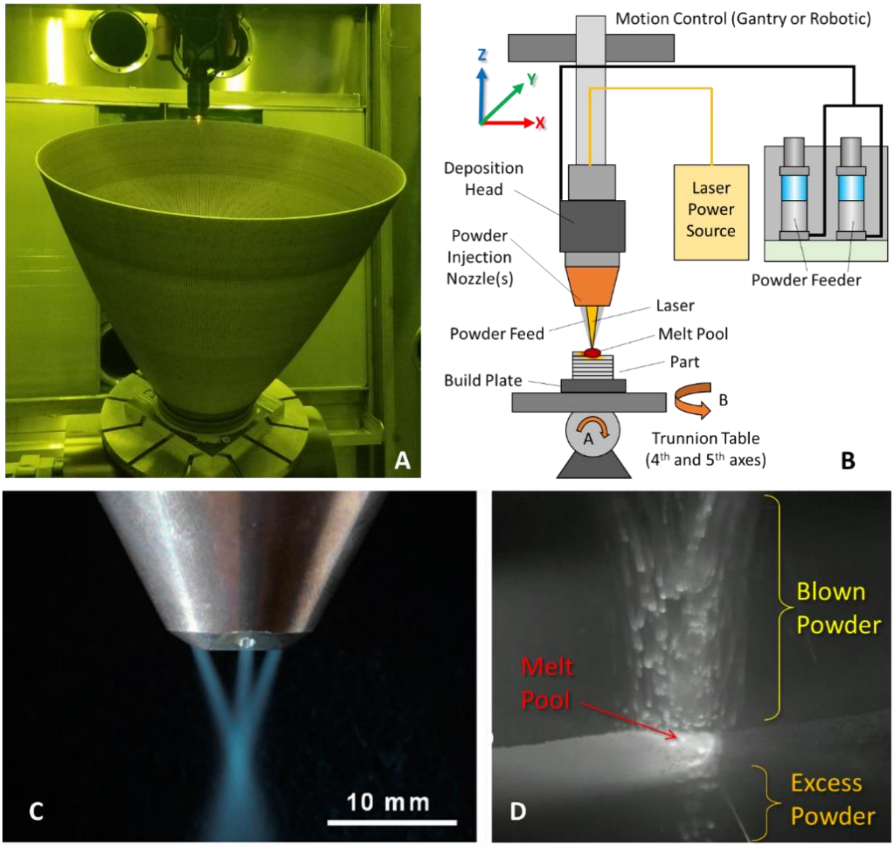

Figure 1.7. Laser Powder DED System. A) Large scale integral channel nozzle (> 1 m diameter) during fabrication, B) Schematic overview of the LP-DED system with its components [51], C) Metal powder flow blown through a three-nozzle configuration (From Zhong [79]; CC BY doi.org/10.3390/met7100443), D) Macroscopic view of metal powder blown into the melt pool and excess powder (Image courtesy of Formalloy, Ref. [49]).

1.5 POTENTIAL AND CHALLENGES OF LP-DED

Contrary to L-PBF, for which extensive research about the design and manufacturing of thin-wall features has been performed [80–82], significant research gaps in the detailed characterization of the LP-DED process affect its more widespread adoption. These gaps encompass surface texture characterization, thin-wall geometry feasibility, repeatability, build angle limitations assessment, wall thickness control, and the characterization of the microstructure (including density) of the material of thin-wall components. Notably, the melt pool generated by LP-

DED is considerably larger (approximately 1 mm) compared to that generated with the L-PBF process (~120 µm), and it is determined by the laser spot size [83,84]. Due to this larger melt pool, the formation of thin walls necessitates a single-pass bead, precluding the use of a contour pass—a method employed in L-PBF to enhance surface finishing [85].

Few fundamental studies on material microstructure have been conducted on thin-walls (<3 mm) produced using the LP-DED process, however these studies do not yield sufficient data to enable the design of microchannels. Liu and Li demonstrated the feasibility of thin-walls in Steel 24 for a thickness down to 0.8 mm, employing a coaxial deposition head and 45-80 µm sized powder [86]. Margerit et al. characterized the microstructure of stainless steel 316L thin wall obtained using a coaxial deposition head with a 0.2 mm layer thickness and a wall thickness of 0.8 mm [87]. Other studies on 316L as a build material focused on microstructure and mechanical properties and were conducted by various researchers who investigated samples with wall thickness ranging from 0.7 to 2.1 mm [88–91]. The evaluation of superalloy Inconel 718 as a build material for thin-wall components was also completed. The experiments concerned single-track wall thicknesses ranging from 1.3 to 2.5 mm [92–94]. Additional research on the use of LP-DED for the manufacturing of thin-wall components referenced in literature include the adoption of Hastelloy X as build material with wall thicknesses ranging from 1.7 to 3.2 mm [95,96], Stainless Steel 410 [97], Stainless Steel 304L (1.2 mm thin-wall thickness) [98], Titanium Ti-6Al-4V [99,100], Gamma Titanium Aluminide (1.5 mm thin-wall thickness) [101], Inconel 625 [102], CrCoNi [103], M4 high speed Steel (1.7 mm thin-wall thickness) [104], and Al-Mg-Mn-Sc-Zr (1.6 mm thin-wall thickness) [105]. Most of these studies focused on parameter development and the resulting microstructure and mechanical properties. The built specimens were often limited in overall height, with many using single beads, and most specimens restricted to <10 mm overall height. While some studies briefly mentioned surface roughness, quantified observations were often limited (*e.g.*, contact profilometry, visual inspection) or not provided.

Surface texture, encompassing roughness and waviness and commonly referred to as surface finish, stands out as a notable drawback of AM if compared to traditional manufacturing technologies [106,107]. This texture significantly influences various characteristics related to heat exchangers, including fluid flow regime, related heat transfer properties, and mechanical properties. Elevated surface texture can detrimentally impact components' performance by diminishing fatigue resistance and, consequently, operational lifespan. It can also increase mechanical friction and wear, negatively influence fluid friction factors within flow channels, leading to higher pressure drop, and enhance corrosion potential in harsh environments [108–111]. The surface roughness of L-PBF-manufactured thin-wall samples made of various metal alloys has been extensively examined in relation to diverse industrial applications [45,112,113]. However, detailed characterization of surface texture of thin-wall surfaces generated with LP-DED remains scarcely documented in the literature [114,115]. Existing studies suggest that surface texture and geometric inaccuracies are drawbacks of the LP-DED process, emphasizing the need for a deeper understanding of processing parameters to facilitate broader commercial adoption [88,116].

Common challenges associated with the use of LP-DED for heat exchangers manufacturing include aspects of surface finishing connected with various surface texture components, from shape deviation (form) to excessive waviness and roughness. Shape deviation can stem from residual stresses and resulting distortion influenced by factors such as part geometry, alloy, build plate geometry, build parameters, and powder feedstock. All these factors collectively affect the thermal history, on which the final quality of the component so much depends [91,117]. Surface waviness is frequently observed in the form of lateral periodic menisci, a consequence of stacked deposited build layers or the stair-stepping effect [118,119]. The identified mechanism causing roughness in LP-DED involves residual unmelted and melted powder emanating from the melt pool, ricocheting, or excess powder not captured in the melt pool, leading to powder agglomerations or adherence to the wall [84]. This powder adherence can be further exacerbated with smaller spot sizes, necessary for thin-walls, due to the low powder efficiency (5-20%) captured in the melt pool [120,121].

1.6 SURFACE TEXTURE AND ENHANCEMENTS FOR LP-DED

The level of the overall surface finish or roughness, as it is often referred to, is identified as one of the key issues affecting the use of additively manufactured parts, and in particular for heat exchangers [122]. Azarniya et al. offer a similar perspective to Careri et al. and identified both the surface finish and geometric inaccuracies as drawbacks specifically of the LP-DED process [116]: post-processing operations may be necessary, which could increase the production lead time and cost, thus surface finish "remains a major challenge that requires additional developments." Alsulami mentions the DED process in the literature review of one of his articles, see Ref. [69], but only in the context that it could provide the possibility of using multiple materials within a build, thus offering additional advantages for the manufacturing of special heat exchangers.

Several references document the knowledge gap affecting specifically the high texture of AM surfaces [44,74,123]. Research conducted by Chua et al. shows that no database about texture of AM surfaces exists yet, and knowledge is lacking regarding the obtainable surface roughness [124]. Although there is extensive discussion on AM surface roughness in various articles, such research predominantly concentrates on its connection to fatigue. Limited information is available regarding its impact on flow performance in case of heat exchangers [125–127]. Hanson et al. analyzed the dependence of flow performance on surface roughness in case L-PBF is the manufacturing technology [128]. This large effect of surface roughness is attributed to the dimension of the irregular structures in comparison to the channel dimensions. Another such study is the thesis by Tommila in 2017 [129], which focused on the surface roughness of a rocket nozzle's interior hotwall at the boundary layer and the theoretical increase in viscous losses in turbulent flows. In another study [130], Stimpson concluded that rough channel surfaces for internal cooling resulting from L-PBF might promote an increase in heat transfer performance and using components in the as-built surface condition may offer benefits.

Numerous post-processing techniques have been suggested to mitigate the effect of excessive surface roughness [131–138]. A summary of these techniques is provided in Table 1.1, based on Ref. [51]. Nevertheless, it is acknowledged that smoothing internal surfaces can pose challenges contingent upon the geometry and scale of the geometrical features [139]. Post-build machining is not a viable option since it involves accessing the interiors of channels after the AM process. Hybrid DED and integral machining is an emerging technical solution to this problem, but it is not feasible for the size and complex geometry of heat exchangers channels because it would create a faceted surface [140]. Shen and Fang authored a review article on L-PBF that focused on the polishing of internal surfaces [141]. They proposed several techniques, including abrasive flow machining, barrel finishing, magnetic abrasive finishing, chemical polishing, electropolishing, and hydrodynamic cavitation abrasive finishing.

Table 1.1. Overview of various surface enhancement techniques for AM and their applicability to LP-DED

	Surface enhancement applicability for LP-DED	
Process	**External surfaces**	**Internal surfaces**
In-process smoothing (contours)	–	–
Chemical milling (CM)	+	+
Chemical Mechanical Polishing (CMP)	+	+
Abrasive flow machining	+	+
Media suspension methods	+	–
Dissolvable / surface sensitization	+	0
Powder enhanced slurry plating	0	0
Electrochemical machining (ECM) or electropolishing (EP)	+	0
Secondary laser polishing (in-process or post)	+	–
Mechanical or Manual polishing (machining, honing, buffing, burnishing)	+	–
Grit or Bead blasting	+	–
Thermal deburring	–	–
Coatings	+	0
Peening methods	+	–
Magnetic abrasive finishing (MAF)	0	+

[a] *Note: +, potential for maturation and/or demonstrated; –, affected by significant challenges; 0, unknown and further development required.*

Surface enhancements, often referred to as polishing or surface finishing, modify the profile of the surface by removing partially adhered powder particles, waviness, pores, defects in general, or other surface anomalies resulting from the AM process. Several review papers provide overviews about surface finishing techniques for AM parts [132,142–145]. Many mechanical and chemical processes, laser-treatments, and coatings that modify the surface without removing material, are discussed in the literature. These finishing processes are often used to improve the fatigue life [146]. Many processes for finishing surfaces require line of sight and access for tooling and are limited to external surfaces. These include machining, grinding, vibratory finishing, grit or sand blasting, laser polishing, rolling, burnishing, peening [133,147,148]. A limited number of surface enhancement processes are feasible or hold potential for altering internal surfaces, and more so microchannels. These surface enhancement techniques include chemical milling, electro or electrochemical polishing, abrasive flow machining, chemical mechanical polishing, thermal energy method, and self-terminating sensitization [51,146,149–151]. Other methods, like hydrodynamic cavitation abrasive finishing [152,153] and magnetic assisted finishing [154,155] have been studied for internal channels. However, these approaches have limited applicability and lack industrialization.

Laser polishing is one of the few surface enhancement techniques that has been researched for application to components produced with the LP-DED process [148,156,157]. Laser polishing uses either the primary laser during the fabrication process or a secondary laser as part of a subsequent step to remelt specific regions on the surface. When performed in situ, the laser polishing process can be carried out between layers, but it poses challenges due to the need for direct surface access, particularly in the presence of complex geometries, including internal features like channels. The laser parameters employed for local smoothing involve lower power, a smaller spot size, and a higher scanning rate compared to the build laser parameters [158]. Focused laser beams melt targeted areas, creating a liquid melt pool that levels the surface through surface tension and gravity. The molten region solidifies rapidly, both across the surface and into surface valleys [159]. Laser polishing has been shown to reduce the surface roughness of LP-DED parts by 80–96% [160]. Figure 1.8 provides an example of laser polishing on an external LP-DED surface from Rosa et al.

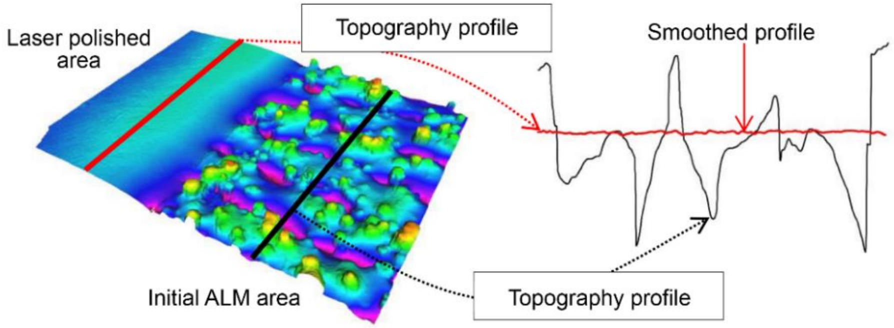

Figure 1.8. Example of laser polishing applied to a Stainless 316L LP-DED sample [161].

The laser remelting process has been demonstrated to generate recast layers approximately 22 µm thick in Inconel 718 LP-DED samples [162]. However, a notable limitation of the laser remelting polishing process is that existing research has exclusively focused on large-area surfaces, thus neglecting its applicability to fine feature [163]. In the context of a heat exchanger, where the internal surfaces of channels are crucial, the significant surface area necessitates the use of multi-axis lasing for effective smoothing.

Chemical milling (CM) and chemical mechanical polishing (CMP) are especially suitable for internal surfaces, more so if the geometry is intricate, because chemical solutions can flow through small and complex channels. [164]. Favero et al. conducted a study on the CM process by using copper chloride and ferric chloride as the chemical solution to finish the internal surface of vertically built L-PBF channels made of pure copper and featuring various internal geometries and a wetting length of 54 mm [165]. Their experimental findings revealed a reduction in the average areal roughness (Sa) of 83%, with a subsequent pressure drop decrease of 78%. However, the study did not delve into a detailed discussion of the specific mechanisms of the altered surface texture that resulted in the reduced pressure drop. Tyagi also evaluated acid-based chemical milling to reduce the average directional roughness (Ra) of an internal surface by 91% [134]. Limited public data on CMP or chemical abrasive polishing exist. Mohammadian et al. demonstrated the possibility of polishing internal wedges of Inconel 625 channels made with L-PBF using a custom CMP setup [166]. A reduction of Ra by 44% and 18% was observed, based on build orientations of 15° and 135°, respectively. Other literature discussed the use of CM and CMP for surface modification of L-PBF-made channels, but comprehensive investigations regarding these surface modifications remain limited [131,167–172].

Min et al. evaluated electrochemical polishing (ECP) for parts built with L-PBF and made of Inconel 718 alloy that included 500 µm holes [173]. A study by Jiang et al. was focused on the use of ECP to polish the inside of 3 mm diameter Hastelloy X channels produced by means of L-PBF. The results indicated an 83% reduction in Ra, but selective dissolution of the cellular structure and dependency on surface build orientation was observed [174]. An et al. demonstrated the use of combined electrochemical and mechanical polishing (ECMP) to finish the internal surface of channels with diameters as small as 18 mm and obtained a reduction of the Sa by 79.9% [175]. One limitation of this procedure is that the geometry must be simple enough to accommodate an electrode [138,164].

Ferchow et al. used abrasive flow machining (AFM) to polish 6 mm diameter internal channels obtained with L-PBF, by removing a maximum of 0.33 mm of material and thus reducing the Ra from 27.7 to 5.5 µm [176]. In another study [177], similar results are reported, but using AFM to improve the surface finishing of 8 mm diameter channels made of Inconel 718 and by means of L-PBF; in this case the Ra was reduced by 93%. Han et al. researched the application of AFM to polish 3 mm diameter maraging steel channels made with L-PBF and reduced the Sa from 7.6 µm to 1.3 µm. The peak regions were removed, but some valleys still remained [178]. Additional studies about the use of AFM for the surface finishing of internal channels were conducted and all concluded that the removal of surface peaks was prevalent but valleys remained [144].

The surface enhancement methods for internal channels detailed here were tested only on parts manufactured with L-PBF, while the use of these surface finishing technologies in association with parts obtained with the LP-DED process is not documented. Researchers have noted that geometry, AM processing, feedstock, microstructure, and heat treatments can all effect post-processing such as surface finishing [179]. Detailed conclusions about surface finishing methods cannot be generalized to different AM processes, alloys, and geometries. If the level of finishing of internal surfaces of microchannels obtained with AM is insufficient to attain the desired flow resistance or fatigue life, then an additional finishing process is required to modify the surface geometry and roughness and to remove defects. However, detailed research must be conducted for each AM process of interest, including LP-DED, as discussed in this thesis.

1.7 AIM OF THE RESEARCH

Using the LP-DED process to manufacture microchannel heat exchangers, especially for extreme environment applications, introduces challenges related to consistent geometry, wall thickness, and high surface texture. While traditional manufacturing methods like machining do not typically have issues with surface roughness and texture, adopting AM for heat exchangers presents new challenges. These require innovative design or manufacturing solutions, as well as thorough research and characterization. Although the fundamental physics of heat exchanger operation remain unchanged, the application of AM technology offers new design opportunities to optimize performance. Surface texture, in particular, emerges as a significant challenge that demands careful consideration and modifications to meet design intent. The design assumption of ideally smooth surfaces is inappropriate for LP-DED, as the actual component differs significantly from its design representation (Figure 1.9). While the obtainable surface texture may initially seem like a drawback for microchannels, it also presents an opportunity. Surface enhancements, (*i.e.*, finishing processes) can be fine-tuned to optimize fluid flow across the microchannels, thereby optimizing flow resistance and heat transfer depending on the application.

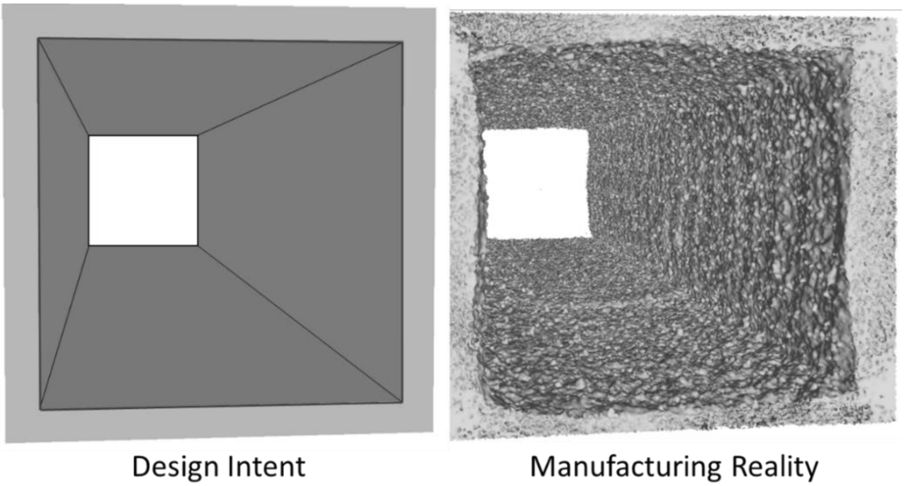

Figure 1.9. Indicative comparison between the idealized representation of a micro-channel typical of design models and the image of the actual object manufactured with the LP-DED process as obtained from a nano-Computed Tomography (CT) scan.

The results suggest that the LP-DED process can be effectively used to fabricate heat exchangers with integral micro-channels, yielding products of comparable quality and performance to those made with traditional fabrication techniques. This research aims to comprehensively characterize and evaluate microchannel fluid flow phenomena and assess the influence of the LP-DED manufacturing process, including surface modifications. The research thoroughly examines each process step, linking it to fundamental process inputs. Detailed surface characterization, analysis, and testing of heat exchanger channel samples with both as-produced (i.e., as-built) and modified surface textures are conducted to evaluate flow resistance in relation to inner surface characteristics.

To achieve this, surface texture – encompassing form, waviness, and roughness – resulting from the LP-DED process and post-processing enhancements have been measured with state-of-the-art techniques. The correlation between surface texture and fluid flow performance was established, demonstrating that LP-DED-made heat exchanger configurations can be obtained by adjusting parameters, or post-processing for specific design requirements. The fundamental aspects of the build process were evaluated, including process parameters and feedstock inputs, microchannel design and geometric limitations, and variations in post-processing techniques that affect channel flow resistance. Figure 1.10 outlines the research steps, emphasizing the variation in surface texture at each stage and its impact on flow, allowing for appropriate surface finish modifications.

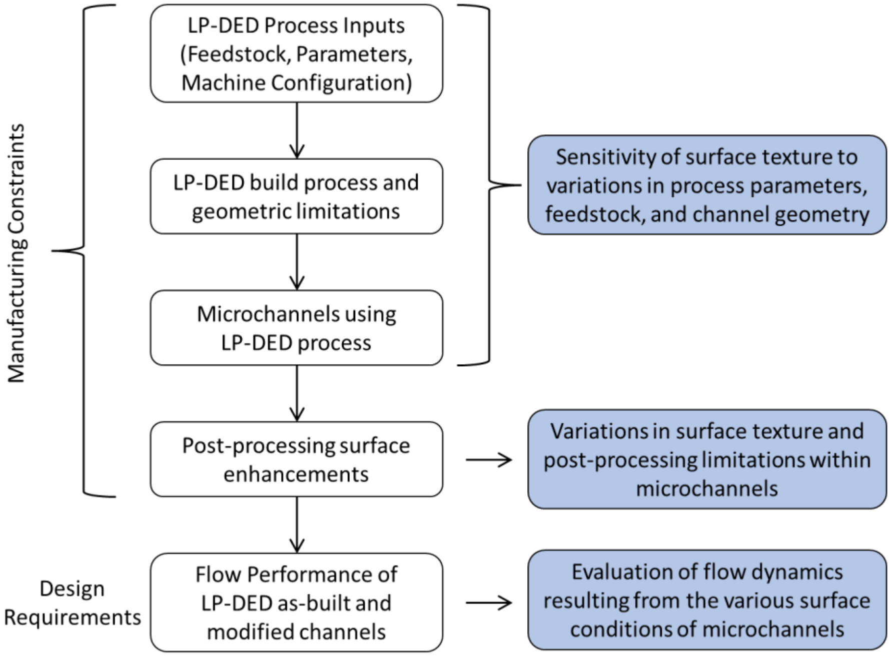

Figure 1.10. Sequential phases of the LP-DED microchannel fabrication process and related studies on surface texture aspects.

1.8 THESIS CONTENT

Chapter 2 outlines the gaps in the current state of LP-DED microchannel process development, introduces the research questions from which the research documented in this dissertation stems, and details the general methodology following the fabrication aspects presented in Figure 1.10.

Chapter 3 delves into LP-DED build process mechanics, build parameters, and their influence on thin-wall surface texture. A literature review illustrates the state of knowledge regarding the use of LP-DED to obtain parts with thin-walls. The sensitivity of the surface texture, porosity, and wall thickness based on changes in process parameters and powder feedstock size is established through a design of experiments (DOE). This chapter is based on a peer-reviewed journal article.

In Chapter 4, the scope of the research is expanded by characterizing the effect of the build angle on thin-wall samples. This establishes a baseline for LP-DED Design for Additive Manufacturing (DfAM) guidelines, addressing process limitations, surface texture, and wall thickness. The characterization of surface texture built at various angles is important for practical applications to heat exchanger designs including disparities in texture for internal and external surfaces. A literature review is also provided, highlighting the gaps related to LP-DED build constraints including wall thickness and geometric characteristics. This chapter is also based on a peer-reviewed journal article.

Chapter 5 provides an overview of microchannel heat exchanger geometry characterization. Based on a conference paper presented at the International Astronautical Congress (IAC), it covers variations in square microchannel sizes, internal and external surface texture, wall thickness, and process repeatability.

Chapter 6 focuses on post-process surface enhancements applied to LP-DED-produced internal microchannels. This chapter evaluates five different surface enhancement processes (i.e. polishing) and presents results from flow testing to determine flow resistance in terms of discharge coefficients. These results aided in identifying the underlying surface texture mechanisms that affect flow resistance in the microchannels. This chapter is based on a peer-reviewed journal article.

Chapter 7 presents a discussion based on the data gathered from all the prior chapters and summarizes experimental results and analysis on 700 mm long LP-DED microchannels modified by means of surface enhancements. This experiment focused on differential pressure measurements to determine the effect of surface texture from the surface enhancements and impact on friction factors and the different surface mechanisms that cause the changes in friction factors. The results from the experiments are discussed and correlations presented.

Finally, Chapter 8 offers brief discussions and conclusions, relating findings to original research questions. It also outlines potential applications and future research directions to expand the work.

Chapter 2

Research Questions and Methodology

2.1 GAPS IN KNOWLEDGE

Additive manufacturing has matured as a fabrication technology for heat exchangers, but currently almost all research, development and deployment efforts are dedicated to the L-PBF technique, as discussed in Chapter 1. However, the L-PBF process is affected by several relevant constraints, above all the maximum component size, and LP-DED is a solution to overcome these limitations, provided that further research and development are carried out.

In addition to the comprehensive literature review presented in Chapter 1, Chapters 3, 4, 6, and 7 provide additional discussions on the state of the art, specifically related to the LP-DED process. Through this extensive review of current knowledge, several research gaps have been discerned, paving the way for further exploration:

1. The application of LP-DED to thin-wall (<1.5 mm) heat exchangers.
2. The detailed evaluation of surface texture resulting from the application of the LP-DED process.
3. The lack of characterization of thin-walls combined with surface texture for enclosed shapes or microchannels.
4. The inadequate investigation of post-build processes like surface enhancements to improve finishing, particularly of the inside of microchannels.
5. Insufficient characterization of surface texture throughout the lifecycle of the LP-DED fabrication process, particularly microchannels.
6. The modification of the internal LP-DED surfaces to tune the flow resistance.

Thin walls are a crucial feature in extreme environment heat exchangers allowing for efficient heat transfer between fluid mediums. As indicated by existing literature, compact heat exchangers require wall thickness ranging from 0.5 to 3 mm, depending on the environmental conditions and anticipated service life [180–182]. However, the LP-DED technique is limited regarding the minimum wall thickness that can be fabricated because the laser spot size and subsequent melt pool cannot be smaller than a certain value and the fabrication time considerably increases with the thinness of walls. Although wall thicknesses as thin as 0.5 mm have been demonstrated, this approach significantly extends fabrication time, increases the risk of distortion, and imposes constraints on the feasible geometries [74]. In the context of this research, a design wall thickness of 1 mm is chosen as the lower value of all considered samples manufactured for experimental characterization. This results in a melt pool and realized wall thickness ranging from 1 – 1.2 mm [78,183].

Several studies, further detailed in chapter 1 and 3, were aimed at the evaluation of surface texture resulting from the application of the LP-DED process and focused on process parameters, deposition nozzle designs, and defect analysis, but limited to single vertical walls. In particular, the microstructure was evaluated and analyzed. Some works mention surface roughness, but characterization is generally limited to average surface texture and the details specific to waviness and roughness aspects are not discussed in detail. Any AM build process results in complex surfaces which necessitate a detailed characterization in order to correlate surface texture with flow performance. The average value of surface roughness is not a reliable indicator if flow resistance and heat transfer are to be predicted.

Surface texture of AM-produced parts of heat exchanging equipment must be characterized in terms of form, roughness, and waviness, with appropriate filtering. A useful analogy for comprehending these surface texture attributes is to envision a wavy potato chip (Figure 2.1). The overall potato chip exhibits macroscopic curvature (*i.e.*, form). To characterize the surface finish (*i.e.*, waviness and roughness), the form (or macroscopic curvature) must be eliminated: a perfectly flat surface can be obtain by digitally filtering out the mathematical representation of the macroscopic shape. The resulting flat surface is referred to as the *primary profile*, which results itself from the summation of both waviness and roughness (see Figure 9). For a more detailed characterization of the surface texture, the data representing the measured profile must be further filtered using a high-pass wavelength filter, denoted as λC, to differentiate between waviness and roughness (see Figure 2.1). Waviness is defined as the deviation from flatness characterized by longer spatial wavelengths, perceptible as the macroscopic "ridges" or regular periodic undulations on the surface of the potato chip. Roughness instead refers to microscopic irregularities on the surface, potentially arising from the deep fried or baked potato particles or salt. To eliminate any noise from the roughness profile, a low-pass filter, λS, may also be applied.

Surface texture analysis and quantification can be performed across the areal surface or based on a selected directional line or lines. Further attributes describing the waviness and roughness components may include the counting of peaks and valleys or their averages, the evaluation of core depth/height, and the calculation of the density (occurrence per unit length) of any of the mentioned parameters. The measurement of these features necessitates optical microscopy methods for characterization, while the more conventional trace profilometry is insufficient. The directional orientation of surface texture significantly influences the results. With reference to Figure 2.1, thus to the potato chip analogy, the characterization of the surface texture is based on a single profile perpendicular to the ridges results in a large value of waviness. Conversely, if the profile used for characterization is parallel to the ridges, whether on top of a ridge or within a valley, a considerably lower waviness is obtained, with roughness becoming comparatively higher. This distinction is critical, particularly in the context of fluid flow, as the build direction may play a significant role in influencing the flow characteristics. This research specifically concentrates on surface texture resulting from the LP-DED manufacturing process, an in particular on components made of specialized Iron-Nickel-Chromium alloy known as NASA HR-1. Emphasis is placed on the surface texture characterization of both thin-walls and enclosed shapes, particularly those encompassing microchannels.

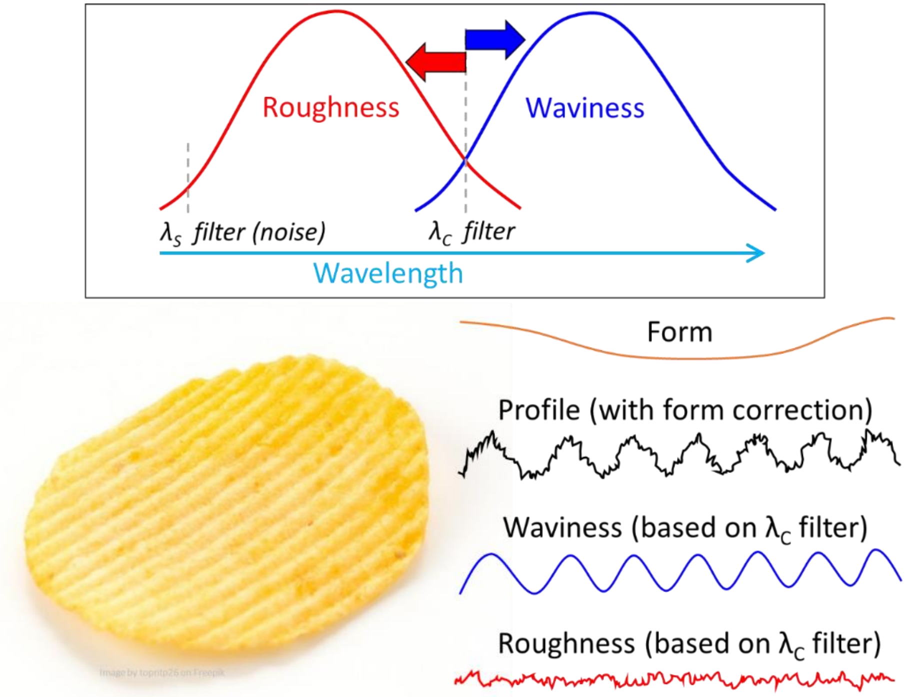

Figure 2.1. Schematic visualization of the attributes of surface texture (form, waviness and roughness): example of a wavy potato chip.

Channels in extreme environment heat exchangers can vary, but are typically measuring less than 4 mm (per side), depending on the design requirements and intended operating environments [184,185]. This experimental research specifically targets square microchannels, a common feature in large extreme environment heat exchangers [186]. Figure 2.2 shows an example of such a LP-DED-made row of channels, featuring a 1 mm wall thickness and 2.5 mm x 2.5 mm channel cross-section. The absence of literature related to LP-DED-made thin-wall channels underscores a notable gap in existing research. A detailed characterization of both the internal and external surfaces of these channels addresses this key research gap, laying the groundwork for subsequent investigations into surface enhancements and flow experiments.

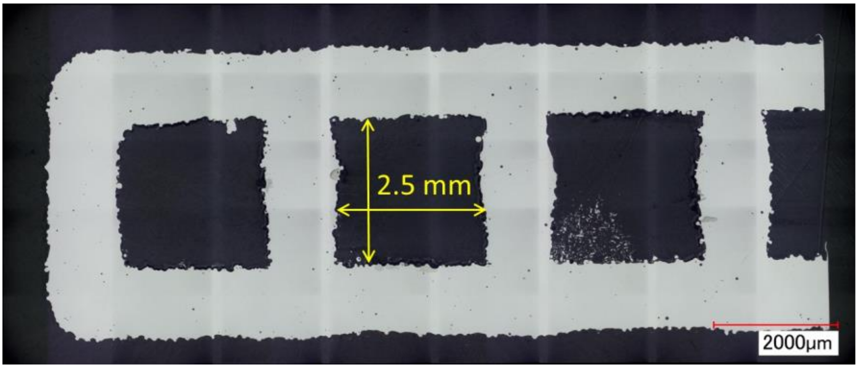

Figure 2.2. Example of typical channel that will be focus of the proposed research using the LP-DED process (Channel details shown in Chapter 5).

The cross-section of a channels row displayed in Figure 2.2 reveals irregularities not only in the surface texture but also in the ribs/lands between the microchannels (see Figure 1.2 for terminology). To address the identified gap, optical techniques were employed to measure both the surface texture and the overall geometry of the channels. This comprehensive evaluation covered various channel sizes, involving measurements and comparisons of cross-sectional areas, with particular attention to the evaluation of repeatability. The aim was to provide a detailed quantification and analysis of the surface features and of the geometric characteristics.

The examination of microchannels like those shown in Figure 2.2 led to hypothesize that the surface texture may not meet the requirements for various heat exchanger applications. A post-processing technique may be needed to modify the surface finish to meet pressure drop requirements. However, references on internal post-processing surface finishing techniques have only been demonstrated with the L-PBF process, with none related to the LP-DED process. This lack of information affect the possibility of properly designing heat exchanger because it is the impossible to accurately flow performance, which is an essential merit parameter for this equipment. Another significant knowledge gap is therefore the development and characterization of surface enhancement methods tailored to the LP-DED manufacturing process.

The effective integration of LP-DED technology into the manufacturing of heat exchangers for extreme environments requires comprehensive characterization and evaluation throughout the entire component lifecycle, not just a single process step [187]. Users of this technology must understand not only the build process but also the inputs and outputs of the process including post-processing operations, such as heat treatment and surface finishing. This includes understanding how a heat exchanger design integrates into the overall system and how both component and system sensitivities respond to changes in characteristics like surface texture. The research documented in this dissertation prioritizes a systems-level comprehension of surface texture from the conceptual and detailed design stages through manufacturing and operation (i.e., lifecycle). This requires experimental data and model validation to address all identified knowledge gaps. Therefore, the primary focus of this research is on thin-wall microchannels post-processed using various surface enhancement techniques, followed by flow testing to determine the impact on friction factors.

2.2 SURFACE TEXTURE AS A SYSTEMS ENGINEERING CHALLENGE

Compact heat exchanger performance can vary significantly due to pressure losses, changes in heat transfer, and fatigue life related to surface texture. Conceptual designs often assume a certain surface texture, but uncertainty persists until hardware fabrication. AM surface roughness can vary significantly from traditional methods, with roughness up to 50 µm, compared to less than 3.2 µm achievable with machining [29,68]. Prior studies have shown that sensitivity to surface texture can lead to component pressure drops exceeding 70% [57]. Additionally, the texture of internal microchannels affects fluid flow, while the outer surface influences hot gas flow and heat load. Research indicates that AM surfaces in the as-built condition can cause 20-30% increases in heat loads [57,108,129,139]. This can offer potential system performance advantages, such as expander engines or alternately cause potential failures with an increase wall temperature. Effectively addressing surface texture early during component conceptualization and systems design requires a comprehensive understanding of the entire design and fabrication lifecycle, particularly its integration with the intended application. The lifecycle encompasses all steps necessary to manufacture a component, from the initial material selection, machining, fabrication, forming, and assembly through to final validation, testing, and system integration.

A component designer must understand potential surface conditions from manufacturing operations to predict pressure and thermal performance accurately. Introducing a new manufacturing method requires establishing a target surface texture to ensure the overall system power balance is met. Performance differences are often tied to the manufacturing process, including incorrect geometry, surface texture, and tolerances. For instance, designers can predict pressure losses through flow passages (i.e., channels or tubes) based on an assumed surface texture for a specific manufacturing method. However, if pressure loss and heat load requirements are not met, secondary manufacturing processes may be needed to modify the surface texture, increasing manufacturing costs.

While an initial goal of AM components might be to achieve a surface finish similar to traditional manufacturing (e.g., machining), the ultimate objective of this research is to fine-tune the surface texture providing options to meet broader system requirements. Understanding and measuring surface texture in AM components immediately after the build process and throughout the lifecycle, including potential changes during post-processing or operation, is essential [188]. Post-processing in AM provides an opportunity to adjust surface texture and optimize heat exchanger performance, such as increasing heat loads or cooling pressure performance [28].

A complete understanding of surface texture throughout the AM lifecycle is crucial. Figure 2.3 introduces a holistic view of this lifecycle and addresses various questions a designer may encounter. Integrating these factors into design and manufacturing processes is key to developing effective heat exchangers for extreme environments.

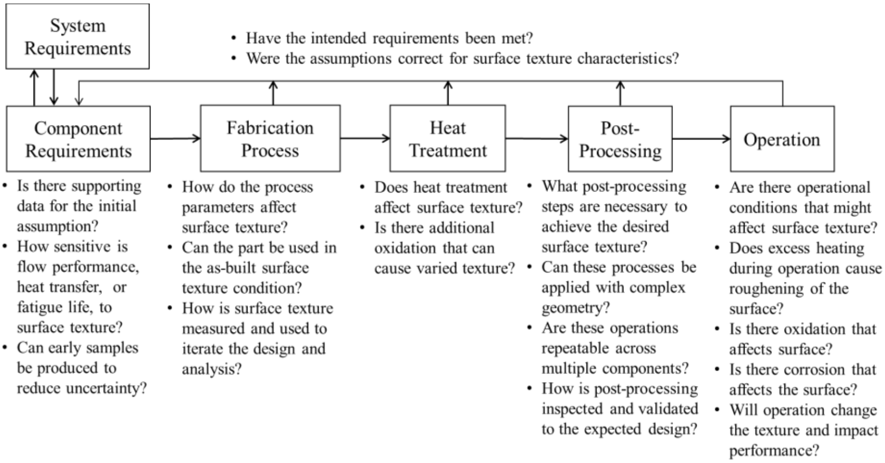

- Have the intended requirements been met?
- Were the assumptions correct for surface texture characteristics?

- Is there supporting data for the initial assumption?
- How sensitive is flow performance, heat transfer, or fatigue life, to surface texture?
- Can early samples be produced to reduce uncertainty?

- How do the process parameters affect surface texture?
- Can the part be used in the as-built surface texture condition?
- How is surface texture measured and used to iterate the design and analysis?

- Does heat treatment affect surface texture?
- Is there additional oxidation that can cause varied texture?

- What post-processing steps are necessary to achieve the desired surface texture?
- Can these processes be applied with complex geometry?
- Are these operations repeatable across multiple components?
- How is post-processing inspected and validated to the expected design?

- Are there operational conditions that might affect surface texture?
- Does excess heating during operation cause roughening of the surface?
- Is there oxidation that affects surface?
- Is there corrosion that affects the surface?
- Will operation change the texture and impact performance?

Figure 2.3. A holistic view of surface texture throughout the AM lifecycle.

2.3 RESEARCH QUESTIONS

This research endeavors to showcase the viability of LP-DED technology for the production of heat exchangers with integrated microchannels. **As discussed in Chapter 1, the primary objective of this research is to attain a comprehensive characterization of microchannel fluid flow phenomena and assess the influence of the LP-DED manufacturing process, including surface modifications.** The tailoring of the surface texture from in-process or post-processing modifications can allow the fluid flow to be optimized based on the specific component and system requirements The following research questions resulting from the analysis of the identified knowledge gaps were addressed, in addition to the listed sub-questions.

Research Question #1 (RQ1)

1. How is the surface texture of heat exchanger microchannels affected by the LP-DED fabrication process?
    a. What are the key surface texture and roughness parameters to evaluate in order to fully characterize the component and its performance?
    b. What are the key process parameters and functional relationships that can influence surface texture during the initial build?

    c. How do various geometries (angles, channel sizes) affect the surface texture?
    d. How is the surface texture impacted during post-processing stages of the fabrication after the initial build?
    e. How does the obtained texture compare to the texture obtained with traditional manufacturing technologies?
    f. What changes can be made to the LP-DED technique to improve the build process?

Research Question #2 (RQ2)

2. What are the geometrical relationships and sensitivities affecting fluid flow performance if heat exchanger channels are manufactured with the LP-DED process?
    a. How can the fluid flow performance be evaluated using LP-DED microchannels?
    b. Can the LP-DED microchannels be used in an application in the as-fabricated condition?
    c. How can the information about microchannel surface texture be effectively used during design and analysis?
    d. What differences are observed with the as-built channel surface texture compared to ideally smooth channels and surface mechanisms that affect the friction factors?

Research Question #3 (RQ3)

3. What improvements can be made to control the surface texture of thin-wall LP-DED internal microchannels?
    a. What post-processing techniques exists and can be further developed to reduce texture?
    b. To what extent can they be used to reduce or modify texture?
    c. What is the level of repeatability of these texture-reducing techniques?
    d. How can the flow performance resulting from the application of these surface improvements be characterized?
    e. What differences are observed between analytical methods and experimental flow data and how can models be improved?

In this dissertation, each chapter treats the research performed to address the mentioned knowledge gaps and to answer the listed research questions. The research outcomes are also published in several peer-reviewed journal articles and a conference paper on which the chapters are based. Figure 2.4 visually illustrates the chapters and their corresponding papers, highlighting the alignment between research questions and chapter content.

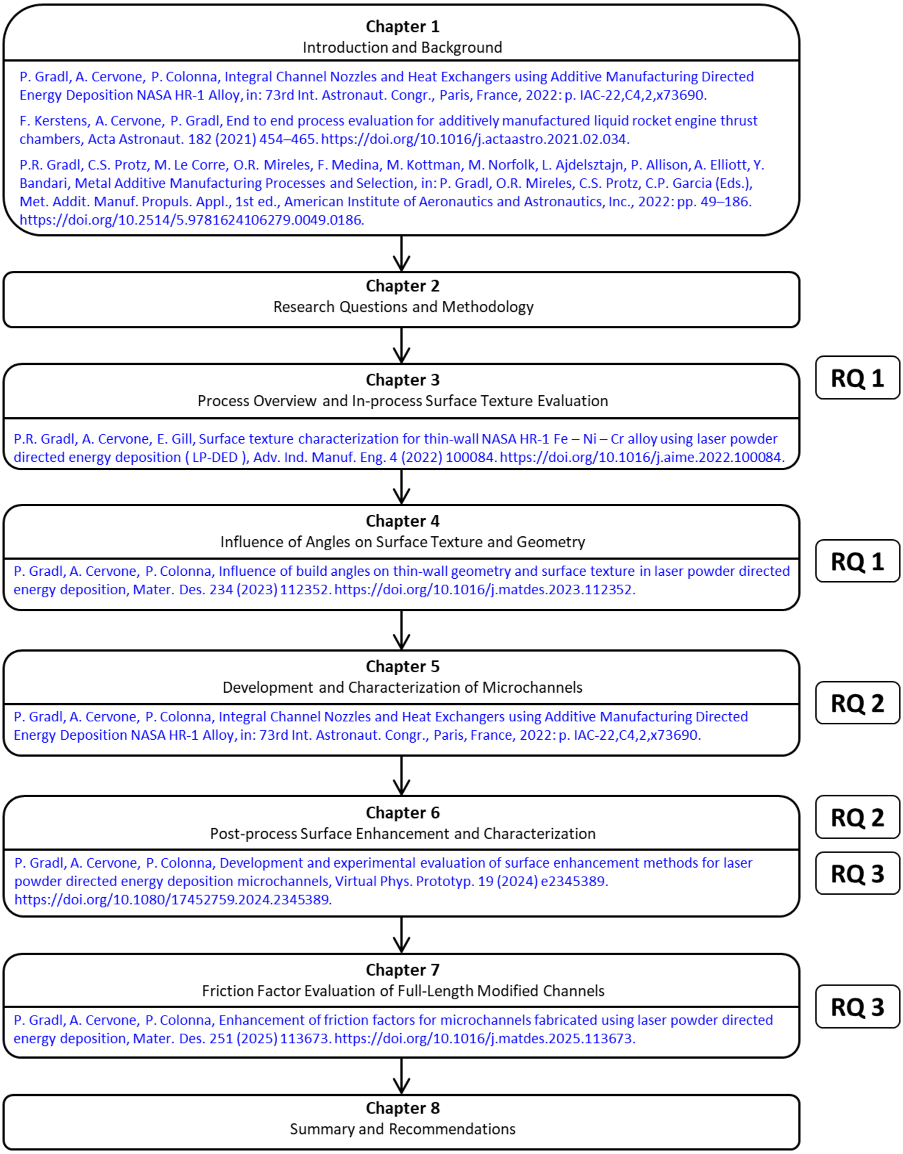

Chapter 1
Introduction and Background

P. Gradl, A. Cervone, P. Colonna, Integral Channel Nozzles and Heat Exchangers using Additive Manufacturing Directed Energy Deposition NASA HR-1 Alloy, in: 73rd Int. Astronaut. Congr., Paris, France, 2022: p. IAC-22,C4,2,x73690.

F. Kerstens, A. Cervone, P. Gradl, End to end process evaluation for additively manufactured liquid rocket engine thrust chambers, Acta Astronaut. 182 (2021) 454–465. https://doi.org/10.1016/j.actaastro.2021.02.034.

P.R. Gradl, C.S. Protz, M. Le Corre, O.R. Mireles, F. Medina, M. Kottman, M. Norfolk, L. Ajdelsztajn, P. Allison, A. Elliott, Y. Bandari, Metal Additive Manufacturing Processes and Selection, in: P. Gradl, O.R. Mireles, C.S. Protz, C.P. Garcia (Eds.), Met. Addit. Manuf. Propuls. Appl., 1st ed., American Institute of Aeronautics and Astronautics, Inc., 2022: pp. 49–186. https://doi.org/10.2514/5.9781624106279.0049.0186.

Chapter 2
Research Questions and Methodology

Chapter 3
Process Overview and In-process Surface Texture Evaluation

P.R. Gradl, A. Cervone, E. Gill, Surface texture characterization for thin-wall NASA HR-1 Fe – Ni – Cr alloy using laser powder directed energy deposition (LP-DED), Adv. Ind. Manuf. Eng. 4 (2022) 100084. https://doi.org/10.1016/j.aime.2022.100084.

RQ 1

Chapter 4
Influence of Angles on Surface Texture and Geometry

P. Gradl, A. Cervone, P. Colonna, Influence of build angles on thin-wall geometry and surface texture in laser powder directed energy deposition, Mater. Des. 234 (2023) 112352. https://doi.org/10.1016/j.matdes.2023.112352.

RQ 1

Chapter 5
Development and Characterization of Microchannels

P. Gradl, A. Cervone, P. Colonna, Integral Channel Nozzles and Heat Exchangers using Additive Manufacturing Directed Energy Deposition NASA HR-1 Alloy, in: 73rd Int. Astronaut. Congr., Paris, France, 2022: p. IAC-22,C4,2,x73690.

RQ 2

Chapter 6
Post-process Surface Enhancement and Characterization

P. Gradl, A. Cervone, P. Colonna, Development and experimental evaluation of surface enhancement methods for laser powder directed energy deposition microchannels, Virtual Phys. Prototyp. 19 (2024) e2345389. https://doi.org/10.1080/17452759.2024.2345389.

RQ 2
RQ 3

Chapter 7
Friction Factor Evaluation of Full-Length Modified Channels

P. Gradl, A. Cervone, P. Colonna, Enhancement of friction factors for microchannels fabricated using laser powder directed energy deposition, Mater. Des. 251 (2025) 113673. https://doi.org/10.1016/j.matdes.2025.113673.

RQ 3

Chapter 8
Summary and Recommendations

Figure 2.4. Chapter outline and associated publications that address the research questions (RQ), see Section 2.3.

In addition, each research question directly correlates with the identified knowledge gaps, as illustrated in Figure 2.5.

Research Questions \ Research Gaps	The application of LP-DED to thin-wall (<1.5 mm) heat exchangers.	The detailed evaluation of surface texture resulting from the application of the LP-DED process.	The lack of characterization of thin-walls combined with surface texture for enclosed shapes or channels.	The inadequate investigation of post-build processes like surface enhancements to improve finishing inside of microchannels.	Insufficient characterization of surface texture throughout the lifecycle of the LP-DED fabrication process, particularly microchannels.	The modification of the internal LP-DED surfaces to tune the flow resistance.
RQ 1: How is the surface texture of heat exchanger microchannels affected by the LP-DED fabrication process?	✓	✓	✓		✓	
RQ 2: What are the geometrical relationships and sensitivities affecting fluid flow performance when heat exchanger channels are manufactured with the LP-DED process?		✓	✓	✓	✓	✓
RQ 3: What improvements can be made to control the surface texture of thin-wall LP-DED internal microchannels?		✓	✓	✓	✓	✓

Figure 2.5. Relationship diagram of research gaps and research questions.

2.4 INNOVATIONS FROM THE RESEARCH AND METHODOLOGY

Several innovations resulting from this research can help facilitate the effective application of the LP-DED process, reducing uncertainty in designing and operating heat exchangers for extreme environments. These innovations include:

1. Determination of the build factors and relationships associated with the surface texture of thin-walls (<1.5 mm) manufactured with LP-DED using a Fe-Ni Superalloy.
2. Characterization and identification of geometric constraints for repeatable LP-DED fabrication of heat exchangers. This information is essential for designers wanting to use this technology.
3. Evaluation and characterization of surface enhancement techniques for internal microchannel features (<3 mm) manufactured with the LP-DED process to tailor the flow characteristics.
4. Development of an analytical model and correlation to estimate the pressure drop of high-roughness channels fabricated with LP-DED. The correlation is validated with experimental data.

To address how the surface texture is affected by the LP-DED fabrication process, a series of thin-wall samples (1 mm) were manufactured using the NASA HR-1 alloy, with variations in deposition parameters and powder size. A Design of Experiments (DOE) was set up to elucidate the relationships between input process parameters, powder feedstock with two different Particle Size Distribution (PSD), and the interactions between the parameters affecting the resulting surface texture. The geometry of the samples for this evaluation were enclosed vertical build boxes. The experiments provided insights into the process inputs and parameters and resulting texture for both internal and external surfaces. These samples were destructively sectioned and meticulously evaluated using optical microscopy, scanning electron microscopy, and optical metrology methods to ascertain wall thickness, porosity, and surface texture. The details of this research are discussed in Chapter 3.

While the enclosed vertical build box samples addressed the process mechanisms affecting the surface texture, they were limited to a vertical wall. For parts fabricated requiring more complex geometry thus with overhang build angles, a series of angled samples were built. This set of samples provided insights into geometric relationships and a full characterization and evaluation of process mechanisms concerning thin-wall samples with overhang angles. This research is described and discussed in Chapter 4. Finally, a set of microchannels with varying sizes were fabricated and characterized through destructive evaluation in Chapter 5. All samples were sectioned and evaluated using optical microscopy, scanning electron microscopy, and optical metrology methods to determine melt pool structure, powder particle adherence, wall thickness, channel area, and surface texture. The results from Chapters 3 and 4 collectively address how the surface texture is affected during the LP-DED fabrication process (RQ1), providing a baseline characterization for the geometric relationships affecting fluid flow performance (RQ2).

The improvements and control of the surface texture is addressed through a series of fabrication trials, experimental testing, and model correlations. Microchannel samples were manufactured (based on the results from chapter 3, 4, 5) and post-build surface enhancements were developed to modify the internal surface of the channels. Selected surface modification processes included abrasive flow machining (AFM), chemical milling (CM), chemical mechanical polishing (CMP), pulsed electrochemical machining (PECM), and thermal energy method (TEM), see Table 1. Initial water flow testing of these samples whose inner surfaces were improved with the mentioned techniques was completed, as well as tests of as-produced (i.e., as-built) channels, to determine the flow resistance and the decrease of pressure drop due to surface treatment. The channels were then destructively sectioned to determine actual flow area, perimeter, particle adherence, and detailed mechanisms causing the surface texture. This data anchored an analysis to determine the surface texture characteristics affecting flow resistance.

To further explore RQ3, a second experiment was conducted using ~600 mm length microchannel samples. Internal surfaces were modified using the AFM, CM, and CMP processes, while additional as-built surface square and round samples were fabricated to use them as baselines for comparison. Each sample underwent water flow testing at various flow rates, with pressure measurements collected to determine the differential pressure drop and resulting friction factors. The samples were destructively sectioned to determine actual flow area, perimeter, particle adherence, and surface texture. These data facilitated the validation of a model to determine the friction factors resulting from various surfaces.

Chapter 3

Process Overview and In-process Surface Evaluation

Major portions of this chapter were published in:

Gradl, P.R., Cervone, A., Gill, E., 2022. Surface texture characterization for thin-wall NASA HR-1 Fe – Ni – Cr alloy using laser powder directed energy deposition (LP-DED). Advances in Industrial and Manufacturing Engineering 4, 100084. https://doi.org/10.1016/j.aime.2022.100084

3.1 ABSTRACT

This experimental study completed a design of experiments (DOE) to determine the critical build parameters that influence surface texture for enclosed thin-wall samples. This study summarizes the characterization work of the LP-DED process for 1 mm enclosed walls with an Fe-Ni-Cr (NASA HR-1) alloy. The LP-DED parameters including laser power, powder feedrate, travel speed, layer height, and rotary atomized powder feedstock were modified in the experiment. An evaluation of the DOE samples and resulting surface texture is provided along with conclusions from these experiments. Results indicate that 3D areal and 2D profile (directional) surface texture is estimated by 2x the powder diameter that becomes captured or partially melted on the trailing edge of the melt pool. The fine powder showed a higher sensitivity to parameter changes but resulted in a higher density material and 23% reduction in roughness. Surface texture was also shown to vary between closed channel shapes (internal) due to ricochets, recirculation, and higher volume of powder available to bond compared to external (outer) surfaces. The understanding of the LP-DED process as-built surface texture is critical to fluid flow applications such as heat exchanges and can modify performance for enhanced heat transfer or can be a detriment to pressure drop.

3.2 BACKGROUND

Several studies evaluated surface texture using the LP-DED process but were limited in the application to thin-walls (< 3 mm). The LP-DED system configuration, spot size, and deposition parameters can vary significantly based on the part geometry and associated wall thickness. Riede et al. completed a study of 316L using a coaxial deposition head and powder sized from 44-106 µm and a layer thickness of 0.91 mm and reported an average areal surface roughness, Sa, of 44 µm [189]. Zhang et al. developed a unique technique for thin-wall LP-DED using a central powder deposition head with surrounding lasers and achieved a surface roughness of 3.2 µm with 75-106 µm Fe313 powder and 2.7 mm wall thickness [118]. Lu et al. completed a similar study using Fe313 alloy with a central laser beam and 75-106 µm powder resulting in 3 µm roughness and a wall thickness of 2.7 mm [190].

A study by Mahamood and Akinlabi on LP-DED Ti-6Al-4V suggested increasing laser power using a 2 mm spot size reduced the surface roughness, but was based on a horizontal cladding deposition strategy [191]. This increase in power allows for more of the powder to be melted and less residual powder available to adhere to the adjacent surfaces, but the increase in power will impact wall geometry. Kim et al. discuss that an increase in laser power and powder mass flow rate will result in increased wall thickness in addition to providing a consistent bead with less porosity [102]. A significant increase of laser power solely for thin-wall structures is not a feasible build strategy since this results in uncontrolled geometry. A study by Mazzarisi et al. also confirmed this through deposition of a 1.5 mm wall using Inconel 718 and concluded that 150% increase in laser power caused the melt pool to enlarge and resulted in a 44% increase in wall thickness [192]. Jinoop et al. completed an experimental evaluation and concluded that power was the primary contributor to the deposition geometry (width, height, and deposition rate) and powder feed rate and travel speed contributed to a lesser degree [95]. The combination of these parameters is also important since independent adjustments may not always achieve the desired results.

Another study by Mahamood and Akinlabi demonstrated that decrease in the travel speed or increase in shielding gas flow rate could reduce surface roughness, but also focused on a horizontal cladding surface [193]. In the thin-wall study by Zhang et al., it was suggested that increasing the travel speed (scan speed) provides a smoother surface due to less dwell time for the excess powder to agglomerate on the surface [118]. Alimardani et al. also provided this conclusion to reduce the travel speed to improve surface roughness, but did not provide any quantification of roughness and only visual [194]. Gharbi et al. completed a more detailed study of surface roughness for the LP-DED process on Ti-6Al-4V with wall thicknesses ranging from 1.7 to 3.5 mm [120]. It was observed that the increased travel speed could reduce the waviness in the form of the periodic menisci by a factor of 5, but only had a limited effect on the roughness (26% reduction) with a short interaction distance. Gharbi et al. concluded that the best surface roughness was obtained using higher travel speeds and higher laser power which results in spreading the melt pool.

Motion control parameters such as layer height, injection nozzle stand-off distance, and laser focal plane are referenced in literature with regards to surface roughness. Several articles suggest that reduction in vertical layer height (Z-direction), which can be partially accomplished by the increased travel speed, can improve surface roughness but may not be as efficient as other parameter adjustments [89,119,120]. The high degree of layering from height changes, resulting in waviness, is commonly observed in literature [90,92,119]. Zhu et al. evaluated an approach to change the injection plane to modify the surface roughness, but was focused on the undulations of the top surface and no quantification was provided for the side surface roughness [195]. Careri et al. discuss that the stand-off and laser focus distance in LP-DED must be critically controlled to avoid high roughness of the side surfaces and uniformity of the top surface as it relates to post-process machining, but do not quantify this either [196].

Powder feedstock is a critical input to the LP-DED process. There are several studies that reference thin-wall deposition using a particle size distribution (PSD) from 45 to 150 µm and a few studies using 15 to 45 µm. Jardon et al. demonstrated 1 mm wall thicknesses using stainless steel 316 L with various PSD, but limited the research to single pass beads on plate and no measurements of surface roughness were provided [84]. Based on visual observations, it was suggested that a lower roughness could be achieved using a finer PSD ranging from 15 to 45 µm. A study by Carroll et al. noted that with continued recycling of gas atomized from 50 to 125 µm Waspaloy powder, the surface roughness increased on the sidewalls of 0.6 mm thick samples [197]. The article observed that the mean particle size was similar through continued recycling, while flowability increased (reduced Hall Flow values). Ahsan et al. studied the LP-DED process using Ti-6Al-4V gas atomized and the plasma rotating electrode process (PREP) with 45 to 105 µm powders [198]. The mean particle diameter was found to be 94 µm for gas atomized and 72 µm for PREP. The resulting surface roughness was shown to be lower for the PREP powder compared to gas atomized as well as reduced porosity for 3 mm thick samples, although not conclusive if specific to powder size or other contributors. Based on this literature comparing various PSD ranges for LP-DED, further research is merited since the impact to surface texture and roughness was not fully quantified.

Prior literature often suggests that LP-DED requires final machining to achieve desired surface roughness for use in final applications [120,199]. Traditional machining is, however, not feasible for many AM parts, including LP-DED, as complexity increases with internal features such as those for heat exchangers. One of the limitations of the available research is the limited quantification of surface texture relative to as-built thin-walls and enclosed features fabricated using LP-DED. Several publications reference an early study by Li and Ma that evaluated horizontal surface roughness for LP-DED and does not allow roughness to be inferred for vertical surfaces [200], which considers cladding and not vertical thin walls deposited in a single bead. For proper application of surface texture for an industrial application, it must be characterized in the alloy of interest with identical geometry and parameters that are being used for the end part. The surface must be understood beyond an average roughness value (ie. Ra, Sa) since the complexity of the surface can impact the fluid pressure drop, heat transfer, and mechanical fatigue properties. Should post-processing surface enhancements be required to help tune the roughness, the value and dominance of peaks and valleys should be characterized in order to determine the proper amount of material to be removed. Considering observations from the literature, the process parameters (*e.g.*, power, travel speed, layer height, stand-off distance, powder feedrate, shielding gas flowrate), nozzle configuration, and both the powder type and size can be modified to change surface roughness but all potentially at a detriment to geometry.

The results of this research provide an in-depth understanding of surface texture (form, waviness, and roughness) as it relates to 1 mm thick walls using LP-DED processed NASA HR-1 superalloy for heat exchanger applications. The powder feedstock, AM process and associated parameters, geometry, and alloy composition can impact the as-built surface texture and the fluid flow, and the heat transfer performance can vary depending on the surface produced. It is necessary to characterize and understand the sensitivity of the process inputs for each alloy and feedstock of interest so that a designer can properly apply this knowledge for the desired end-use application. NASA HR-1 (Section 3.3.2) is a Fe-Ni-Cr superalloy used for high pressure hydrogen applications, such as heat exchangers and rocket engine nozzles. The advantage of using NASA HR-1 for these applications is its high conductivity, high fatigue strength, increased yield strength and ductility over other hydrogen-resistant alloys, and excellent hydrogen environment embrittlement (HEE) resistance. Prior literature has shown the advancements made with the NASA HR-1 alloy using LP-DED, but limited to the metallurgical aspects of the material [201,202].

Other critical aspects of this research include the detailed characterization of the as-built complex LP-DED surface texture of multi-layer single-bead deposition 1 mm walls using different sizes of rotary atomized NASA HR-1 powder. Prior studies focused on gas atomized powder. This study instead considers as-built inner (enclosed) surfaces and outer (external) surfaces with varying parameters and powder sizes, which were not discussed in prior literature for thin-wall LP-DED. A design of experiments (DOE) was conducted using the LP-DED process parameters and non-contact measurements to characterize the complex as-built surface texture. The as-built surface assumes no post-processing. While the surface texture is critical for design and end-use, the resulting geometry from the build must be balanced with consistency and repeatability of the wall thickness and material density. These were both studied using optical microscopy image analysis. This study provides a quantification for the surface conditions of the LP-DED NASA HR-1 alloy permitting designers to properly account for it and control it for thin-wall applications. This research is relevant for large scale applications (>1 m diameter) where the LP-DED process has advantages for freeform fabrication while still maintaining thin-walls (1–1.2 mm thick). The results presented are relevant to future LP-DED thin-wall components to be used on their as-built surface texture of the walls to reduce post-processing due to costs or the inability to post-process due to complexity.

3.3 METHODOLOGY

The LP-DED process uses a laser beam to create a melt pool and metal powder is injected into this pool using an inert carrier gas through a deposition head. As the deposition head traverses an area that was deposited the material cools and then solidifies creating the bead. The deposition head is attached to a motion control system, such as a multi-axis robotic arm or Cartesian coordinate gantry system. The Cartesian coordinate gantry system is preferred and was used in this study allowing for better accuracy and repeatability, which is critical for single-width bead wall thickness. After a single layer is built for the samples or part, additional layers are deposited until the final part is created. LP-DED also has the advantage of using multiple axis for complex geometries and is not limited to only 3-axes.

The samples created for this study were single-width bead racetracks with 75 mm length, 25 mm in height, and 1 mm wall thickness (adjacent walls spaced 25 mm apart). These were deposited as a racetrack as opposed to a freestanding wall to provide geometric stability and eliminate any distortion. Each sample was deposited according to the parameters established for the DOE and then measured using non-contact microscopic imaging to evaluate roughness and texture. Further characterization of the wall thickness and porosity was evaluated using microscopic and scanning electron microscope (SEM) imaging.

The LP-DED system has several subsystems that include the powder injection and purge gas flow system, the laser power supply and optics, and the motion control. Each of these subsystems must work congruently to provide the desired bead, resulting geometry, and material characteristics. These subsystems use support hardware and input parameters that can be adjusted to affect the material characteristics, including surface roughness. The laser and optical system include many of the laser parameters and optical hardware that derive the beam delivery including the power, spot size, focus position, profile of beam, type of laser, and laser operational mode (such as continuous or pulsed). The powder injection system includes systems and inputs such as the powder feedrate, type of carrier gas, core shielding gas and/or secondary gas flow (mass flow rate and gas type), and the powder nozzle design (annular or multi-nozzle). The motion control system manipulates the movement parameter for the deposition head that includes the travel speed, sets layer height, standoff distance, angle of the head, and hatching (or step-over). While these parameters are fundamental to the basic build geometry, other factors may be more specific to component build geometry, such as spacing between features, build plate configuration, and toolpath build strategy. The major subsystems and parameters for LP-DED are shown in Figure 3.1.

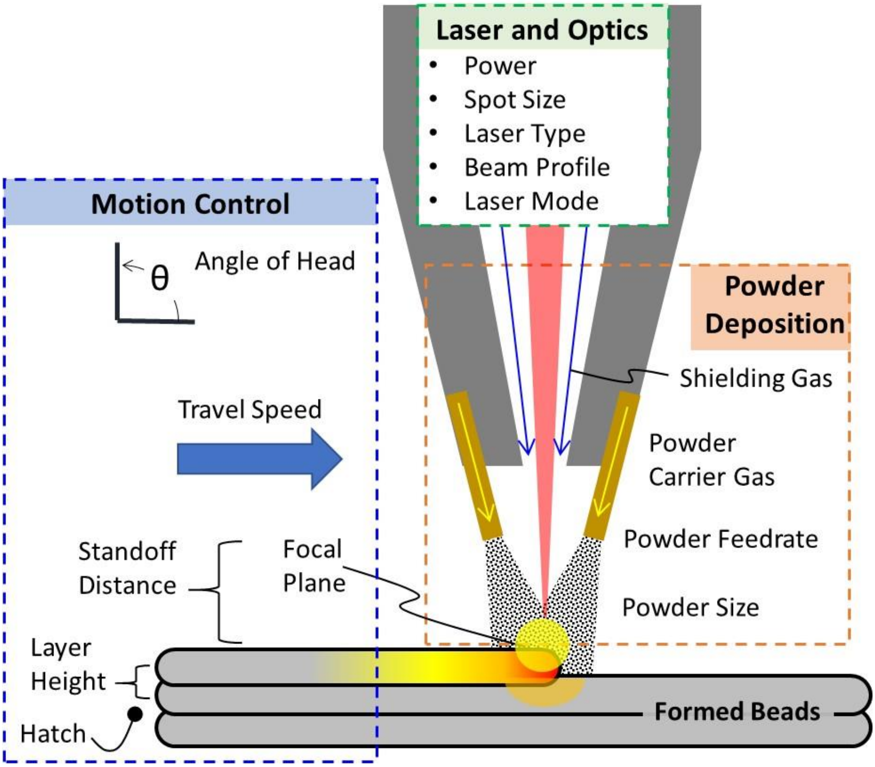

Figure 3.1. Overview of LP-DED Process Parameters.

The primary parameters that are critical to the LP-DED process include laser power, travel speed (also called feedrate or scan speed), powder feedrate, laser spot size, hatching (also called stepover spacing or track overlap), and layer height (or layer thickness) [203]. These parameters and some of the other process inputs shown in Figure 3.2 determine the melt pool and resulting geometry. The melt pool and powder carrier gas derive the general surface roughness [204]. An unstable melt pool can cause spatter, porosity, or irregular beads and increase occurrences of unmelted or partially-melted powder adhering to the surface.

3.3.1 LP-DED Experiment Parameters

This study specifically focused on five key input parameters and impacts to the resultant surface texture. The down selected parameters include the laser power, travel speed, layer height, flow rate of powder, and powder size and are highlighted in Figure 3.2. Several parameters were fixed based on the geometry desired and also system configuration. The spot size selected was determined by the desired wall thickness, in addition to the type, mode and subsequent profile of the laser were all fixed. The standoff was also considered but is accurately controlled in the motion system with monitoring. The angle of the head is fixed normal to the surface. Other parameters such as angle of the head, hatching, and build strategy were not applicable since the experiment involved single bead width thin-wall deposition.

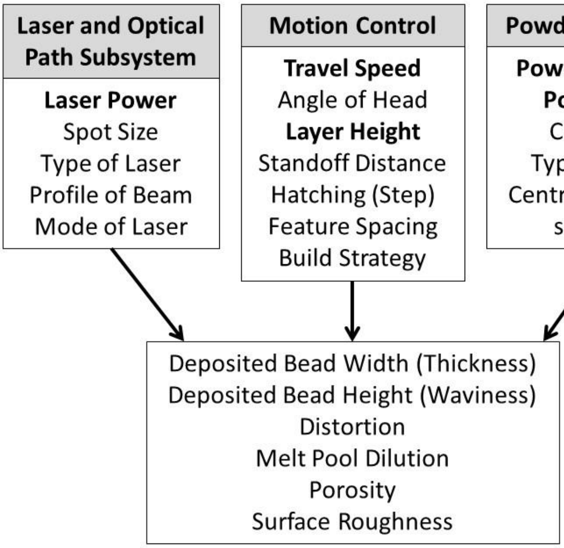

Figure 3.2. LP-DED parameter inputs that can impact surface texture and the deposited bead geometry. The highlighted parameters were varied in this study.

A total of 35 samples were fabricated on an RPM Innovations 557 machine with a 3-nozzle Argon-carrier gas powder injection and Argon central purge deposition head. This was a gantry-type system, and the build box was fully inert with Argon to reduce oxidation. The laser used was an infrared (IR) 1064 nm continuous wave with Gaussian profile. All samples were single bead width deposition tracks in the Z-direction. The sample tracks were fabricated on a 13 mm thick mild steel build plate.

The baseline parameters were established through initial experimentation to demonstrate a low porosity NASA HR-1 build that would meet geometric requirements as well as optimal deposition time. The variation in parameters for this experiment were selected to be 5% from nominal for power, travel speed, powder feedrate, and 10% for layer height. These were selected to ensure that all build samples would be successful to full height for data analysis in addition to meeting wall thickness range of 1 to 1.2 mm. While parameters could be varied further, this would result in incomplete or failed samples and data could not be collected. Other studies suggest that a higher increase in laser power of 25% or more could improve surface roughness [120]. However, core material microstructure and desired geometry must also be considered. With increased power for thin-wall LP-DED, the melt pool increases resulting in thicker walls, increased size and quantity of the columnar grains, and results in a more porous structure [102]. Additionally, the

NASA HR-1 could be adversely impacted with increased laser power through vaporizing of strengthening elements or segregation of these elements, both resulting in a poor material microstructure and properties [202].

Each sample was deposited using racetrack configuration (flat walls and 180° radii) to provide dimensional stability and allow for surface texture (waviness and roughness) to be measured on both the inner (internal to racetrack) and outer (external) surfaces (Figure 3.3). The samples were 76 mm in length (Y-direction), 25 mm in height (Z-direction) and opposing walls spaced 25 mm apart (X-direction). The area selected for surface measurements was 40 mm in width and 13 mm in height. The samples were sectioned from the build plate via bandsaw and were cleaned in Isopropyl alcohol to remove any excess machine oil. No mechanical cleaning was used to preserve the surface. The samples are referenced by a unique indicator (1-35), however the last four samples in the series (32-35) were labeled as A-D to indicate nominal parameters. A built plate with samples (1 through 6, 32, 33) is shown in Figure 3.3A. The typical surface from a coarse powder sample (45-105 µm) is shown in Figure 3.3B and fine powder (10-45 µm) in Figure 3.3C.

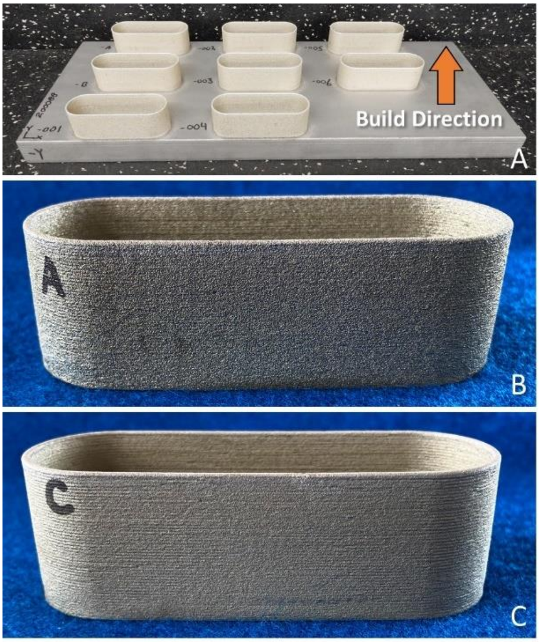

Figure 3.3. Fabricated experimental select samples. A) Deposited samples on build plate, B) Sample A (Run 32) with nominal parameters using 45-105 µm powder, C) Sample C (Run 34) with nominal parameters using 10-45 µm powder.

3.3.2 NASA HR-1 Material

The NASA HR-1 alloy was selected for this study due to the importance of this alloy for use in hydrogen based heat exchanger applications [201]. The NASA HR-1 alloy was developed at NASA Marshall Space Flight Center in the late 1990's as a hydrogen environment resistant (ie. "HR") superalloy for use in high temperature and high pressure hydrogen applications [205]. NASA HR-1 is a Fe-Ni-Cr Superalloy that provides high strength and high ductility in these harsh environments and originally derived from JBK-75. The alloy has been demonstrated in several applications focused on liquid rocket nozzles and high temperature hydrogen environment heat exchangers [77]. While other alloys exist that could meet these general requirements, such as A-286, JBK-75, and the 300 series stainless steel (304, 310, 316), they can be limited in strength for such heat exchanger applications [13].

Two powder lots (HRA9 and HRA4) of rotary atomized NASA HR-1 from Homogenized Metals Inc. (HMI) were used for the sample deposition in a fine cut (10-45 µm) and coarse cut (45-105 µm). The powder chemistry was within nominal ranges including any trace elements that were measured (C, Mn, Si, P, S, B) as seen in Table 1. Chemistry was measured using Inductively Coupled Plasma (ICP) at HMI.

Table 3.1. Chemistry for NASA HR-1 powder used in this study (Wt. %).

Element	**Powder Lot**		**Nominal Chemistry**
	HRA9	**HRA4**	**Ref** [201]
PSD	***10-45 µm***	***45-105 µm***	
Fe	41.24	41.78	Bal
Ni	33.91	33.71	33.7 – 34.3
Cr	14.66	14.49	14.3 – 14.9
Co	3.79	3.75	3.6 – 4.0
Mo	1.83	1.82	1.6 – 2.0
Ti	2.41	2.31	2.2 – 2.6
Al	0.243	0.24	0.23 – 0.27
V	0.302	0.30	0.28 – 0.32
W	1.60	1.59	1.4 – 1.8

The rotary atomized powder was characterized using a Microtrac (Version 10.1.0.6) and imaged using a Hitachi S3000H Scanning Electron Microscope (SEM) to evaluate the general morphology. The fine and coarse cut powder SEM images can be seen in Figure 3.4. The Microtrac calculated the peak distribution of the powder at 70 µm for the coarse powder (45-105 µm). The SEM showed mostly spherical shape with a few oblong ellipsoidal particles and some traces of satellites for the coarse powder. Oblong particles can cause issues with flowability or clog the nozzle during deposition. The fine powder (10-45 µm) showed a peak at 34 µm from the Microtrac characterization. While a majority of the finer powder is spherical observed in the SEM, the oblong shaped morphology is also observed along with several sphere and satellites and granular particles.

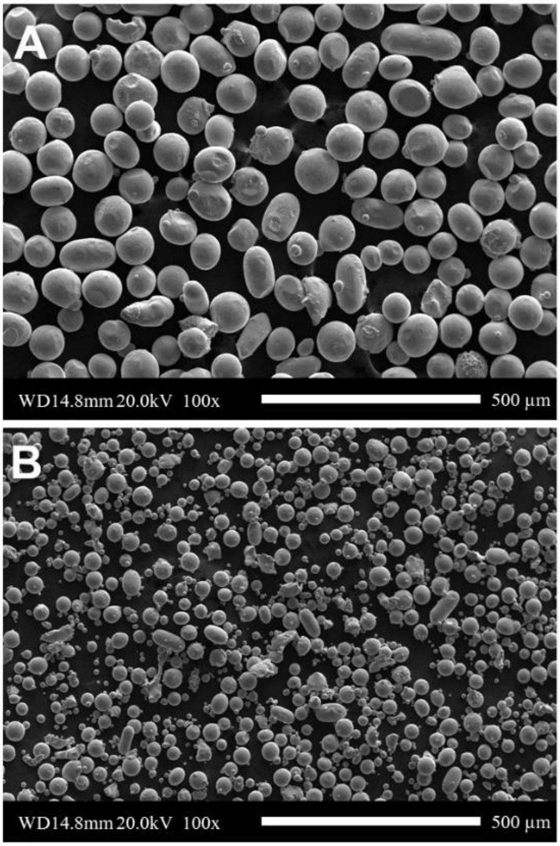

Figure 3.4. SEM Images of the NASA HR-1 Powder. A) Coarse cut 45-105 µm powder and B) Fine cut 10-45 µm powder. Note: both images are at the same magnification (100X)

3.3.3 Design of Experiment (DOE) Samples

A DOE was developed to understand the relationships between the input process parameters, powder feedstock in two different PSDs, as well as significant interactions of the parameters on the resulting surface texture and roughness. A split design grouped by powder size was selected for the DOE because of the difficulty of powder changes. This avoided changing powder every run, which was not feasible for the experiment. A total of 35 runs (Runs 1 – 35) were completed at varying parameters including four distinct runs (two with each powder size) at the predetermined optimal set of parameters from prior development work on this alloy. The predetermined optimal set of parameters was laser power = 350 W, powder feedrate = 23 g/s, travel speed = 762 mm/s, and layer height = 0.254 mm. The summary of parameters used for this study is shown in Table 3.2.

The DOE was analyzed using analysis of variance (ANOVA) to determine the significance and extent of influence for the LP-DED process parameters that impact surface texture [206]. The overall model and influence of the individual factors and interactions were considered significant if the probability value (p-value) was less than the set significance level ($\alpha = 0.05$). This analysis was conducted using DesignExpert software. The final model that best fit the data was a two-factor interaction (2FI), with several terms eliminated that were not significant. Other models were evaluated including quadratic but did not provide any significance.

Table 3.2. Selected Parameters and Powder for DOE runs.

Sample ID	Powder Change	Laser Power	Powder Feedrate	Travel Speed	Layer Height	Powder Size
		W	grams/min	mm/min	mm	µm
1	1	333	23.0	724	0.254	45-105
2	1	350	21.9	724	0.279	45-105
3	1	333	24.2	762	0.229	45-105
4	1	350	24.2	762	0.254	45-105
5	1	333	21.9	800	0.229	45-105
6	1	368	23.0	762	0.254	45-105
7	2	333	21.9	762	0.254	45-105
8	2	368	24.2	800	0.229	45-105
9	2	350	23.0	724	0.229	45-105
10	2	350	21.9	762	0.254	45-105
11	2	368	23.0	724	0.279	45-105
12	2	333	24.2	800	0.279	45-105
13	3	350	23.0	762	0.254	10-45
14	3	350	23.0	762	0.279	10-45
15	3	368	24.2	724	0.229	10-45
16	3	368	21.9	800	0.229	10-45
17	3	333	24.2	800	0.229	10-45
18	3	333	21.9	800	0.279	10-45
19	3	333	21.9	724	0.229	10-45
20	4	350	23.0	800	0.254	45-105
21	4	368	24.2	762	0.279	45-105
22	4	368	21.9	724	0.229	45-105
23	4	350	24.2	724	0.254	45-105
24	4	333	23.0	762	0.279	45-105
25	4	368	21.9	800	0.279	45-105
26	5	333	23.0	800	0.254	10-45
27	5	368	21.9	724	0.279	10-45
28	5	350	23.0	762	0.254	10-45
29	5	333	24.2	724	0.279	10-45
30	5	368	24.2	800	0.279	10-45
31	5	350	23.0	762	0.229	10-45
32	1	350	23.0	762	0.254	45-105
33	1	350	23.0	762	0.254	45-105
34	5	350	23.0	762	0.254	10-45
35	5	350	23.0	762	0.254	10-45

3.3.4 Roughness Measurements and Microscopy

Each sample was then measured using a non-contact Keyence VR-5200 patterned light projection profilometer with three telecentric lenses at 80x magnification and image stitching with an overlap of 20%. The samples were first measured on the outer surface, then sectioned inside the radii and measurements were completed on the inner surface. A surface form correction was used on the entire area to remove the tilt and any curvature, and a reference plane was then established. No filtering was used in the analysis of the surface topography data since the entire surface is of interest for potential thin-wall applications. All measurements were completed and reported according to ASME B46.1 [207]. The surface scanning covered an area of 43 mm by 16 mm to remove any edge effects, and areal measurements for average roughness (Sa), max height of surface (Sz), max peak height (Sp), max valley depth (Sv), skewness (Ssk), kurtosis (Sku) were determined from this region. Waviness was obtained in the horizontal and vertical directions with a high-pass filter (λc) of 0.25 mm and low-pass (λs) of 0. The focus of this study was on the sidewall vertical surface roughness, which is in the direction of flow for heat exchanger applications. The measurement uncertainty was obtained by repeating measurements on a single sample for each fine and coarse powder PSD samples. A 99% confidence interval for measurement uncertainty is calculated and presented in the data plots.

In addition to areal surface analysis, five vertical lines and three horizontal line profiles were obtained from the surface areal profile. The vertical direction corresponds to the build direction and also flow direction in heat exchangers fabricated with LP-DED. The 2D profile directional line texture parameters analyzed were average profile height (*Pa*), average maximum profile height (Pz), reduced peak height (Pp), reduced valley depth (Pv), skewness (Psk), and kurtosis (Pku). The profile texture measurements (Pa, Pz, Pp, Pv, Psk, Pku) were used for this experiment which is inclusive of waviness and roughness that could impact the application for flow in heat exchangers. This is synonymous with the traditional Ra (average roughness) but are not filtered for waviness. The line profile data is important to the end application, and directionality should be considered for specific applications [208], such as fluid flow, and included as an outcome of this study. The 2D directional profile measurements were equally spaced across the region of interest in the vertical and horizontal directions. The regions of interest for the areal surface roughness and directional texture measurements are shown in Figure 3.5. For data reporting, the five vertical texture measurements were averaged, as well as the three horizontal measurements averaged, to provide a single value. All measurements were repeated for the inner and outer surfaces for each sample.

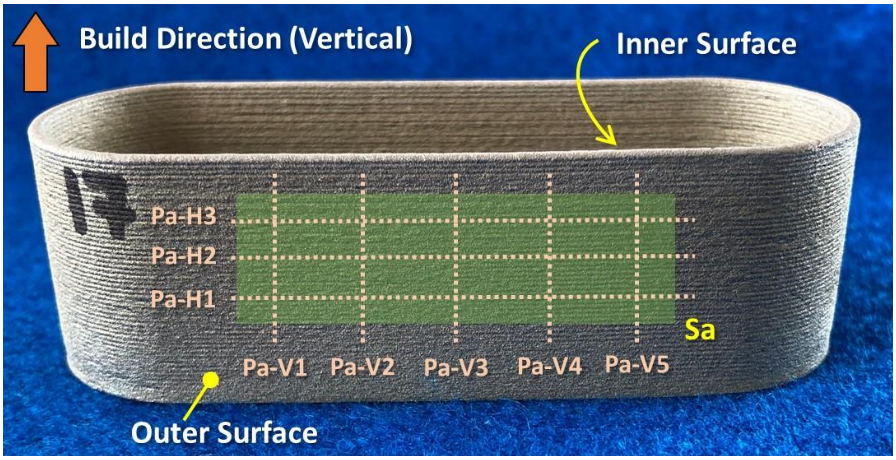

Figure 3.5. Nomenclature and measurement locations for areal and directional profile line texture measurements. The build direction also corresponds to the flow direction for heat exchanger applications.

Following the texture measurements, SEM imaging was completed on a Hitachi S3000H for select samples on the inner and outer surfaces within the central region of the sample. The samples were then sectioned and mounted to evaluate porosity and microstructure. The micrographs were imaged using a Keyence VHX digital microscope. The samples were prepared per ASTM E3 using a Presi automatic polisher. The samples were prepared to evaluate porosity were polished using 0.05-micron colloidal silica, but not etched. This allowed for image characterization of the potential defects independent of the visible grain structure. Select samples were etched using etchant #13 (10% Oxalic Acid, Electrolytic) to determine the deposition melt patterns and general grain structure.

The porosity was measured on the polished samples using ImageJ software (Version 1.53e). The image was adjusted to 8-bit to allow for differentiation between pores and other stains or burns that can occur from polishing. The entire area of the sample was then selected, and the areas of porosity quantified; any edge effects were eliminated to minimize error. The samples thickness was measured using ImageJ at five transverse locations and then averaged to provide a single value.

3.4 EXPERIMENTAL RESULTS

3.4.1 Visual and SEM

All samples from the LP-DED process were built successfully (no failures, no process stops, no issues noted) to the nominal dimensions. The samples were removed from the build plates and evaluated in the as-built condition (*i.e.*, no stress relief or subsequent heat treatments; no surface modifications). The coarse powder samples appeared to have a higher degree of texturing across the surface, and the fine powder samples emerged smoother from visual inspections. The SEM images show the surface roughness being impacted by the powder size, as seen in Figure 3.6. The coarse powder samples have a random powder scattering across the surface (Figure 3.6A) of partially melted and loosely adhered powder (Figure 3.6B). Several powder particles can be seen barely protruding from the surface encapsulated by the solidified surrounding material, while the partially melted and solidified material forming a radius with the underside of the particles. The fine powder samples (Figure 3.6C, Figure 3.6D) show a higher number of particles adhered, covering adhered covering almost the entire surface. There is minor visual evidence of the macro waviness observed in Figure 3.6C, potentially from layer height. There are many instances of fully melted and partially melted fine particles similar to the coarse powder. The diameter of the particles measured normal to the surface on the SEM images match the PSD of the powder sizes used for respective samples.

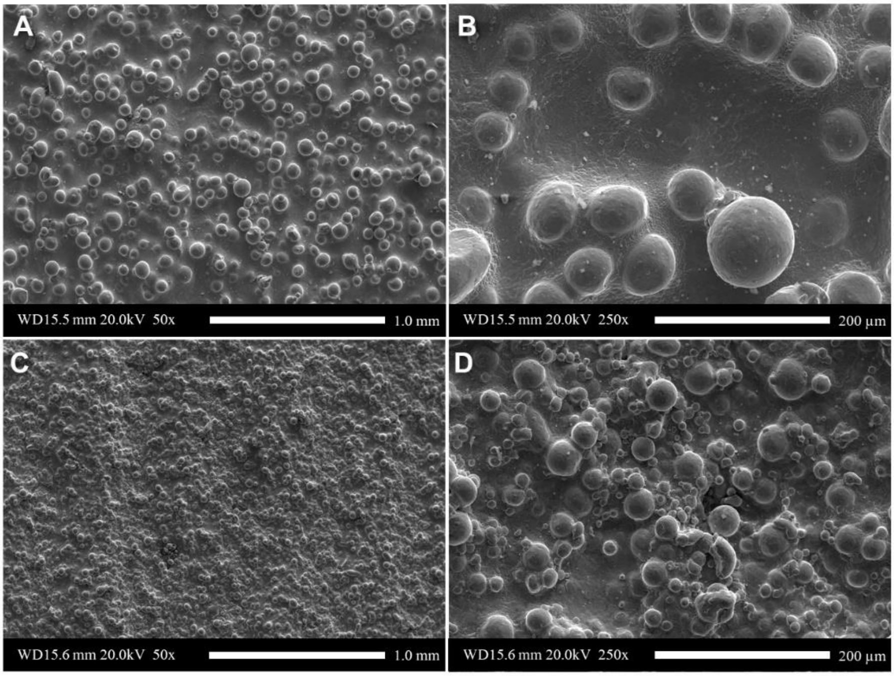

Figure 3.6. SEM images of select samples. A) Sample 32 inner surface with coarse powder at 50x, B) Sample 32 inner surface with coarse powder at 250x, C) Sample 34 inner surface with fine powder at 50x, D) Sample 34 inner surface with fine powder at 250x.

3.4.2 Microstructure

Representative sectioned and etched samples for coarse and fine powder are shown in Figure 3.7. The sample with coarse powder (Fig. 7A, B, C) displays the particles adhered to the surface with solidified material forming a tangential radius between. In most instances, the melted and solidified material extends about 50% of the width of the particle, forming the roughness on the surface assuming powder particles protrusions are defined as roughness and the layering is defined as waviness, as suggested by Diaz [127]. There are a few instances observed with subsurface particles that are not fully melted into the surrounding material and shown to be a maximum of 2x the diameter of the powder PSD. The unmelted coarse particles extend about 150 µm subsurface measured normal from the surface. The fine powder sample (Fig. 7D, E, F) shows a higher number of instances and higher density of unmelted powder across the surface and subsurface. There are multiple layers of unmelted or partially melted fine powder observed subsurface with solidified material between the particles. The unmelted particles extend about 100 µm into the subsurface when measured normal from the external surface.

The melt pools are clearly visible in the etched samples. The microstructure is characteristic of the LP-DED process with epitaxial dendrite grain growth that traverse across melt pools [209–211]. The dendrite arm growth is random, but also shows a tendency to solidify from the outer surface of the melt pool towards the center. Small grains are observed on the external surface of the samples due to the rapid cooling [212]. The rapid cooling of the exterior surfaces trap excess powder with solid material, surrounding these loose particles.

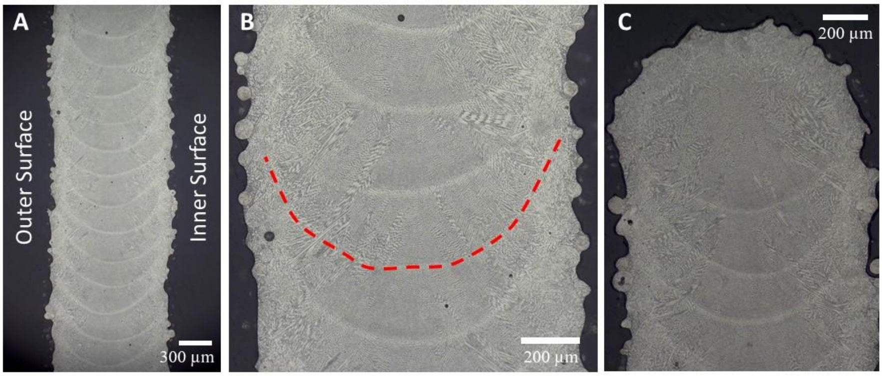

Sample 32 – Coarse Powder (45 – 105 µm)

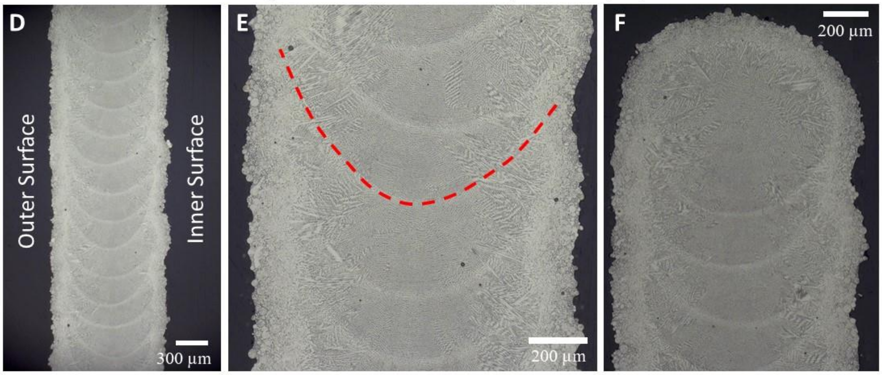

Sample 34 – Fine Powder (10 – 45 µm)

Figure 3.7. Sectioned and etched samples with inner and outer surfaces. A, B, C) Sample 32 using coarse powder, D, E, F) Sample 34 using fine powder.

3.4.3 Areal Measurements

The areal roughness measurements (Sa, Sz, Sku, and Ssk) for all of the specimens are summarized in Figure 3.8. Sa is the typical areal parameter used to quantify roughness of surfaces but does not capture the complexity and discriminate between peaks and valleys. The Sz, Sp, Sv, Sku, and Ssk parameters define the magnitude of the peaks and values that can be used in fluid flow evaluations for heat exchangers or material removal estimates for post-processing operations (*e.g.* machining or polishing). The DOE samples were each built with a varying set of parameters and identified by sample number on the X-axis of plots, which is synonymous with the run number (Table 3.2). The average areal roughness (arithmetic mean deviation), Sa, in Figure 3.8A clearly shows the fine powder is lower compared to the coarse powder in almost all samples, which is consistent with prior observations [84,213,214]. The dotted lines shown in Figure 3.8 pair the inner and outer wall measurments for readability.

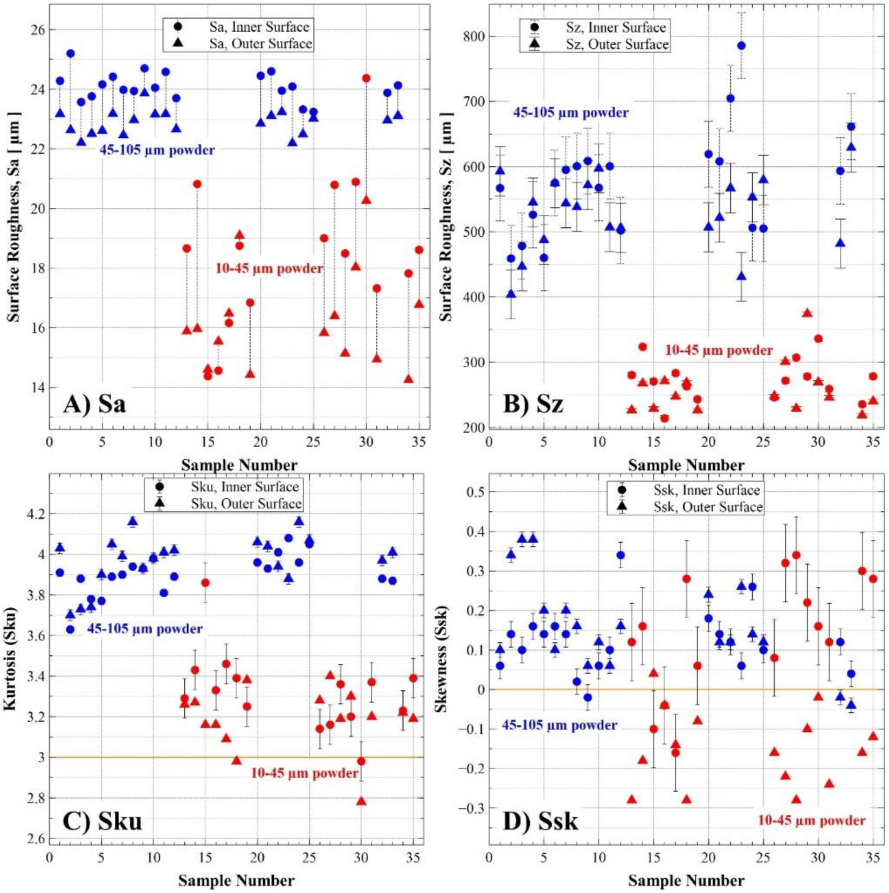

Figure 3.8. Areal texture measurements for all samples. A) Average area roughness [Sa], B) Maximum height of surface [Sz], C) Kurtosis [Sku], D) Skewness [Ssk].

Another trend observed is the difference between the inner and outer surface with the inner surface showing higher roughness in almost all instances for both fine and coarse powders. This is due to ricochets, recirculation, and higher volume of powder available on the internal volume of the racetrack sample to bond to the trailing edge of the melt pool during solidification. There is a high volume of powder available due to the low efficiency (<10%) with thin-wall depositions such as this. The Sa for the coarse powder shows a tight grouping of data independent of the changes in parameters, where the fine powder has more variation. The fine powder shows higher sensitivity in changes to build parameters. The areal roughness, Sa, for the fine powder showed a downward trend as a function of energy density. The coarse powder was stable as a function of the energy density. From the dataset, sample 30 appears to be a clear outlier, which is partially impacted from the waviness from the layering. This was the only sample where all build parameters were set to the higher range (power = 368 W; powder feedrate = 24.2 g/s; travel speed = 800 mm/s; layer height = 0.279 mm).

The amplitude parameters for Kurtosis (Sku) and skewness (Ssk) were evaluated and shown in Figure 3.8C and D. The high Sku (> 3.0) indicates that all samples have a high degree of peaks and valleys across the surface. The coarse and fine powder samples show minor variation within the groups and indicates the predominance of peaks across the surface (based on Ssk). Most of the coarse samples are dominated by peaks. Ssk trends downward as energy density increases independent of powder PSD, but only for the inner surface.

3.4.4 Directional Profile Measurements

The 2D directional profile texture results are similar to the areal parameters and shown in Figure 3.9. These parameters were measured in the vertical direction at a length of 16 mm. The trends are very similar with the coarse powder PSD showing higher values than the fine powder PSD. The dotted lines in Figure 3.9A pairs the samples together for readability. For a majority of samples the average profile height of the inner surface (Pa) has a higher texture than the outer surface, although some are reverse compared to Sa such as samples 1, 8, 25. Pa is a localized measurement and any excess powder, particularly with the coarse PSD, in a localized area could change the values. The largest disparity is 9% (sample 8) and with the measurement uncertainty cannot be shown statistically different.

The average maximum profile height for the vertical (Pz) measurement is grouped tighter for the coarse powder and similar for the fine powder. The high measurement uncertainty for the coarse powder represents the random coarse particle adherence causing larger peaks and valleys. The Pz of the inner surface is generally higher than the outer surface, but variations can be attributed to location dependency. The Pku is similar to the Sku and the surface is dominated by a high degree of peaks and valleys for all coarse samples and to a lesser degree the outer surface fine powder samples. The peaks (Pp) and valleys (Pv) for the inner surface is observed in Figure 3.9A and Figure 3.9D for the outer surface. The Psk indicates that peaks are still dominate on most of the samples. The 2D profile values, specifically Pa, Pz, Pp, Pv, Pku, Psk are also important to report since fluid flow in heat exchangers is directional and may be used in flow performance evaluations such as friction factors.

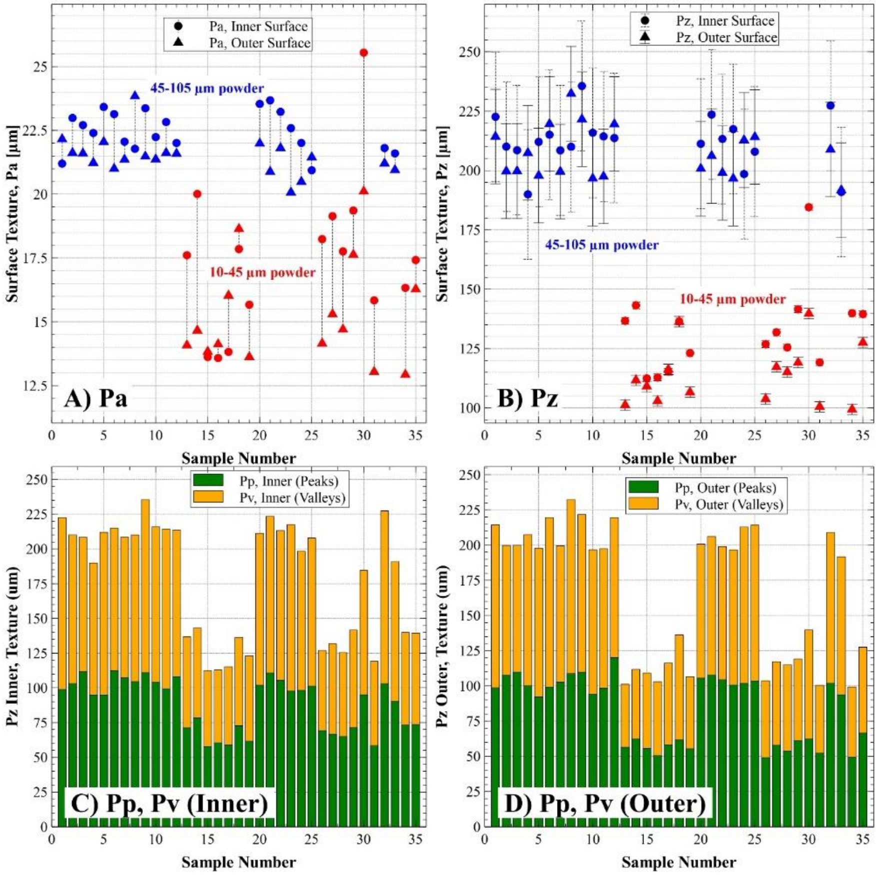

Figure 3.9. Directional vertical texture per sample. A) Average profile height [Pa], B) Average maximum profile height [Pz], C) Measured peaks [Pp] and valleys [Pv] for inner surface, D) Measured peaks [Pp] and valleys [Pv] for inner surface.

3.4.5 Waviness

Typical LP-DED samples have shown layering undulations from the dilution of vertical melt pools created on the sidewalls forming waviness [120,215]. In prior literature this layering is apparent in the cross-section of the deposited samples [92,119]. Within this current study, the layering and undulations are not visible in the sectioned samples. The vertical waviness is shown in Figure 3.10 and shown to be more preferential to the inner surface. The dotted lines are provided to enhance pairing of samples for readability. The coarse samples vary by 15% of the average, with the exception of sample 12. The coarse samples did not show any statistical trends in waviness compared to layer height, while the fine samples indicated increased waviness with increased layer height. The finer powder PSD samples have a higher degree of variation showing higher sensitivity to the process parameters and resulting melt pool geometry [213]. Sample 30 has higher waviness compared to other samples with all the deposition parameters set at the highest values. The increased layer height in addition to higher power and increased powder feedrate causes the melt pool to spread, resulting in higher waviness.

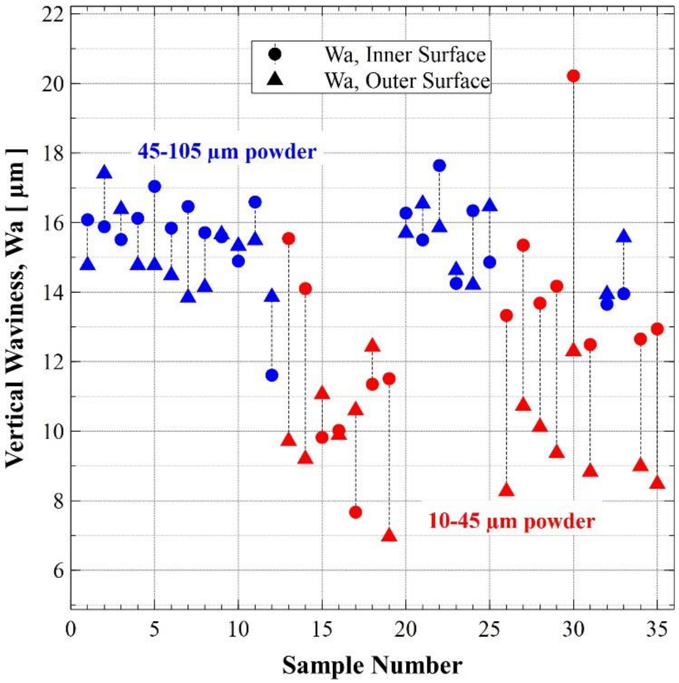

Figure 3.10. Vertical waviness for inner and outer surfaces.

3.4.6 DOE Results

The DOE data were analyzed using ANOVA with the process parameters as the factors and the surface roughness (Sa) data as the response. The final model that best fit the data was a two-factor interaction (2FI), with several terms eliminated that were not significant. The results from the ANOVA of the inner surface roughness are provided in Table 3.3 with an overall R^2 fit of 97.8% for the selected factors. The results show that powder size is the major contributor at 71% of the overall model, as observed in the average areal roughness data. The layer height is also a contributor and the interaction between layer height and powder size at 10% each. Other interactions of the parameters were significant in the model, but not major contributors to the texture or roughness. Prior studies by Gharbi et al. and also Ahsan showed a correlation between the roughness and the energy density that as energy density increased the roughness also increased [120,216]. A major difference in those studies compared to this was a significant variation in power, where this study focused on a 5% difference. This study was also focused on maintaining a consistent and thin wall, so significant increases in energy density would increase the melt pool diameter and subsequent wall thickness.

Table 3.3. ANOVA for average inner surface roughness (Sa).

Source	**Sum of Squares**	**DoF**	**Mean**	**F-value**	**p-value**
Model	359.2	11	32.7	91.3	<0.0001
A-Laser Power	0.1	1	0.1	0.2	0.6432
B-Powder Feedrate	1.2	1	1.2	3.3	0.0804
C-Travel Speed	0.0	1	0.0	0.1	0.7212
D-Layer Height	35.3	1	35.3	98.8	< 0.0001
E-Powder Size	259.6	1	259.6	725.9	< 0.0001
A*C	1.2	1	1.2	3.4	0.0782
A*D	4.7	1	4.7	13.1	0.0014
B*C	5.7	1	5.7	15.8	0.0006
B*D	2.8	1	2.8	7.7	0.0106
B*E	2.4	1	2.4	6.7	0.0163
D*E	37.0	1	37.0	103.6	< 0.0001
Residual	8.2	23	0.4		
Lack of Fit	7.7	19	0.4	3.4	0.1236
Pure Error	0.5	4	0.1		
Cor Total	367.5	34			

3.4.7 Porosity

The porosity of each sample compared to the Sa values is shown in Figure 3.11. All fine powder samples have a measured porosity of less than 0.061%, average of 0.031% ±0.01% and low value of 0.014% (range of 0.047%) consistent among all fine PSD samples. The coarse powder samples had a much wider distribution of porosity and ranged from 0.052% up to 0.307% and average of 0.13% ±0.07%.

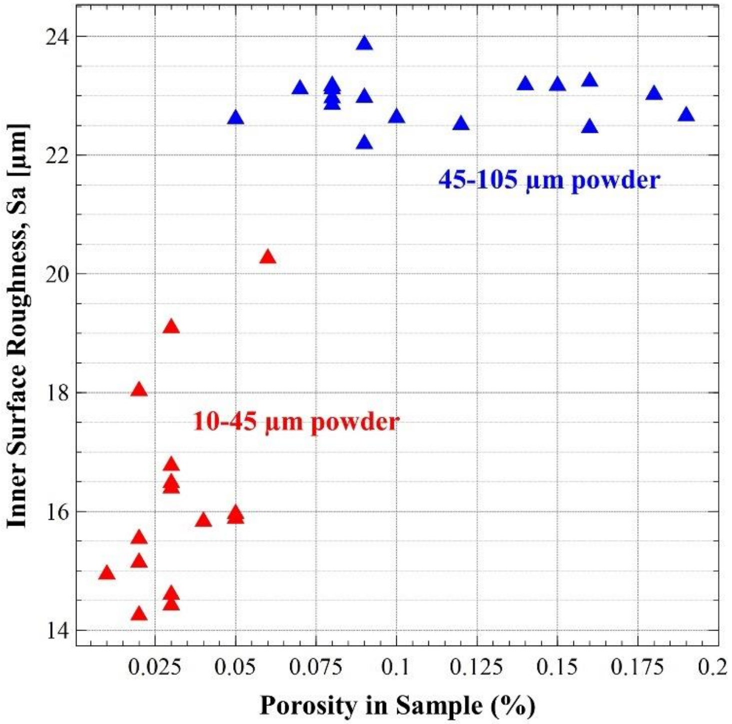

Figure 3.11. Porosity measurements in samples compared to inner average areal surface roughness (Sa).

3.4.8 Sample Wall Thickness

Thickness variation was evaluated through direct measurements of the cross sectioned samples. The results of the overall thicknesses along with powder size and laser power are shown in Figure 3.12. An ANOVA was also established to evaluate the build parameters impacting thickness. While the model showed several factors were significant for several factors and interactions, the R^2 fit was only 82.7%. A major contributor to the thickness model was laser power (25.3%) and travel speed (22.3%). Layer height had a small contribution (5.5%) as well as powder size (4.6%) and interactions of the parameters (16.6%). Figure 3.12 indicates some visual correlation of thickness to laser power, although all parameters are being adjusted simultaneously.

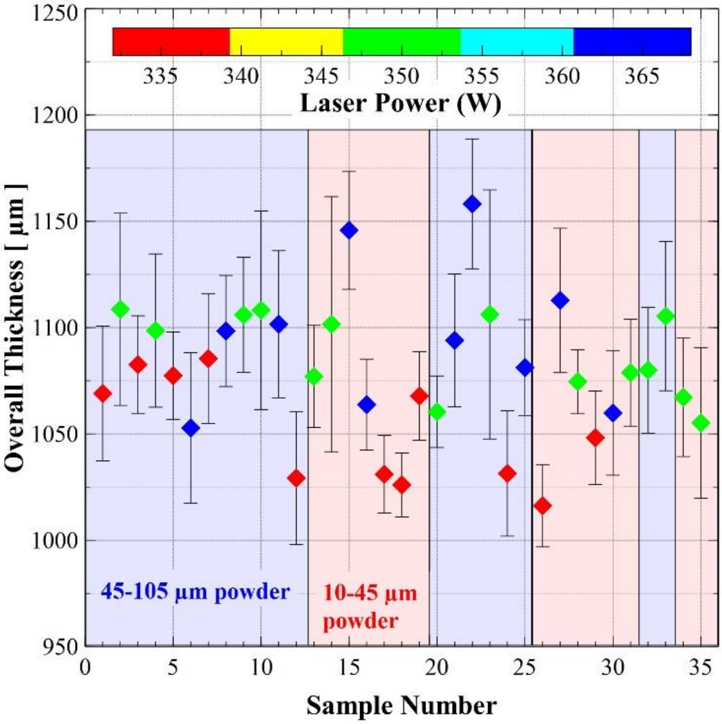

Figure 3.12. Sample cross-sectional thickness compared to powder PSD and laser power.

The process hardware and setup for building the desired wall thickness can have an impact on the final surface roughness. The melt pool resulting in 1 mm wall thickness results in a lower catchment efficiency of 5-20% [120]. The powder that is captured in the melt pool is often drawn to the center due to Marangoni flow [75]. Particles that are not fully molten can be expelled from the melt pool and adhere to the sidewalls or trailing edge [208]. The residual powder (80-95%) not captured is then available to bond to the trailing edge of the melt pool in the outmost surface and then rapidly cooled [217,218]. This is further exasperated in thin-walls due to low thermal mass and accelerated cooling rate. For practical applications of the LP-DED process, the geometry also needs to be considered. There can be differences in powder consumed during the process based on primitive (simple) geometry compared to complex surface geometry and dependent upon laser-on time (building versus positional movements).

The Pz parameter is compared with the Pa parameter and plotted as a function of layer height in Figure 3.13. The coarse powder does not show a sensitivity to average or maximum texture profile based on layer height. The fine powder shows a more apparent trend with the lower layer height providing a lower average and maximum texture profile, although data does not match for all samples with other parameter variations.

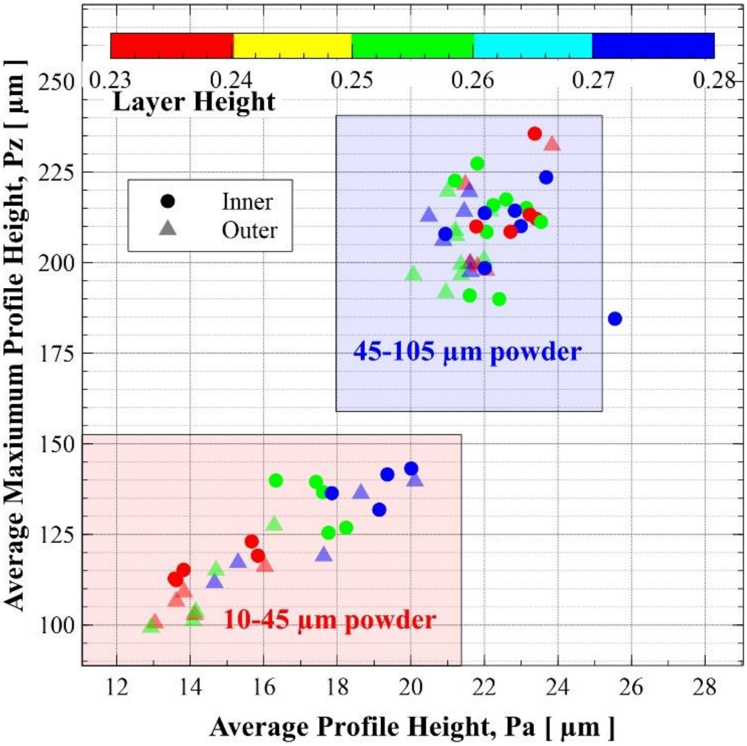

Figure 3.13. Comparison of average profile height (Pa) to average maximum profile height (Pz).

The vertical orientation along the direction of the build was the primary interest for surface texture, but horizontal profile texture was also evaluated to evaluate differences. This is shown in Figure 3.14. The line on the graph is provided as a reference assuming an arbitrary slope of 1. The coarse powder PSD indicates little difference (1%) between the vertical and horizontal directions. The fine powder profile is biased toward the vertical direction with a difference of 9%.

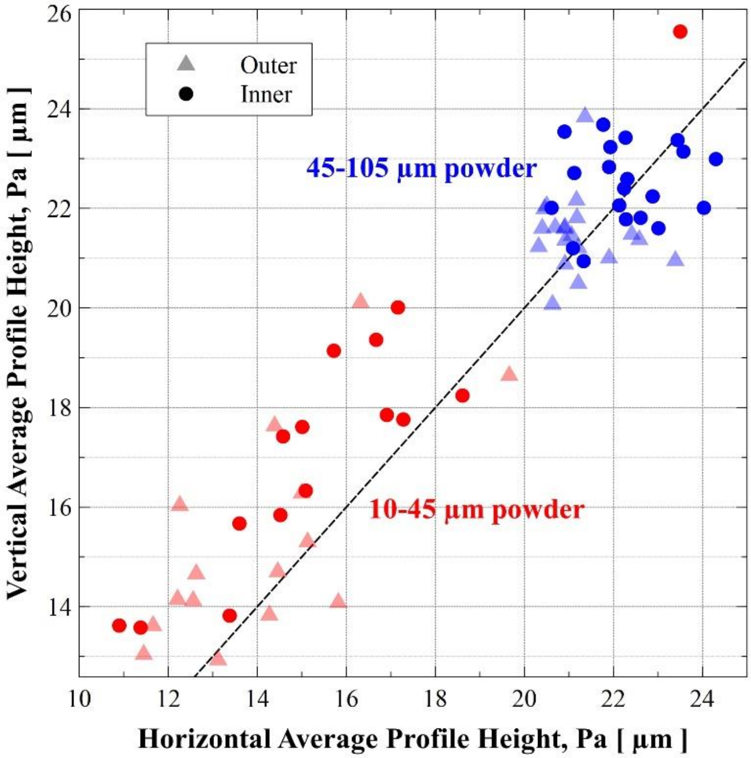

Figure 3.14. Comparison of vertical and horizontal average profile height, Pa.

3.5 DISCUSSION

The finer powder has more instances of subsurface particles than the coarse particles observed in the micrographs, because of the propensity for rapid solidification during the build [219]. This does not impact the surface texture and the finer powder still provides lower values overall. While literature reports that the finer powder tends to have flowability issues [220,221], there were no issues observed with the 3-nozzle system used in this study. The fine powder samples indicate that the inner surface is predominately peaks while the outer surface is mostly valleys. The high degree of peaks for the inner surface indicates that powder particles are adhering to the surface as the NASA HR-1 starts to cool (ie. excess powder capture). Due to the reduced volume, the finer powder requires less thermal energy to melt [222]. The finer powder PSD combined with the higher likelihood of powder trapped and recirculating in the enclosed racetrack increases the excess powder capture to the inner surface. During deposition of the fine powder, it was observed that powder was suspended in the build chamber, which was likely the lower end of the fine PSD (less than 25-30 µm). The higher velocity of the fine powder in the gas stream is ejected from the nozzle and causes rebounds off solidified surfaces [223]. The coarse particles were shown to be more likely to break through the surface tension of the melt pool and likely to be melted or partially solidified [75].

While the Sa had a tighter range for the coarse powder than the fine powder, the opposite was true when evaluating with the Sz parameter (Figure 3.8B). This indicates a higher range in the peaks and valleys with the coarse powder, which follows the visual observations of the full adherence or partial melting of the coarse powder overcoming the surface tension. There are limited instances of unmelted coarse powder observed subsurface. The coarse powder samples are dominated by the peaks for the inner and outer surface with the solidified material forming a tangential radius between the partially melted particles. The fine powder has a high concentration of unmelted particles across the surface and subsurface. The fine powder shows an approximate split of peaks and valleys, although valleys shown to be marginally higher for most samples. The concentration of these unmelted particles make up these peaks and valleys bonded by solidified material (Figure 7F).

Uniform and consistent roughness is a significant consideration in component design fabricated from LP-DED, but the material quality and process ability to meet geometric requirements consistently is equally important. These factors can include the material density and the wall thickness. The lower porosity with fine powder has been observed in studies in other alloys [224,225], which can also be related to the increase in efficiency for the finer powder [226]. Townsend et al. points out that surface conditions may act as a fundamental observation to more underlying material defects [227]. The results from the current study align with this observation in that the reduced surface texture also resulted in a material with lower levels of porosity, although no significant defects were noted in either set of samples with varying powder PSD. This alone does not indicate that mechanical and thermophysical properties will match intended requirements, and the properties need to be confirmed with testing.

A prior study by Jinoop et al. indicates 38% increases in wall thickness with 83% increase in power [95]. Other studies also reference the increase of the wall thickness due to the larger melt pool observed with increased laser power [228,229]. Low laser power can generate lack of fusion and detrimental effects on surface roughness and mechanical behavior, so a proper balance is required [230]. The reduction of travel speed also leads to increased wall thickness [231]. Fine powders allow for uniform flow in the deposition nozzle and promote a small melt pool from the laser [68]. However, in this study there was not a significant difference observed in the wall thicknesses between the fine and coarse powder with the power changes observed. The NASA HR-1 alloy also has tendency to be more sluggish during the build and the melt pool does not tend to flow out compared to other alloys.

The mechanisms that produce surface texture in the vertical and horizontal directions differ for thin-walls. The vertical roughness is related to the bead geometry (width and height), layer height, and the adherence of unmelted (residual) and partially melted powder to the outmost surfaces. The horizontal roughness relates to the adherence of the residual and partially melted powder assuming measurements are made nearly parallel with the bead. The low difference between the vertical and horizontal surfaces from this study provides validation that the surface roughness is near uniform, and the anisotropy is coming from the waviness. The parameters selected in this study provide good dilution of the melt pool eliminating discontinuities between layers for an optimal processing window [232,233].

The major contributor to roughness in this study is the powder PSD with fine powder providing lower areal roughness and directional profile texture. The surface roughness map for samples 32 (coarse powder) and 34 (fine powder) is shown in Figure 3.15. The particles are bonded at various time periods during the solidification of the NASA HR-1 with some fully encapsulated with melted material and others partially bonded. The fine powder has a much higher sensitivity to the build parameters compared to the coarse powder when build parameters are changed. The volumetric heat capacity of the fine powder is 18% of the coarse powder and will tend to heat up quickly in the laser beam and become fully molten as it is injected into the melt pool [234].

The layer height did have a significant impact, albeit lower influence on surface texture. There was a higher degree of waviness present on the inner surface of the racetracks. Many prior studies showed the layering and obvious lateral menisci from LP-DED process. This was not readily apparent in the 1 mm thick NASA HR-1 samples, and waviness is not impacted by layer height. The directional surface roughness was within 9% for horizontal and vertical directions and considered uniform.

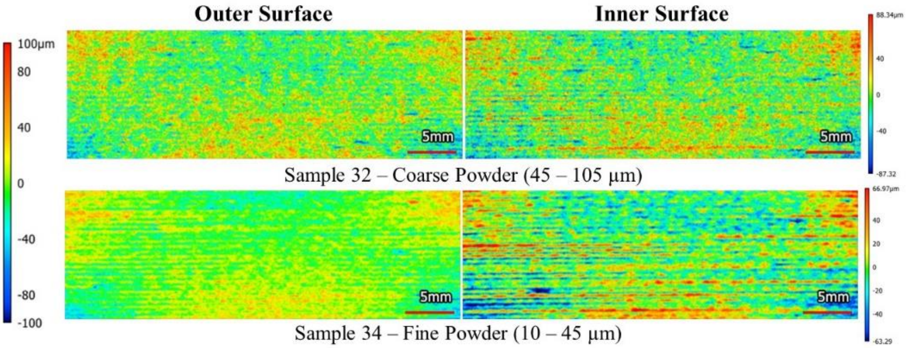

Sample 32 – Coarse Powder (45 – 105 µm)

Sample 34 – Fine Powder (10 – 45 µm)

Figure 3.15. Comparison of areal surface roughness map for coarse and fine powder, inner and outer surface.

Based on the average, the inner surface has 1.67 µm higher roughness than the outer surface. This difference was also confirmed to be significant with a paired t-test for the mean at 0.01 significance level (99% confidence). This difference was also more pronounced in the fine powder sample (2.3 µm average) compared to the coarse powder (1.2 µm). It should be noted that there are four runs where the outer surface is higher than the inner surface. However, the differences were similar at 0.2 – 0.3 µm, while one sample was 1 µm, and all parameters were modified in unison. The commonality of these four runs is when layer height is set to the lowest (0.229 mm) or travel speed is set to the highest (800 mm/s).

Based on the DOE results and observed changes in parameters, the surface roughness can be reduced. The contour plots observing Sa as the factor are shown in Figure 3.16. Similar plots were completed for vertical Ra showing nearly identical results. To reduce surface roughness to the lowest value for the NASA HR-1, the layer height should be set to the lowest values along with using the fine powder. The interaction of the other parameters only had minor contributions and did not impact results enough, so were maintained at nominal values. The fine powder and low layer height also provided low porosity material and desired wall thicknesses.

A practical balance of parameters should also be considered as results are used for parts production. While surface roughness was reduced with the lower layer height (0.229 mm) from the nominal (0.254 mm), the build time would increase. The roughness is increased from 15.6 µm at the lower layer height by 1 µm when the layer height is increased to 0.254 mm. This represents a 6% increase in average roughness (Sa), but a build time increase of 17%. The build time was calculated with a simple primitive geometry model changing the layer height, assuming a constant travel speed.

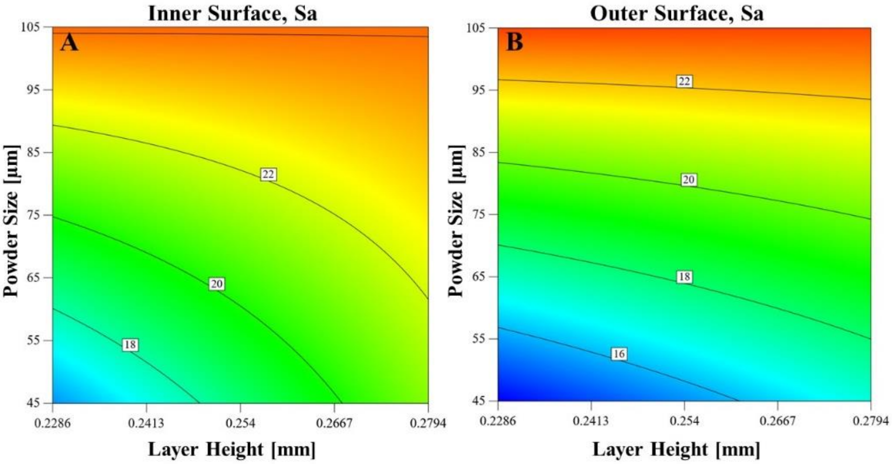

Figure 3.16. Contour plot for average areal surface roughness with powder size and layer height interaction. The powder size is shown in maximum value (45 and 105 µm) and average areal roughness (Sa) units in µm.

3.6 CONCLUSIONS

Industrialization of additively manufactured parts requires a detailed characterization of the microstructure and the resulting geometry such as wall thickness, defects such as porosity, and the surface texture for successful use in critical applications. In this study, closed racetrack NASA HR-1 1 mm thin-wall samples were built using the LP-DED process with rotary atomized fine and coarse powder to evaluate surface texture (roughness and waviness), basic geometry, and microstructure. These samples were successfully built using a single-bead deposition wall to a height of 25 mm. A design of experiments (DOE) was setup to evaluate the variation in parameters to determine the correlation and influence of the build parameters and powder particle size distribution (PSD). A total of 35 samples were successfully deposited with various parameters and were measured using a non-contact patterned light projection profilometer in the as-built condition. The samples were also evaluated using optical microscopy and scanning electron microscope (SEM) and sectioned to evaluate thickness, porosity, and roughness. The results are presented and summarized, and the following conclusions are drawn from the NASA HR-1, 1 mm thin-wall samples.

- Surface roughness of LP-DED material is derived from excess or partially melted powder captured on the outmost surface of the trailing edge melt pool. The areal average surface roughness (Sa) is thus dominated by peaks of these particles.
- Partially or unmelted powder can be solidified in the subsurface and was observed to be a maximum of 2x the diameter of the powder PSD.
- Fine powder (10-45 µm) produces on average roughness 23% lower compared to the coarse powder (45-105 µm).
- The inner (enclosed) surface shows a higher average surface roughness, texture, and waviness compared to the outer surface due to ricochets, recirculation, and higher volume of powder available to bond to the surface during solidification. This is further exasperated with thin-wall depositions where powder efficiency is reduced and more powder available to bond to the outmost surface during solidification.
- The resulting surface roughness from the fine powder indicated a higher sensitivity to the parameter changes where the roughness with the coarse powder showed little change.
- The analysis of variance indicated that the powder, layer height, and interaction of these accounted for 90% of the inner surface roughness and 95% of the outer surface roughness.
- The fine powder produced samples with lower overall porosity and averaged 0.03% ±0.01%, while the coarse samples had a higher range and averaged 0.13% ±0.07%
- A wall thickness of 1.05 to 1.15 mm can be properly maintained with either coarse or fine powder and related to the laser power.
- Waviness was minimized using a lower laser powder (<333 W), higher layer height (<0.28 mm) along with increased travel speed (800 mm/min) and increased powder feed rate (24.2 grams/min) to produce a uniform surface with minor waviness. The typically reported menisci of layering were not observed in the NASA HR-1 thin-wall samples deposited with the optimized parameters and 3-nozzle configuration.
- Surface roughness can be minimized by using fine powder, laser power of 350 W, powder feedrate of 23 g/min, travel speed of 762 mm/min, and a low layer height of 0.229 mm. While the surface roughness is reduced at these parameters a balance should also be evaluated based on process economics. With the decreased layer height, the build time is increased by 17%. The layer height could be increased to 0.254 mm, and the impact on surface roughness would be a 6% increase (+1 µm).

The LP-DED process is maturing and was demonstrated to successfully deposit freeform thin-wall features. This process can provide an alternative to the laser powder bed fusion (L-PBF) process for large-scale parts that require thin-walls, such as heat exchangers with internal channels or flow passages. While AM has shown surface roughness higher than traditionally manufactured parts, this study showcases a detailed understanding of the surface textures. The understanding of surface texture is critical for increased or debits to flow performance in heat exchangers allowing enhanced heat transfer or increases in pressure drop. This study also demonstrated the repeatability of LP-DED thin-walls and a high-density deposition using the NASA HR-1 alloy for use in high-pressure hydrogen applications.

Chapter 4

Chapter 4 – Influence of Angles on Surface Texture and Geometry

Major portions of this chapter were published in:

Gradl, P., Cervone, A., Colonna, P., 2023. Influence of build angles on thin-wall geometry and surface texture in laser powder directed energy deposition. Materials & Design 234, 112352. https://doi.org/10.1016/j.matdes.2023.112352

4.1 ABSTRACT

The characterization of geometric capabilities and limitations is critical for establishing guidelines for end users of the technology. Within this study, several samples of enclosed vertical tracks were fabricated and characterized using LP-DED, with 1 mm-thick walls and varying inclination angles up to 45° using the NASA HR-1 alloy (Fe-Ni-Cr). The wall thickness, melt pool, and surface texture, inclusive of waviness and roughness, were evaluated and results presented. The experimental results indicate that the wall thickness increases exponentially above 30°. The surface texture was shown to be dependent on 1) excess powder adherence, 2) melt pool irregularities causing material droop, and 3) excess material. The experiment revealed that the mean roughness reduces with increasing wall angle for the downskin. The upskin roughness reaches a maximum peak at 20° and slowly reduces as powder adheres within valleys. Both the downskin and upskin surface textures are dominated by irregular waviness generated by the melt pool.

4.2 BACKGROUND

Research has been conducted to explore the feasibility of creating vertical single-bead thin-walls (<1.5 mm) using the LP-DED process, but focused on materials characterization and mechanical testing of vertical or horizontal surfaces [92,94,103,104,118,190,195,235–237]. A gap in prior LP-DED studies is the characterization of thin-wall geometric limitations including build angles, features (holes, channels, slots, etc), thickness variation, surface texture, and the combination of these attributes [5,238–240]. These features, including thin-walls and internal flow passages, are common in complex AM parts, particularly in applications such as aerospace or industrial heat exchangers. Thin-wall feature characterization is particularly important due to decreased powder efficiency in the process, which can impact the geometry [120]. The understanding of the DfAM guidelines for thin-wall LP-DED bridge the divide between fundamental research and practical implementation [74].

A few studies explored LP-DED of thin angled walls limited to stainless steel (SS) alloys. Kalami and Urbanic conducted LP-DED experiments to produce a SS 410 dome structure with 2 mm walls, which focused on developing an algorithm for process planning multi-axis toolpaths and collision avoidance of the deposition head and the part [97]. The research was expanded to study surface roughness (Ra) and concluded that the interfaces between toolpath partitions caused significant changes in roughness [208]. As a result of utilizing partitioned toolpaths and maintaining the deposition head in a normal position, no definitive conclusions could be drawn regarding the impact of changing angles on surface roughness. Kaj et al. studied 2 mm walls deposited with LP-DED SS 316L and focused on 5-axis motion control [183]. The research indicated a 32.5° wall was achievable with LP-DED but did not provide any corresponding surface texture or roughness data. Wang et al. deposited 1 mm thick angled walls up to 32.9° using SS 17-4PH with collapses occurring above that angle [241]. The research concluded that lowering the layer height (Z-increment) to 0.43 mm resulted in more consistent angles (+/-0.9°), but also collapsed above 31°; no data on the surface texture was included.

Surface texture is another key geometric attribute for design since it can impact mechanical properties such as fatigue life, and, in case of internal fluid flows, heat transfer, and friction factors [106]. It is well known that the surface texture for AM produced parts is higher compared to traditional manufacturing techniques [242,243]. Proper filtering of measurements is of paramount importance when analyzing surface texture, encompassing form, waviness, and roughness. When defining roughness as an input for fluid flow analysis, relying solely on roughness data may not provide an accurate representation of the complete surface profile. [127,244]. The combination of height, spatial, hybrid, and functional parameters within comprehensive parameter groups enables a holistic understanding of the surface properties. [245]. Each of these texture parameters aid in describing results from manufacturing processes or end-use function (i.e. wear, lubrication, friction, fatigue, sealing, etc) [245]. Surface texture measurement is important during manufacturing to validate design assumptions and reduce uncertainty. It is also critical to measure and characterize surfaces during manufacturing operations. These experimental data are used to discern the underlying mechanisms behind the observed texture, such as waviness and roughness. This helps guide the total amount of material that needs to be removed during subsequent polishing or machining operations if a certain texture is required.

Surface texture is a direct outcome of the AM build process and is influenced by various factors, including the build orientation, wall angles, feedstock, process parameters, wall thickness, and the material being used [68]. It is known for L-PBF that surface texture varies significantly based on the angle and orientation (upskin or downskin) of a surface [126,246]. It has been shown that increasing the angle of downskin surfaces, relative to the build direction, increases the surface roughness due partially to unmelted powder adherence and dross formation [112,247]. Dross is excess material from overheating that forms at surface as the laser melts the powder and the material subsequently cools [85,248]. These studies all focused on evaluating the upskin and downskin surface texture related to L-PBF, but a gap exists related to this characterization for LP-DED.

Prior studies about L-PBF and LP-DED indicated that the observed stair step (or stair case) effect increases the surface roughness [115,236,249]. The stair stepping is the result of slicing the part into defined layers. The part is built in these layers with a determined height increase (Z orientation step up) of the deposition head that is programmed. The step is a resultant of these layers, which can be more pronounced as the surface angle increases relative to the build direction [209,250]. While the literature addresses the impact of the stair step as a form of roughness, it often does not segregate the data to distinguish waviness, creating a gap with respect to the full characterization of the LP-DED process.

This chapter summarizes research that used a variety of experimental data to characterize the geometry dependency of various samples fabricated using LP-DED. The study focuses on 1 mm wall thickness samples fabricated at angles up to 45° using hydrogen-resistant NASA HR-1 (Fe-Ni-Cr) alloy. These samples were deposited as freeform “racetracks”, with a straight wall on each side and 180 bends. The purpose of this experiment was to characterize deposition angle dependency for build limitations, upskin and downskin surface texture, wall thickness, and general microstructure. An equation was developed to predict wall thickness. These results are intended to advance the understanding of DfAM for the LP-DED process and to establish attributes for design and research engineers. The experimental results obtained are specifically applicable to the NASA HR-1 alloy. However, it is worth noting that the observed trends may have broader applicability to other alloys, provided that additional data collection is conducted.

4.3 METHODOLOGY

4.3.1 DED System and Samples

Ten NASA HR-1 alloy samples at angles varying every five degrees were deposited on an RPM Innovations (RPMI) 557 LP-DED machine with an argon-inert build chamber. The 557 system incorporated an infrared (IR) continuous wave gaussian profile 3 kW IPG laser, three coaxial nozzle within the deposition head, 5-axis motion control, and disc powder feeder with agitation capabilities. The motion control system was a Cartesian gantry-type system with a tilt and rotate trunnion table, although the trunnion table was not used in this experiment. The samples were built using a 2+1 axis approach, meaning each layer was deposited and the deposition head translated in height by +0.254 mm to deposit the next layer. The deposition head remained perpendicular to the build plate for all samples.

The samples were deposited as an enclosed racetrack (straight walls and 180° radii) to provide for dimensional stability. The baseline sample was built vertically, with the identifier referencing the build direction (0°); subsequent samples are identified in reference to the angle offset from the vertical build direction (5°, 10°, …45°). The baseline 0° sample geometry was identical to a prior study in which deposition parameters were varied using the same NASA HR-1 alloy [251]. While the use of 5-axis systems is possible, it is not feasible for every part and the practical application of complex LP-DED parts still uses a 2+1 (layer-wise slicing) and a combination of multi-axis toolpath planning. The samples were single-width passes (1 mm) at 76 mm length (Y-direction), 25 mm height (Z-direction), and 25 mm span between the adjacent wall (X-direction). The samples were built on an A36 mild steel 12 mm thick base plate. The layers for each sample were built individually, but simultaneously to allow for proper cooling between passes. All samples were evaluated in the as-built condition with no stress relief or other heat treatments and no surface cleaning or post-processing. The samples were removed from the build plate using a bandsaw and deburred on the bottom edge only. The samples from each angle are shown in Figure 4.1.

The upskin is referred to as the surface angled upward relative to the deposition head. This is also the outer surface on all samples. The downskin is the downward facing and the inner surface. The upskin and downskin terminology is consistent with previous L-PBF research [42].

The samples were built successfully up to 30° (Figure 4.1). The 35° and 40° specimens featured discontinuities in the radius. The 45° specimen had discontinuities in the radius and failed in the opposing wall. Once the deposition had challenges in a layer, this discontinuity would propagate and become worse with increased height. The straight wall that was successfully built served as the basis for all characterization and analysis.

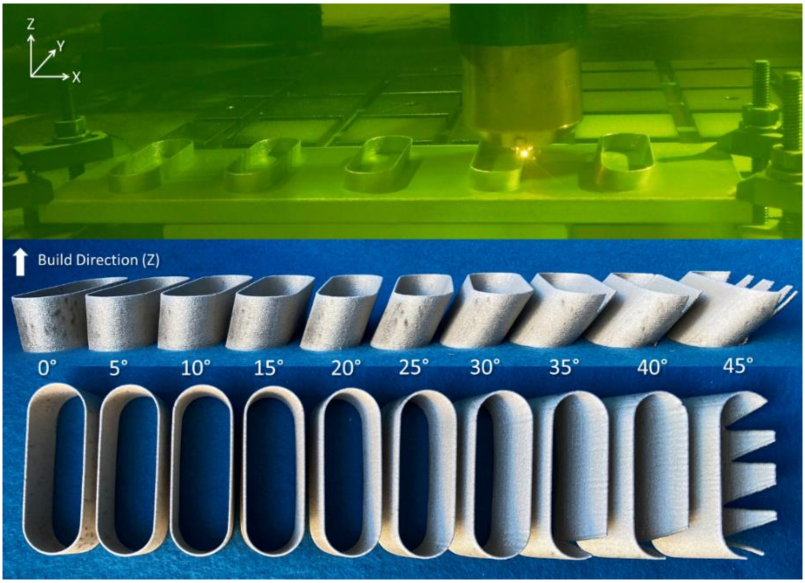

Figure 4.1. As-built NASA HR-1 alloy angled specimens removed from the build plate.

4.3.2 Deposition Parameters

The deposition parameters used for the experiment are listed in Table 4.1. The optimal parameters were selected based on a prior design of experiments to optimize high density microstructure and reduced build time [77,251,252]. Argon was used as the carrier and shielding gas. The deposition head was fixed normal to the surface and the standoff distance was actively monitored and controlled. The layer height remained constant at 0.254 mm and X-axis translation adjusted based on the angle of the sample. The start and stop points were randomized for each sample. The trunnion table was locked and not used for these samples. While acknowledging that the use of a trunnion table could potentially increase the maximum build angle, it is important to note that this build approach for thin-wall complex hardware designs may not always be feasible and is not the primary focus of this study.

Table 4.1. Parameters used for angled racetrack sample deposition.

Power (W)	**Powder Feed rate (grams/min)**	**Travel Speed (mm/min)**	**Layer Height (mm)**
350	23	762	0.254

4.3.3 NASA HR-1 Alloy

NASA HR-1 is a Fe-Ni-Cr superalloy used in high pressure hydrogen components, such as heat exchangers. It was developed for resistance to hydrogen environment embrittlement (HEE). NASA HR-1 provides high strength and high ductility in harsh hydrogen environments such as liquid rocket engine nozzles and heat exchangers and it is derived from the A-286 and JBK-75 alloys [253,254]. The powder was rotary atomized by Homogenized Metals Inc. (HMI), with a particle size distribution (PSD) of 55-105 µm meeting +140 mesh at 0% and -325 mesh at 3.2% per ASTM B214 using a Microtrac (Ver 11.1.0.6), and chemical composition provided in Table 2 (HMI powder lot HRA7). A SEM image of the morphology is shown in Figure 3. The Oxygen content was 59 ppm and Nitrogen content was 9 ppm. The chemistry was measured using Inductively Coupled Plasma (ICP) at HMI. The peak powder size was 69 µm and a Vega3 Tescan Scanning Electron Microscope (SEM) using Backscatter Electron (BSE) showed mostly spherical particles with a few satellites and random distribution of occasional oblong particles. The powder cumulative distribution has 10% of particle sized below 58 µm (D10), 90% below 85 µm (D90), and 99% below 105 µm (D99) with a median particle size of 69 µm. Virgin powder was used for all builds. The samples were evaluated in the non-heat treated (as-built) condition.

Table 4.2. Chemical composition of NASA HR-1 alloy powder (HMI Lot HRA7).

	Fe	Ni	Cr	Co	Mo	Ti	Al	V	W
Wt. %	Bal.	34.03	14.64	3.75	1.84	2.46	0.23	0.3	1.59

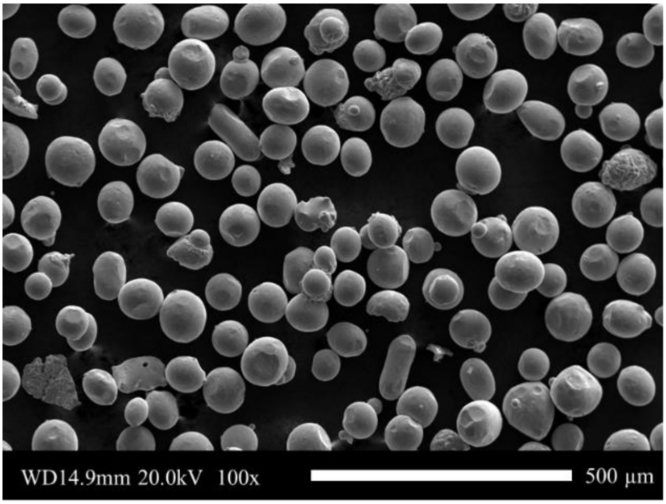

Figure 4.2. SEM image of NASA HR-1 (55-105 µm) powder morphology.

4.3.4 Surface Metrology and Imaging

Surface texture measurements were obtained using a non-contact Keyence VR-5200 pattern light projection profilometer. The setup included three telecentric lenses with 80x magnification capability and an overlap of 20%. Each sample was measured on the upskin (outer) surface and then sectioned inside of the radii to allow access to the inner surface. The downskin (inner) surface was then measured. The surface scanning covered a total area of 43 mm by 16 mm shown in Figure 4. Areal surface measurements were reported in addition to directional legacy measurements. The texture measurements are reported along with a brief explanation and mathematical definition [244,245,255] in Table 3.

Table 4.3. Description of surface parameters and definition.

Description of Surface Parameter	Mathematical Definition
Average texture (Sa) – average areal roughness across the entire 3D surface relative to a best fit plane.	$Sa = \frac{1}{A}\iint_A \lvert Z(x,y)\rvert \, dx\, dy$
Root mean square (RMS) height (Sq) –standard deviation of the height distribution.	$Sq = \sqrt{\frac{1}{A}\iint_A \left\lvert \left(Z(x,y)\right)^2 \right\rvert dx\, dy}$
Maximum peak height (Sp) – absolute highest single points found on the 3D	$Sp = \max\left(Z(x,y)\right)$

surface, filtered to eliminate erroneous peaks.	
Maximum valley depth (Sv) – absolute lowest single points found on the 3D surface, filtered to eliminate erroneous peaks.	$Sv = \left\|\min\left(Z(x,y)\right)\right\|$
Maximum surface height (Sz) – defined as the total surface height based on the summation of the maximum peak height and valley depth	$Sz = Sp + Sv$
Skewness (Ssk) – Represents the asymmetry of the surface texture based on a nominal plane, where 0 is ideal, >0 is dominated by peaks, and <0 is valleys.	$Ssk = \frac{1}{Sq^3}\left[\frac{1}{A}\iint_A \left(Z(x,y)\right)^3 dx\,dy\right]$
Kurtosis (Sku) – Determines inordinately high peaks or valleys, where 3.0 is ideal, >3.0 is peaks, and <3.0 is valleys.	$Sku = \frac{1}{Sq^4}\left[\frac{1}{A}\iint_A \left(Z(x,y)\right)^4 dx\,dy\right]$
Developed interfacial area ratio (Sdr) – Percentage of the overall surface area that contributes to the texture amplitude and spacing compared to an ideal plane across the entire measured area.	$Sdr = \frac{1}{A}\left[\iint_A \left(\sqrt{\left[1 + \left(\frac{\partial z(x,y)}{\partial x}\right)^2 + \left(\frac{\partial z(x,y)}{\partial y}\right)^2\right]} - 1\right) dx\,dy\right]$
Core roughness (Sk) – defined as the distance between the highest and lowest levels of the core surface height, filtered to eliminate predominant peaks and valleys.	$Sk^* \approx Sz - Spk - Svk$
Arithmetic mean directional roughness (Ra) – average deviation from a mean line based on a direction such as parallel (vertical) to the build direction or perpendicular (horizontal). Data are filtered	$Ra = \frac{1}{Lx}\int_0^{Lx} \|Z(x)\|\,dx$

using < λc, which removes form and waviness of the surface.	
Average directional maximum profile height (Rz) – average height difference between highest peaks and lowest valleys (using 5 of each) along a sampling length in a defined direction (vertical build direction). Data are filtered using < λc, which removes form and waviness of the surface.	$Rz = \max\big(Z(x)\big) + \big\vert min\big(Z(x)\big)\big\vert$
Arithmetic mean directional waviness (Wa) – average height of widely spaced component of the overall profile along a direction such as parallel (vertical) to the build direction or perpendicular (horizontal). Data are filtered using < λc, which removes form and waviness of the surface.	$Wa = \frac{1}{Lx}\int_0^{Lx} \vert Z(x)\vert \, dx$

**Sk is approximated and detailed procedures to obtain can be found in [256] and [207].*

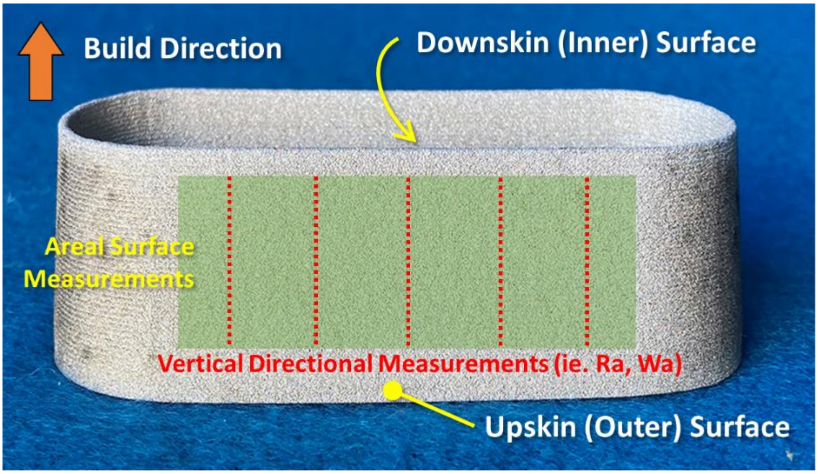

Figure 4.3. Terminology for sample measurement (example of 20° wall sample).

All areal surface measurements are reported according to ISO 25178-2:2021 [255,257]. A surface form correction was applied to remove any tilt and curvature from any residual stress distortion of the samples. The data around the edges of the measurement was eliminated using an end effect correction. A reference plane was then established. For the area surface measurements, the primary texture profile was unfiltered (denoted as primary) using form correction only. To extract roughness from the areal surface, a λc spatial frequency cut-off filter of 0.8 mm (*i.e.,* a roughness filter) was applied per ISO 4288-1996. A λc of 2.5 mm was also evaluated but was too large. Measurement uncertainty was obtained by repeating measurements on a single sample five times to determine a 95% confidence interval.

When analyzing texture measurements, it is important to consider the end use application to obtain appropriate results [208]. One potential application of the thin-wall LP-DED process is the fabrication of heat exchangers with integral channel fluid flow. These heat exchangers are built with the channels running in the vertical build direction (Z). Thus, the directional measurements are reported in the vertical build direction (Figure 4). Five symmetrical vertical lines were placed on the sample image and measurements averaged to report the waviness and roughness. For the directional measurements, form correction was also applied along with λc of 0.8 mm and a λs of 2.5 μm to eliminate noise at a 300:1 ratio (λc/ λs) per ISO 4228-1996. This allowed for the segmentation of directional waviness (Wa) and roughness (Ra) effects. Directional measurements are reported according to ASME B46.1 [207].

The surface samples were imaged using a Hitachi S3000H SEM on the upskin and downskin. Each sample was then sectioned along the center axis and mounted and polished according to ASTM E3 using a Presi automatic polisher. The samples were polished using 0.5 μm colloidal silica and optical images obtained. Samples were then etched using etchant #13 (10% Oxalic Acid, Electrolytic) and optical imaging completed again. All optical images were obtained using a Keyence VHX digital microscope. Porosity, thickness, meltpool, and powder particle count measurements were analyzed using *Image J* (Version 1.53e). Eight thickness measurements were obtained normal to each wall (across) and averaged. The distance between each melt pool (height), perpendicular to wall thickness, was also measured for each wall and averaged. The low angle samples (<10°) included approximately 12 melt pool measurements and angles >10° were measured with a minimum of eight melt pools. A 95% confidence interval was calculated and reported for these measurements. Particle count was determined by examining the number of particles in two 1 mm^2 areas and averaging. This was obtained from the SEM image at 50x.

4.4 RESULTS AND DISCUSSION

The measurements were obtained in a sequential order per sample: texture, SEM, optical images. However, they are presented here per type of measurement with the aim of providing a comprehensive understanding of the surface texture and associated geometry.

4.4.1 SEM Image Analysis

SEM images are shown in Figure 5. Visually, the adhered powder drastically reduces on the downskin with increasing angle. The opposite is observed with the upskin whereby more powder adheres to the surface. As the angle of incidence increases relative to the deposition nozzle, the powder can bond more directly to the trailing and edges of the melt pool for the upskin. The downskin surface is more protected as the angle increases. An illustration of the vertical and angled powder impingement in the samples is shown in Figure 6. Despite the enclosed racetrack samples, particle impacts are still possible. This is evident from the observations of ricochets and the recirculation of powder, as previously put into evidence [251].

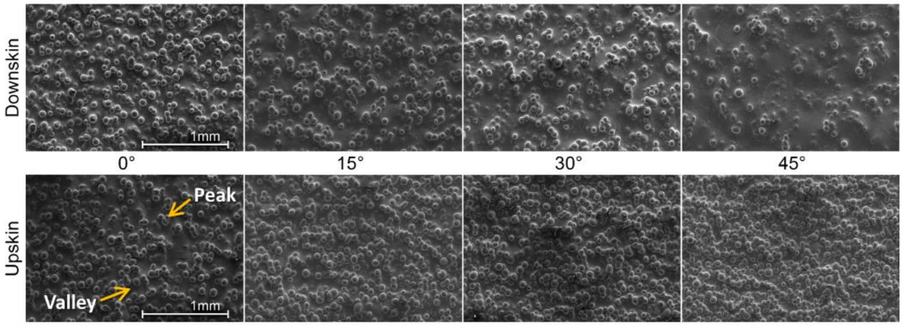

Figure 4.4. SEM images of the normal surface for upskin and downskin surfaces (additional images provided in supplemental materials). Scale is the same for all images.

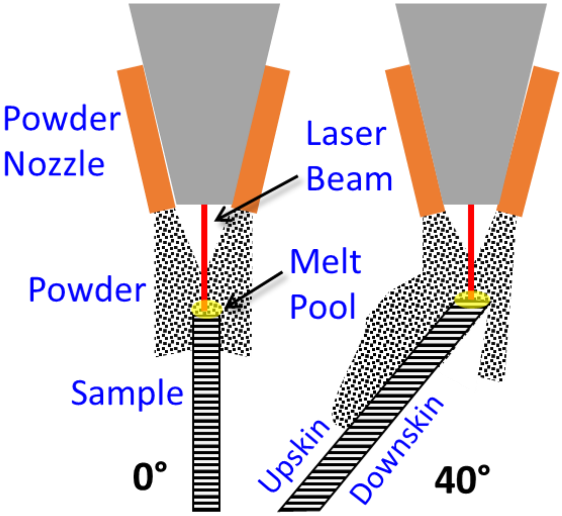

Figure 4.5. Example of powder impingement for vertical and angled sample.

Based on the SEM images, the particle count (per mm^2) was determined at two locations on the surface and averaged. These data sets are shown in Table 4. The particle count analysis confirms the increase in adherence for the upskin and reduced powder for the downskin, although no inference should be made from this observation related to surface texture without proper filtering for roughness. The increase in angle facilitates a longer particle resonance time due to flow stagnation from the impingement of the deposition nozzle (Figure 6). Additionally, the smaller diameter melt pool (< 1 mm) decreases the powder capture efficiency, leaving approximately 80% of the powder available to adhere to the surface of the solidified material [120,258]. A depiction of the smaller melt pool (1 mm) is shown in the supplemental materials. Due to gravity, the powder will move down the surface of the angled wall and bond to the melt pool as it is cooling as indicated by the increased particle count.

Table 4.4. Data from SEM and Optical Image Measurements.

Angle (°)	Particle Count, Downskin (Inner)	Particle Count, Upskin (Outer)	Normal Wall Thickness (µm)	Melt Pool Height (µm)	Optical Porosity (%)
0	96	93	1056 ±24	253 ±8	0.13
5	92	99	1046 ±26	252 ±17	0.11
10	92	120	1082 ±17	259 ±14	0.04
15	84	122	1079 ±13	259 ±10	0.07
20	80	126	1115 ±15	269 ±16	0.07
25	80	140	1132 ±13	272 ±10	0.10
30	68	142	1192 ±14	287 ±14	0.14
35	63	166	1306 ±21	308 ±13	0.05
40	54	179	1370 ±15	336 ±12	0.03
45	36	181	1535 ±18	361 ±18	0.05

4.4.2 Optical Image Analysis

From optical images of the sectioned samples several sets of data were collected. The porosity was measured for each sample in the polished unetched condition (non-heat treated) with the highest porosity being 0.14%, as shown in Table 4. This is consistent with prior results on vertical 1 mm thick NASA HR-1 specimens [251] and no trends are apparent based on the angle of the sample. Density was also obtained using the Archimedes method and is provided in the supplemental materials; there were no correlations observed on samples based on the wall angle. The wall thickness was measured for each sample normal to the wall and results provided in Table 4. Figure 7 shows that, as the angle increases, there is a corresponding increase in the normal wall thickness. The wall thickness linearly increases of 7% from 0° to 25° and then increases exponentially from 25° to 45°. The optical images indicate a transition from partially melted and adhered powder at lower angles to a more random surface profile as the angles increase, more so for the downskin surface (Figure 8). The downskin surface at the high angles shows instances of subsurface unmelted powder. The partially melted and adhered powder is observed regularly on the upskin surface with more instances at the higher angles.

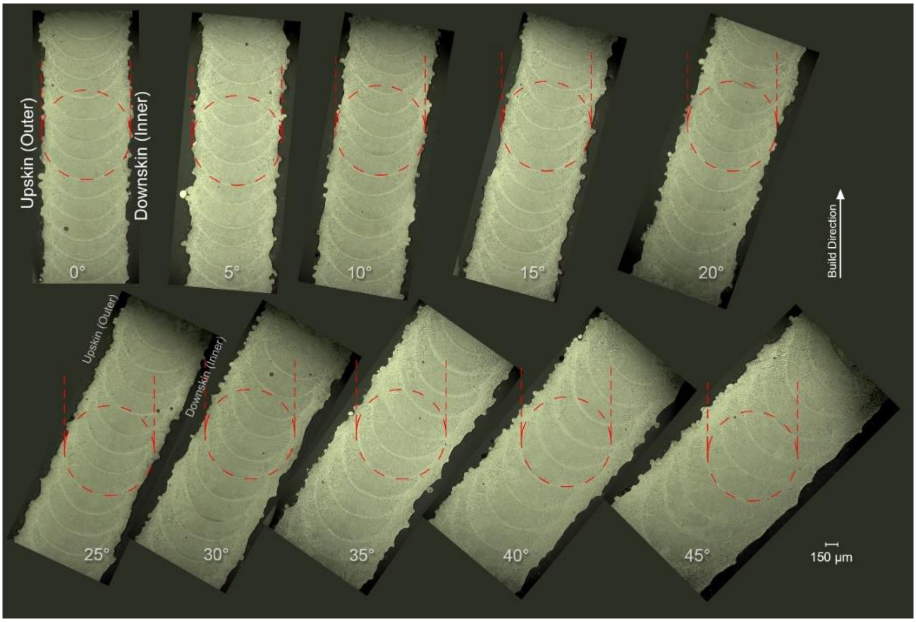

Figure 4.6. Wall thickness and melt pool visualized on angled wall samples.

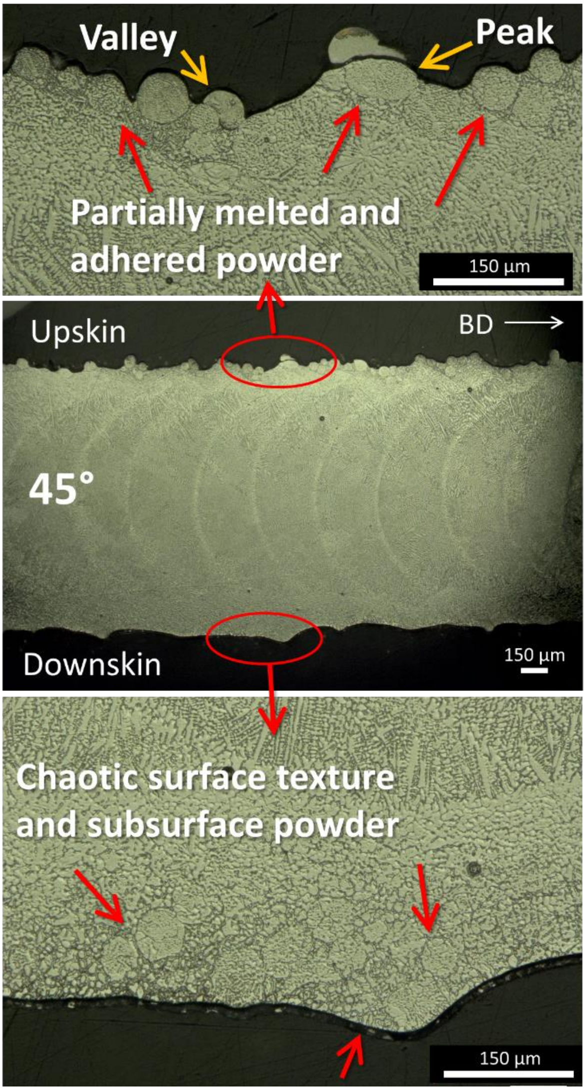

Figure 4.7. Partially melted and adhered powder shown for the upskin surface and chaotic texturing and subsurface powder shown for the downskin of the 45° wall sample.

The increased wall thickness is due to the material droop on the downskin side and excess material deposited on the upskin side. The visualized melt pool can be observed in Figure 7 along the centerline of the sample. The material droop is made evident by the color change of etched samples and below the nominal melt pool. The Marangoni forces moves the material outwards in the melt pool and this material is solidified at the edges causing this chaotic texturing [192,229]. Unmelted subsurface powder is also observed below the chaotic texturing (Figure 8). Above 30°, gravity has an impact, breaking the surface tension and causing the fluid metal to droop below the nominal melt pool and then solidify. This droop is distinctively different from the dross phenomenon in L-PBF [248] since the melt pool terminates prior to the downskin edge of the specimens. The excess material above the nominal melt pool increases due to the direct impingement of the powder and inert gas and causes the remelted and deposited material to flow upwards, in addition to outwards [259].

It was observed from the experimental dataset, that the wall thickness could be normalized when divided by the cosine (α) function, where α is the angle of the deposited wall. The adjusted wall thickness has been demonstrated to exhibit a high level of consistency, which is corroborated by the measured thickness data (Figure 9). Based on the observation that the wall thickness can be adjusted with the angle, this concept was applied to predict the wall thickness based on deposition parameters. Mazzarisi et al. reviewed and evaluated multiple models to predict wall thickness for single-beads based on laser power (P) measured in watts (W), powder feed rate (F) measured in grams/min, and traverse scan speed (V) measured in mm/min [192]. The validation testing has demonstrated a reasonable correlation with the proposed models. Kalami et al. discuss the relationship between the build layer height and its variation based on the angle. However, they do not specifically explore the relationship between the build layer height and the resulting wall thickness. [97]. With the help of this dataset, these approaches were modified resulting in an equation to predict the wall thickness (Wt) measured in mm, which reads

$$Wt = \frac{\frac{P}{VF^{n}} K'}{\cos \propto} \qquad \textbf{4.1}$$

where, Wt = thickness in mm; n = Exponent (0.005); K’ = Proportionality constant (2.35); and α = angle of wall in degrees. The exponent and constant were fitted using the experimental data. The model shows a good correlation with the measured thickness and peak error of 3.5% for the current set of NASA HR-1 samples.

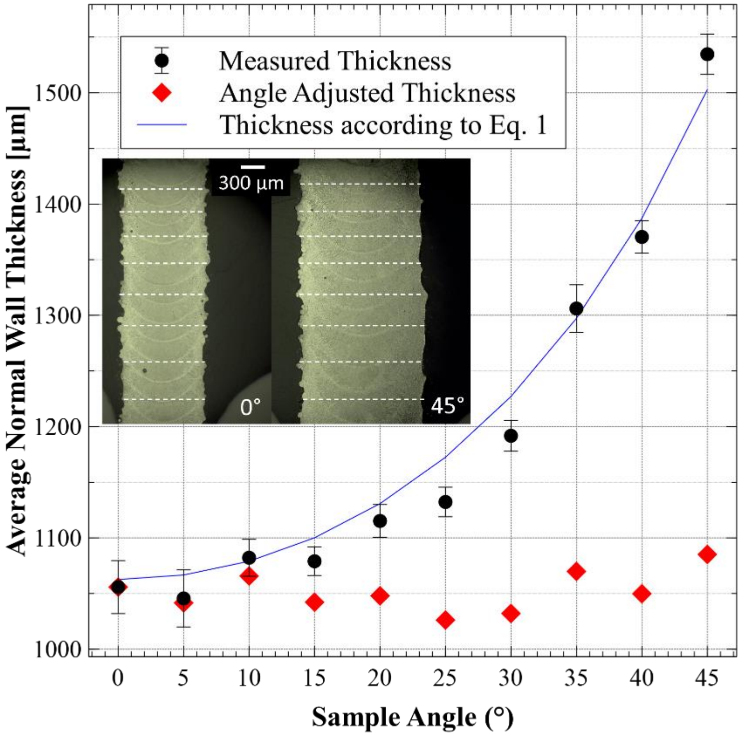

Figure 4.8. Measured and adjusted wall thickness of the angled samples.

The melt pool can be distinguished in the etched optical images and was measured perpendicular to the wall and along the centerline. The vertical distance between the visible melt pools was obtained and averaged. Based on thickness of the sample at 0° and prior research of the NASA HR-1 melt pool with identical parameters [251], a size can be assumed and overlayed for each sample in Figure 7. From this, the number of layers penetrated with subsequent deposition layers can be determined. An average of four deposited layers were subjected to remelting with each subsequent pass when the angles were less than 25°. When the angles exceeded 25°, three layers were remelted. The perpendicular melt pool height is shown in Figure 10. The melt pool height was adjusted using the cosine function and shown in the graph. The measurements indicate that as the distance of the melt pool is increased when measured vertically. However, the adjusted step over used to create the desired angle, along with the fixed Z-height of 0.254 mm, demonstrates highly repeatable motion control, a stable melt pool, and a satisfactory solidification process. The adjusted angle wall thickness (Figure 9) also indicated a consistent melt pool. These findings establish the melt pool's robust stability, ruling out arbitrary material deposition related to height or thickness. The adjusted data sets confirm that the downskin droop and upskin excess material are not related to an unstable melt pool, but rather to gravity effects.

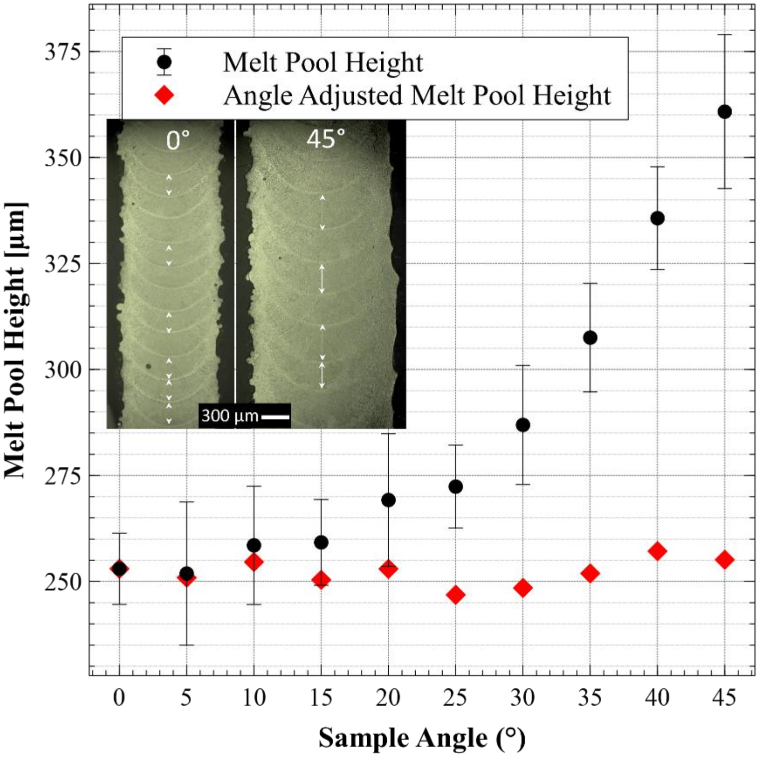

Figure 4.9. Perpendicular melt pool height and adjusted height of the angled samples.

4.4.3 Surface Texture Characterization

4.4.3.1 Surface Texture with Primary Filter

The initial areal surface texture was measured and evaluated using a form correction factor only. This allowed to analyze the full profile in terms of waviness and roughness. The Sa is shown in Figure 11a: the inner and outer surfaces of the vertical wall (0°) feature a similar average surface texture. The average areal surface texture of the inner surface is slightly higher than the external surface consistent with prior measurements [251]. This is due to the enclosed racetrack walls allowing for powder rebounds and recirculation causing excess adherence. A minor change in the wall inclination of 5° results in a reduced amount of powder adhering to the downskin (inner surface) as it angles away from the deposition nozzle. The average texture of the outer surface increases with the direct impact of the powder from the deposition nozzle. The upskin texture is driven by roughness from the powder but also by variations in the solidification of the melt pool, and it continues to increase linearly up to an angle of 35°, stays near level and then a slight drop occurs at 45°. The downskin texture shows no appreciable differences up to an angle of 30°, while for larger angles it increases exponentially. This indicates that particle adhesion alone cannot be used to determine texture and that other mechanisms cause this drastic change. The observed downskin texture varies with the angle and aligns with the thickness data and occurrence of material droop.

The maximum height of the surface (Sz) in Figure 11b shows that the upskin surface texture decreases with increasing angles. Greater powder adherence is observed, but several particles have the capability to fill in the valleys, thereby contributing to a decrease in the observed effect. This is corroborated by the observation that the maximum peak height (Sp) decreases, while the maximum valley depth (Sv) remains constant. The downskin suggests a general increase of maximum height, where peaks dominate the surface texture. In order characterize this attribute, the skewness and kurtosis parameters were evaluated and are shown in Figure 11c and Figure 11d, respectively. The skewness (Figure 11c) is plotted with the normal wall thickness to identify abnormalities related to symmetry. The plot therefore reveals that the upskin is symmetric about the plane, whereby peaks and valleys are randomly distributed. Up to an angle of 30°, the inner surface is symmetric. Beyond this angle, a predominance of peaks becomes evident, which is coherent with the drastic changes observed in the wall thickness. The powder count analysis demonstrates that powder is less adherent in this case, therefore the asymmetrical peaks are governed by the droop of the material.

Figure 11d allows to evaluate the kurtosis for excessively high peaks or valleys. A similar trend is observed in the Sz data of the upskin surface, which demonstrates a general decrease in the number of peaks as the angle increases. The downskin surface shows again a general increase of excessively high peaks with the increase in angle.

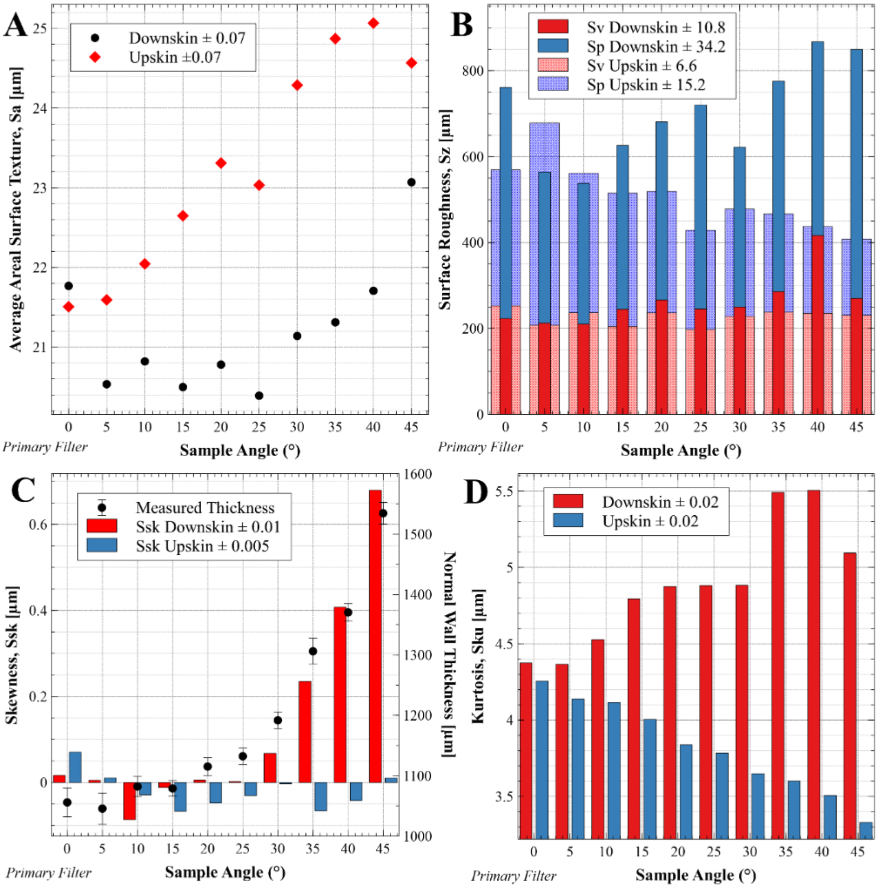

Figure 4.10. Primary texture of areal surface: a) Sa, average surface texture; b) Sz, Sp, Sv, peak and valley height of surface; c) Ssk, skewness; and d) Sku, Kurtosis.

4.4.3.2 Areal Roughness and Particle Count

The surface texture and filtered roughness are further examined in relation to the adherence of the powder to determine the factors contributing to the formation of the observed texture. Using no profile filter (*i.e.*, primary), the texture of the upskin linearly increases with increasing particle count (Figure 12a). This could indicate that powder adherence is dominant for the upskin roughness but cannot be determined conclusively without proper filtering. Figure 12a also shows that the texture of the downskin surface initially decreases with reduced particle count. Starting at 30°, the surface texture linearly increases up to 40° and at 45° rises even more steeply. This indicates that the texture of the downskin surface is related to the powder adherence based on particle count.

The roughness filter, see section 2.4, was applied to the areal surface and plotted as a function of the particle count in Figure 12b. The roughness (less than 0.8 mm wavelength) shows a clear trend for the downskin surface: the average roughness decreases with decreasing powder adherence, and this is also evident in the SEM images. The upskin surface exhibits a similar trend but only up to 20°. Beyond 20° the average roughness is constant, and it is much lower at 45°. Above 20°, the particles continue to bond to the trailing edge of the melt pool as it cools but valley voids are filled. The optical images reveal that the texture extends to a depth of two powder particles, indicating that the excess particles are effectively filling in the valleys of the surface. The core roughness (Sk), whereby the predominant peaks and valleys were removed [256], was also evaluated, and its trend is identical to that of the Sa with the roughness filter. The Sk values ranges from 38 ±0.2 µm to 51 ±0.2 µm for the downskin surfaces and from 50 to 58 ±0.2 um for the upskin surfaces. The filtered Sdr was also assessed, because it determines the overall contribution to the texture amplitude (shown in supplementary materials). The trends are identical to those obtained for the Sa and the Sk: the roughness is proportional to the particle count for the downskin surfaces and it reaches a maximum at 20° for the upskin surfaces.

This roughness comparison displayed in Figure 12 put into evidence the significance of using appropriate filtering techniques. Significantly different conclusions could be drawn about the mechanism for the texture without properly evaluating all filtering options [260].

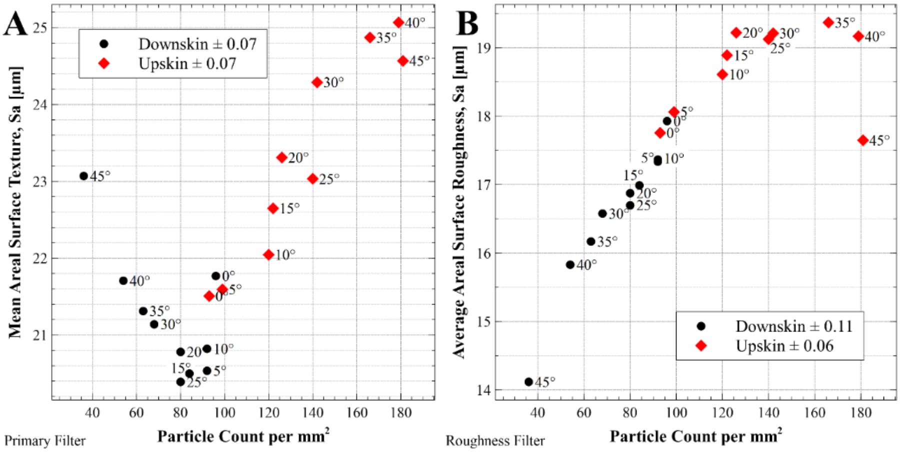

Figure 4.11. Roughness compared to particle count from SEM. a) Primary filter and, b) Roughness filter.

4.4.3.3 Vertical Directional Roughness and Waviness

To better characterize roughness (Ra) and waviness (Wa) in the vertical build direction, the data set was filtered as discussed in section 2.4 and a comparison is shown in Figure 13a. The directional average roughness for the upskin is higher than that of the downskin and driven by the direct particle impact with the melt pool. In contrast to the Sa values (Figure 12), the upskin Ra does not indicate a reliance upon the angle and roughness values are similar at all angles. The upskin Wa does increase at angles above 30° due to chaotic disturbances in the melt pool creating the texture. It can be hypothesized that the increased melt pool disturbance can reduce the presence of partially assimilated surface particles [204]. This is observed in the maximum height roughness (Rz) in Figure 13b, which is driven by the particle count above 25°, and also the waviness portion of the surface texture.

The downskin surface indicates similar directional roughness and waviness at angles 0° to 30°. A linear increase in waviness and decrease of roughness is observed starting at 35°. Literature often suggests that the stair-stepping effect due to the build layers creates periodic waviness [116,239], but this is not observed in these samples with a layer thickness of 254 µm. The waviness is driven by chaotic irregularities from the melt pool on the surface due to the gravity slump, or material droop. The directional Ra was also compared with the particle count and showed identical trends to the areal Sa. The maximum height roughness (Rz) is depicted in Figure 13b and shows similar trends to Ra with the peak of 114 µm, which is the upper limit of the PSD for the powder. The Rz peak height of the upskin surface is constant up to the higher values of the angles, where the powder fills in valley voids and thus Rz decreases.

Prior literature documented that Rz can be approximated by the upper PSD of the powder for L-PBF [147,261]. The experimental data suggest that, for LP-DED, the Rz peak can be approximated by using the maximum PSD. In the downskin surface, there is a decrease in Rz where the surface is shielded from the direct impingement of larger particles. However, the rebounds and recirculation of particles are driven by the smaller and medium-sized particles (ranging from 55 to 95 µm) due to their mass and velocity differences. The 115 µm diameter particle has 83% larger mass than the 85 µm particle, where the difference between the 55 and 115 µm is 337%. The velocity in the powder injection has been shown to vary based on mass and surface area of particles as well as nozzle focal plane, thus the likelihood of rebounds and recirculation is higher with the smaller particles. [220,262]. SEM images confirmed that the size of the particles adhered to the downskin 40° and 45° walls is less than 90 µm.

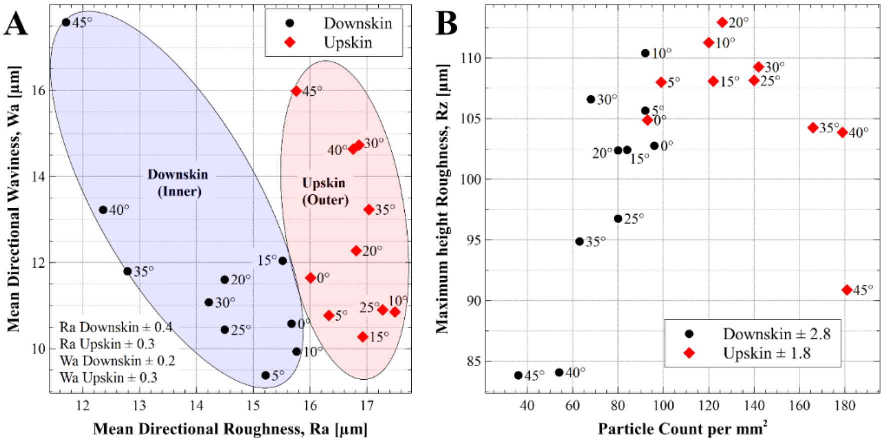

Figure 4.12. a) Directional vertical roughness and waviness. The shaded blue region indicates the downskin surface and shaded red the upskin surface. b) Maximum height (Rz) and particle count.

The relationship between waviness and wall thickness is shown in Figure 14. The waviness is higher on the upskin for most of the angles, although differences are minor at angles below 30°. There is A clear trend of waviness increasing with the wall thickness can be observed and it is due to the surface irregularities from material droop on the downskin. The upskin waviness is driven by the excess material deposition above the nominal melt pool. This results from direct impingement of the particles and remelted material flowing upwards and outward breaking the surface tension [263,264]. This phenomenon has been evaluated in single bead LP-DED walls [265], but this study has demonstrated that it is amplified in the angled walls. Prior studies concluded that waviness was caused by the layer thickness [190,233]. This work has proven that the waviness is an order of magnitude lower that Lu et al and Shim et al and uncorrelated to the layer thickness.

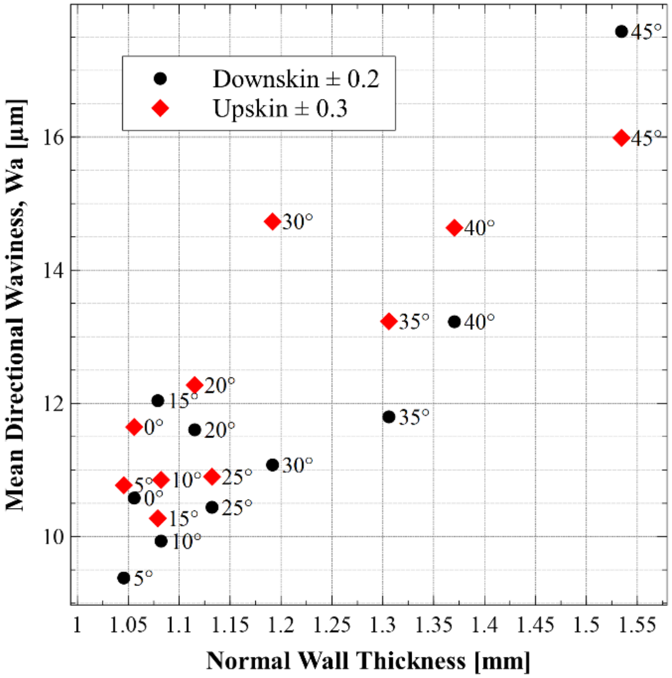

Figure 4.13. Directional waviness and normal wall thickness.

4.5 CONCLUSIONS

It was shown that the LP-DED process can produce low porosity (<0.14%) angled walls with target thickness of 1 mm and with an inclination angle of up to 45° using the NASA HR-1 (Fe-Ni-Cr) alloy. The geometric aspects of the samples including wall thickness, melt pool, and surface texture were evaluated. The surface texture was filtered to properly segment the waviness and roughness parameters to determine their contribution and the causing process mechanisms. From the experimental observations, optical micrographs, SEM images, and optical surface texture measurements, the following conclusions are drawn:

- Walls featuring angles of up to 30° are stable, but angles above that threshold pose higher risks of a build failure. In such cases, it may be necessary to incorporate adjacent wall stiffening to ensure structural integrity.
- The primary areal surface texture (Sa) exhibits an increase with the rise in wall angle, which can be attributed to surface irregularities arising from the melt pool and material droop. Peaks are dominant for the downskin surface with the increasing angle and reduced for the upskin.

- The waviness and subsequent wall thickness increases with the increased wall angle due to the chaotic surface irregularities from material droop on the downskin. The upskin waviness is driven by the excess material deposition above the nominal melt pool. This is due to direct impingement of the particles and remelted material flowing upwards and outwards.
- Proper filtering of the texture measurements is required to segregate roughness and waviness. Differing conclusions could be drawn about the mechanisms leading to texture if proper filtering is not considered. The λc of 0.8 mm was an appropriate cut-off filter to extract directional roughness and waviness for these thin-wall samples.
- As the angle increases, the filtered average areal and directional surface roughness (Sa, Ra) of the downskin surface significantly decreases. This reduction can be attributed to a decrease in the number of adhered particles on the surface. This trend contradicts the observations documented in the literature regarding surfaces manufactured with the L-PBF process.
- The upskin surface exhibits an increase in average areal (Sa) with an increase in particle count. The roughness crests at 20° and remains constant until the adhered powder filled in voids, resulting in a reduction in roughness at higher build angles.
- The wall thickness increases exponentially with the angle, reaching an inflection point at 30° where the thickness starts to significantly increase due to melt pool droop. A correlation for the estimation of the wall thickness was developed using the data related to the samples made of NASA HR-1 alloy.
- The results obtained from single-pass angled walls indicate that, for LP-DED, the directional maximum profile height (Rz) can be estimated using the maximum particle size distribution. Only particles with size less than 85 µm adhere to the downskin surface at angles above 35° due to higher rebounds and recirculation.
- The stair stepping typically observed in the LP-DED was not detected with a layer height of 0.254 mm and remelting of 4-5 previously deposited layers.

The complex geometry of a part being fabricated inherently alters surface texture due to varied angles. This change is influenced by the build parameters and resulting melt pool. Thickness variation and powder adherence for upskin and downskin follow comparable trends based on wall angle, driven by process mechanisms. Surface texture, encompassing roughness and waviness, varies with alloy, parameters, and resulting LP-DED melt pool. Designers must adhere to geometry guidelines and characterize surface texture, which can impact fatigue life, corrosion, heat transfer, and fluid flow performance. Previous views on LP-DED mandated post-machining, but experiments show properly designed LP-DED can approach L-PBF surface finishes. LP-DED manufacturing holds potential for aerospace, power generation, and industrial heat exchangers.

Chapter 5

Development and Characterization of Microchannels

This chapter was partially published in:

Gradl, P., Cervone, A., Colonna, P., 2022. Integral Channel Nozzles and Heat Exchangers using Additive Manufacturing Directed Energy Deposition NASA HR-1 Alloy. 73rd International Astronautical Congress. Paris, France, IAC-22,C4,2,x73690.

5.1 ABSTRACT

This chapter focuses on the process development and characterization of microchannels made from the NASA HR-1 alloy. In Chapters 3 and 4, samples with 1 mm walls were produced and characterized, establishing a baseline for the microchannel fabrication. Microchannels of varying internal width/height dimensions (12.7, 10.16, 7.62, 5.08, and 2.54 mm) were successfully deposited down to 2.54 mm without powder entrapment, and 1 mm wall thickness was achieved with high reproducibility. Optical microscopy, scanning electron microscopy, and optical surface texture measurements were employed to destructively section and characterize these channels. The analysis included determining cross-sectional area, surface texture, wall and rib thickness, and the repeatability of these measurements. The study revealed that the areal surface roughness is significantly influenced by the size of the powder feedstock used in microchannel deposition, consistent with Chapter 3 results. While the as-built cross-sectional area exhibited high repeatability, the area was consistently smaller than the as-designed nominal area due to powder adherence and melt pool undulations, as discussed in Chapter 4.

5.2 INTRODUCTION

For effective utilization of LP DED in heat exchanger manufacturing, it is imperative to demonstrate and characterize various aspects of the geometry. Chapters 3 and 4 have discussed the fabrication and characterization of thin-wall geometry samples, establishing a baseline for demonstrating microchannels. To illustrate microchannels and, ultimately, heat exchangers, multiple geometric attributes must undergo evaluation. These include angles, manufacturing tolerances, wall thicknesses, internal features, and surface texture (refer to Figure 5.1). Characterization of these various aspects is critical for using LP-DED for heat exchangers manufacturing as the heat transfer and associated pressure drop can be tuned to meet the optimal design requirements.

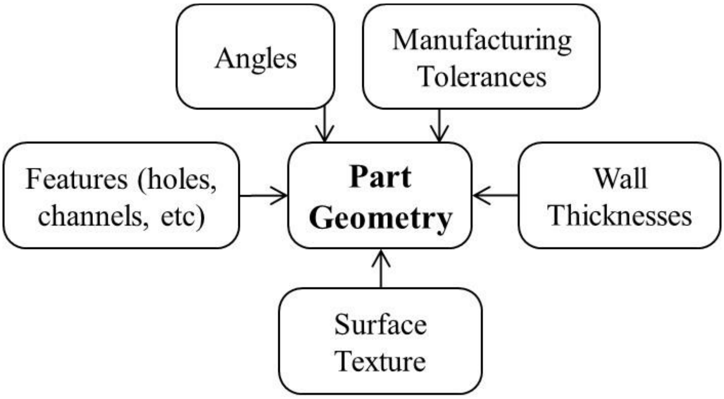

Figure 5.1. Aspects affecting the LP-DED process that need to be studied to characterize overall geometry limitations inherent in the manufacturing technique.

While the main emphasis of this dissertation is on microchannel geometry, it recognizes that achieving the final quality of a component involves characterizing its microstructure and resulting mechanical and thermophysical properties. The entirety of the Design for Additive Manufacturing (DfAM) lifecycle is defined by factors such as process inputs and parameters, geometry limitations, microstructure, and material properties, as well as considerations for post-processing, part validation, and application. The application of DfAM best practices is crucial for ensuring successful builds and commissioning parts into service [62]. The LP-DED process was originally designed for applications unrelated to microchannel heat exchangers. Consequently, developmental lessons needed to be gleaned to adapt this process for integral microchannel heat exchangers.

5.3 CHANNEL PROCESS DEVELOPMENT AND CHARACTERIZATION

5.3.1 Microchannel Deposition

The microchannel samples of NASA HR-1 were deposited using an RPM Innovations (RPMI) 557 LP-DED machine equipped with an argon-inert build chamber. This system is identical to the one discussed in Chapters 3 and 4, featuring an infrared (IR) continuous wave Gaussian profile 3 kW IPG laser, a deposition head with three coaxial nozzles, 5-axis motion control, and a disc powder feeder with agitation capabilities. Deposition parameters remained consistent with those detailed in Table 4. The powder was rotary atomized by Homogenized Metals Inc. (HMI). The coarse powder had a particle size distribution (PSD) of 55-105 µm and mean PSD of 72 µm as measured using a Microtrac (Ver 11.1.0.6). The fine powder has a PSD of 10-45 µm and chemistry shown in Table 6. The chemistry was measured using Inductively Coupled Plasma (ICP) at HMI. The chemical composition of coarse is also provided in Table 6 .

The coarse powder exhibited an oxygen content of 75 ppm and a nitrogen content of 6 ppm, while the fine powder had an oxygen content of 143 ppm and a nitrogen content of 15 ppm. It is typical that finer powder has elevated oxygen content due to the increased surface area [266]. It is important to note that all powder chemistry adhered to the specifications for the NASA HR-1 alloy [201,205]. Virgin powder was used for all builds.

Table 5.1. Chemical composition of NASA HR-1 alloy powder.

PSD / Lot ID		**Fe**	**Ni**	**Cr**	**Co**	**Mo**	**Ti**	**Al**	**V**	**W**
Coarse, HRA8	Wt%	Bal.	33.87	14.86	3.80	1.84	2.36	0.23	0.30	1.60
Fine, HRA15	Wt%	Bal.	34.24	14.78	3.75	1.84	2.41	0.23	0.30	1.61

5.3.2 Channel Geometry

To evaluate the range of microchannel geometries that could be produced, the LP-DED process was tested on various channel shapes. These included tube-like structures, both round and oval, which are more representative of traditional tube-wall rocket nozzles (Figure 5.2). These types of channels offer an advantage in terms of heat transfer as they help cool the rib or land regions [184]. More traditional square and rectangular channels were also built. Finally, Hybrid D-shaped channels were deposited allowing for increased cooling of the ribs and a smooth coldwall for easier secondary processing or fabrication such as a composite overwrap structural jacket [267]. All channels were built with a targeted 1 mm wall thickness using a single-bead deposition strategy as shown in Figure 5.3. The graphic shows the order of the channels being built. This process starts with the inner wall (1) and outer wall (2) being deposited first (indicated in yellow). This is followed by deposition of the channel ribs in alternating directions as indicated by numbers 3 – 9 (orange and red) in Figure 5.3.

Channels with widths as small as 1.4 mm were successfully demonstrated; however, these narrower channels frequently experienced powder packing, making post-processing difficult. The samples were deposited without openings at the interface with the build plate, preventing free powder flow. Later samples, deposited with a width of 2.54 mm and incorporating powder outlets at the build plate interface, did not encounter issues with packed or trapped powder. This highlights the importance of including openings in the channels to ensure powder flow. Various channel geometries deposited using coarse powder (55–105 µm) are shown in Figure 5.2.

Figure 5.2. Various types of small channels built with LP-DED 45 – 105 µm powder. From top to bottom: Oval, D-shaped, Rectangular, Round (tube-like). Wall thickness is approximately 1 mm.

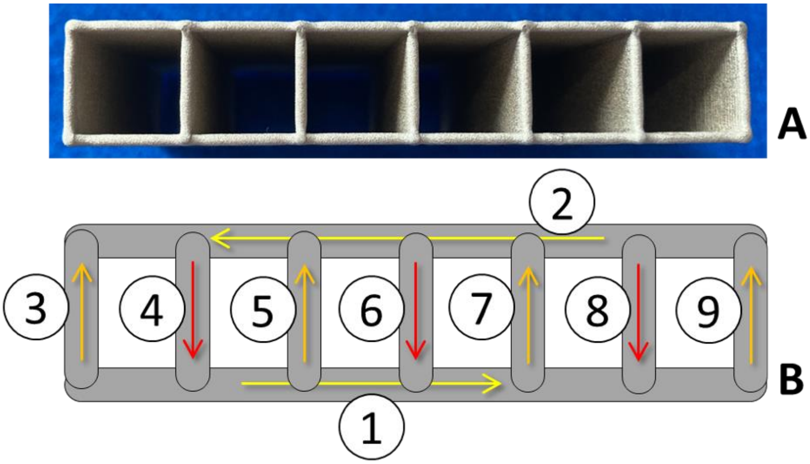

Figure 5.3. Tool path strategy and general order of operations to build single wall microchannels. A) An example of a larger channel (12.7 mm). B) The inner wall and outer walls are first deposited in a layer (yellow) followed by the ribs of the channels as shown in the sequence (orange, red).

The design of heat exchangers made of channels obtained with this technique requires the understanding of various manufacturing characteristics, including the expected flow area and surface texture. Therefore, a study was conducted that focused on square channels of different sizes to determine the repeatability of the process, the differences from the design nominal, and the resulting surface texture. Five sets of square channels were produced with internal widths of 12.7, 10.2, 7.62, 5.08, and

2.54 mm. These samples were all built in the vertical build orientation (representative of the same build approach for a heat exchanger) and included powder outlets at the bottom of the channels as shown in Figure 5.4. Two sets of samples for each channel size were deposited, using coarse powder (45 – 105 µm) and fine powder (10 – 45 µm). The fine powder square channels of different sizes are shown in Figure 5.4 and coarse powder channels using the same toolpaths are shown in Figure 5.5. The samples were all deposited successfully and did not experience any packed or trapped powder. The same machine toolpath was used for each of the coarse and fine powder samples.

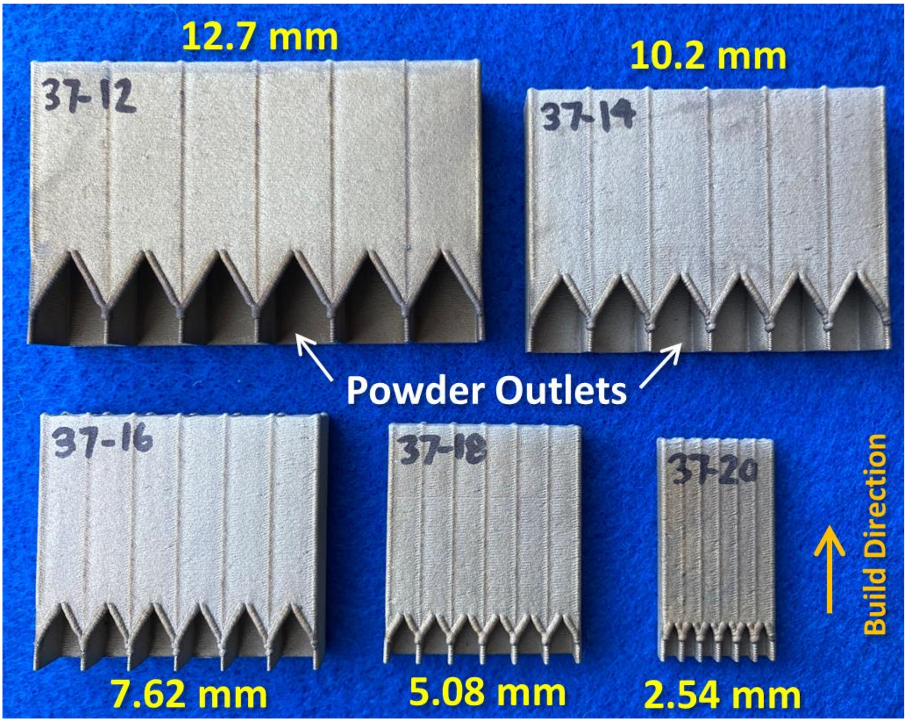

Figure 5.4. Various sized channel samples shown with fine powder and powder exits. Build direction shown with arrow.

5.3.3 Characterization Methods

The channel samples underwent sectioning for SEM, optical microscopy, and surface texture analysis, as illustrated in Figure 5.5. These samples were sectioned perpendicular to the build direction, approximately 6 mm from the top of the build. Subsequently, they were mounted in epoxy and polished according to ASTM E3 using a Presi automatic polisher. The samples were polished using 0.5 µm colloidal silica and optical images were acquired using a Keyence VHX digital microscope. The images were analyzed using ImageJ to determine the area and perimeter of each channel [268]. Additionally, extra samples were sectioned from the channels and cut along the axis parallel to the build direction for SEM using a Hitachi S3000H and surface texture imaging.

Surface texture measurements were obtained using a non-contact Keyence VR-5200 pattern light projection profilometer, equipped with three telecentric lenses offering 80x magnification capability and a 20% overlap. Areal surface measurements were obtained along with directional legacy measurements. All areal surface measurements were reported in accordance with ISO 25178-2:2021 standards. In the case of areal surface measurements, the primary texture profile was unfiltered and denoted as "primary," utilizing form correction only. Measurements were taken both on the external surface and internally within the channels. All characterization techniques are identical to those described in Chapter 3, 4, and 6.

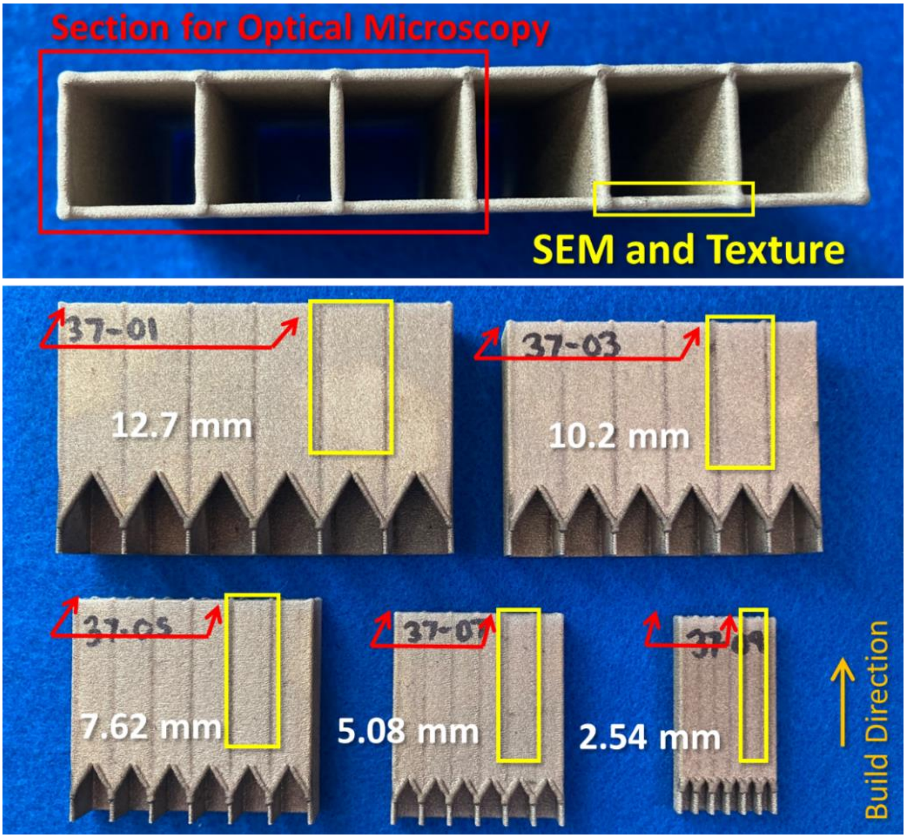

Figure 5.5. Sectioning plan for microchannel samples (coarse powder samples shown).

5.4 MICROCHANNEL CROSS-SECTIONAL AREA AND PERIMETER

In this study, the cross-sectional area and comparisons between channels of the same size, derived from the same set of samples, were analyzed and demonstrated to be highly reproducible (Figure 5.6). For each sample size (12.7, 10.16, 7.62, 5.08, 2.54 mm), three microchannels were measured. The results indicate an approximately 1% difference between channels of the same size. The only outlier in this data is the 2.54 mm fine powder channel, exhibiting a 2.7% difference between channels. Some of this error can be attributed to a single (end) channel with additional stock added to the outer radius, as later shown in Figure 5.11. While variations from the designed nominal to as-built channels are noticeable, the reproducibility data underscores that, with established parameters and feedstock, consistent microchannels can be reliably produced.

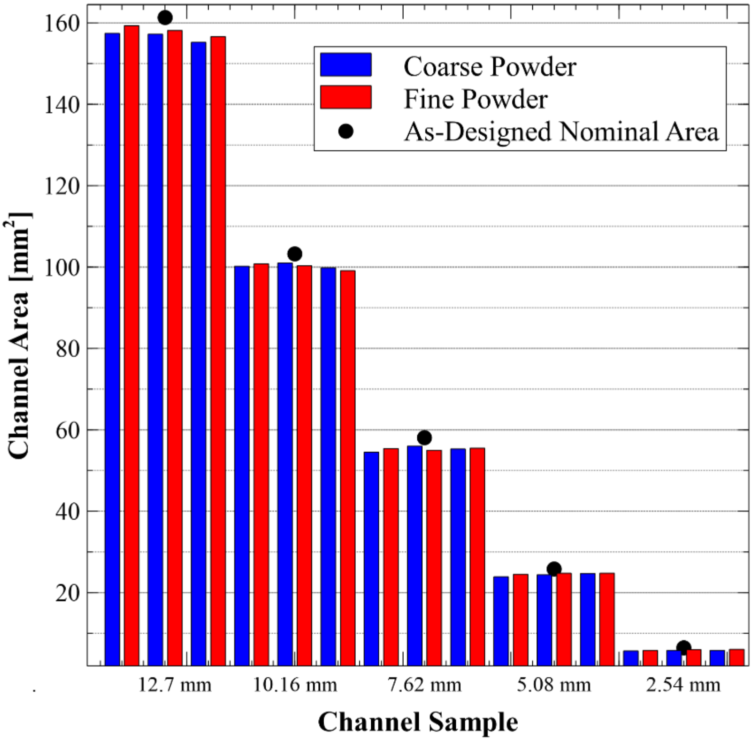

Figure 5.6. Reproducibility results of channel cross-sectional area for each of the channel samples.

The difference of the measured area from the as-designed area is plotted in Figure 5.7, which also shows the effect of manufacturing with a coarse and fine powder PSD. It can be observed that the measured area is always smaller than the specified area and that the deviation generally increases as the channel size decreases. However, as further explained, this reduction in area appears larger with the smaller channels but is exacerbated due to the relative area of the surface texture in comparison to the overall channel area. One cause of the resulting smaller dimensions of the channels is the slight shrinkage occurring during the deposition process as the samples cool. However, the main cause is the adhered powder and melt pool undulations on the surface.

The channels fabricated with fine powder consistently show a larger area (less difference from designed area) compared to identical channel samples fabricated with coarse powder. However, there appears to be more variation in the fine powder samples as the trends is not consistent with decreasing channel size. The samples produced with fine powder demonstrated more variation in texture and waviness when produced with varying parameters in section 3.4.3. This may be attributing to some of the differences observed in the 5.08 mm sample, but the exact reason is not known.

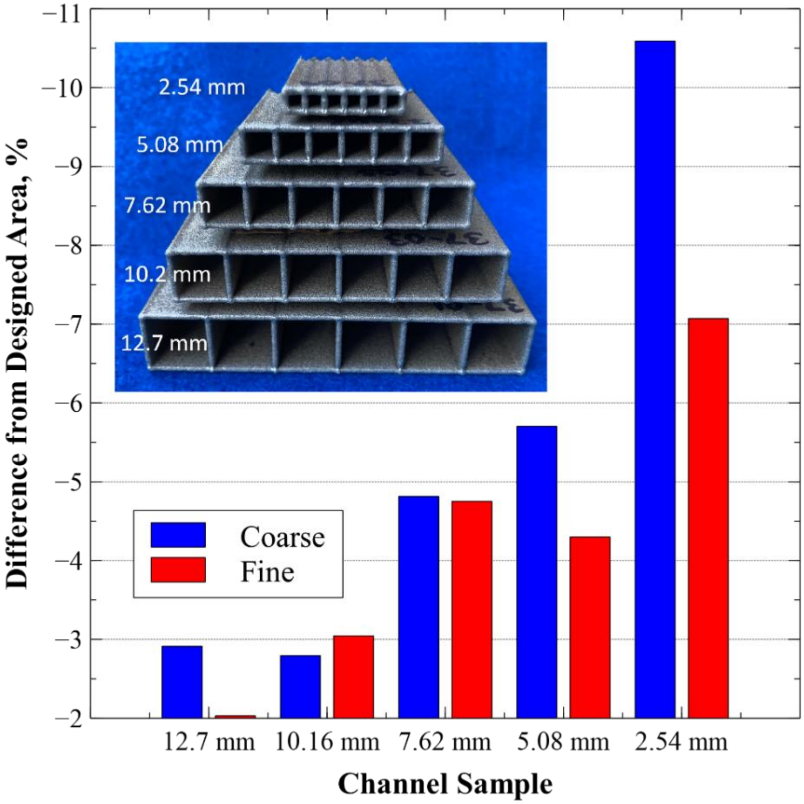

Figure 5.7. Difference of cross-sectional area (compared to as-designed area) for each channel sample.

The observed variation in the cross-sectional area of the LP-DED channels, attributed to powder adherence, melt pool undulations, and process shrinkage, affects the ability to design precisely to a nominal area. The experimental data suggests that an adjusted cross-section can be approximated by using 96% of the designed area to account for these effects. This adjustment, which includes the 4% additional material from these factors, is illustrated in Figure 5.8A for channels of varying widths. Figure 5.8B shows the absolute error for the adjusted areas, combined with data from the square microchannel samples in Chapters 6 and 7. A smaller cross-sectional area is observed with decreasing channel width, as surface texture contributes a larger percentage of the overall area, consistent with the trend shown in Figure 5.7. The absolute error across all channel samples is less than 5%.

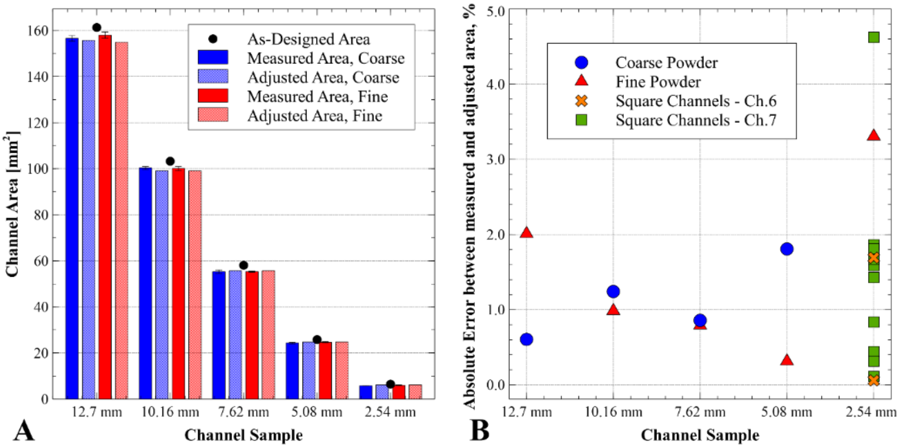

Figure 5.8. Adjusted cross-sectional channel areas. A) Measured and adjusted areas for coarse and fine powder samples along with as-designed nominal area, b) Absolute error from adjustments including data from microchannel samples in Chapters 6 and 7.

The perimeter of each channel was measured on each sample and is depicted in Figure 5.9. The as-designed channel perimeter assumes a flat surface, but the perimeter of the as-built channels is up to 32% higher, which includes data from the channels characterized in Chapters 6 and 7. This increased perimeter is consistently attributed to the adhered powder and melt pool undulations causing the resulting texture. The perimeter from each channel fabricated with fine powder exhibits less error compared to the identical channels built with coarse powder. However, the perimeter is still higher by more than 16% for each channel size. While the fine powder channels consistently have a lower perimeter, the reduction is limited to 3% for the smaller channels (5.08 and 2.54 mm).

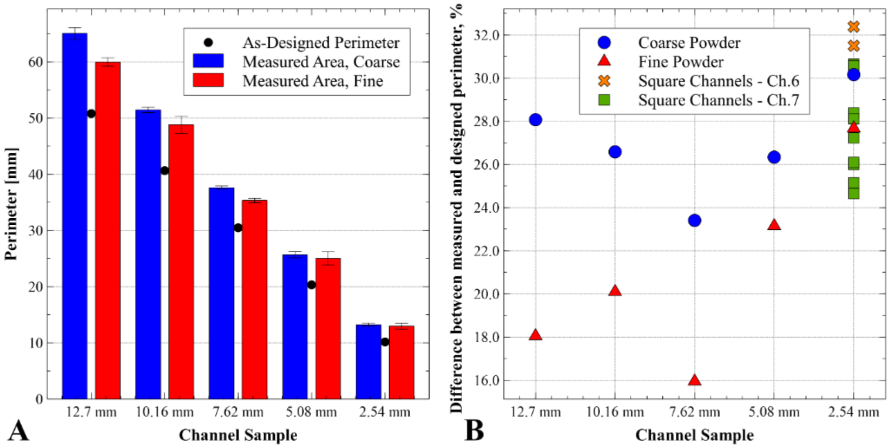

Figure 5.9. A) Measured perimeter for coarse and fine powder samples compared to the as-designed perimeter B) Differences between measured and designed perimeters along with microchannel samples in Chapter 6 and 7.

5.5 SURFACE TEXTURE

Due to the importance of surface texture from the component and system perspective, the surface texture of channels is critical for heat exchanger design. The study in Chapter 3 evaluated the surface texture of the LP-DED process using 1 mm thin-wall NASA HR-1 alloy oval racetracks while varying the build parameters [251]. Using fine powder reduced the roughness by 23% compared to coarse powder. There was also a discernible difference in surface texture between the inner surface (trapping additional powder) and the outer (external) surface. This distinction was due to the enclosed volume trapping excess powder that recirculated into the melt pool as it solidified. It's important to note that while the samples in Chapters 4 and 5 were thin-walled, the spacing between walls was about 25 mm, where heat exchanger designs with microchannels would be less than 10 mm.

The primary average areal surface texture, Sa, was measured for each sample on both the inner (internal) and outer (external) surfaces. Sa was chosen to provide a general comparison of these samples, as it is a commonly used parameter for characterizing roughness in AM components due to the complexity of the surface [227]. The Sa data is plotted for the coarse (45 – 105 µm) and fine (15 – 45 µm) powders in Figure 5.10. The samples built with coarse powder consistently exhibit a higher Sa compared to the fine powder samples for each channel size. This increased texture is consistent with the data sets in Chapters 3 and 4, but to a higher degree (45% compared to 23%). The surface roughness across the various sizes of channels is roughly constant for the same powder size, except for the 2.54 mm channel. The 2.54 mm coarse powder channel shows an increase with respect to the other channels that averages 17%, while the fine powder 2.54 mm channel increase averages 10%.

The difference between the inner and outer surfaces is minor but shows a slightly higher average texture on the outer surface. For the fine powder, the average difference is about 6% when comparing inner and outer surfaces. This finding is in contrast to what was demonstrated in the oval racetracks shown in Chapter 3 [251]. The channel samples in the current study have an outlet designed at the bottom of each channel (Figure 5.5). This design allows the powder to fully exit and prevents recirculation internally within the channel. The central gas used for inert purge of the deposition and carrier gas for the powder travels through the internal channel at a high velocity, allowing excess powder to flow through the channel instead of stagnating, compared to the samples in Chapter 3 [251]. One observation during the build process with the fine powder was that a portion of it remained suspended in the machine atmosphere. This is likely the finer particle on the lower end of the PSD. This phenomenon may introduce additional particles onto the outer surface, influencing the overall surface roughness.

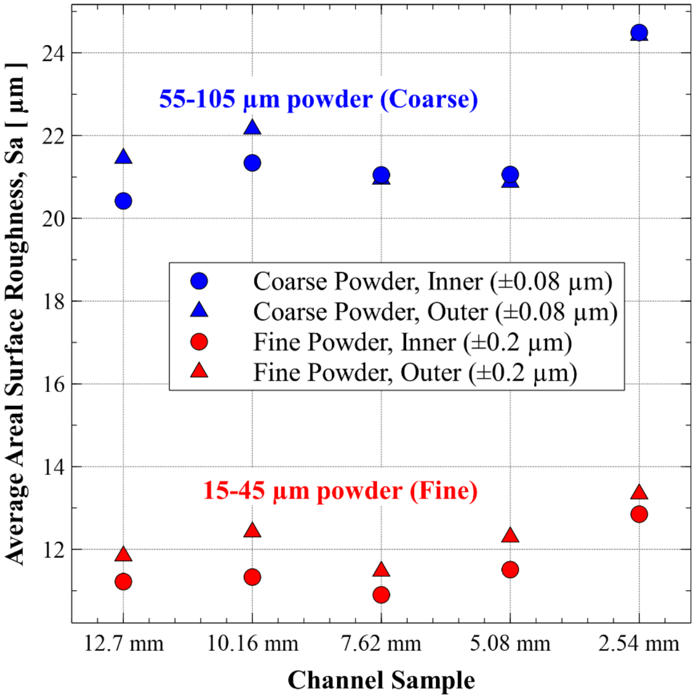

Figure 5.10. Average surface texture (Sa) of various sized channel samples.

The difference in texture is also visually apparent from the cross-sectional micrographs presented in Figure 5.11. The coarse powder samples exhibit visual distinctions, particularly noticeable at lower magnifications for the 5.08- and 2.54-mm samples. The wall thickness is also observable in the cross sections, with slight thinning as the center rib approaches the outer walls. Slightly raised areas on the outer surfaces, where the ribs tie into the inner and outer walls during deposition, are more pronounced on the fine powder samples. The raised region on the 2.54 mm channel using fine powder averages 118 µm, whereas with coarse powder, it averages 35 µm.

This raised region is not a significant concern for heat exchangers, given its parallel orientation to the direction of fluid flow (assuming a vertical build orientation). Additionally, this region may be removed or reduced during post-processing operations.

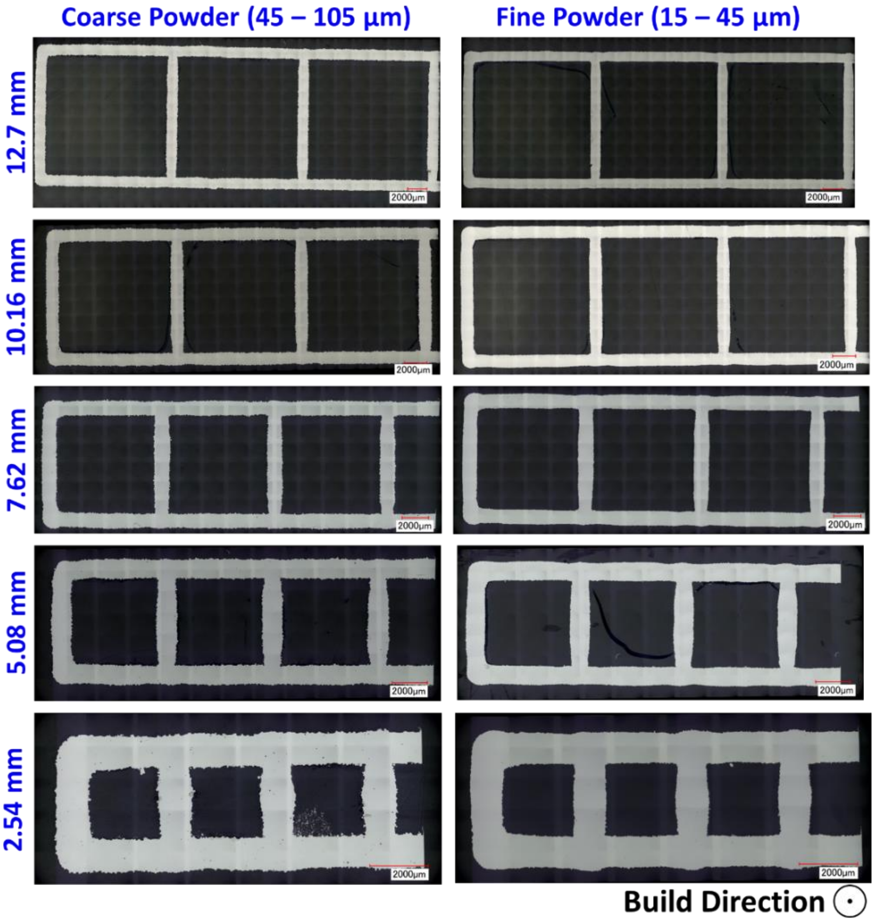

Figure 5.11. Optical micrographs of selected channel samples showing fine and coarse powder for each channel size.

The SEM images are presented in Figure 5.12 for each internal channel sample with coarse and fine powder. Each image is at the same magnification, and the adhered particles per unit area are similar for each-sized sample built with the coarse and fine powder, respectively. The differences in particle sizes are evident between coarse and fine particles. The coarse particles are around the mean distribution of the PSD, approximately 65–75 µm in diameter. Many of the fine particles are biased toward the upper end of the PSD at 30–35 µm in diameter, but several particles sized 10 µm and below are adhered to the channel surfaces. The samples fabricated with fine powder also show some bands of powder, indicating some macro waviness, while the coarse powder exhibits a more randomly distributed pattern.

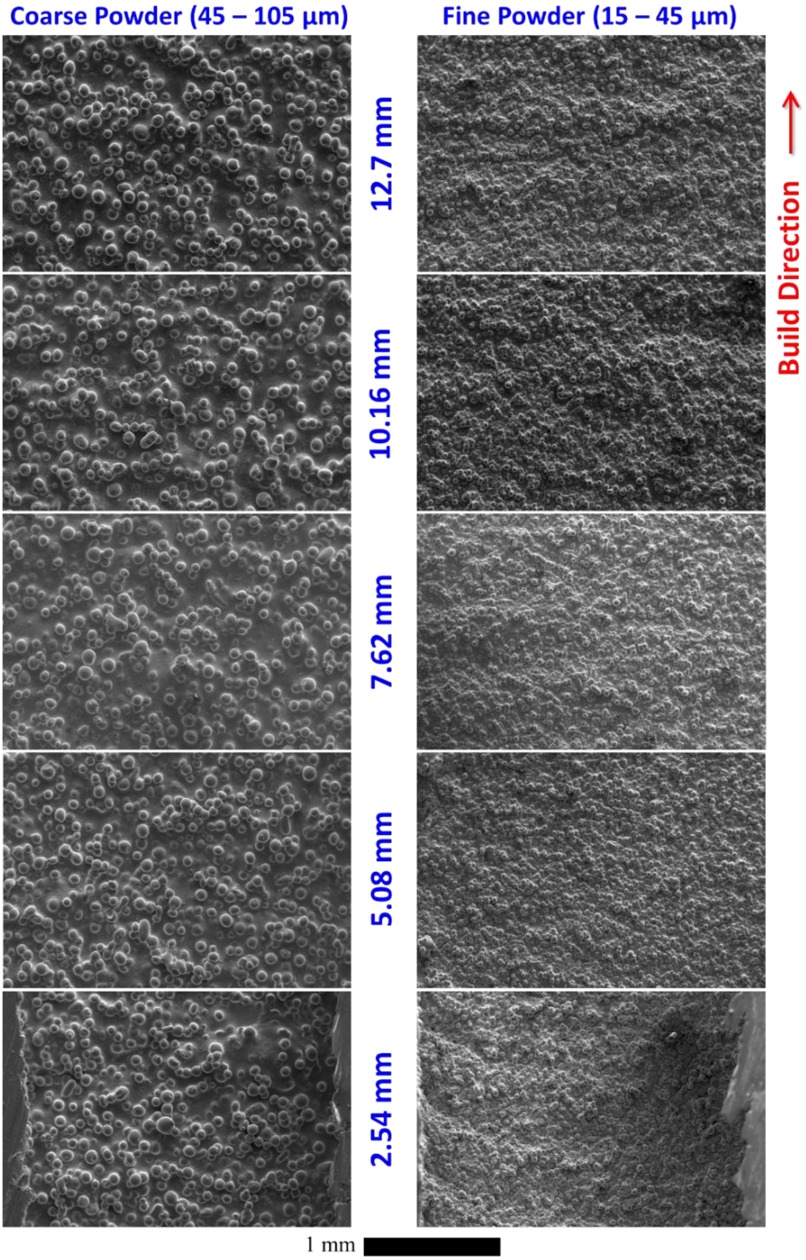

Figure 5.12. SEM Images of Internal Channels at the bottom of the channels.

5.6 WALL THICKNESS

Wall thickness is an important characteristic in heat exchanger design as it impacts heat transfer and the peak temperatures experienced by the walls during operation. The wall thickness must be thin enough for proper cooling but provide adequate thickness to maintain positive structural margins for strength and fatigue life. The rib thickness between the channels is also significant as it influences the cooling of the hotwall (for combustion chambers and nozzles) through conduction. Consistently maintaining a wall thickness of 1.05 to 1.165 mm was achieved for both the fine and coarse powder samples, which aligns with the findings of the prior study in Chapter 3 [251]. Summary data sets that measured both the rib thickness and the outer wall (i.e. simulated hotwall) thickness of the various width channel samples is shown in Figure 5.13. Three measurements were collected from each channel rib and outer wall in the cross-sectioned sample and the data was averaged and standard deviation provided in the graph. The measurements were taken in the areas where the wall is constant without the thinning (as shown in Figure 5.11).

It is observed that the coarse powder samples are slightly thicker by about 2.6%, driven by the larger particle size distribution (PSD) of the powder causing this difference. There is also a difference observed between the outer wall thickness of coarse and fine powder samples, approximately 3.8%. Another observation from this study is the slight difference between the rib wall thickness and outer wall thickness, averaging 2.5% and 3.7% for coarse and fine powder, respectively. This difference in wall thickness is due to slightly different build parameters. The outer wall is deposited at a constant travel speed, while the rib wall is deposited at a varying travel speed to ensure that the intersection with the outer wall is not overbuilt (acceleration and deceleration leading into the intersection). The thickness was expected to be constant between channels since the build parameters do not change based on the channel size. However, the differences in rib and outer wall thickness, as well as differences between coarse and fine powder samples, are not statistically significant based on a t-test comparison.

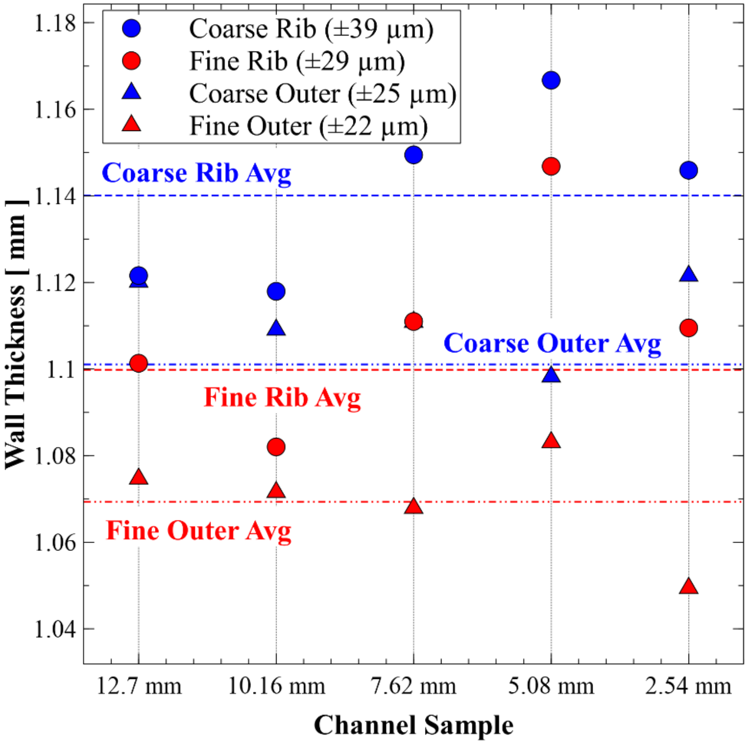

Figure 5.13. Summary of rib and outer wall thickness for channel samples.

5.7 SUMMARY AND CONCLUSIONS

The results presented in this chapter built upon the lessons learned in Chapters 3 and 4 to produce heat exchanger channel geometries. Various types of channel geometries were successfully deposited using the LP-DED process and the NASA HR-1 alloy (Fe-Ni-Cr). These geometries included round, oval, square and D-shaped. These channels provide new design opportunities for designers compared to round tubes or square channels for traditionally manufactured tube-wall or channel wall nozzles. Several square channel sizes were successfully deposited with highly reproducible width down to 2.54 mm. Smaller width channels were also fabricated successfully, but could result in higher risk for excess powder being trapped within. The following conclusions can be drawn based on detailed characterization of various square channels.

- Repeatable fabrication of microchannels is achievable using established parameters and feedstock. Results indicate a 1% average difference between channels of identical sizes, with a portion of this variation attributed to a singular end channel where additional stock was introduced to the outer radius.

- Cross-sectional channel areas, when measured, consistently deviate from the designed areas, with greater disparities observed as channel size decreases. The variation primarily arises from excess powder adhering to the internal surface, contributing to surface texture, along with shrinkage from deposition. An adjusted area, accounting for the build process's shrinkage, additional texture from powder adherence and melt pool undulations, and heat treatment-induced shrinkage, can be determined by taking 96% of the as-designed area.
- The as-built perimeter of channels exhibits up to a 32% increase for coarse powder and as low as 16% for fine powder, attributed to the partial melting and adherence of powder particles.
- Coarse powder samples consistently have a higher measured average surface texture (Sa) than fine powder samples across all channel sizes, exhibiting a more pronounced increase compared to the study in Chapter 3 (45% vs. 23%). Specifically, the 2.54 mm coarse powder microchannel shows an average increase of 17%, surpassing the fine powder channel's average of 10%.
- The difference in surface texture between inner and outer surfaces is minor, with the outer surface exhibiting a slightly higher average texture. Specifically, for fine powder, the average difference is approximately 6% when comparing inner and outer surfaces. This finding contrasts with the observations in oval racetracks presented in Chapter 3. Notably, the channel samples in the current study feature an outlet designed at the bottom of each channel, facilitating the complete exit of powder and preventing internal recirculation.
- Wall thickness, ranging from 1.05 to 1.165 mm, remains highly reproducible with minimal variations observed between powder sizes, internal channel rib, and outer wall. Although these differences are not statistically significant, the data aligns with findings in Chapters 3 and 4, demonstrating consistency in wall thickness even with the fabrication of these small microchannels.

While this study focused exclusively on square channels, it highlights crucial aspects in the development of novel processes for constructing heat exchangers. Future research opportunities lie in conducting additional studies to characterize various channel geometries, including round, oval, and D-shape configurations. Additional materials could also be evaluated to provide more design solutions for various heat exchanger applications.

Chapter 6

Post-process Surface Enhancement and Characterization

Major portions of this chapter were published in:

Gradl, P., Cervone, A., Colonna, P., 2024. Development and experimental evaluation of surface enhancement methods for laser powder directed energy deposition microchannels for laser powder directed energy deposition microchannels, Virtual Phys. Prototyp. 19:1. e2345389. https://doi.org/10.1080/17452759.2024.2345389.

6.1 ABSTRACT

This chapter focuses on the development and characterization of surface enhancement methods for microchannels created via the LP-DED process. Various surface finishing techniques, such as abrasive flow machining, chemical milling, chemical-mechanical polishing, electrochemical machining, and thermal energy method were applied to modify the internal surfaces of microchannels made of NASA HR-1 Fe-Ni-Cr alloy. Flow testing to measure the discharge coefficient was performed on microchannel samples whose internal surfaces were processed using the mentioned techniques. After the testing, each sample was characterized using optical microscopy, Scanning Electron Microscopy (SEM), and Computed Tomography. Variations in the surfaces resulted from the powder adherence, melt pool undulations, and polishing mechanisms. The results indicated that removing an average of 70 µm of material, equivalent to the mean powder diameter, is essential to reduce surface roughness and impact the discharge coefficient. Reduction of flow resistance can be accomplished by planarizing both the roughness and waviness peak height and density and a ratio is proposed. This research resulted in thorough surface characterization in relation to hydraulic flow which enables tailored surface adjustments for specific end-use applications.

6.2 INTRODUCTION

This chapter is focused on the experimental characterization and test results of surface enhancement methods applied to microchannels produced using the LP-DED process. These enhancements included abrasive flow machining, chemical milling, chemical mechanical polishing, pulsed electrochemical machining, and the thermal energy method. These processes were applied to modify the internal surfaces of LP-DED microchannels built using a hydrogen-resistant NASA HR-1 alloy. This research addresses a notable knowledge gap, as microchannels created using LP-DED have limited data available [5], and research on the improvement of finishing of their internal surfaces is limited. This work involved a comprehensive characterization of the surface texture, using scanning electron microscopy (SEM), optical microscopy, and computed tomography (CT). Hydraulic flow testing was conducted to assess discharge coefficients and provide comparisons between each of the surface enhancement processes. The discharge coefficient was used as a quantitative measure to determine flow resistance in microchannels, considering variations in surface texture. The research objective was to characterize the various surface enhancement methods and their impact on flow resistance, focusing on evaluation rather than optimization for a "smooth" surface. These various surface conditions may, in turn, allow designers to fine-tune these surfaces to meet specific requirements of end-use applications. This potential extends to leveraging additive manufacturing to balance factors including heat transfer, fluid flow friction, corrosion, mechanical fatigue life, and aesthetics.

6.3 METHODOLOGY

Several channel samples were built using the LP-DED process. Surface enhancements were used to modify the internal perimeter of the channels. These channels samples were flow tested to determine the discharge coefficients of each channel. Following testing the channel samples were sectioned to characterize the internal surface and flow area to anchor the test data.

6.3.1 Fabrication of DED Samples and Processing

The channels were designed with a nominal width and height of 2.54 x 2.54 mm square and built using LP-DED. Figure 1 illustrates the LP-DED build and subsequent processing of the channel samples. The length of the square microchannel section was approximately 150 mm. A 25 mm blended transition from the square channel to a round extrusion was designed to allow welding of a universal AN-type fitting as shown in Figure 1D. The channels were built as part of larger sample boxes (Figure 1B) using the NASA HR-1 alloy and then individually sectioned (Figure 1C and 1D). This Fe-Ni-Cr superalloy is resistant to hydrogen environment embrittlement (HEE) in high pressure components [77]. It was developed for high strength and high ductility in harsh hydrogen environments, like those occurring in liquid rocket engine nozzles and heat exchangers. It is derived from the A-286 and JBK-75 alloys [253,254]. The boxes were built with an RPM Innovations (RPMI) 557 LP-DED machine equipped with an argon-inert build chamber (Figure 6.1A). The 557 system incorporated an infrared (IR) continuous-wave gaussian profile 3 kW IPG laser, three coaxial nozzles within the deposition head, 5-axis motion control, and disc powder feeder with agitation capabilities. The samples were built on top of an A36 mild steel 12 mm thick base plate. The laser power was 350 W, with powder feed rate of 23 grams/min, a travel speed of 763 mm/min and a layer height of 0.254 mm. Based on previous development work, this set of parameters was optimized to produce crack-free material, resulting in very low porosity [251,269].

The powder was rotary atomized by Homogenized Metals Inc. (HMI), with a particle size distribution (PSD) of 55-105 µm meeting +140 mesh at 0% and -325 mesh at 3.8% per ASTM B214 using a Microtrac (Ver 11.1.0.6). The chemical composition is listed in Table 2 (HMI powder lot HRA4). The Oxygen content was 61 ppm and the Nitrogen content was 7 ppm. The chemical composition was measured using Inductively Coupled Plasma (ICP). The peak powder size was 70 µm and a Vega3 Tescan Scanning Electron Microscope (SEM) using Backscatter Electron (BSE) showed mostly spherical particles with a few satellites and random distribution of occasional oblong particles. Virgin powder was used for all builds.

The sample channel boxes were stress-relieved at 1066°C for 90 minutes with a slow furnace cooling, prior to removal from the build plate with a bandsaw (Figure 6.1B). The boxes were then homogenized at 1163°C for 6 hours in vacuum and Argon-quenched. A solution anneal was performed at 1066°C for 60 minutes, with an Argon-quench followed by age-hardening at 690°C for 16 hours. The boxes were then furnace cooled to 621°C and held for 16 hours (total aging time of 32 hours) [252,270]. Individual channel samples were then sectioned from the boxes using a water jet (Figure 6.1C). The samples were cleaned and an AS5174-04 stainless steel fitting was laser welded to the inlet end of the samples (Figure 6.1D). The channels were tagged according to the surface enhancement processes. Several samples were used for process development and not tested. The internal surfaces of the channels were processed according to surface enhancements described in section 2.2 Following the polishing of the internal perimeter, a 0.75 mm diameter hole was drilled at two locations and a 3.175 mm diameter tube was welded as shown in Figure 6.1E.

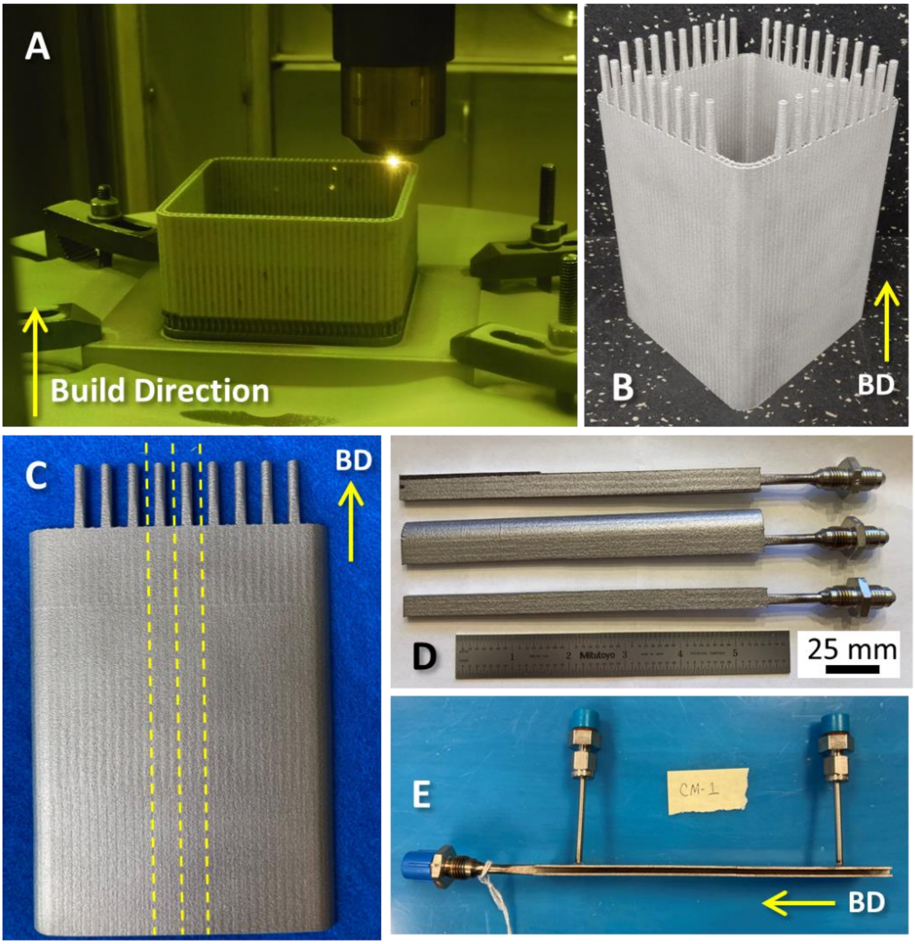

Figure 6.1. Channel specimen fabrication: A) LP-DED of channel sample boxes, B) complete NASA HR-1 box after stress relief and sectioning from the build plate, C) Panels excised from boxes, D) Individual channel samples with welded inlet port, and E) drilled and welded instrumentation ports. Build Direction (BD) shown with arrow.

Table 6.1. Chemical composition of NASA HR-1 alloy powder (HMI Lot HRA4).

	Fe	Ni	Cr	Co	Mo	Ti	Al	V	W
Wt.%	Bal.	33.71	14.49	3.75	1.82	2.31	0.24	0.3	1.59

6.3.2 Surface Enhancement Processes

Several internal surface enhancement processes were selected with the ultimate goal of testing the possibilities of improving the flow friction characteristics of heat exchangers channels. These included abrasive flow machining (AFM), chemical mechanical polishing (CMP), chemical milling (CM), pulsed electrochemical machining (PECM), and thermal energy method (TEM) or thermal deburring. These enhancement processes were selected among the many available [126,133,142,149,271], based on the ability to modify internal microchannels with a cross section of less than 2.54 x 2.54 mm [51,131,146,272]. The primary goal of this research was not to minimize surface roughness or to allow for the best possible surface polishing of the channels, but to analyze the varying levels of surface polishing that can be obtained to gain a better understanding of how the polishing can be tuned to the requirements in terms of flow resistance.

AFM uses a viscous fluid polymer that contains suspended abrasive particles. The slurry is pressurized and pumped through the channels using a single or bi-directional flow [273,274], thus providing abrasion, and the removed particulate is carried away with the media. This process is also referred to as *extrude-honing* or *slurry-honing*. The slurry type, volume, time, and number of cycles were adjusted to modify the channel surfaces. The pressure was 68.9 bar and the flow was unidirectional and the flow rate ranged from 0.56 L/min to 4.47 L/min. Following the AFM process, the slurry was removed with compressed air and rinsed with a cleaning solution. The channels were then dried with compressed air, ultrasonically cleaned, rinsed with water, and again dried.

CM, or chemical polishing, consists of flowing a chemical solution through the channels that attacks the grain structure and dissolves the metal at the surface [127,135]. The dissolved material is flushed out with the hydrofluoric solution. Longer exposure times yield more material removal. The temperature of the solution pumped through the channels varied from 52 to 60°C and the surfaces were exposed to the solution for a period that ranges from 4 to 19 mins. The parts were rinsed following the chemical milling.

CMP is a process in which chemical and mechanical forces are applied to remove surface material along preferential directions thus reducing the peaks height [275]. The chemical solution removes most of the material, while abrasive media planarizes the surface. The chemical solution and micro-abrasives were flowed through the channels and any removed particles flushed with the solution. The flow rate of the chemical solution, temperature, time of flow, and weight of the microabrasives was varied for each channel. The flow rate was varied from 0.4 to 2 L/min at temperatures of 50 to 60°C and runs with and without microabrasives (up to 10%). The exposure time was also varied between 10 to 20 mins.

PECM obtains the surface improvement by applying a local direct current (DC) pulse using an electrode to dissolve metal [276]. The electrode was inserted inside of the channel and dragged through, thus providing the proper offset gap. A limited portion of the electrode was exposed. The channel was actively flushed with an electrolytic sodium chloride solution.

TEM is a process where parts are placed in a sealed chamber, which is pressurized with a mixture of gaseous fuel and oxygen, and ignited [277,278]. The high temperature of the combustion process vaporizes (thin) areas with low thermal mass. The part was fixtured to prevent damage in the 25 cm diameter chamber operating at a combustion pressure of 6 bar with a total processing time of 30 seconds.

The surface enhancement processes were outsourced to commercial vendors actively working production. Prior to conducting the flow testing and characterization, each vendor received development samples for trials. This step was necessary because both material composition and geometry can influence the parameters used. Although general parameters were outlined above in Section 2.2, detailed parameters and specific setups for each of the channel samples were deemed proprietary to the vendors. The objective of this research was to introduce variations in the surfaces of the channels rather than achieving an ideally "smooth" surface. To meet this objective, vendors employed distinct parameter sets for each channel to generate the data for this study. The general setup of the surface enhancement processes is illustrated in Figure 6.2.

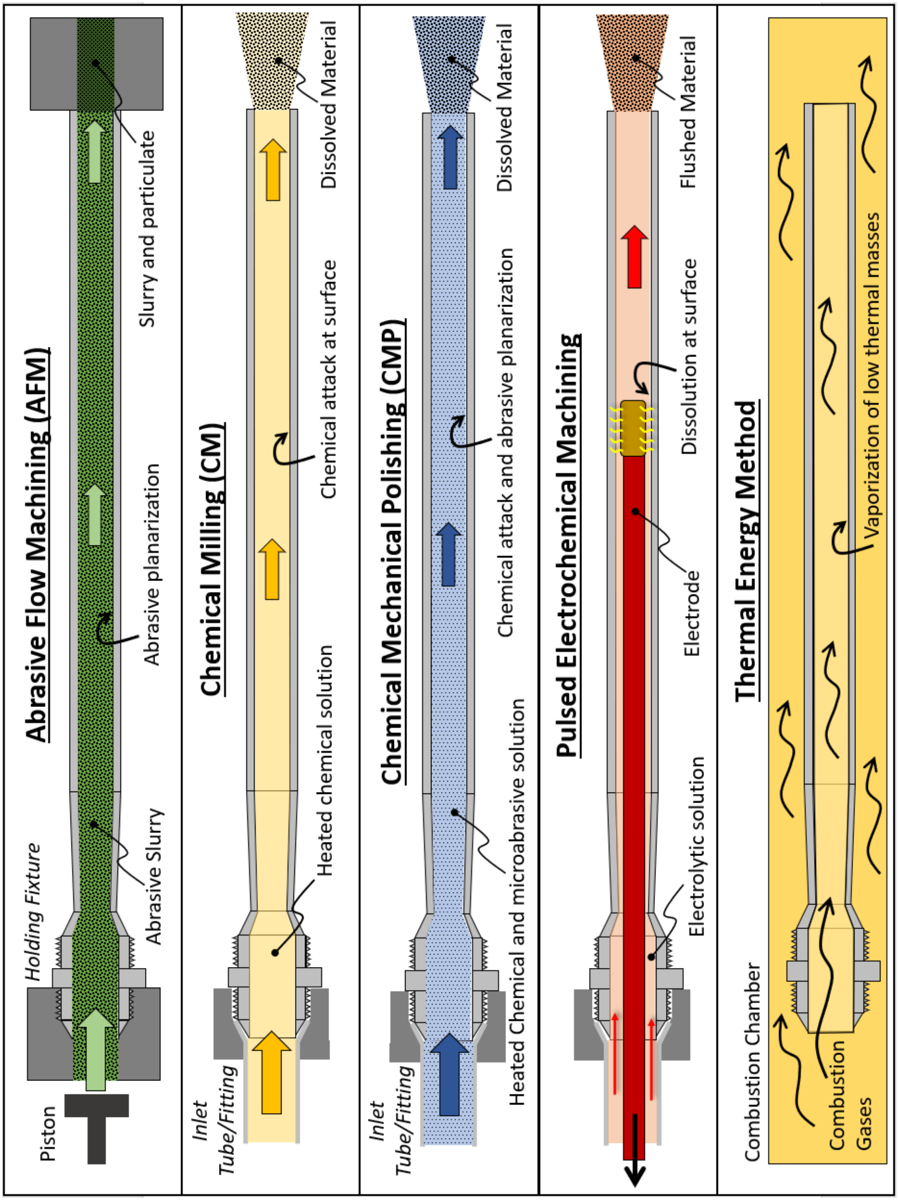

Figure 6.2. Overview of surface enhancement processes used for internal LP-DED microchannel samples.

6.3.3 Test Configuration and Procedures

Testing was conducted at the NASA Marshall Space Flight Center component development facility. A 379-liter GN_2 pressurized tank provided deionized (DI) water to the system depicted in Figure 6.3. A 10 µm filter was placed immediately downstream of the tank after the main valve. A Potter Aero RAA-1/2-301-1/2-5440A flowmeter (3.4 to 36 l/min) was installed in a bypass leg of the system in addition to a 1.143 mm diameter cavitating venturi (Cd = 0.980) to control the mass flow through the channel test articles. The venturi cross-sectional area was sized to be smaller than the smallest cross-section area of the test article. Pressure and temperature measurements were installed at locations indicated on the diagram of Figure 6.3 and on the channel test article. The test article was installed in a blast containment due to the operating pressures. The Sensotech A-105 pressure transducers (0 to 40 bar, ±0.1% full scale), Omega E type thermocouples (-200 to 900°C ±1.7°C), flowmeter, and cavitating venturi were all calibrated prior to testing. Instrumentation checks were completed every day of testing.

Each channel test article was flushed with DI water at 7 bar for a minimum of 10 seconds prior to data collection. The tank was then pressurized at increments of 34, 69, 138 Bar and held for 10 seconds at each pressure. The selected pressures were based on the maximum allowable tank pressure, whose value is of the same order of magnitude of the pressure at which high-pressure heat exchangers are operated (*e.g.*, rocket nozzles, components of power and propulsion systems). A Dewetron data acquisition system was used in conjunction with the LabVIEW software for system control. Following pressurization of the test articles at the three set points, all pressure in the system was vented and a new test article installed. A total of 20 channel samples were tested. Each sample was uniquely numbered based on the processing (AB = As-built; AFM = abrasive flow machining; CM = chemical milling; CMP = chemical mechanical polishing; PECM = pulsed electrochemical machining; TEM = thermal energy method).

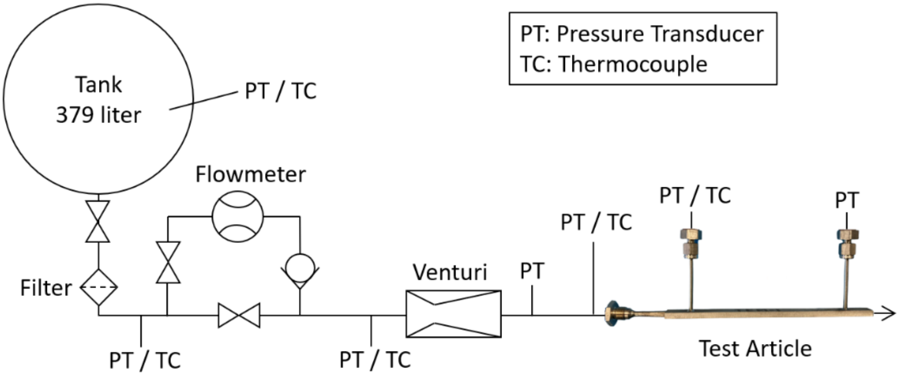

Figure 6.3. Flow test configuration.

6.3.4 Sectioning and Imaging

Following flow testing, the channel samples were sectioned to characterize the channel geometry and surfaces using optical microscopy, optical imaging surface texture, SEM imaging, and computed tomography.

6.3.4.1 Optical Images

Each channel sample was cross sectioned at three axial locations perpendicular to the flow (Figure 6.4). The samples were mounted and polished according to the ASTM E3 standard using a Presi automatic polisher. The samples were polished using 0.5 µm colloidal silica and optical images obtained. Samples were then etched using etchant #13 (10% Oxalic Acid, Electrolytic) and optical imaging completed again. All optical images were obtained using a Keyence VHX digital microscope. The *Image J* image processing software [268] was used for analysis to obtain the cross sectional area and the wetting perimeter. The porosity of each sample was also measured, and the results are provided in the supplementary materials. The results were averaged, and standard deviation reported from the three cross-sections. Each image was also overlayed to compare the processed sample to an as-built sample (identified as AB-2). These overlay images were used to measure the approximate amount of material removed per side, according to the hypothesis that the removal was uniform on all sides. The material removal was measured normal to the wall at 20 locations and data averaged. From the images, this hypothesis is only partially verified, since some surface enhancement processes removed more material in the center of the channel wall as opposed to the corners. The perimeter of each channel was measured at the three axial locations and the average is reported.

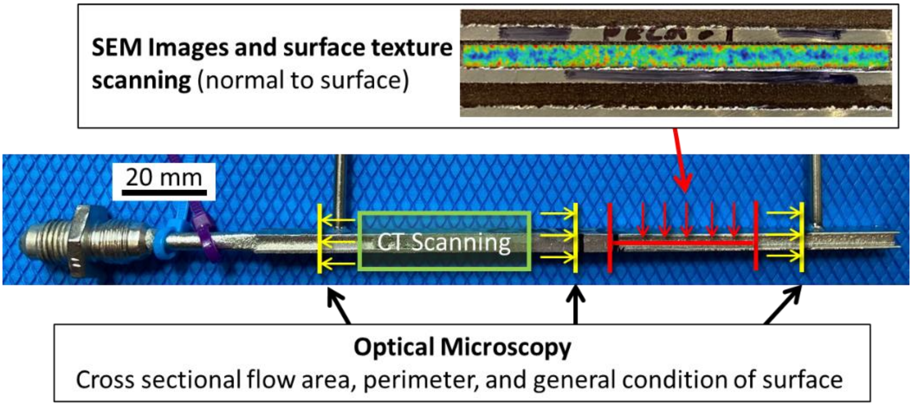

Figure 6.4. Sectioning of channels post-flow testing. An example scan of the areal surface texture is provided along the length of the channel.

6.3.4.2 SEM Imaging

The surface perpendicular to the flow was imaged using a Hitachi S3000H Scanning Electron Microscope (SEM) (Figure 6.4). The particle count was determined by examining the number of particles in two 1 mm^2 areas and averaging. This was obtained from the SEM image at 50x.

6.3.4.3 Surface Texture Measurements

Surface texture measurements were obtained using a non-contact Keyence VR-5200 pattern light projection profilometer. The setup included three telecentric lenses with 80x magnification capability and an overlap of 20%. An area approximately 38 mm long and 1.6 mm wide was measured for each sample. All areal surface measurements are reported according to ISO 25178-2:2021 [255,257]. The surface data intersecting the corners of the channels were eliminated using an end-effect correction. A surface form correction was applied to remove any tilt and curvature, addressing any residual stress distortion of the samples, and establishing a reference plane. For the areal surface measurements, the primary texture profile was left unfiltered (denoted as primary) using only the form correction. To extract roughness and waviness from the areal surface, a λc spatial frequency cut-off filter of 0.8 mm (*i.e.*, a roughness filter) was applied following the ISO 21920-3 guidelines. To obtain directional roughness and waviness (*i.e.*, Ra and Wa, respectively), a virtual line was created along the center of the channel, and data were extracted to report the results. Various areal data sets such as average texture (Sa), maximum surface height (Sz), core texture depth (Sk), reduced peak height (Spk), and roughness peak density (Spd) were obtained for evaluation based on prior literature [269]. Directional data sets for average roughness (Ra), average waviness (Wa), waviness peak height (Wp), and waviness peak density (WPc) were also evaluated along the direction of flow.

6.3.4.4 Computed Tomography Scanning

Micro-computed tomography (µCT) scanning was completed on seven samples including AB-2, AFM-2, AFM-15, CM3-, CM-20, PECM-1, and CM-20. These samples were selected to evaluate each of the surface enhancement processes and the range of the calculated discharge coefficient. A fully intact 17 mm length portion of the channel samples were CT-scanned as shown in Figure 6.4. The specimens were scanned on a Zeiss Xradia Versa 620 using 159kV and 23W and exposure of 8.7 seconds. A variable exposure scan technique was employed to help reduce noise while simultaneously reducing the overall scan duration. The imaging covered an area of 19 mm^2 per scan and the estimated pixel size is 10.03 µm. This resulted in a feature resolution of ~30 µm, which is typically 3-5 times the pixel size [279].

6.4 RESULTS AND DISCUSSION

6.4.1 Image Analysis

6.4.1.1 Optical Images

The cross sections of each channel are documented in Figure 6.5. The channel cross section is overlayed with the AB-2 channel colored in gray, while the removed material is depicted in orange. The AB-2 channel sample was used as the baseline since this is unprocessed. These micrographs were obtained at the first pressure port on the test article. The images were used to determine the area, perimeter, and approximate thickness of the removed material, per side. The as-built sample displays pronounced texturing due to excessive powder adherence and disturbances of the melt pool [269]. This texturing increases the wetting perimeter by 32% compared to the as-designed (nominal) channel. Corners are created at the intersection of the melt pool solidification with the upper and lower walls extending to the intersecting ribs (depicted vertically in Figure 6.5). A minor thickness increase is noticeable at the mid-span center of the ribs, accompanied by a gradual thinning of the ribs as they approach the upper and lower walls. This is the region where the laser is triggered off to prevent excessive material deposition at the wall intersections.

All samples were crack free and the microstructure of the samples was identical to 1 mm thick walls evaluated in prior studies [251,269]. The grain structure is shown to be fully homogenized. The average porosity across all samples was 0.042% with a maximum porosity of 0.108% on sample CMP-1 due to a single pore in the bulk of the material. The polished and etched sample images are shown in supplemental and a table with the measured porosity for each sample.

Varying degrees of material removal were present on all samples, as expected since this was one of the objectives of the experiment. The cross-section micrographs reveal that the walls of the AFM samples exhibit a visually smooth surface. The internal surface increased in comparison to the as-built channel by as much as 2% to 12% across the different AFM samples, and the perimeter increased up to 15%. The corners indicate sharp stress risers, revealing that abrasive machining was less effective in the corners. The AFM process selectively removed material from the mid-span thickness of the ribs. This resulted in nearly flat ribs with some AFM walls showing concavity. The AFM overlay with the as-built sample confirms the selective material removal in the rib mid-span and no removal in the corners.

The internal surfaces of chemically milled samples are larger compared to that of the other samples and the corners are fully rounded. The walls appear jagged at high magnification and much smoother as more material is removed. This is due to the milling solution following the as-built profile of the surface. The area increased by 16% to 36% if compared to the as-built state depending on the CM sample, and the perimeter increased by 12 to 20%. The overlay images show that around the edges and corners the milling is uniform. The processing time for CM is the shortest and the surface changes are directly related to the increase of milling time and flow rate.

CMP allows for the removal of the widest range of material and therefore a wider control over the determination of the inner surface, as it allowed to obtain an area change spanning from 8 to 27%. At high magnification, the CMP samples revealed jagged features on the walls which gradually smoothed out as more material was removed. The perimeters were 11 to 19% larger compared to the nominal perimeter of the channel. There were some remnants of residual powder with material removal uniform on the walls and corners. Visually, there appears to be a smooth wall profile indicating reduced texture. PECM cross sections indicate some removal of material from the walls, but the surfaces still show significant texture. There is no change to the corner geometry and perimeters increased (18 to 24%), indicating some reduction in material. The TEM sample does not exhibit any visual change compared to the as-built. The overlay with the as-built sample looks nearly identical and this observation is confirmed by perimeter and area measurements.

For all the surface enhancement processes, the increase in measured area is related to the amount of material removed per side. The perimeter length exceeds the design value and is notably influenced by the extent of powder adherence, as demonstrated by both the as-built and the TEM samples. Most processes eliminated the partially adhered powder particles except for TEM. Although a small number of residual particles persisted on the samples, a minimum material removal of 45 µm on each side is required to eliminate over 90% of the particles.

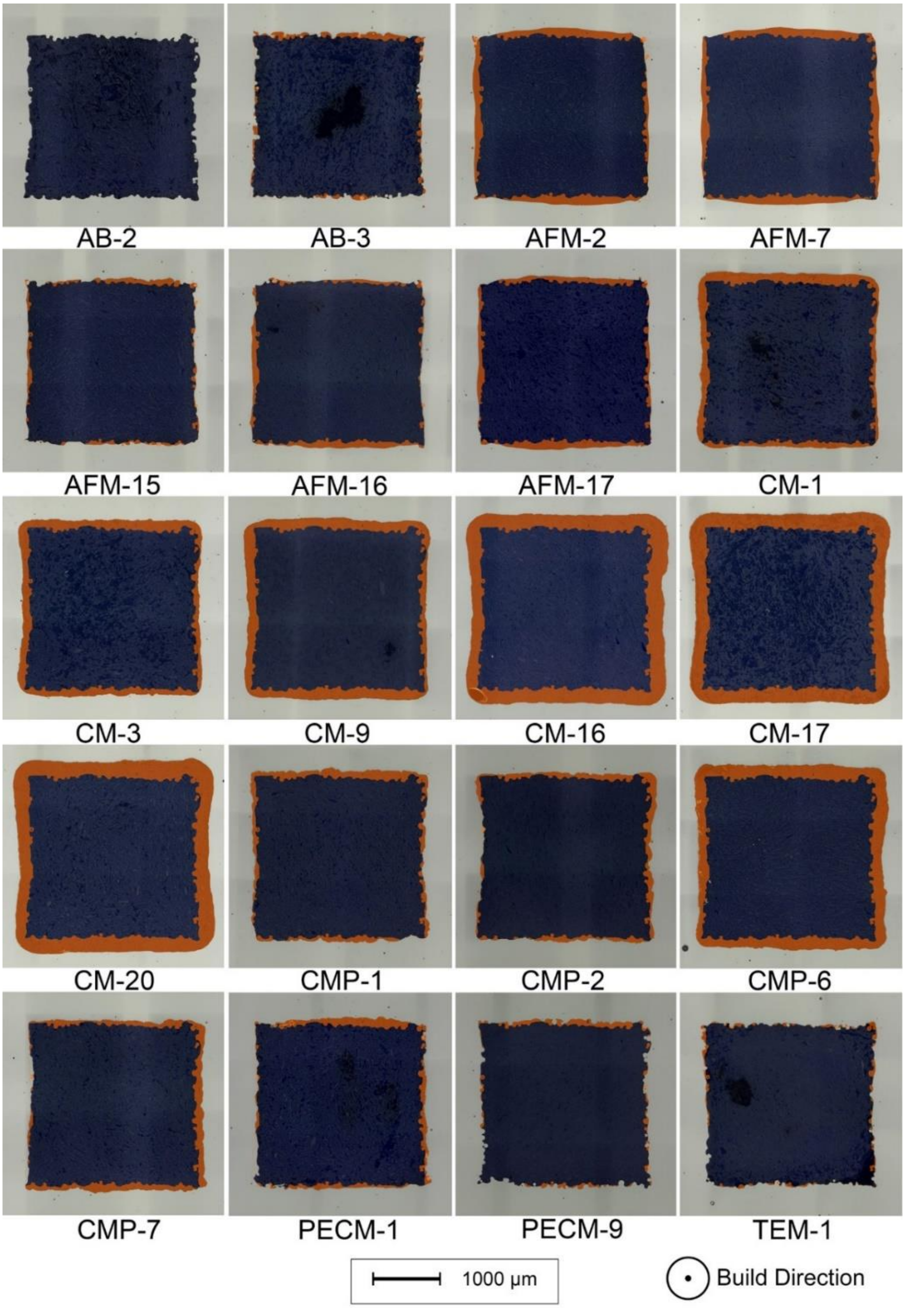

Figure 6.5. Polished cross section of channel samples incorporating an overlay of the section of an as-built (AB-2) channel (gray). Orange indicates the material removal from the sample.

6.4.1.2 Scanning Electron Microscope

Figure 6.6 shows the SEM images of the inner surface samples, taken normal to the surface. The as-built samples indicate excessive powder adhered to the surface, previously reported to vary based on build angle and geometry [269]. The adhered powder particles were tallied per millimeter of area and averaged. The powder count for the AB-2 and AB-3 samples were similar, and that of TEM-1 was only slightly lower. Since the powder is partially melted into the solidified material, the TEM process does not provide sufficient energy to vaporize the material because the thermal mass is too much. The AFM samples reveal excess powder in the corners, which aligns to observations related to the micrograph of the cross sections. The visual SEM of the surface indicates some periodic texturing and varies with the AFM parameters. The AFM-15 sample reveals a substantial amount of adhered powder that has been partially removed, leaving only a portion still attached. This indicates that not enough material was removed (41 µm). At higher SEM magnification (Figure 6.7), visible lines (*i.e.*, scratches) are indicated in the direction of flow due to the abrasives in the slurry [280].

The CM samples are characterized by some jagged edges and irregularities, which are more visible at higher magnification. The surface texture also exhibits directionality, more pronounced in CM-9 and CM-17. The surface texture aligns with the chemical solution flowed, which is indicated explicitly in CM-17, where flow was disrupted by an adhered particle. Several remnant particles and crystals can also be observed along with some evidence of delamination of selected particles. The delamination is likely due to a partially adhered particle where a gap was present, and the chemical solution could flow.

The results of the CMP process are similar to those obtained with CM, whereby some surface directionality can be observed and it is due to the flow of the chemical solution. However, the jagged features observed on the surface of the CMP samples are coarser if compared to those visible on the surface of the CM samples and the surface is smooth, in general. The CMP-2 and CMP-6 samples indicate selective etching at grain boundaries, which is superficial, along with annealing twins. Some random micro-pitting is also present on the surface of the CMP samples, indicating that the material was over-exposed to the chemistry during processing. CMP-7 displays an uneven surface characterized by round particle and fractures. Some evidence of brittle fractures are observed and cleavage fractures which indicate the polishing media impacted and sheared loosely adhered powder particles.

The PECM process sample also illustrates micro-pitting, which is typical of corrosion when the electrolytic residues remain on the surface [281]. The surface characteristic are similar to those of surfaces obtained with L-PBF and finished with ECP, as documented in the work of An et al. [175]. A limited number of powder particles can be observed on the surface of the PECM samples. The center of the channel exhibits less pitting than the edges near the sidewall due to the shape of the used electrode and to differences in local current.

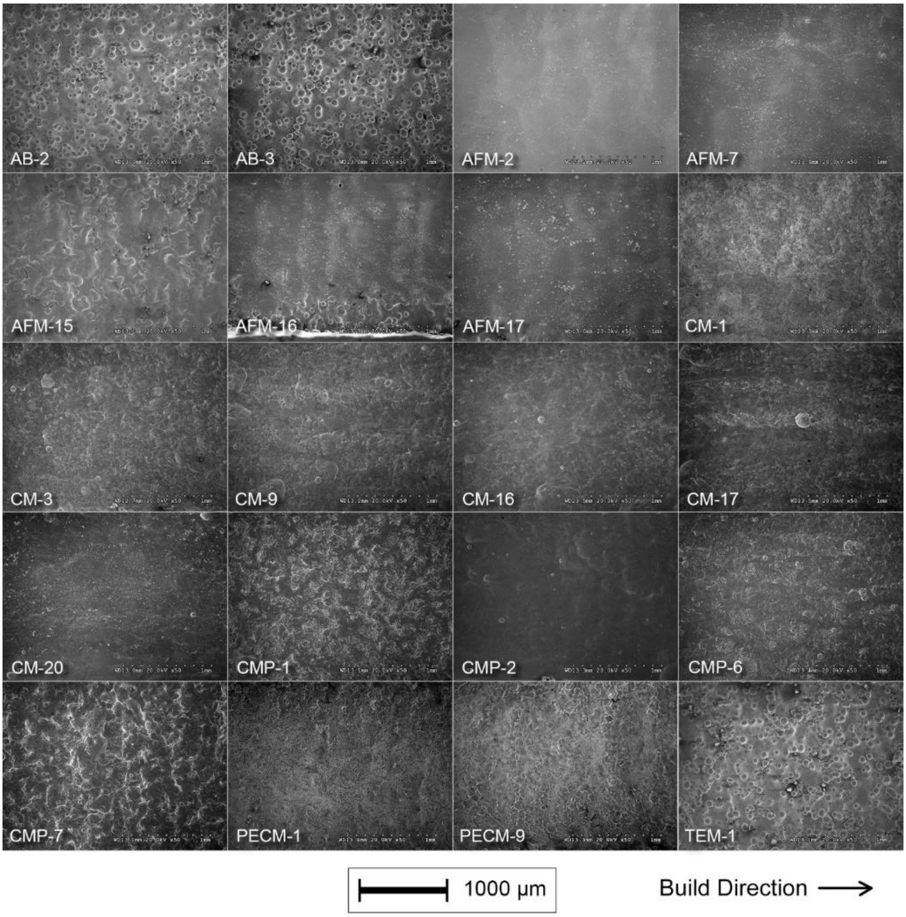

Figure 6.6. SEM 50x magnification images of the surface of each channel. Images are taken normal to the surface.

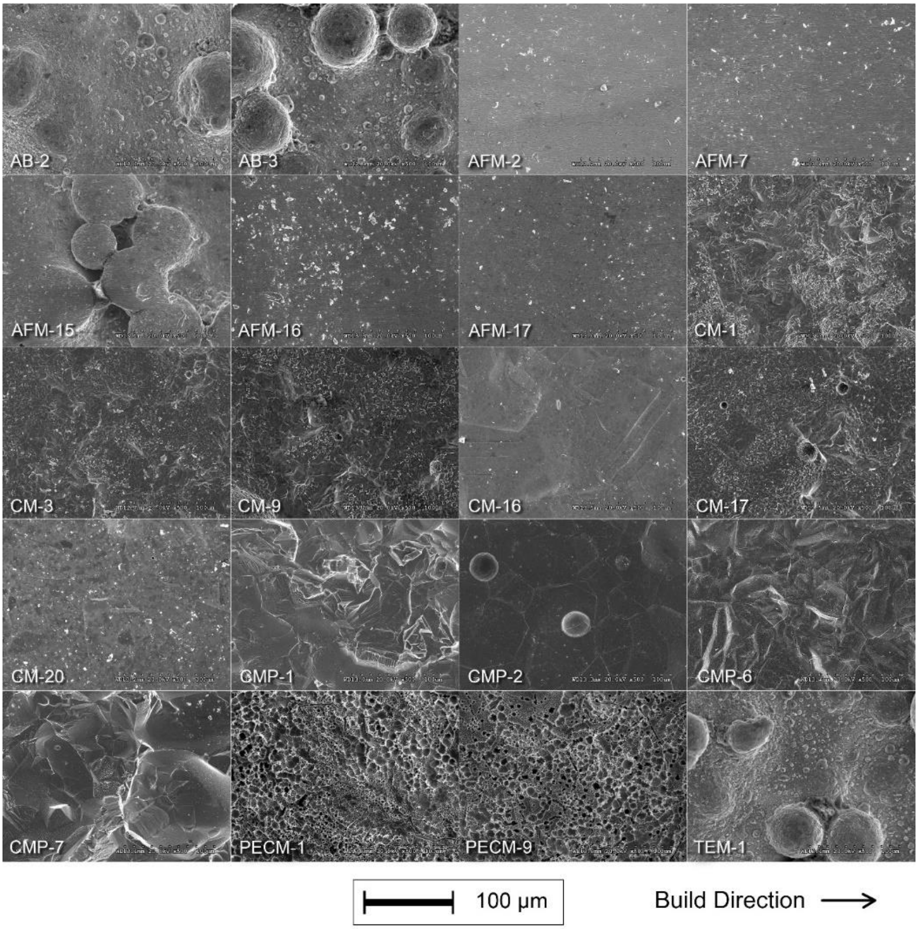

Figure 6.7. SEM 500x magnification images of the surface of each channel. Images are taken normal to the surface.

6.4.1.3 Computer Tomography

The selected samples that were μ-CT scanned (Figure 6.8) included AB-2, AFM-2, AFM-15, CM-3, CM-20, PECM-1, and CMP-6. The resulting images may not be fully representative of each of the corresponding processes since process parameters varied for each. The μ-CT data sets were reconstructed into a mesh with gaussian smoothing applied. The macro visual observations are similar to the optical and SEM images. The as-built samples indicate significant powder particle adherence. It is difficult to distinguish the corners and edge transitions and any potential waviness on the surface is masked by the high density of powder. The AFM-2 and AFM-15 samples show random particle adhesion with significant particle accumulation in the corners and waviness along the length. The periodicity of the waviness varies based on the sample.

The images of the CM-3 and CM-20 samples show significant rounding of the corners along with some waviness along the length. There are also some indications of non-uniform material such as mid-points of the sidewalls. The PECM-1 sample exhibits fine roughness along the walls, which is smaller than the powder observed characterizing the image of AB-2. There is a high density of powder in the corners and some indication of waviness along the length. The image of CMP-6 shows some indications of powder adherence and waviness along the length with a similar pattern to what can be observed in the image of CM-3.

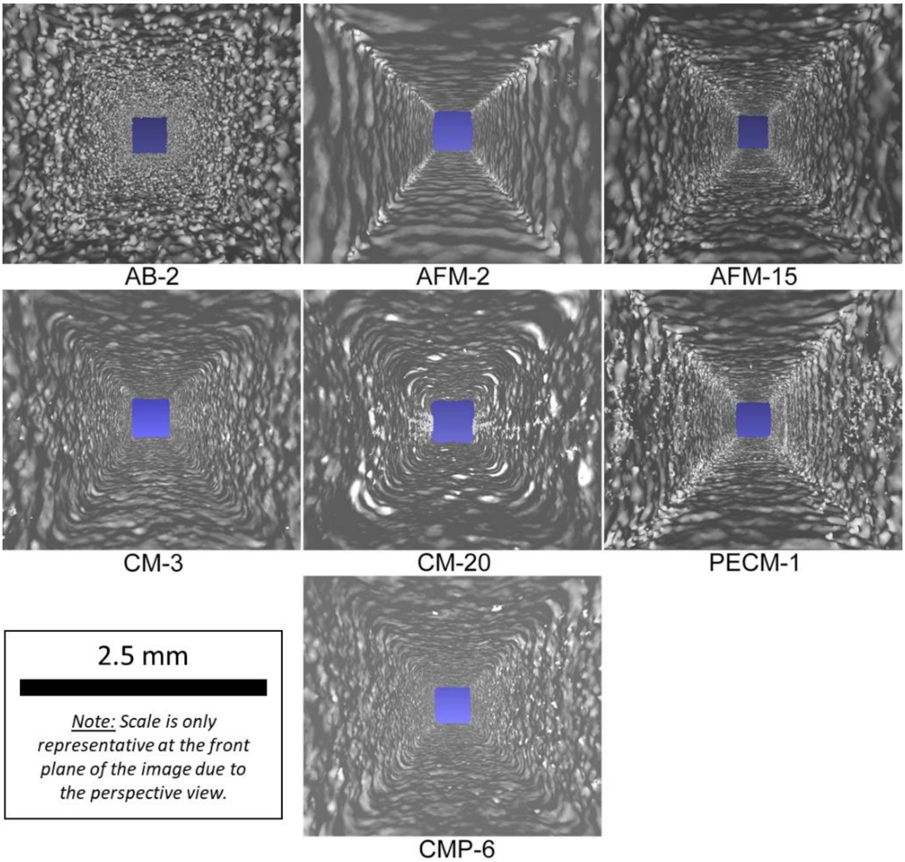

Note: Scale is only representative at the front plane of the image due to the perspective view.

Figure 6.8. Micro-CT Scanning images related to various surface enhancement processes. The images are taken normal to the channel cross-section and looking in the same direction as the direction of the flow.

6.5 FLOW TESTING

A total of 60 tests were completed with three pressure settings for each of the 20 channel samples. The measurement results of the optical and SEM images are listed in Table 6.2 along with the calculated discharge coefficient (*Cd*). The *Cd* was used to establish a relative comparison of the various surfaces resulting due to the polishing processes and is calculated according to

$$Cd = \frac{\dot{m}}{\rho A v} = \frac{\dot{m}}{A\sqrt{2\rho \Delta P}} \qquad \textbf{6.1}$$

where ṁ is mass flow rate (gram/second), A is area (mm^2), ρ is density of the water (grams/cm^3), and P is pressure (Bar) at the port.

The *Cd* is reported based on the actual measured area of the channels, and the standard deviation is computed from three distinct pressure runs conducted for each channel. The mass flow rate was based on the measured value. The variance between the flow rate calculated using the venturi and that measured by the flow meter was within a margin of less than 2% across all tests. The cavitation of the venturi was verified based on the exit pressure to inlet pressure ratio (<0.80) for each test run. The water mass flow rates remained uniform for each test, approximately measuring 85 ±0.0086 g/sec, 118 ±0.0075 g/sec, and 167 ±0.0078 g/sec corresponding to the respective tank pressures. The pressure and temperature data were taken from a 10 second period (100 samples/sec) and averaged. The change in area is calculated from the average of six measurements (AB-Avg) from the AB-2 and AB-3 channels.

Table 6.2. Optical and SEM image geometric measurement and discharge coefficient results and standard deviations.

Sample ID	Perimeter (mm)	Area (mm^2)	Area Change from AB-Avg (%)	Material Removed (µm per side)	Avg Particles (per mm^2)	*Cd*, Actual	*Cd* Change from AB-2 (%)
AB-2	13.36 ± 0.45	6.19 ± 0.038	-0.8%	0	98 ± 1	0.44 ± 0.004	0.0%
AB-3	13.45 ± 0.18	6.30 ± 0.038	0.8%	0	93	0.43 ± 0.007	-1.9%
AFM-2	10.87 ± 0.12	6.85 ± 0.027	9.7%	88 ± 9.4	0	0.85 ± 0.002	92.9%
AFM-7	10.64 ± 0.12	6.97 ± 0.059	11.7%	87 ± 16.7	2	0.88 ± 0.003	98.8%
AFM-15	11.64 ± 0.19	6.37 ± 0.050	2.0%	41 ± 8.0	18 ± 0.5	0.59 ± 0.004	34.0%
AFM-16	11.33 ± 0.11	6.53 ± 0.059	4.6%	51 ± 14.0	2	0.71 ± 0.003	60.7%
AFM-17	11.28 ± 0.40	6.67 ± 0.094	6.9%	61 ± 14.6	0	0.75 ± 0.002	70.5%
CM-1	11.52 ± 0.04	7.36 ± 0.077	17.9%	85 ± 14.3	5 ± 1	0.76 ± 0.011	73.4%
CM-3	11.54 ± 0.10	7.24 ± 0.015	16.1%	97 ± 13.0	4 ± 1.5	0.76 ± 0.023	73.1%

CM-9	11.37± 0.06	7.29 ± 0.136	16.8%	121 ± 17.2	3 ± 1	0.75 ± 0.018	69.6%
CM-16	11.98 ± 0.12	8.28 ± 0.214	32.8%	207 ± 12.8	2	0.94 ± 0.017	113.5%
CM-17	12.20 ± 0.18	8.20 ± 0.170	31.6%	197 ± 16.1	1	0.85 ± 0.032	92.8%
CM-20	12.06 ± 0.03	8.50 ± 0.032	36.4%	213 ± 18.1	1 ± 0.5	0.97 ± 0.016	120.7%
TEM-1	13.45 ± 0.39	6.28 ± 0.102	0.6%	17 ± 7.0	87	0.44 ± 0.005	-0.9%
PECM-1	12.55 ± 0.50	6.53 ± 0.035	4.6%	61 ± 16.6	3 ± 0.5	0.55 ± 0.006	26.0%
PECM-9	12.02 ± 0.25	6.47 ± 0.211	3.6%	47 ± 14.0	2	0.55 ± 0.009	24.3%
CMP-1	12.14 ± 0.29	6.75 ± 0.049	8.1%	62 ± 15.3	0	0.50 ± 0.005	13.5%
CMP-2	11.31 ± 0.37	6.89 ± 0.208	10.4%	53 ± 11.3	8	0.81± 0.010	83.4%
CMP-6	11.97 ± 0.07	7.94 ± 0.083	27.3%	162 ± 17.3	6	0.89 ± 0.024	103.0%
CMP-7	11.63 ± 0.13	6.82 ± 0.039	9.3%	58 ± 12.9	8 ± 1	0.56 ± 0.007	26.7%

The discharge coefficient is plotted against measured cross-sectional area, measured perimeter, and average areal texture and depicted in Figure 6.9. The *Cd* is calculated using the measured area. At *Cd* below 0.6, the differences due to the as-designed (6.452 mm^2) to actual as-built area were minor. However, above a *Cd* of 0.7 when the nominal as-designed area is used to calculate *Cd*, it overpredicts its value since it is smaller than actual area (Supplemental). This is an important aspect related to additively manufactured surfaces since the actual as-built areas can be smaller due to powder adherence, melt pool irregularities, dross formation. The area of the CM samples increased by 36% resulting in a 120% change of the *Cd*. The as-built samples and the TEM samples featured the highest resistance, as expected, and the area value is smaller than the as-designed value by 4%. The obvious trend is the increase in cross sectional area due to the various processes resulting in larger *Cd*. However, for several channels with similar area, there were differences in the *Cd*. AFM-2, AFM-17, CMP-1, CMP -2, and CMP-7 all featured similar areas, but the *Cd* varies by more than 78%. Alternatively, comparable *Cd* values of around 0.9 were measured for AFM-2 and CM-17, despite a notable disparity in their cross-sectional areas, which differ by 19.7%. Similar cross-sectional areas were measured for AB-2, AB-3, TEM-1, and AFM-15, while AFM-15 is characterized by a higher *Cd* value. These variations can be attributed to differences in surface texture, perimeter, and the resulting resistance within the channel.

As the perimeter increases, the *Cd* generally decreases linearly. The larger perimeter, in the as-built samples, is caused by the partially adhered powder creating boundary layer turbulence and increased resistance [251]. The as-built perimeter is 30% larger than the as-designed nominal perimeter. Figure 6.9B also depicts AFM-2 and AFM-7 among the smallest perimeters. This is due to the reduction of the sidewall texture, removing the mid-span rib material from the convex shape to flat. Additionally, there is powder remaining in the corners of several AFM samples creating a radius. This indicates the excess powder in the corners of the AFM samples did not have a significant impact on the *Cd*. There are a few outliers in perimeter plot, namely CM-16, CM-17, CM-20, and CMP-6. These outliers have lower average surface texture among the data set but their peculiar behavior in the perimeter plot cannot be solely explained by the average Sa. There is an increase of *Cd* when the texture increases, as expected. There is a linear rise in *Cd* up to 0.6 based on a decrease of the surface texture. According to this data set, the surface texture below 14 µm plateaus although there is an increase in *Cd*.

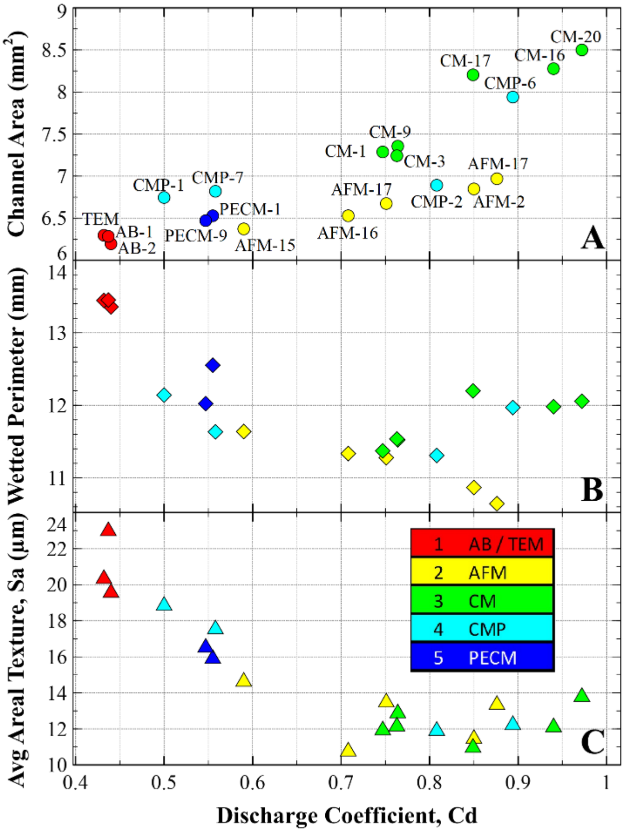

Figure 6.9. Summary of *Cd* and comparison to: A) measured channel cross-sectional area, B) measured perimeter, and C) measured average areal texture, Sa. The data is colored based on the surface enhancement process.

Sa represents an average value and does not provide a comprehensive characterization of the surface and its flow resistance. To gain a deeper insight into how surface texture impacts *Cd*, the data is evaluated based on the magnitude of the peaks and valleys and the density of these disturbances. While the maximum height of the surface, denoted as Sz, can serve as a measure, it may not always accurately depict the true surface characteristics due to the presence of outliers, such as extremely elevated peaks or deep valleys. Sz, which sums the maximum peak height (Sp) and maximum valley depth (Sv), was compared to the *Cd* and no correlations were observed (Supplemental). This implies two key points: 1) the existence of anomalous localized peaks does not affect *Cd*, and 2) Sz is an inadequate measure to understand the surface texture mechanism influencing *Cd*. Instead, core roughness depth (Sk) is utilized as a substitute for Sz, representing the average peak-to-valley distance. The surface texture parameters discussed in this section are provided in Table 3.

Figure 6.10 shows that Sk reveals that as the peak-to-valley depth diminishes, *Cd* rises and then stabilizes around a depth of approximately 40 µm. The peak height, referred to as reduced peak height (Spk), as indicated in Figure 6.10, illustrates that higher peaks contribute to greater resistance. For the samples featuring the highest *Cd* (CM-16 and CM-20), Spk constitutes roughly 8% of the surface, whereas it accounts for 13% in samples with lower *Cd*. The remaining portion of the surface comprises core roughness depth. Conversely, reduced valley depth (Svk) was assessed but no correlation was observed with *Cd*.

Table 6.3. Summary of Surface Texture Measurements.

Sample ID	Primary Sa (µm)	Primary Sz (µm)	Primary Sk (µm)	Primary Spk (µm)	Spk, Lc=0.8 (µm)	Primary Spd (µm)	Wp, (µm)	WPc, (µm)	Ra, (µm)
AB-2	19.6	317.6	59.2	32.7	28.6	146.7	34.3	17	13.8
AB-3	20.3	262.6	64.6	28.9	26.9	157.3	34.5	14	12.9
AFM-2	11.5	177.4	35.8	15.2	7.1	470.0	24.7	15	4.6
AFM-7	13.3	143.4	43.6	16.1	6.1	483.6	24.8	15	4.7
AFM-15	14.6	223.1	45.8	18.6	12.0	248.6	36.7	15	9.9
AFM-16	10.8	276.9	32.7	14.7	10.8	367.2	23.2	16	5.4
AFM-17	12.9	144.6	40.4	12.6	7.5	380.1	29.8	8	4.8
CM-1	12.1	227.8	36.5	12.5	9.0	414.8	26.8	9	5.1
CM-3	11.9	216.4	38.3	12.8	8.0	403.7	24.3	9	4.5
CM-9	13.5	257.1	42.2	17.5	9.7	394.9	29.8	13	4.9
CM-16	12.1	250.7	38.7	11.2	10.7	344.9	22.4	10	5.6
CM-17	11.0	225.5	34.5	12.4	8.1	463.5	23.5	7	4.3
CM-20	13.8	373.5	40.5	10.9	12.1	452.6	23.1	8	3.5
TEM-1	23.0	608.3	71.9	37.3	33.7	135.1	52.1	18	17.2
PECM-1	15.9	216.6	49.9	24.6	12.8	335.5	30.2	14	7.1
PECM-9	16.5	177.5	50.9	26.2	14.2	291.8	30.7	12	7.2
CMP-1	18.8	382.8	59.4	22.6	17.2	351.2	42.2	13	10.5
CMP-2	11.9	273.8	37.0	14.1	10.2	393.2	32.9	10	5.0
CMP-6	12.2	231.8	38.7	14.5	8.4	493.4	22.8	12	5.4
CMP-7	17.5	506.2	52.6	22.0	16.4	399.2	36.6	12	11.7

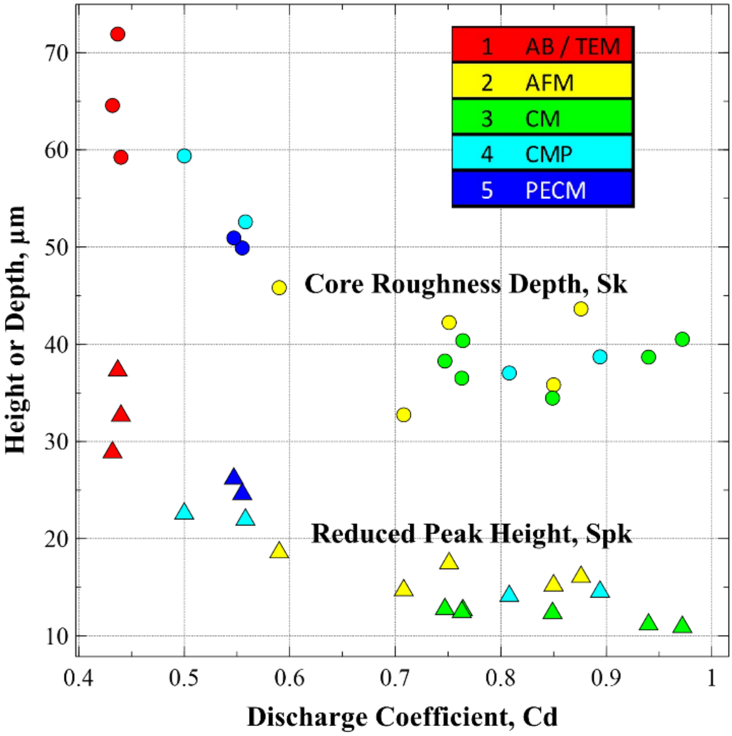

Figure 6.10. Discharge coefficient in relation to core roughness and reduced peak height.

The roughness is due to powder adherence and melt pool irregularities. To better illustrate this relation, Figure 6.11 reports the average texture as a function of the average material removal per side in. The value of *Cd* is displayed as colored dots whose shade is related to a scale. The value of *Cd* is consistently higher than 0.75 whenever and amount of sidewall material equivalent to the average powder size (70 µm) was removed. This led to a reduction in surface texture to values below 14 µm and is independent of the surface enhancement process. The results of these experiments revealed a strong variation of *Cd* if only the minimum powder size (55 µm) was removed, and limited discrete particles remained. According to particle count analysis, a material removal of 45 µm eliminated 90% of the adhered powder. However, this still resulted in higher Sa values due to remaining melt pool surface irregularities, which has an adverse impact on *Cd*. Particle density alone does not correlate with the *Cd* associated with the applied surface enhancement treatment. While material removal does play a role, its value alone cannot be used to predict the value of *Cd*. Certain processes, such as AFM, could achieve lower resistance with significantly less material removal if compared to that achievable with CM. For certain applications, the aim might be to minimize material removal while simultaneously achieving the lowest possible surface texture.

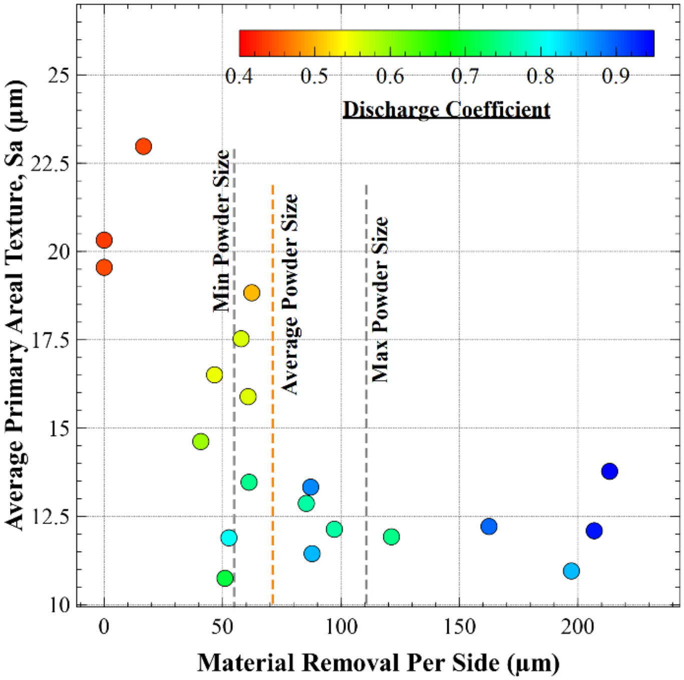

Figure 6.11. Average areal texture compared to material removal per side.

The average texture (Sa), as depicted in Figure 6.9C, levels out as the discharge coefficients measured for the samples exceed a *Cd* of 0.7. Sa, being an average value, does not fully characterize the surface and cannot be directly related to variations of *Cd*. To characterize the variations of *Cd* in relation to surface features, the surfaces were categorized based on their roughness peaks and on the density of these peaks. Reduced peak height (Spk) and density of peaks (Spd) are plotted in Figure 6.12A and B, respectively, alongside the channel cross-sectional area. The Spk represents the mean height of peaks which are present above the core roughness based on an areal material ratio curve (~10% of surface) [282]. This representation allowed for a clear correlation between the surface treatment of a sample and the associated measured *Cd*.

In samples whose associated *Cd* was less than 0.7, roughness is primarily caused by partially adhered powder, accounting for more than 70% of the surface texture. Directional measurements, such as profile (Pa) and roughness (Ra), were also examined but did not provide sufficient resolution in the surface characterization to correlate with measured *Cd*. This is an important result, since Ra is typically reported but is simply an average directional (single line) value. Since the peaks are one of the primary contributors to flow resistance, the Ra is insufficient to fully characterize the surface in case accurate *Cd* predictions are the final objective.

In addition to the peak height (Spk), the density of the peaks (Spd) also contributes to flow resistance, as illustrated in Figure 6.12B. Spd is traditionally used for bearing surface evaluation and would indicate a larger contact surface area. For surface enhancements and flow characterization, higher Spd values imply that there are more peaks per unit area but that they have been smoothed away. The samples featuring the lowest *Cd* were planarized, thus they the peaks were smoothed and this is correlated with higher Spd values.

Waviness was also evaluated using a cutoff filter of 0.8 mm. Waviness is visually observed in all samples (Figure 6.8). However, samples whose internal surfaces are characterized by identical waviness value still generated flows with significantly different *Cd*. To better explain this phenomenon, the waviness peaks (Wp) were evaluated and their values suggest that lowered peaks cause an increase of *Cd*, as seen in Figure 6.12C. The waviness valleys (Wv) were also evaluated and cannot be correlated to *Cd*. To further validate result of the waviness peaks, the periodic waviness peak density (Wpc) was analyzed and it was observed that it features different values for samples associated with higher *Cd*. Wpc is defined as the number of peaks per the unit length. In this case the sampling length was 38 mm. As the density of the waviness decreases, the *Cd* increases. The CM samples featured the lowest Wpc, which was approximately 50% lower than that of the as-built samples. It is observed that the waviness has a stronger impact on samples associated with *Cd* greater than 0.7.

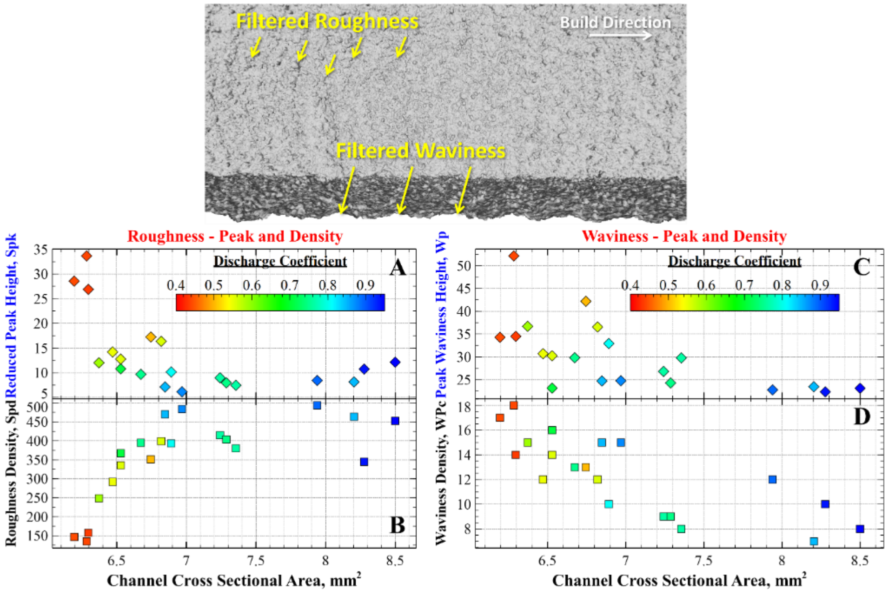

Figure 6.12. Channel cross sectional area compared to A) Reduced peak height, Spk, B) density of peaks, Spd, C) waviness peak height, Wp, and D) Density of waviness, WPc.

These observations indicate that an effective surface enhancement process should remove the partially and fully adhered powder particles (roughness peaks and their density) and smooth the waviness peaks and density thereof to reduce resistance within the channel. It is important to note that, as the peak waviness decreases, the average waviness decreases, but then valleys eventually become the primary contributor to the flow resistance. Achieving full planarization of a surface necessitates reducing both peaks and valleys related to waviness, requiring a larger amount of material removal.

The impact of the combined texture effects is corroborated by the analysis results depicted in Figure 6.13, namely the comparison between a ratio of roughness peak/density (Spk/Spd) with waviness peak/density (Wp/WPc). *Cd* increases significantly with lower values of roughness and density. As the roughness ratio approaches 0.04, a trend can be observed: the surface waviness begins to exert a more pronounced influence on the increase of *Cd*. However, to reduce the waviness necessitates more material removal compared to the roughness and an increase in surface area for planarization.

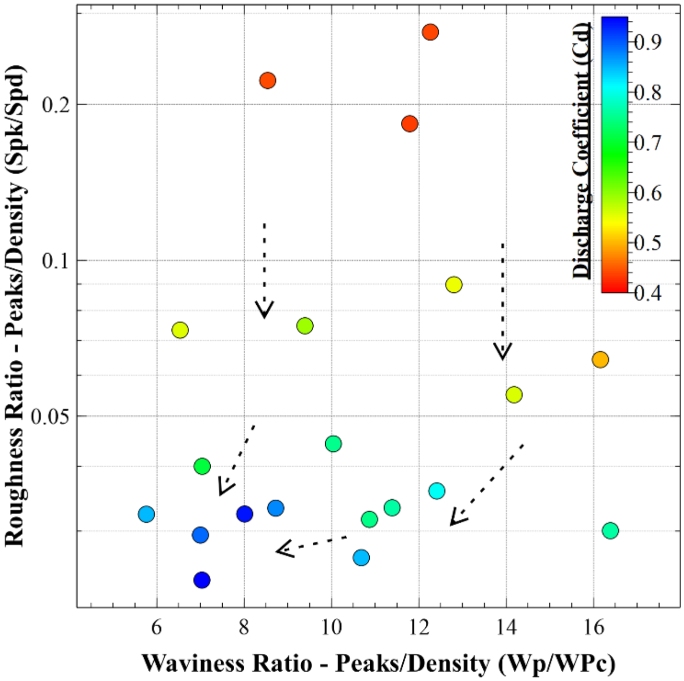

Figure 6.13. Ratio of roughness peaks to density (Spk/Spd) compared to the ratio of waviness peak to density (Wp/WPc). Note Y-axis is Log scale.

The experimental data underscored that an increase in area causes an increase of *Cd*, as expected. According to this experiment, approximately 65% of *Cd* variation can be attributed to changes in area. The wetted perimeter also contributes to flow resistance (8%). The ideal perimeter should match the mathematical definition, in theory, but in application varies along with the area. For instance, in a square channel, each sidewall is fully planarized or flat. The surface texture accounts for approximately 25% of the variation in *Cd*. The surface roughness due to the adhered powder and waviness resulting from irregular melt pools and build layering affect not only the perimeter, but also the overall 3D surface in the direction of the flow. This is evident since in several channels that had the same perimeter and channel area, the *Cd* varied based on the resulting texture due to the various surface enhancements.

The goal of this testing and characterization was to demonstrate differences in surfaces resulting from each of the surface enhancement processes. The performance from each of the different microchannels with surface enhancements, along with a comparison to as-built baseline samples was summarized in Table 2. Chemical milling and CMP demonstrated the potential to reduce or eliminate the powder adherence and minimize waviness. However, these processes also removed the most material. Sample CM-17 featured some of the lowest peak and density values for roughness and waviness and with a slightly larger area would have likely achieved a performance in terms of *Cd* equal to that provided by the samples associated with the highest *Cd*. The evaluated surface enhancement technologies could also be improved by adopting optimized process parameters. One goal may be to minimize material removal while achieving a reduction of roughness and waviness peaks and density. The material removal must be balanced with the processing economics, as increased material removal increases the cost.

6.6 CONCLUSIONS

This work demonstrated that various surface enhancements can be applied to internal square microchannel samples produced using LP-DED with 1 mm thick walls. The samples featured a 2.54 x 2.54 mm square cross section and were built using the NASA HR-1 (Fe-Ni-Cr) alloy. Several techniques were demonstrated including abrasive flow machining (AFM), chemical milling (CM), chemical mechanical polishing (CMP), electrochemical machining (PECM), and thermal energy method (TEM) to modify the internal surfaces. Flow testing was performed to characterize the flow resistance of the resulting channel surfaces and the samples were then destructively evaluated using SEM, µ-CT, optical microscopy, and optical surface texture. The goal of this study was to demonstrate how variations in the LP-DED surfaces can be obtained, and to understand the underlying causes for corresponding changes in the resulting flow resistance. This data could then be used to provide requirements for additively manufactured components, such as heat exchanges.

The following conclusions can be drawn:

- The various surface enhancements result in different surface characteristics deriving from the mechanics of the process. These include: remnant powder, jagged edges and crystals, scratches, pitting or selective grain boundary attack.
- The CM and CMP processes removed the largest amount of material per side (up to 213 µm) resulting in a larger cross-sectional area (36%) compared to the as-built samples.

- The as-built perimeter was 32% longer than nominal perimeter (the design perimeter). This is due to the adhered powder particles and surface irregularities resulting from the melt pool and build layering.
- A 121% increase in *Cd* could be achieved using chemical milling with a 36% increase in area.
- 65% of the change in flow resistance is attributed to the area change; 8% depends on the perimeter and 25% on the surface texture.
- To increase the *Cd*, the surface enhancement process should eliminate adhered powder (roughness peaks and their density) and planarize peaks and density related to waviness. This implies that an effective surface enhancement process necessitates reducing both peaks and density thereof related to surface roughness and waviness, requiring increased material removal.
- The material removal should be at least equal to the average powder diameter (70 µm) to achieve reductions in flow resistance. While material removal equal to the minimum powder diameter (45 µm) results in 90% of powder elimination, it also results in significant variations of *Cd*.
- The ratio of roughness and waviness peak and density (Spk/Spd and Wp/WPc) is proposed as a relevant surface characterization parameter. Using this parameter, it is possible to observe a transition where the effect of surface roughness due to peaks is reduced, and a reduction of the surface waviness is required to increase the *Cd*.

The application of surface enhancements to surface geometries obtained with the LP-DED process demonstrated that a surface could be modified based on a set of requirements. This data along with future testing can tailor a surface for fluid friction factors, fatigue life, corrosion, heat transfer, or even aesthetics. This is particularly important in heat exchangers, where each of these attributes are balanced during the design process. A combination of the LP-DED process and surface enhancements can be used to fabricate large scale components for aerospace, power generation, and industrial heat exchangers. Future research might combine processes, such as AFM and CM/CMP, using the advantages of the unique surfaces from each. This study engaged commercial vendors for the development of surface enhancements. It is anticipated that these processes could be effectively and economically utilized for future applications requiring surface variations to meet specific requirements.

Chapter 7

Friction Factor of Channels with Improved Surface Finishing

Major portions of this chapter were published in:

Gradl, P., Cervone, A., Colonna, P., 2025. Enhancement of friction factors for microchannels fabricated using laser powder directed energy deposition. Materials & Design 251, 113673. https://doi.org/10.1016/j.matdes.2025.113673

7.1 ABSTRACT

Designing high-performance and aerospace-grade heat exchangers requires detailed characterization of the as-manufactured geometry, including cross-sectional area and surface texture, to reduce uncertainties in performance prediction and issues regarding subsequent system integration. This chapter presents experimental testing and analysis of 600 mm length channels fabricated using the LP-DED process. Surface finishing is often required for heat exchangers built using AM to meet the desired pressure drop specifications. Moreover, the highly textured as-built surfaces result in a measured pressure drop higher than what is predicted by current correlations. Various surface enhancement techniques were applied to the internal surfaces of the channels to tailor flow dynamics and induce variations in pressure drop. The study focused on evaluating the pressure drop and friction factor variations depending on the type of surface and its conditions. A novel method for calculating the hydraulic diameter, accounting for surface texture variations, is proposed and used to correlate and analyze all the collected experimental data.

Surface enhancements, including abrasive flow machining (AFM), chemical milling (CM), and chemical mechanical polishing (CMP), were compared to the as-built surface. Based on experimental testing, channels processed with surface enhancements provide a tenfold reduction in differential pressure compared to the as-built channels. After testing, the samples were destructively sectioned to obtain geometric and detailed surface texture information. This characterization helped to inform a new prediction method for determining equivalent sand grain roughness, thus reducing the uncertainty of predicted friction factors. The new correlation allows to estimate friction factor and pressure drop with a deviation from the experimental data that is within 20% of their value. The identification of the mechanisms at the basis of the formation of surface texture allowed to categorize distinct aspects:

roughness peaks, peak smoothing/reduction, minimized roughness, and combined waviness and valley reduction. These aspects of surface texture can be associated to specific friction factor ranges.

7.2 INTRODUCTION

Critical design features of high-performance, aerospace-grade heat exchangers include the geometry of internal channels and their surface finish. These characteristics are fundamental for the transfer of thermal energy between fluids and the flow friction, which ultimately determine whether the component and the overall system function properly. Designing these channels is often an iterative process that aims to minimize the associated pressure loss, maximize heat transfer, and maximize the service life of the component. Optimizing pressure drop, heat transfer, and fatigue life involves compromising between contrasting requirements. Surface texture significantly affects pressure losses and heat transfer. In this respect, Chapters 5 and 6 document research on LP-DED microchannels and the related first-order flow resistance in terms of discharge coefficient, while this chapter focuses on the study of friction factors, their relationship with sand grain roughness and the derivation of a correlation, the definition of hydraulic diameter suitable for this case, and the correlations for the prediction of pressure losses in square microchannels.

The Moody diagram, established decades ago, provides nondimensional values of the friction factor as a function of the Reynolds number and relative pipe roughness [283]. Moody developed this diagram valid for laminar and turbulent flows using experimental data from Darcy-Weisbach and Nikuradse [284,285]. Relative pipe roughness relates the height of surface roughness to the hydraulic diameter, however it cannot provide a merit parameter that is adequate for the complexity of additively manufactured surfaces and its relationship to the original sand grain roughness characterizing the experimental data of Darcy-Weisbach and Nikuradse. The proportionality relationship between relative roughness and friction factor is well known: as roughness increases, the friction factor also increases, and this is mathematically expressed by the Colebrook-White correlation [286,287]. Early experiments by Darcy, Nikuradse, and Colebrook were limited to values of relative roughness lower than 5% [288]. Researchers like Kandlikar et al. expanded the measurement range to values of relative roughness up to 14% [289]. Additive manufacturing (AM) offers several advantages if adopted for the fabrication of special heat exchangers, especially in terms of complexity and miniaturization of channels, therefore it is becoming more prominent. However, traditional correlations for the modeling of the fluid dynamic effect of surface texture perform very poorly in case of surfaces obtained with AM, resulting in actual values of the friction factor that are higher than those predicted by correlations based on prior experimental data [290]. McClain et al. [291] highlighted the necessity of accurately characterizing and measuring surface texture and equivalent sand grain roughness for accurate predictions because the roughness to hydraulic diameter ratio is high, and outside the range of validity of current correlations.

Several authors have investigated flow friction associated with simple- and complex-geometry channels made with L-PBF and as-built surfaces. Richermoz et al. [292] experimented on circular and round channels made of Alloy 600 and manufactured with L-PBF. The channels featured alternating 90° serpentine bends. They measured a 37% increase in friction factor over traditionally manufactured channels. However, they noted that uncertainty in hydraulic diameter affected the results, which were measured using CT and basic directional roughness measurements. Zhou et al. [169] investigated changes of hydraulic diameter in L-PBF-made channels, depending on build angle, dross formation, and warping. They proposed a linear model adjustment but did not relate such adjustment to physical geometry. These differences highlight the importance of perimeter biasing due to internal channel texture as this affects the hydraulic diameter.

Snyder et al. [293] reported that varying L-PBF parameters reduced surface roughness by 50%, resulting in a proportional reduction of the friction factor. Kirsch et al. [294] found a three-fold increase in friction factor with a 30% difference in hydraulic diameter at Reynolds numbers from 3,000 to 10,000. Hartsfield et al. [295] concluded that sand grain roughness does not correlate with profilometer roughness measurements of L-PBF surfaces. These researchers therefore proposed to approximate the value of sand grain roughness as 50% of the mean powder diameter. Zhu et al. [167] estimated that values of relative roughness can be estimated by multiplying the average areal surface texture (Sa) from each surface by a factor of two. This work considered solely L-PBF-made horizontal round tubes with diameters greater than 6 mm and as-built surfaces. Jamshidinia et al. [113] put into evidence that surface roughness resulting from L-PBF is related to process heat input, emphasizing the importance of build parameters. However, the friction factor correlations they obtained cannot be broadly applied to channels produced with different AM processes.

Most documented research on flow friction associated with additively manufactured channels focused on channels with as-built surfaces, thus no post-processing of the surfaces was considered. Favero et al. [165] performed friction measurements on oval copper channels made with L-PBF and post-processed with chemical milling. They concluded that pressure drop could be reduced by an order of magnitude with a six-fold reduction in average roughness. The developed correlations are based on a hydraulic diameter calculated based on area and perimeter, but no sand grain roughness was considered. Kaur and Singh [168] emphasized the need for thorough research on the localized influence of surface texture.

The build mechanics of the LP-DED is fundamentally different from that of L-PBF. Results regarding the flow friction of channels made with L-PBF cannot be applied broadly and friction factors associated to channels made with LP-DED are expected to vary due to differences in powder feedstock, process parameters, and environmental process factors like purges and surrounding powder. The derivation of friction factor correlations is further complicated if surfaces are treated with enhancement.

Comprehensive experimental data and correlations valid for additively manufactured microchannels with similar geometry and different surface texture are not available yet. Full characterization of surface topography is crucial to understand the underlying mechanisms causing the texture. Moreover, such surface enhancement methods enable the possibility to improve the internal channel finish and ensuing flow friction through post-processing. Designers of additively manufacture heat exchangers require options to prescribe surface finishing to tune the flow characteristics to meet design objectives, rather than accepting as the only option what results from as-built surfaces. This chapter summarizes therefore an experimental study to determine the pressure drop associated with square channels fabricated with LP-DED and processed with various surface enhancements, resulting in a wide range of surface textures and topographies. The experimental data allowed to establish 1) a new definition of hydraulic diameter which eliminates perimeter bias due to surface texture, 2) an equivalent sand grain roughness, and 3) new correlations that considerably improve friction factor predictions for such channels. The surface texture characteristics are evaluated in detail, providing roughness and waviness attributes which can be directly related to the friction factor.

7.3 METHODOLOGY

Channel samples were fabricated specifically for differential pressure drop testing. The experimental campaign took place at the same facility utilized for the discharge coefficient testing detailed in Chapter 6. The test sections of the square microchannels described in this chapter were approximately 615 mm in length. Numerous channels were fabricated and tested in their as-built condition, while several others underwent surface enhancements before testing. After the testing phase, the channel samples were sectioned to characterize the internal surface and flow area to validate assumptions for the analysis and correlations.

7.3.1 Fabrication of DED Samples and Processing

The 600 mm length test channels were designed with a nominal width and height of 2.54 x 2.54 mm and built using LP-DED. They are shown in Figure 7.1. The square test section included a length of 615 mm with a 25 mm blended transition segment from the square channel to a round extrusion on both ends (Figure 7.1C). This design facilitated the welding of a universal AN-type fitting onto either end as an interface with the rest of the facility. The channels were constructed with the same RPMI 557 machine, utilizing an A36 mild steel base plate. The boxes were built using consistent parameters, including a laser power of 350 W, powder feed rate of 23 grams/min, travel speed of 763 mm/min, and a layer height of 0.254 mm. All these parameters are the same as those utilized for the channels described in Chapters 5 and 6.

A coarse powder was used for most of the samples, with some samples fabricated using fine powder feedstock. The coarse powder used in the process was rotary atomized by Homogenized Metals Inc. (HMI), featuring a particle size distribution (PSD) ranging from 45 to 105 µm. The specific lot number of the powder was HRA11, with an average size of 73 µm. Notably, the oxygen content measured 68 ppm, and the nitrogen content was 12 ppm. The fine powder featured a PSD of 10-

45 µm and average size of 32 µm. The oxygen content was 145 ppm and nitrogen was 10 ppm. The higher oxygen content in the fine powder is attributed to the larger area per volume of the powder. The composition, as determined using ICP, is detailed in Table 7.1. Virgin powder was employed for all builds.

Table 7.1. Chemical composition of the NASA HR-1 powder utilized to build the channel samples (HMI Lot HRA11/Coarse and HRA9/Fine).

Size		Fe	Ni	Cr	Co	Mo	Ti	Al	V	W
Coarse	Wt.%	Bal.	33.98	14.74	3.78	1.84	2.36	0.24	0.3	1.6
Fine	Wt.%	Bal.	33.91	14.66	3.79	1.83	2.41	0.24	0.3	1.6

The channels were initially fabricated as larger boxes, as illustrated in Figure 7.1, and then underwent a series of heat treatments, including stress relief, homogenization, solution annealing, and double aging. These heat treatment operations were identical to those described in Section 6.3.1. Following the heat treatment, the boxes were removed from the build plate using a bandsaw. Subsequently, the boxes were individually sectioned using water jet cutting and the ends of the channels were machined in preparation for the welding of the ports. The channels were cleaned, and subsequently an AS5174-04 Inconel 625 fitting was laser-welded to each of the inlets and outlets of the samples (Figure 7.1C). The channel that was tested is indicated by the yellow lines, and stock regions were fabricated to either side of the channel to allow it to be sectioned. Each sample was then individually tagged and provided to the vendors for surface enhancement processing (Figure 7.1D).

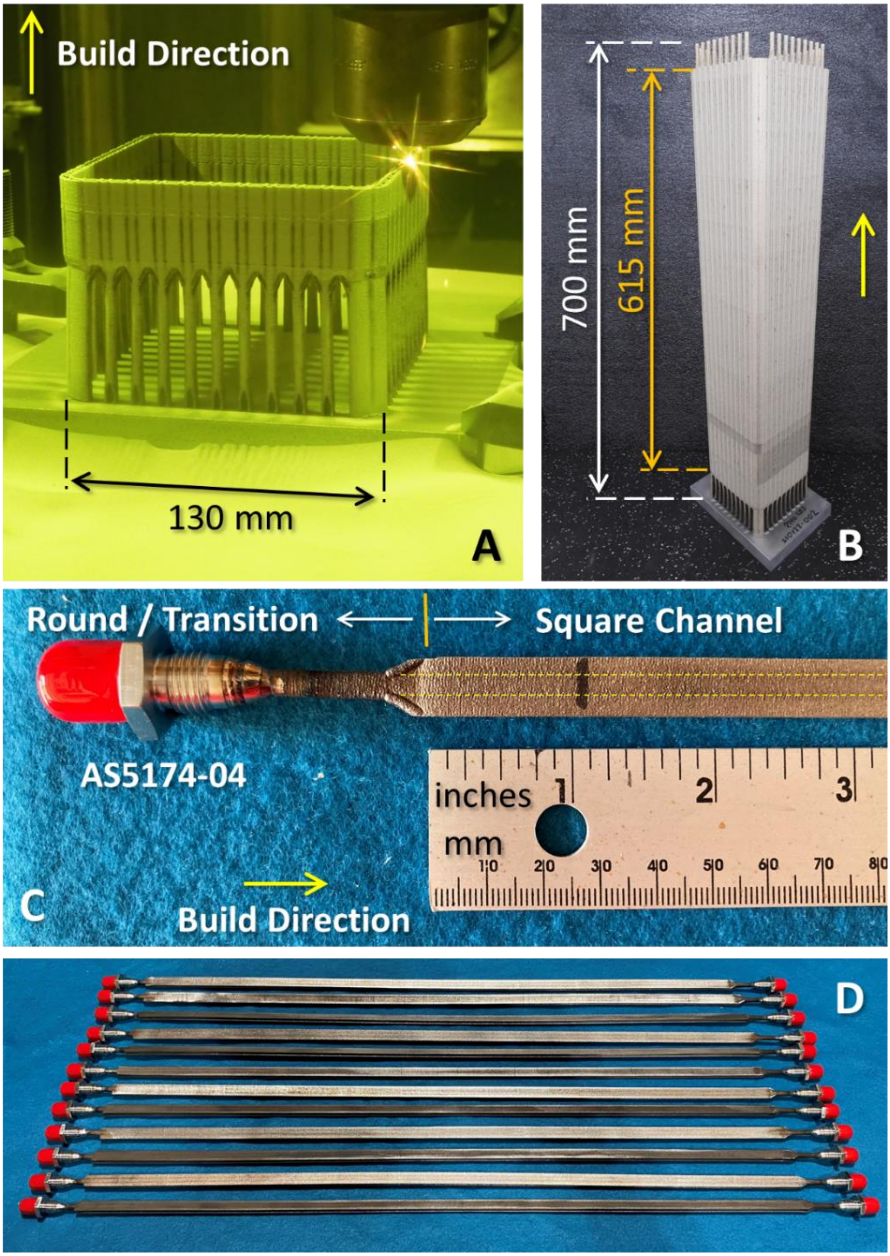

Figure 7.1. Channel sample fabrication. A) LP-DED build of boxes with multiple channels, B) Completed boxes following deposition, C) Laser-welded fittings; the square channel width is indicated by yellow dotted lines, D) Channel sets with welded inlet and outlet fittings.

The internal surfaces of the channels underwent surface enhancements identical to those described in Section 6.3.2, except for the PECM and TEM processes, which were not applied. Following the polishing of the internal perimeter, a 0.75 mm diameter hole was drilled at six locations for the pressure transducer port tubes (sequentially tagged as PT03 through PT08), and a 3.175 mm diameter tube was laser welded, as depicted in Figure 7.2. PT01 and PT02 were used for the measurement of the tank pressure prior to the test article. The distances between the tubes are shown in Figure 7.2C. It should be noted that the distance between PT6 and PT7 for some tubes was reduced to ~76 mm (increasing the distance of PT5-PT6 to ~178 mm) due to a mismeasurement during drilling. Further details of the inlet and outlet ports are also shown in Figure 7.2A and B.

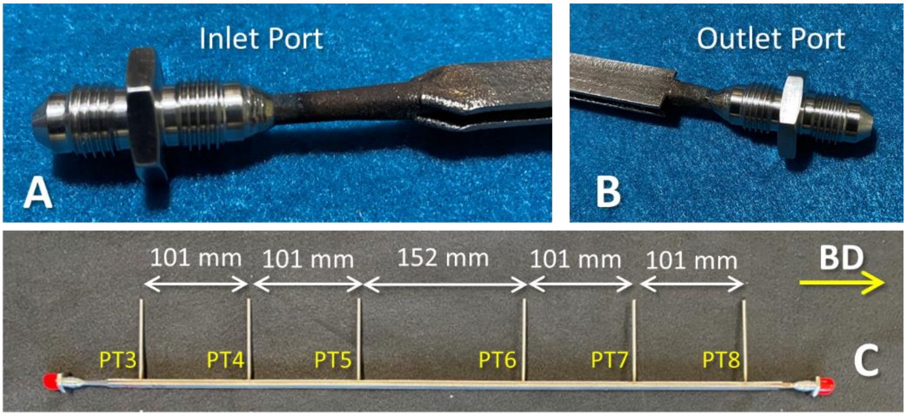

Figure 7.2. Channel fabrication of inlet/outlet ports and instrumentation. A) Inlet port welding, B) Outlet port welding, C) Welding of the instrumentation tubes for pressure transducers. Build direction denoted as BD.

In addition to the baseline as-built samples and those whose surfaces were enhanced, additional as-built samples were fabricated with a round channel and a larger area of the square channel. The intended use of the round channels was to provide an appropriate hydraulic diameter conversion from the round to square channels. The channels with larger area were conceived to investigate the comparison between channels with surfaces in the as--built condition and channels with modified surfaces but with an equivalent cross--sectional area. The round (tube) channels were designed with a diameter of 2.87 mm to match the cross-sectional area of the square channels. As discussed in section 7.4.4, it was later discovered that the tubes shrank more than anticipated, and the actual diameter was ~2.7 mm instead of 2.87 mm. The larger square channels were designed to be 2.95 mm in height and width.

7.3.2 Surface Enhancements of 600 mm Length Channels

The objective of the surface enhancements of the internal surfaces was similar to that driving the tests addressed in Chapter 6 [296]. The objective was therefore to obtain a range of surface conditions (i.e., variations) of the internal channels for each of the utilized surface enhancement processes. The same processing parameters as those discussed in 6.3.2 were used to achieve the desired surface modifications. The only difference was that the AFM, CM, and CMP processes could be performed bidirectionally since ports were located on each end. The configuration of the channels is shown in Table 7.2 and the corresponding channel identifiers in Table 7.3. The samples processed with the surface enhancements (AFM, CM, CMP) were all built with coarse powder (45-105 µm).

Table 7.2. Characteristics and nomenclature of the tested channels.

Channel Identifier	**Surface Enhancement Process**	**Notes**	**Target Channel Geometry (mm)**
AB-xx	None	As-built surface; Coarse 45-105 µm powder	2.54 x 2.54 (width/height)
AFM-xx	Abrasive Flow Machining	Slurry extrusion pressure of 69 bar; flow rate ranging from 0.56 L/min to 4.47 L/min	2.54 x 2.54 (width/height)
CM-xx	Chemical Milling	Hydrofluoric acid; temperature 52 to 60°C; and exposure from 4 to 19 mins	2.54 x 2.54 (width/height)
CMP-xx	Chemical Mechanical Polishing	Flow rate 0.4 to 2 L/min; temperature 50 to 60°C; exposure from 10 to 20 mins; up to 10% microabrasives	2.54 x 2.54 (width/height)
AB-53	None	As-built surface; Fine 15-45 µm powder	2.54 x 2.54 (width/height)
AB-54-L	None	As-built surface; **15-45 µm powder**	2.95 x 2.95 (width/height)
AB-55-R	None	As-built surface; **15-45 µm powder**	2.95 mm diameter
AB-56-R	None	As-built surface, **45-105 µm powder**	2.95 mm diameter
AB-58-R	None	As-built surface, **45-105 µm powder**	2.95 mm diameter

Table 7.3. Identifiers of the 600 mm channel samples.

As-built Square	AFM	CM	CMP	As-built Round
AB-51	AFM-A1	CM-A2	CMP-A2	AB-55-R
AB-53	AFM-A2	CM-A4	CMP-A3	AB-56-R
AB-57	AFM-A3	CM-A6	CMP-A4	AB-58-R
AB-A2	AFM-A4	CM-B1	CMP-A5	
AB-A3	AFM-A6	CM-B2	CMP-A6	
AB-A4	AFM-B1	CM-B3	CMP-A7	
AB-B1	AFM-B2	CM-B4	CMP-A8	
AB-54L	AFM-B3	CM-B5	CMP-B1	
	AFM-B4	CM-B6	CMP-B3	
	AFM-B5		CMP-B4	
	AFM-B6		CMP-B5	
			CMP-B6	
			CMP-B7	
			CMP-B8	

7.3.3 Test Configuration and Procedures

The facility available at NASA Marshall Space Flight Center (MSFC) and reported in Chapter 6 was used for the experimental campaign aimed at obtaining friction factors. The schematic of the test setup is shown in Figure 7.3. The 379-liter GN_2 pressurized tank was filled with deionized (DI) water and a 10 µm filter was incorporated downstream of the tank after the main valve. A Potter Aero RAA-1/2-301-1/2-5440A flowmeter (3.4 to 36 l/min) was installed in a bypass leg of the system in addition to a 1.016 mm diameter cavitating venturi (Cd = 0.980) to control the mass flow through the channel test articles. The venturi cross-sectional area was sized to be smaller than the smallest cross-section area of the test article. Pressure transducers and thermocouples were installed at locations indicated on the diagram of Figure 7.3. The test article was installed in a blast containment due to the operating pressures.

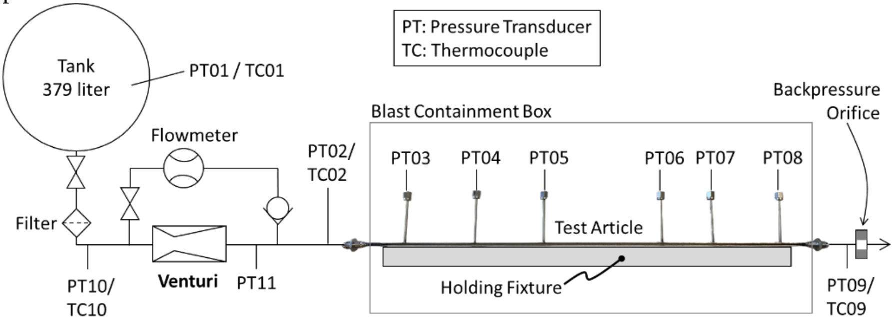

Figure 7.3. Schematic of the experimental setup realized to test 600 mm length channels.

The test articles were bolted into a fixture within a groove to hold the channel sample as shown in Figure 7.4. This is due to the concern that the pressurization of the water would cause some distortion of the rather long test articles. In addition, some bowing of the channels was observed following fabrication. Images of the test facility and the fixture installed in a safeguard blast chamber are shown in Figure 7.5. Each channel test article was flushed with deionized (DI) water at 7 bar for a minimum of 10 seconds prior to data collection. The tank was then pressurized at increments of 34, 69, 138 Bar and held for 10 seconds at each pressure with water flowing through both the flow meter and a cavitating venturi (1.106 mm dia. throat). The cavitation of the venturi was verified based on the exit to inlet pressure ratio (<0.80) for each test run. A second set of data was collected at identical tank pressures bypassing the venturi allowing for the flow rate to be maximized for each channel. The pressures for the experiments were selected based on the maximum allowable tank pressure and on the criterion that they should be similar to typical heat exchanger operating pressures. A Dewetron data acquisition system was used in conjunction with the LabVIEW software for system control. Six sets of data were collected per channel sample.

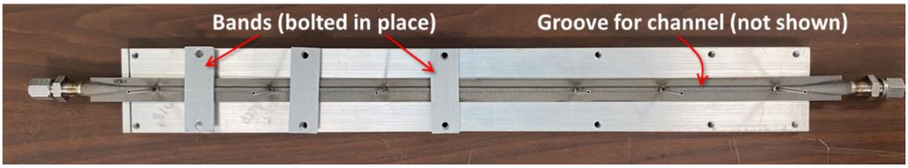

Figure 7.4. Holding fixture for channels with a groove (not shown) and bands to secure the test article.

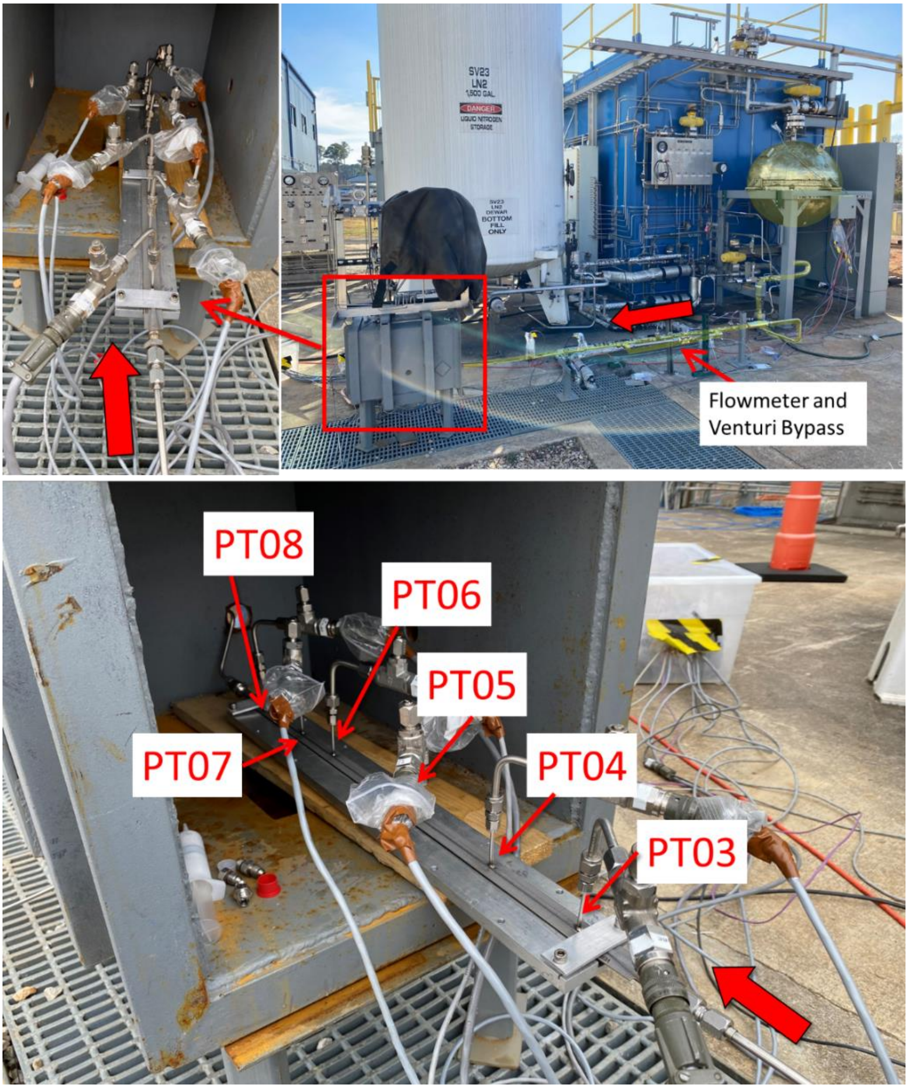

Figure 7.5. Test facility with channel sample and holding fixture installed in blast chamber.

Information about the instruments whose locations are shown in Figure 7.3 is detailed in Table 7.4. The pressure transducer (PT), thermocouples (TC), flowmeter, and cavitating venturi were all calibrated prior to testing. Instrumentation checks were completed every day of testing.

Table 7.4. Instrumentation log for the testing of 600 mm length channels.

Instrument ID	Type and Description	Accuracy
PT1	Wika Tecsis 99-6776-0004 (0-138 bar)	±0.05% full range
PT2	Delta Metric XPMF04-2KS (0-138 bar)	±0.06% full range
PT3 – PT11	Wika Tecsis 99-6776-0002 (0-138 bar)	±0.05% full range
TC01-TC10	Omega E type (-200 to 900°C)	±1.7°C
Flowmeter	Potter Aero RAA-1/2-301-1/2-5440A (3.4 to 36 l/min)	±0.1% full range

After testing was completed, all recorded data were tabulated for each of tested channel and each tank pressure set point. Figure 7.6 shows an example of the recording of the data related to channel AB-B1. At each pressure set point, the pressure was kept constant, and data acquired for approximately 10 seconds. The time periods determining the data to be averaged are highlighted in Figure 7.6 as colored vertical bands. The finite pressure differential is obtained by subtracting values of absolute pressures at the selected ports. Mass flow was measured using the flow meter.

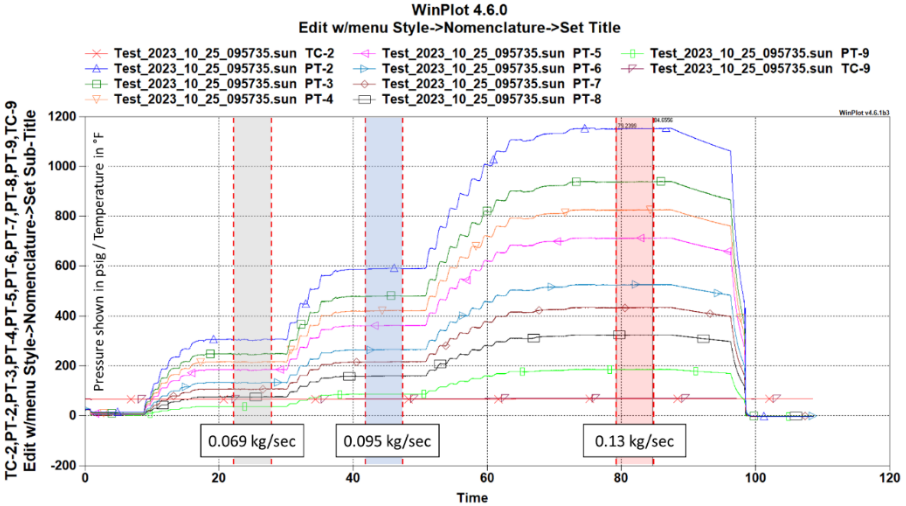

Figure 7.6. Example of raw data set for channel AB-B1 with cavitating venturi [runs AB-B1-4 (gray), AB-B1-5 (blue), AB-B1-6 (red)].

The necessary fluid properties were obtained for each data set and run. The density of water (g/cc) was calculated with a reference model [297] using the average temperature at the inlet and outlet of the channel and the average channel pressure to identify the thermodynamic state. The dynamic viscosity (Pa-s) at the same thermodynamic state was obtained as

$$\mu = \mathrm{v}\rho \tag{7.1}$$

where v is the kinematic viscosity (m^2/sec) and ρ is the fluid density.

The mass flow rate is defined as

$$\dot{m} = \rho A v, \tag{7.2}$$

where ρ is the fluid density, A is the area, and v is the linear velocity. The fluid velocity can therefore be obtained as

$$v = \frac{\dot{m}}{\rho A}, \tag{7.3}$$

with measured values for $\dot{m}$ and A.

7.3.4 Post-test Channel Measurements

7.3.4.1 Port Distance Measurements

After the testing was complete, the channels were visually inspected and measured to obtain the as-produced geometry. The distance between each of the ports was measured using two different sets of digital calipers while the channels were rigidly clamped to prevent any bowing. The port distances measuring less than 152 mm were measured using Mitutoyo 500-160-30 (±0.02 mm) vernier calipers. For distances greater than this value, a Mitutoyo 500-506-10 (±0.05 mm) caliper with higher range was used. The procedure to obtain the center of the tube port was to measure between each port on the outside of the instrumentation tubes and subtract the value of the diameter of the tube. Figure 7.7 shows photographs to clarify how these measurements were performed. All the resulting measurements are tabulated in Table 7.5. The nomenclature of full, mid, and short distances was representative of the distances between pressure transducers PT3-PT8, PT4-PT8, and PT5-PT6, respectively. The maximum error determined between these measurements was determined to be 0.043% for the full length and 0.1% for the mid length.

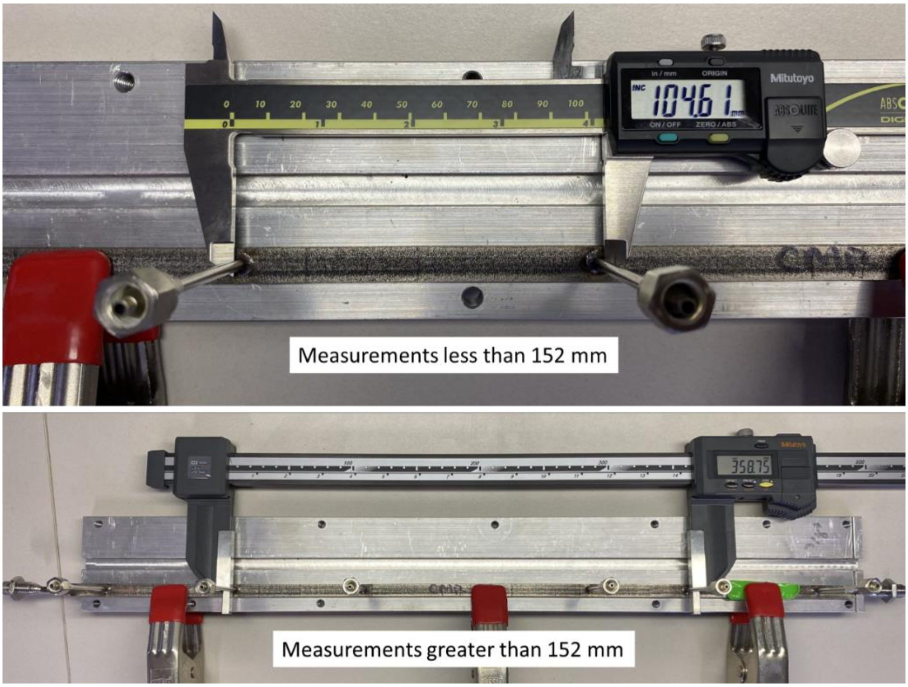

Figure 7.7. Caliper measurements to determine exact distance between ports for analysis.

7.3.4.2 Sectioning of the Channels

Following visual inspections and port distance measurements, the channel samples were sectioned to determine their cross-sectional area, perimeter, surface, and microstructure details of the surface. Three sections, perpendicular to the flow, were taken (Figure 7.8): the first at the midpoint between PT3 and PT4, the second offset from the center between PT5 and PT6, and the third at the midpoint between PT7 and PT8. These sections, selected along the length of the channel, allow to evaluate any axial length variations resulting from surface enhancement processing. The samples were tagged according to the channel number, with -1, -2, and -3 suffixes for traceability during microscopic imaging. Due to the time required for preparation and measurement, a single section normal to the bottom surface and parallel to the flow was taken at the axial midpoint of the channel for SEM imaging and surface texture measurements.

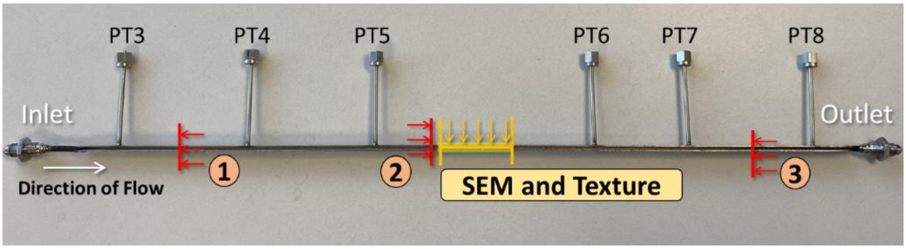

Figure 7.8. Location of the sectioning of the 600 mm length channels. The direction of the flow is the same as the direction of the build.

7.3.4.3 Optical Images, SEM, and Surface Texture Characterization

The samples from the sections (-1, -2, and -3) were mounted, polished, and etched using identical procedures as those described in Section 6.3.4.1. All optical images were obtained using a Keyence VHX digital microscope. The images were processed using the software *Image J* (Version 1.53e) [268]. The values obtained for the area and the perimeter were averaged for the subsequent analysis and to obtain their standard deviation. Additional measurements were taken on the round channels to determine the diameter (Appendix Figure 12.4). The diameter of the round tubes was measured in 10 circumferential locations and averaged.

The surface texture was obtained using a non-contact Keyence VR-5200 pattern light projection profilometer. An 80x magnification was selected and an overlap of 20%. The scanned internal area of interest was approximately 38 mm long and 1.6 mm wide and reported according to ISO 25178-2:2021. The procedures were identical to those described in section 6.3.4.3. An end-correction factor was applied in addition to a form correction to remove any tilt and curvature. The unfiltered primary surface texture (denoted as *primary [P]*) of the samples was evaluated in addition to the filtered roughness (denoted as *[R]*) and waviness using a λc spatial frequency cut-off filter of 0.8 mm per ISO 21920-3 guidelines. Directional profile, roughness, and waviness parameters (*i.e.*, P*x*, R*x*, and W*x*, respectively) were also extracted from the data using a line along the center of the sample, equidistant from the edges. This directional roughness and waviness are in the direction of the flow, which also corresponds to the direction of the build. Several surface texture parameters are evaluated to characterize the samples including Sa, Sq, Sz, Sk, Spk, Spd, Pa, Ra, Rk, Wa, WP, and WPc. These are defined and discussed in detail in Sections 4.3.4 and 6.3.4.3.

Additional surface texture characterization was obtained on selected samples using a Keyence VKX-1100 laser scanning confocal microscope. The field of view for this microscope was much smaller and required more scanning time and an overlap of 5% was used in the X-direction. The scan area was approximately 1.45 mm width by 1.9 mm in length. These samples were scanned with a 20x magnification lens with a height repeatability of 50 nm and width repeatability of 120 nm in laser confocal mode. The same texture parameters were extracted using identical filtering. The main purpose of measuring these data was to obtain some surface contour maps to provide visual comparisons to supplement the SEM and optical images.

7.4 RESULTS AND DISCUSSION

7.4.1 Channel Geometry Characterization

The physical appearance and measurements resulting from the surface enhancements and as-built channels were similar to those of the channel samples presented in Chapter 6 [296]. The SEM images revealed identical artifacts from the processing of the channels as those shown in section 6.4.1.2. The SEM images of all the square channels are compiled in Figure 7.9. The as-built (AB) samples indicate that adhered particles are randomly distributed on all the samples. The difference between samples fabricated with fine powder (AB-53 and AB-54-L) and the other AB samples fabricated with coarse powder is clearly visible. The fine powder covers nearly the entire surface of the sample, while the coarse powder particles cover about 30% of the channel surface and are randomly distributed.

The SEM images for the AFM samples indicate that a high number of particles can be identified also after processing. Several of the samples such as AFM-A1, AFM-A2, AFM-B1, AFM-B2 appear to be unchanged from the AB baseline samples. In the other AFM samples, many powder particles are still present, but the peaks of the particles were removed. The remaining powder particles are still present on the material or smeared. On a limited number of AFM samples such as AFM-A4, AFM-A6, AFM-B4, AFM-B5, material is observed to be removed from the central portion or biased towards an edge. Powder particles are still present along the edges or on the side. This indicates that the process may not be completely uniform and was not as effective on the longer samples compared to the AFM samples reported in Section 6.4.1.

The CM samples, shown in Figure 7.9, indicate that most of the powder particles were removed. Some random particles are still present and there are indications of etching of the grains. Some indications of periodic waviness or texture can be observed, particularly on the CM-A6, CM-B5, and CM-B6 samples. Crystals can also be observed on several samples, similarly to what was observed for the short samples discussed in Chapter 6. CMP was effective at removing almost all particles. There is some evidence of macro texturing and significant etching of the grain boundaries for CMP and CM samples.

Figure 7.10 displays the polished cross-sectional micrographs obtained from the #2 mid-span samples (between PT05 and PT06). These are zoomed in to show the inner wall and resulting surface from the enhancement processes. Figure 7.11 shows the chemically etched samples. The images reveal the entire wall thickness and grain structure. The images of the cross-sections of the surfaces, each treated with a different enhancement method, show similar trends as those belonging to the short samples whose investigation reported in Chapter 6. The images of the AB samples indicate high texturing around the perimeter. The coarse particles are apparent.

Texturizing can be noticed on the images of the samples built with fine powder (AB-53 and AB-54-L), but greatly reduced and similar to one that is also notable on the surfaces of the channel samples treated Section 5.5. Samples AB-53, AB-57, AB-54-L were built without any adjacent channels, and support ribs along the midspan, observed in Figure 7.11. This caused the samples to feature slightly round corners compared to the corners of the other AB channels. Images show that most of the AFM-processed samples exhibit some partially adhered powder. The images of CM-processed samples indicate rounding of the corners and material removal from the entire inner perimeter. The cross-sectional area of the CM-processed samples is noticeably larger. Sample CM-B2 is the only one for which some loose powder is visible, and it may be a result of the sample preparation and mounting; the powder did not appear to be attached.

Figure 7.11 illustrates that the CMP-processed samples now have smaller radii compared to their previously more squared corners. The walls appear to be visually smooth. The image of sample CMP-A4 shows a potential powder particle in the upper left corner but it is not attached and likely related to polishing.

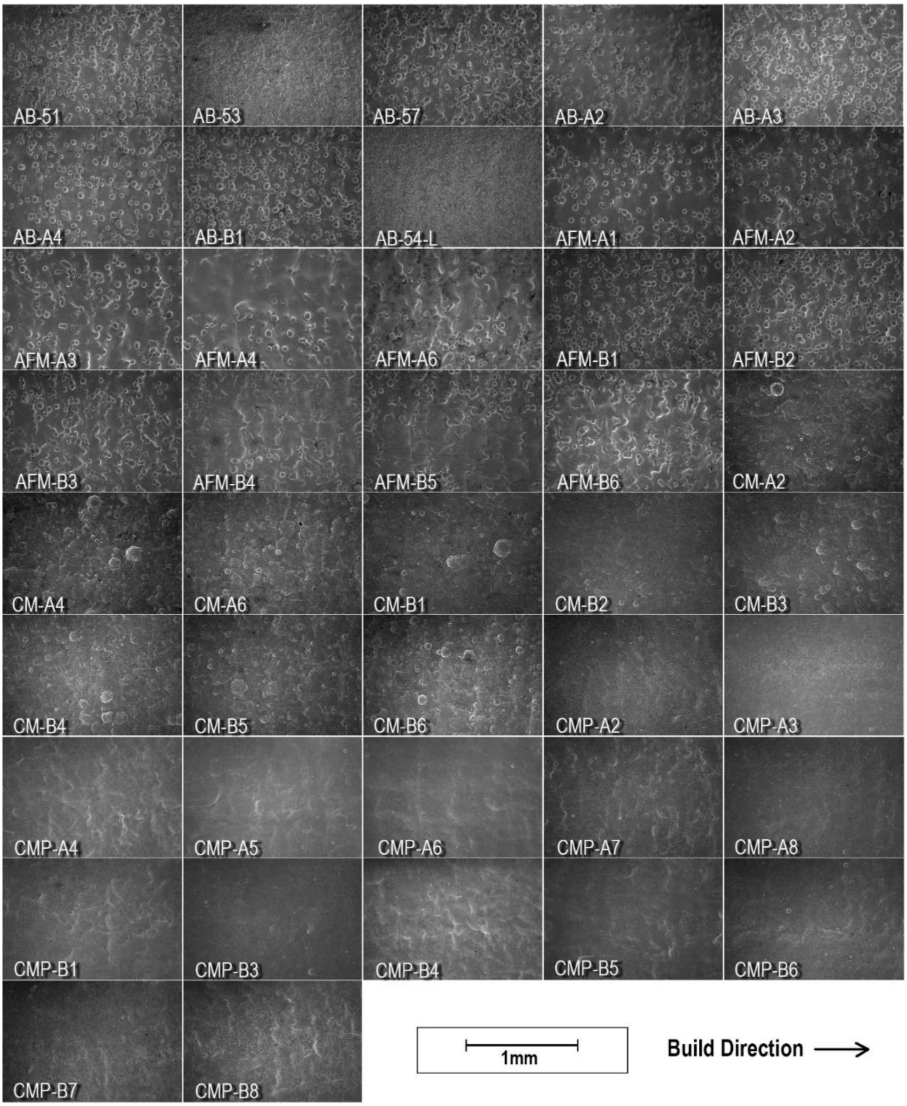

Figure 7.9. SEM images of the inner surfaces of the 600 mm length square channel samples.

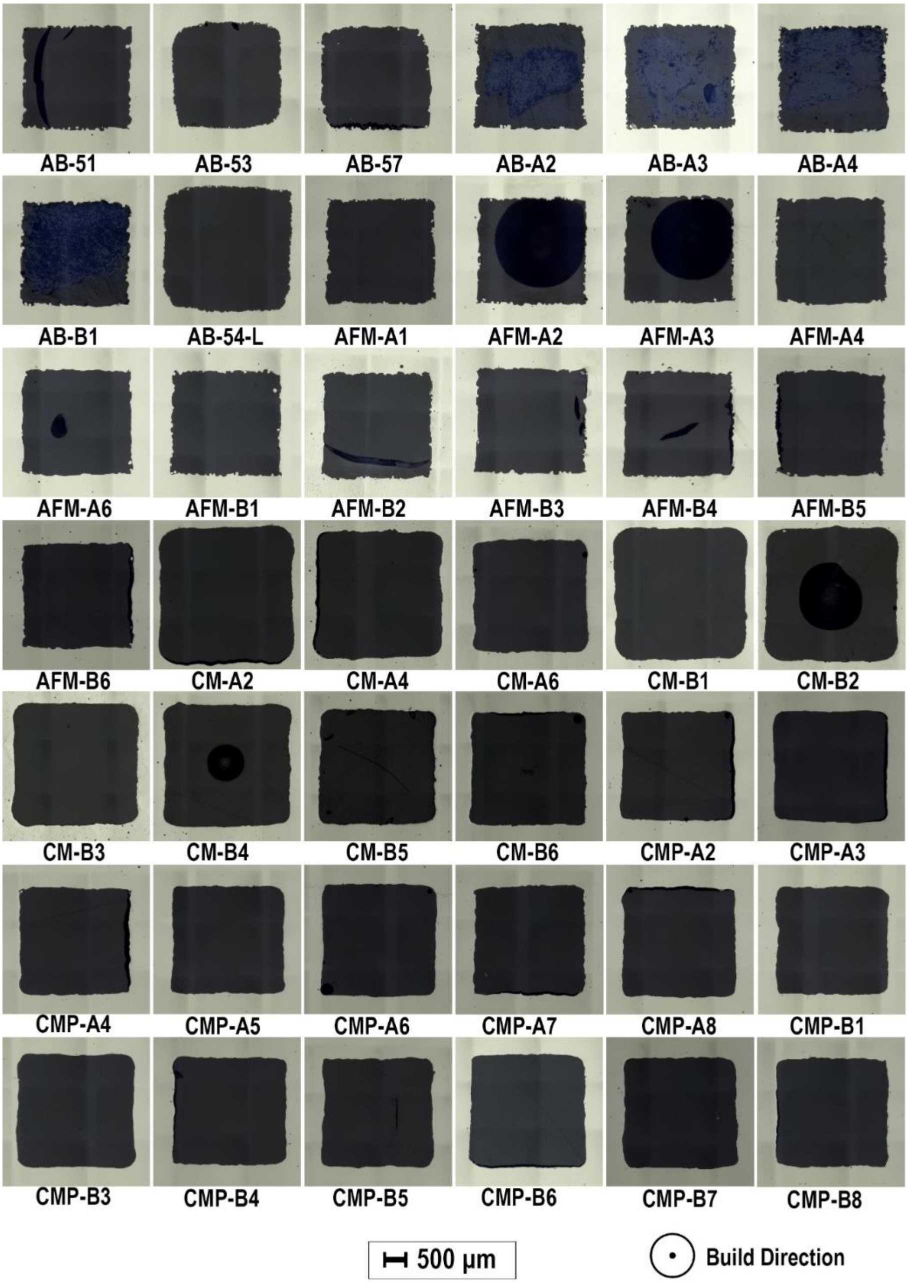

Figure 7.10. Micrographs of the cross-sections of the square 600 mm channels. The cross-section is the one indicated as #2 in Figure 7.8.

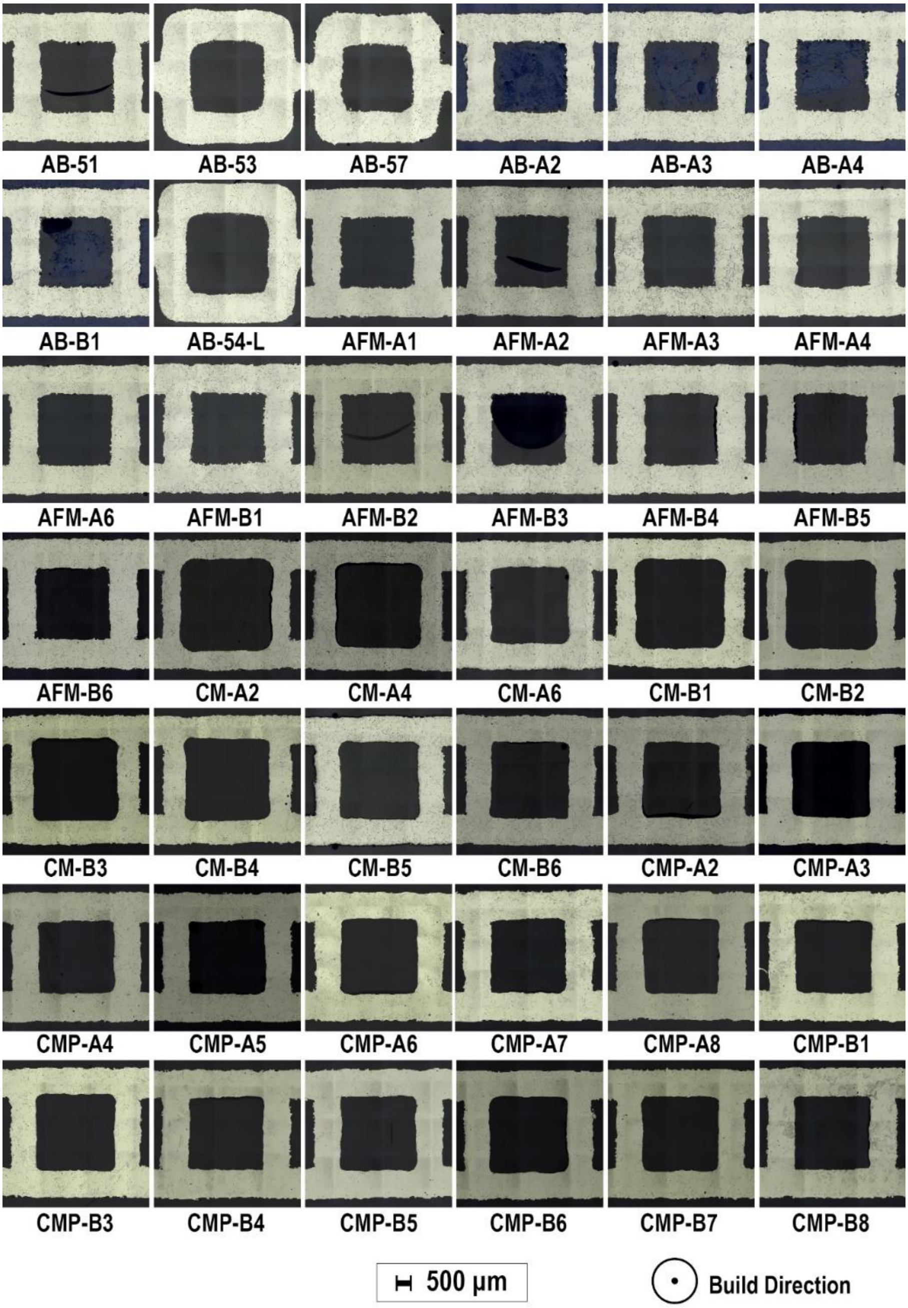

Figure 7.11. Micrographs of the etched square channel cross-sections. These images were obtained to reveal the grain structure.

The information resulting from the analysis of the channel micrographs and from the geometric measurements is tabulated in Table 7.5. The data include the area and perimeter measured from the three cross-sections of each channel sample and averaged. The full perimeter was measured for each sample, and it includes all adhered powder and variations from the deposition process. The standard deviation is also provided. The difference between the measured values of the area and perimeter and the nominal (as-designed) values is also presented, together with the distances between the full and mid pressure ports with their standard deviation determined from the measurements taken different calipers. The standard deviation of the measurements features a maximum coefficient of variation of 0.043% for the full-length measurements and 0.1% for the mid distance measurements.

Table 7.5. Summary of the geometric data of channels obtained with caliper and cross-sectional measurements.

Channel ID	**Area, Avg**	**Perimeter, Avg**	**Area, Diff. from design**	**Perimeter, Diff. from design**	**Full Dist. PT3-PT8**	**Mid Dist. PT4-PT7**
	mm^2	**mm**	**%**	**%**	**mm**	**mm**
AB-51	6.20 ±0.064	12.81 ±0.156	-3.9%	26.1%	561.87 ±0.013	358.52 ±0.127
AB-53	6.17 ±0.078	13.02 ±0.212	-4.3%	28.1%	562.08 ±0.178	358.99 ±0.216
AB-57	5.92 ±0.073	12.08 ±0.164	-8.2%	18.9%	561.67 ±0.081	358.60 ±0.005
AB-A2	6.31 ±0.087	12.80 ±0.541	-2.2%	26.0%	561.71 ±0.191	358.64 ±0.051
AB-A3	6.31 ±0.025	13.04 ±0.267	-2.2%	28.4%	561.98 ±0.063	358.80 ±0.025
AB-A4	6.28 ±0.021	13.27 ±0.418	-2.6%	30.6%	562.05 ±0.013	358.71 ±0.051
AB-B1	6.25 ±0.093	13.27 ±0.443	-3.2%	30.6%	561.75 ±0.178	358.65 ±0.051
AB-54-L	8.37 ±0.186	14.38 ±1.021	-3.6%	22.0%	561.47 ±0.089	358.71 ±0.025
AB-55-R	6.05 ±0.125	11.73 ±0.364	-11.2%	26.7%	562.09 ±0.038	359.02 ±0.165
AB-56-R	5.62 ±0.035	11.85 ±0.509	-17.6%	28.0%	561.76 ±0.038	358.58 ±0.089
AB-58-R	5.50 ±0.100	10.85 ±0.230	-19.3%	17.2%	561.75 ±0.114	358.85 ±0.241
AFM-A1	6.34 ±0.064	12.44 ±0.325	-1.8%	22.4%	561.80 ±0.317	358.83 ±0.432
AFM-A2	6.40 ±0.013	12.42 ±0.226	-0.9%	22.2%	561.57 ±0.102	358.44 ±0.064
AFM-A3	6.42 ±0.032	12.17 ±0.071	-0.5%	19.8%	562.15 ±0.267	359.11 ±0.330
AFM-A4	6.33 ±0.091	12.00 ±0.739	-1.9%	18.1%	561.72 ±0.089	358.78 ±0.013
AFM-A6	6.40 ±0.088	11.65 ±0.254	-0.9%	14.7%	561.90 ±0.076	358.84 ±0.089
AFM-B1	6.34 ±0.028	13.28 ±0.290	-1.7%	30.7%	562.10 ±0.178	358.99 ±0.267
AFM-B2	6.37 ±0.027	12.50 ±0.574	-1.3%	23.1%	561.78 ±0.114	358.62 ±0.140
AFM-B3	6.44 ±0.053	12.17 ±0.615	-0.1%	19.8%	561.91 ±0.000	359.12 ±0.051
AFM-B4	6.40 ±0.023	11.81 ±0.252	-0.8%	16.2%	562.08 ±0.229	359.24 ±0.216
AFM-B5	6.39 ±0.141	11.92 ±0.192	-1.0%	17.4%	562.18 ±0.038	358.95 ±0.178
AFM-B6	6.45 ±0.014	11.39 ±0.494	-0.1%	12.1%	561.85 ±0.178	358.83 ±0.102
CM-A2	10.25 ±0.05	13.82 ±0.455	58.9%	36.0%	562.00 ±0.025	358.86 ±0.013
CM-A4	8.81 ±0.179	12.38 ±0.282	36.5%	21.9%	561.92 ±0.127	358.58 ±0.051
CM-A6	7.16 ±0.095	11.41 ±0.185	11.0%	12.3%	561.80 ±0.152	358.64 ±0.013
CM-B1	9.75 ±0.111	12.88 ±0.093	51.1%	26.8%	561.84 ±0.127	358.75 ±0.076
CM-B2	9.81 ±0.052	13.02 ±0.136	52.0%	28.2%	561.67 ±0.025	358.64 ±0.013
CM-B3	8.51 ±0.052	12.26 ±0.108	31.9%	20.7%	561.67 ±0.140	359.23 ±0.114
CM-B4	8.51 ±0.052	12.34 ±0.204	31.8%	21.5%	562.19 ±0.406	359.52 ±0.483
CM-B5	7.35 ±0.010	11.41 ±0.058	13.9%	12.3%	561.85 ±0.127	359.00 ±0.051
CM-B6	7.37 ±0.100	11.54 ±0.113	14.2%	13.5%	562.06 ±0.254	359.16 ±0.203
CMP-A2	7.07 ±0.178	11.23 ±0.175	9.5%	10.5%	561.70 ±0.127	358.80 ±0.241

CMP-A3	7.06 ±0.026	10.92 ±0.142	9.5%	7.5%	561.59 ±0.025	358.53 ±0.064
CMP-A4	6.57 ±0.041	10.85 ±0.104	1.8%	6.8%	561.98 ±0.013	358.58 ±0.178
CMP-A5	6.77 ±0.090	10.91 ±0.076	4.9%	7.4%	561.92 ±0.254	358.75 ±0.191
CMP-A6	7.07 ±0.062	11.01 ±0.109	9.5%	8.3%	561.92 ±0.076	358.90 ±0.191
CMP-A7	6.55 ±0.145	11.00 ±0.074	1.5%	8.3%	561.59 ±0.140	358.52 ±0.089
CMP-A8	6.87 ±0.028	10.78 ±0.057	6.4%	6.1%	561.56 ±0.114	358.74 ±0.127
CMP-B1	6.74 ±0.039	10.85 ±0.160	4.4%	6.8%	561.70 ±0.267	358.69 ±0.152
CMP-B3	7.40 ±0.085	11.30 ±0.029	14.7%	11.2%	561.98 ±0.305	358.74 ±0.076
CMP-B4	6.77 ±0.064	10.87 ±0.168	4.9%	7.0%	561.92 ±0.038	358.65 ±0.102
CMP-B5	6.82 ±0.105	10.94 ±0.101	5.7%	7.7%	561.70 ±0.127	358.57 ±0.051
CMP-B6	7.28 ±0.020	11.36 ±0.244	12.8%	11.8%	561.89 ±0.406	358.65 ±0.216
CMP-B7	6.95 ±0.089	10.87 ±0.033	7.8%	7.0%	561.58 ±0.089	358.60 ±0.038
CMP-B8	6.74 ±0.063	10.91 ±0.060	4.5%	7.4%	561.66 ±0.076	358.57 ±0.038

The data of Table 7.5 are plotted in Figure 7.12 to elucidate their dependency on the channel type and surface processing methods. The values of the cross-sectional areas of the as-built channels are consistently smaller than the nominal design values due to powder adherence and shrinkage during processing (Figure 7.12A). This was expected and it was observed also for the similar data discussed in Chapters 5 and 6. The value of cross-sectional area of the AFM-processed channels are similar and close to the nominal design values. Despite the slurry flow rate and pressure were varied, there appears to be a limit to the amount of material that can be removed. Increasing the flow rate and pressure of processes that are abrasive may be necessary to enlarge the channel area. CM-processed channels cause significantly larger values of the cross-sectional area compared to the as-built value and the nominal design value, as previously observed. The CMP samples indicate consistent areas and perimeters despite processing parameter variations.

Figure 7.12C reports the values of measured perimeters depending on the post-processing treatment. As expected, the perimeter value of as-built samples is higher than the design value (which is an ideal value formed by perfectly straight segments), which is 10.16 mm for most samples. The AB-54-L sample was designed with a nominal perimeter of 11.79 mm. The perimeter value of as-built round samples (9.017 mm) similarly deviate from the nominal design values. AFM samples feature a higher perimeter value, similar to the value of as-built samples, due to the presence of residual powder particles. The larger value of the area of CM samples results from the higher amount of removed material, which effectively eliminates adhered powder and even some of the underlying surface. CMP processing effectively removes particles while keeping to a minimum material removal, allowing for more precisely controlling the value of the area and perimeter. The data sets of Figure 7.12C indicate that the CMP process can effectively reduce and planarize the perimeter with minimal area increase.

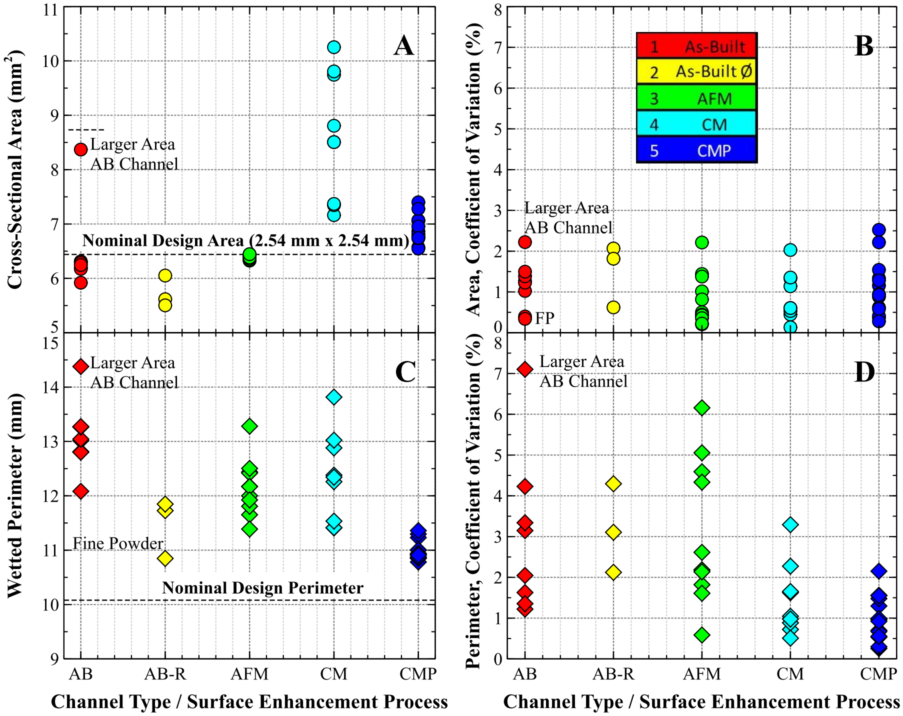

Figure 7.12. Measurements characterizing the inner surface of channels. A) Cross-sectional area, B) Area Coefficient of Variation, C) Perimeter, D) Perimeter Coefficient of Variation. [FP = Fine Powder].

Figure 7.12B shows values of the coefficient of variation (CV) for the area of each channel type, while Figure 7.12D displays the value of CV for the perimeter. The CV, calculated as the standard deviation divided by the mean, indicates the variance between cross-sections along the length of the channel. The areas and perimeters are based on the average of three cross-sections, with the means presented in Figure 7.12A and Figure 7.12C, respectively. This CV is a merit parameter measuring the capability of surface enhancement processes in producing consistent uniform area and perimeter along the channel length. A high CV suggests significant variation.

Regardless of the surface enhancement process, the value of CV for the area along the channel lengths remains within 2.5%. This variation accounts for both the effects of surface processing and measurement error, indicating consistent processing conditions. The area of the AFM samples vary by 2.2% along their length, despite having nearly identical absolute cross-sectional areas.

The perimeter CV range is higher than the cross-sectional area CV range, as shown in Figure 7.12D. No clear trends link perimeter CV to area CV; variations appear as random error (Refer to Appendix Figure 12.1). As-built samples with randomly adhered powder show consistent area and perimeter variation along the length, in line with the results from section 6.5. AFM processed samples exhibit the highest CV due to processing inconsistencies, with some powder remaining adhered to the walls while other areas are cleared, leading to a higher perimeter variation (5.6%). CM samples demonstrate consistent perimeter measurements along the channel length, with a CV within 3.3%. The CMP process shows excellent consistency, maintaining perimeter variations within 2.2% along the channel length.

7.4.2 Surface Texture Characterization

All samples were scanned to obtain quantitative information on the surface texture at the mid-point of the channels as indicated in Figure 7.8. The scans provided the amplitude of the primary and roughness areal texture, spatial, functional, hybrid, and material ratio parameters. Additionally, the 2D profile, roughness, and waviness parameters were obtained along the centerline of the channel. The primary [P] and roughness [R] filtering to obtain these parameters is discussed in Section 7.3.4.3 and 6.3.4.3. Table 7.6 lists a summary of the selected parameters.

The 95% confidence interval (C.I.) of the values was obtained by repeating four times the measurements characterizing a single as-built sample. Reporting values related to the as-built sample introduces bias in the confidence interval for parameters associated with single-point high peaks and due to the powder particles, such as Sp. The confidence interval characterizing samples with enhanced surface texture is likely much higher (>95%). Additionally, directional measurements (Wa, Ra, Pa) are affected by much larger deviation, as slight changes in line placement can result in significant variations of peak height or valley lengths. In contrast, areal measurements are affected by lower deviation since all texture artifacts of the measured area comprise the calculated value (i.e, Sa, Sq, Sp, etc). As noted, the Sp value is based on a single peak value across the entire surface therefore bound to be biased towards higher values and a higher standard deviation. This issue underscores the importance of using a merit parameter such as reduced peak height (Spk) and core roughness (Sk).

Table 7.6. Summary of the measured values of parameters identifying surface texture, roughness, and waviness. [P] is the *primary* texture and [R] denotes the *filtered roughness* texture.

Channel ID	**Sa [P]**	**Sq [P]**	**Sp [P]**	**Sv [P]**	**Sk [P]**	**Spk [P]**	**Sa [R]**	**Wp**	**Wa**	**Pa**	**Ra**	**Rk**
	µm	**µm**	**µm**	**µm**	**µm**	**µm**	**µm**	**µm**	**µm**	**µm**	**µm**	**µm**
95% C.I. (±)	0.12	0.12	33.9	1.98	0.54	0.39	0.09	2.16	0.73	1.09	0.42	1.57
AB-51	23.3	29.9	275.2	186.1	71.3	38.9	18.6	49.2	13.0	22.7	15.3	44.6
AB-53	17.4	21.9	119.2	122.2	55.8	20.6	12.5	30.5	8.9	16.2	11.3	36.7
AB-57	31.6	40.3	226.9	313.2	99.8	41.2	22.2	63.8	19.2	31.4	19.3	54.7
AB-A2	28.4	37.1	279.0	304.5	85.0	47.9	20.4	68.7	14.4	23.7	16.4	43.9
AB-A3	29.2	37.6	341.8	260.9	89.2	45.8	22.3	47.6	13.2	24.3	18.3	49.5
AB-A4	31.2	40.5	327.8	284.6	94.9	56.4	20.4	49.2	13.0	23.2	16.1	44.6
AB-B1	28.2	37.3	318.1	269.2	87.2	47.6	21.8	74.0	14.4	26.0	18.9	54.4
AB-54-L	18.1	22.9	128.8	145.5	57.9	22.5	12.7	32.3	9.4	17.5	11.8	39.1

AB-55-R	15.5	20.5	105.2	133.3	46.3	18.3	11.3	24.8	9.0	14.2	9.8	30.3
AB-56-R	28.2	36.8	171.1	244.0	83.7	40.2	22.1	61.6	16.5	28.1	18.4	53.0
AB-58-R	32.3	41.8	177.1	444.4	96.9	49.8	26.1	85.0	19.8	30.7	18.3	54.0
AFM-A1	29.0	36.8	196.0	360.3	90.9	43.4	20.1	33.4	11.5	22.6	15.4	44.0
AFM-A2	26.6	34.3	338.9	199.4	83.7	45.7	19.3	49.4	16.0	23.3	15.5	48.0
AFM-A3	25.8	34.2	303.3	239.9	80.3	47.1	19.5	41.5	12.2	22.6	15.6	48.1
AFM-A4	26.3	34.4	281.3	309.6	79.8	46.0	19.1	39.0	12.6	22.0	14.9	44.2
AFM-A6	27.6	36.9	284.4	279.3	73.2	58.8	14.1	33.4	11.5	17.0	9.7	29.3
AFM-B1	26.9	34.9	340.7	330.4	81.9	41.5	20.4	49.4	16.0	25.0	17.1	48.3
AFM-B2	25.3	32.8	283.1	236.9	76.6	38.3	20.4	41.5	12.2	22.2	16.0	46.4
AFM-B3	22.5	29.5	243.2	301.5	70.0	34.9	18.3	34.3	11.5	19.4	13.2	39.1
AFM-B4	20.9	27.5	292.4	259.0	63.8	33.4	16.5	34.6	10.3	17.5	11.7	35.2
AFM-B5	22.6	30.0	384.0	248.5	66.1	40.3	16.8	37.4	11.0	18.8	11.9	35.7
AFM-B6	21.4	28.3	333.1	262.2	62.7	39.7	16.1	32.4	10.2	17.0	11.7	34.2
CM-A2	12.4	16.0	262.5	222.1	39.0	14.0	6.7	21.1	8.2	10.0	4.2	12.1
CM-A4	13.5	18.2	140.6	280.0	39.9	13.0	8.8	26.2	9.1	12.7	6.0	16.9
CM-A6	15.1	19.4	110.5	232.1	47.4	19.0	11.6	29.7	8.7	14.0	9.0	28.4
CM-B1	14.3	18.5	104.9	220.5	43.5	12.4	7.0	22.9	11.2	12.1	4.9	13.8
CM-B2	12.2	15.7	89.4	174.8	37.2	12.9	6.3	20.5	7.8	9.1	4.4	13.2
CM-B3	11.3	15.2	165.9	199.4	33.9	12.3	7.6	22.8	7.8	10.2	5.7	15.6
CM-B4	12.6	16.5	84.4	202.8	37.6	12.9	7.4	22.3	8.6	10.5	5.4	15.8
CM-B5	13.1	17.4	290.4	186.9	40.5	19.3	8.9	31.9	8.3	12.2	7.3	23.1
CM-B6	13.7	17.7	169.9	229.3	42.7	14.0	9.1	25.1	8.1	13.0	7.2	22.3
CMP-A2	12.7	16.4	426.4	137.7	41.0	15.4	6.8	28.4	10.6	11.9	5.1	16.0
CMP-A3	11.8	15.0	155.5	130.9	35.8	19.7	5.3	27.2	8.3	9.9	3.6	11.1
CMP-A4	14.0	17.7	165.0	189.5	44.9	19.7	8.6	27.9	8.6	12.4	6.7	21.5
CMP-A5	13.0	17.0	146.0	348.8	41.0	16.8	10.3	29.2	9.1	11.7	5.7	17.4
CMP-A6	12.8	16.7	172.8	123.0	38.8	23.9	6.5	22.7	8.0	10.1	4.8	15.8
CMP-A7	18.6	23.3	89.0	189.2	59.6	24.1	10.6	40.3	12.9	16.5	8.3	25.6
CMP-A8	17.0	21.7	285.2	162.6	52.1	26.4	7.1	35.9	10.0	12.2	5.1	16.2
CMP-B1	16.4	20.7	135.1	168.6	52.1	19.8	9.4	36.9	12.3	15.2	6.8	22.1
CMP-B3	15.6	21.3	259.4	308.1	48.3	25.5	6.5	28.5	10.6	12.1	3.7	11.5
CMP-B4	15.6	20.0	151.7	148.6	48.8	23.5	9.9	39.2	11.0	15.5	7.5	24.1
CMP-B5	14.1	18.6	235.7	338.1	43.4	23.6	8.5	34.1	10.3	13.0	5.8	18.2
CMP-B6	15.3	19.4	112.1	101.3	48.8	24.1	6.5	44.0	11.6	13.2	4.6	14.4
CMP-B7	11.9	15.5	118.8	184.1	36.2	17.3	7.1	24.7	8.4	10.8	5.4	16.6
CMP-B8	15.7	22.0	279.7	221.0	48.6	31.3	10.2	38.6	10.0	14.4	7.3	20.8

Samples treated with each of the post-processing techniques were selected among all those available and were mapped on a VK-1100 microscope. Figure 7.13 displays the 3D height maps overlayed on the laser scanned and optical images. The scan windows measured ~1935 µm in the X direction and ~1450 µm in the Y-direction. The textures are consistent with those of the cross-section SEM images of the samples discussed in Chapter 6. The SEM images (Figure 7.9) do not adequately provide depth data due to the limited depth of field, therefore the overlay optical and laser scan images provide additional information (Figure 7.13). The images of the square and round as-built samples indicate a random distribution of adhered powder particles and appear visually similar. This suggests that images of these samples, being built with coarse powder, can be used as an appropriate reference to determine the effective diameter of the square and of the round channels.

The images of AFM samples show higher peaks along with a few powder particles on the surface. Some of the powder particles are reduced or smeared, as indicated by the elongated peaks along the flow direction (X). The images of CM samples display lower peak heights across the surface, but some pitting can be observed (cool colors). This pitting could be attack of the surface from the chemical or pull-out of powder particles from the surface. A jagged surface is apparent in the optical images and height mapping overlay. The images of the selected CMP sample also reveals reduced peak heights with some preferential direction for material removal. Increased surface height in the scanned window can be observed, and some material is selectively attached to the grain boundaries.

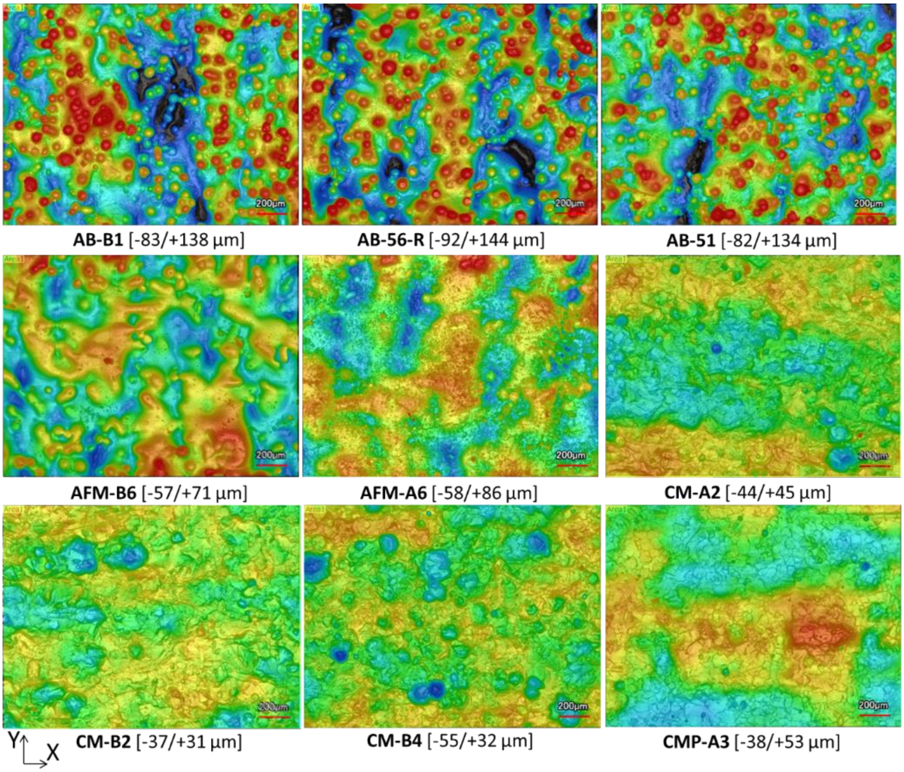

AB-B1 [-83/+138 μm] **AB-56-R** [-92/+144 μm] **AB-51** [-82/+134 μm]

AFM-B6 [-57/+71 μm] **AFM-A6** [-58/+86 μm] **CM-A2** [-44/+45 μm]

CM-B2 [-37/+31 μm] **CM-B4** [-55/+32 μm] **CMP-A3** [-38/+53 μm]

Figure 7.13. Surface texture maps overlayed on the optical+laser images. The warm colors represent peaks above the average surface level, while cool colors represent valleys below the average surface level. The scales are not shown since they are all different, but minimum and maximum heights are shown in the captions between square parentheses. Note: The direction of flow is from left to right. X also indicates the build direction.

Figure 7.14 presents a typical 3D contour image of the as-built surface obtained with the VK-100 microscope (sample AB-B1). The adhered particles and the waviness are clearly distinguishable. The build orientation is the X-direction, which also corresponds to the direction of the flow during testing. The measured maximum height of the surface from sample AB-B1 is 137.5 µm and the maximum valley is –83 µm for a range of 220.5 µm.

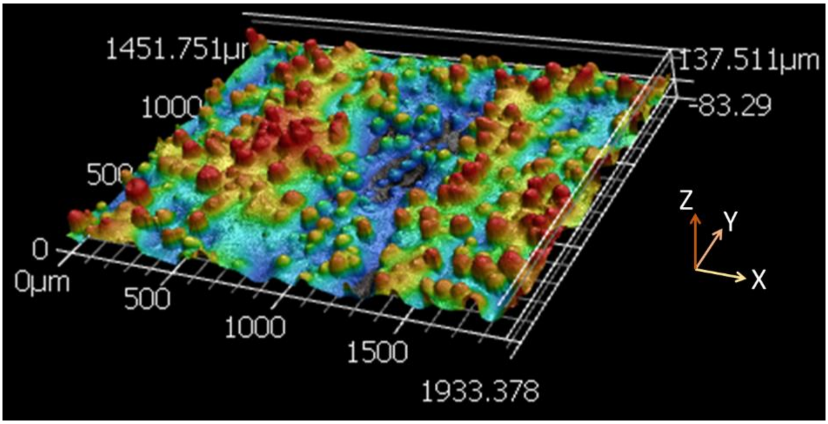

Figure 7.14. 3D Contour Plot of as-built sample AB-B1 on the Keyence VHX-1100 microscope. The indicated X-axis provides the build direction and the flow direction.

7.4.3 Discharge Coefficient

The discharge coefficient was calculated according to its definition, namely

$$Cd = \frac{\dot{m}}{\rho \dot{V}} = \frac{\dot{m}}{A\sqrt{2\rho \Delta P}} \qquad \textbf{7.4}$$

where $\dot{m}$ is mass flow rate in kg/sec, A is area in mm^2, ρ is density of water in grams/cm^3, and ΔP is the differential pressure between PT08–PT03 in bar. The discharge coefficient was evaluated for each channel sample at each test pressure. The area is based on the average of three measurements (shown in Figure 7.8) and listed in Table 7.5.

Figure 7.15 shows the functional relationship between *Cd* and the cross-sectional area, perimeter and the average primary texture. The trends are nearly identical to those that can be observed in Figure 6.9. The estimated *Cd* depends on the tests due to the significantly longer length of the channels compared to those treated in Section 6.5. The effect of surface enhancement processes on flow resistance is similar, with CM and CMP causing the lowest resistance (highest *Cd*). The *Cd* increases with the cross-sectional area, as expected. The large square as-built channel (AB-54-L) features an area that is nearly identical to that of channels CM-B3 and CM-B4 and its average *Cd* is 38% lower. The *Cd* of the large as-built AB-54-L channel is higher therefore the flow resistance is lower than that of the as-built channels featuring smaller cross-sectional area, as expected. A slight difference in flow resistance can be observed between AB channels with the larger and smaller cross-sectional area, which suggest that other factors, such as the texture, have a higher influence on the flow resistance.

Figure 7.15 also shows that the value of *Cd* increases with decreasing perimeter lengths down to *Cd*=0.3. For a range of perimeter values, it remains constant and equal to approximately 0.3, then increases again starting from *Cd*=0.4. This is expected since the powder adherence and surface undulations cause the value of the perimeter to increase at lower *Cd* values. The decrease of the perimeter value for *Cd* in the range from 0.2 to 0.3 is due to the full removal or partial removal of powder particles with sizes lower than the average particle size (73 µm). The larger perimeter values associated with values of *Cd* higher than 0.4 is mostly due to the increase in the channel cross-sectional area resulting from material removal.

Figure 7.15C displays how the flow resistance decreases exponentially with decreasing values of the average areal texture (primary), Sa. The Sa strongly decreases down to ~*Cd*=0.32, while for larger values of *Cd* it decreases very slightly for values of from *Cd*=0.32 up to 0.5.

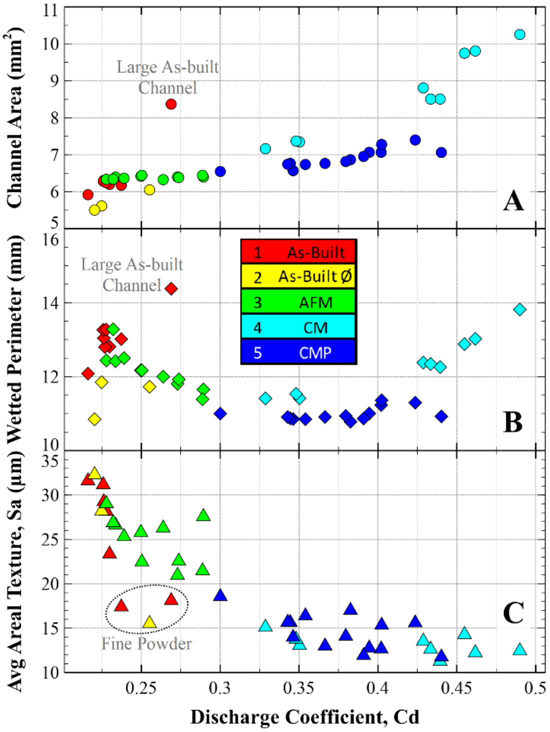

Figure 7.15. Relationship of the estimated *Cd* with A) Measured cross-sectional area, B) Measured perimeter, and C) Measured average primary texture. The color of the symbols is associated to the surface enhancement process as listed in the legend.

In Chapter 6 it is discussed that other surface texture parameters deemed necessary for flow characterization include the core texture depth (Sk) and reduced peak height (Spk). These values allow to better to discern the average distance between peaks and valleys, thus filtering out the maximum heights of peaks and valleys. Figure 7.16 shows how Sk and Spk vary with *Cd*. The functional dependence is identical to that of the data visualized in Figure 6.10: as the core peak-to-valley depth reduces, the *Cd* increases. The value of Sk becomes approximately constant for heights of peaks or valleys of ~50 µm, and it weakly decreases for values of *Cd* up to 0.5. The trend of Spk is similar, although not as pronounced. Overall Sk and Spk decrease exponentially with *Cd*.

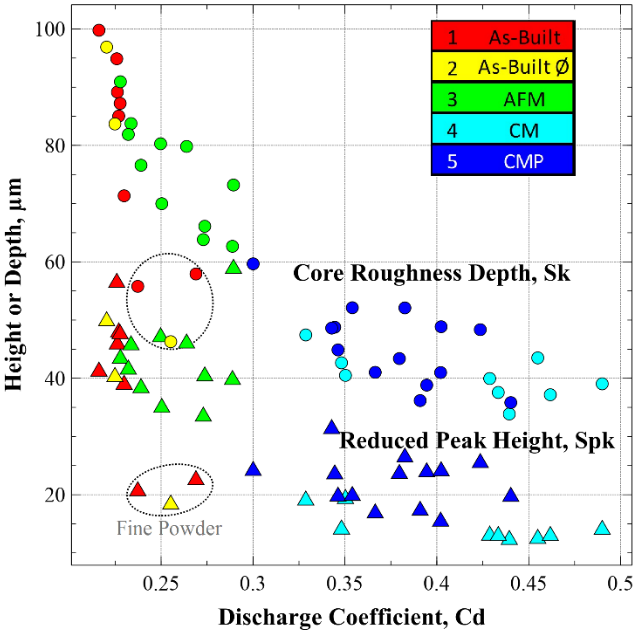

Figure 7.16. *Sk* and *Spk* as a function of *Cd*. The color of the symbols is associated to the surface enhancement process as listed in the legend.

It can be concluded, in analogy with the considerations reported in Section 6.6, that flow resistance depends for the most from roughness-related peaks and their density, as well as from the planarization of waviness and their density. Figure 7.17 presents the summary of the relations between *Cd* and Spk, Spd, Wp, and WPc and the cross-sectional area. These trends are similar to those reported in Figure 6.12 for shorter channels. Given that material is removed from the surface due to the enhancement treatment, the resulting channel cross-sectional area is larger and Spk is lower. Compared to the Spk of the as-built channels (AB-xx), the Spk of channels whose surfaces are treated is lower by 79%, and the density of these peaks (Spd) is lower by 74%. Similar results hold for waviness, with Wp and WPc being lower by 76%. The calculated Reynolds number (discussed in section 7.4.4) indicates that the channels operate in the turbulent regime. Higher micro peaks, macro waviness, and their density distribution along the channel length increase boundary layer turbulence and fluid dynamic losses. Effective removal of these features is crucial for reducing flow resistance.

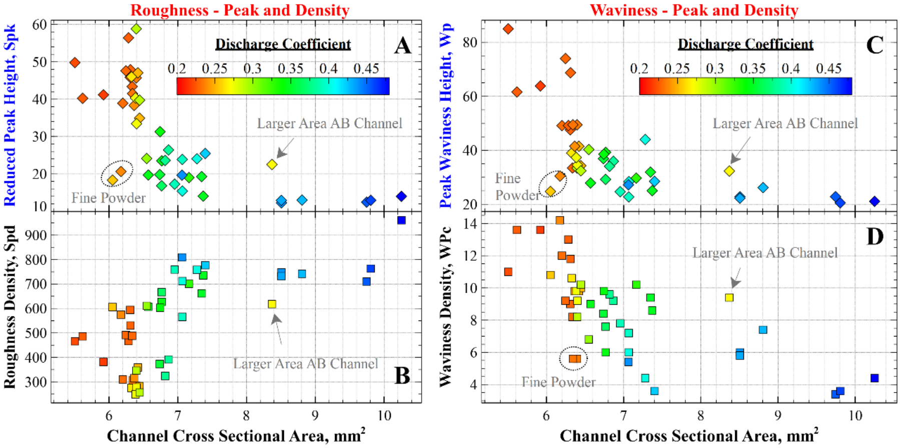

Figure 7.17. Flow resistance dependence for roughness and waviness of all the tested channels: A) Spk, B) Spd density, C) Wp, and D) WPc density.

To allow to better estimate the amount of material removal required to obtain a specified flow resistance, Figure 7.18 provides the visualization of the relationship between material removal (MR) per side and Sk, Spk, and Wp. To obtain Figure 6.11, MR was measured at 20 locations for each channel. MR per side is calculated based on the simplifying assumption that

$$MR = \frac{\sqrt{A_{\mathrm{Ch}}} - \sqrt{A_{\mathrm{AB}}}}{2} \tag{7.5}$$

where A_{Ch} is the average cross-sectional area of the channel calculated measured at three locations and A_{AB} is the value of the average as-built area. The results discussed in Section 6.5 show that the average powder size correlated to the material removal necessary to effectively increase the *Cd*. The results in Figure 7.18 suggest that removing powder of the minimum size (diameter of 45 µm) is required to reduce the flow resistance by approximately 40%, but to reduce flow resistance by >75% the powder of maximum size (105 µm) must be removed. The removal of large-size powder eliminates all the adhered powder particles and decreases flow friction within the boundary layer.

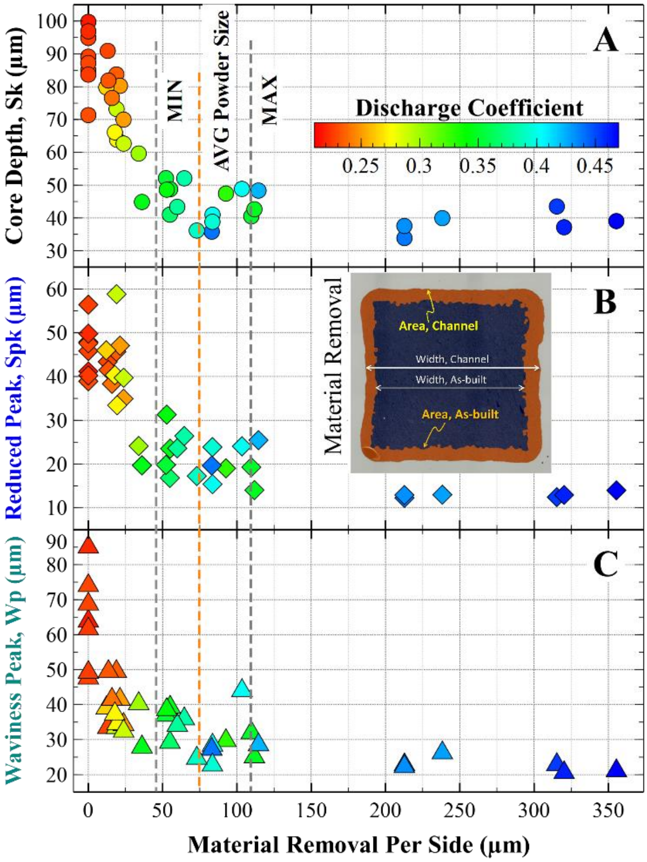

Figure 7.18. Relationship between material removal per side based on: A) Core Depth, Sk, B) Reduced Peak Height, Spk, and C) Waviness peak height, Wp.

7.4.4 Differential Pressure and Friction Factor

In order to calculate the Colebrook-White friction factor using existing methods, Reynolds number, pressure difference and hydraulic diameter (D_h) [298] must be determined. According to conventional methods, all these calculations assume a circular tube and methods to convert these quantitates for the case of non-circular geometry are documented in several publications [299–301]. The conventional definition of hydraulic diameter for a square channel is

$$D_h = \frac{4A}{P} \tag{7.6}$$

where A is the area in mm^2 and P is the wetted perimeter in mm. These values were measured as part of the detailed characterization of the channel cross sectional areas and perimeters documented in Section 7.4.1. The hydraulic diameter was calculated according to equation 7.6 for all channels and values are reported as black triangles on the plot of Figure 7.19. This figure shows that values of D_h calculated with equation 7.6 depart significantly from the expected linear relation between area and perimeter for samples featuring small values of the area and comparatively large value of perimeter. The channels with as-built surfaces feature a measured perimeter approximately 30% higher than that of a nominally designed channel with smooth walls. The plot of Figure 7.19 shows that the deviation from linearity is significant for the points referring to as-built and AFM channels with cross-sectional areas less than 6.8 mm^2. In those cases, the value of the perimeter is much larger than the nominal value due to the surface texture resulting from the adhered powder and waviness, yielding a value of the D_h which deviates from the one given by the linear trend by around 18%.

Other issues affect the deviation from the linear dependence of D_h. First, the perimeter exhibits a higher coefficient of variation (CV) compared to the CV of the cross-sectional area (see Figure 7.12), introducing additional uncertainty in the D_h values. Second, using D_h with large perimeter values could further bias the estimation of the friction factor. Since sand grain roughness (relating to surface texture in section 7.4.5) is already incorporated into the friction factor correlation, accounting for the increased perimeter due to high roughness would effectively result in "double bookkeeping" of the texture values.

Given the unsatisfactory ability of the conventional definition of hydraulic diameter of correlating the cross-sectional area and the perimeter of the additively manufactured channels, an alternative definition D_h evaluated for a square cross-section channel is

$$D_{h1} = \sqrt{A_\mathrm{meas}} \qquad \mathbf{7.7}$$

where A_{meas} is the measured cross-sectional area, whose values for the considered channels are listed in Table 7.5. The justification for this definition is that the D_h for a square channel is simply the length of a side [289], as previously mentioned. Values of D_h1 are shown as white circles in Figure 7.19 together with their correlating function displayed as a dotted line. The values of D_h, associated with an area larger than 6.6 mm^2, form a linear function and the values of D_h1 appear to be offset from this. This observation leads to a definition of hydraulic diameter valid for square channels that includes a texture attribute, namely

$$D_{h2} = \sqrt{A_{meas}} - 2Sk \qquad \mathbf{7.8}$$

where Sk is the core texture height. This definition of hydraulic diameter incorporating a correction term twice the surface texture attribute is similar to definitions for determining a representative cross-sectional area in AM mechanical testing [302,303] and also adopted in constricted flow theory presented by Taylor et al. [288,304]. The introduction of a texture correction term eliminates the bias resulting from the case of a highly texture perimeter: channels with high texturing (those with a cross-sectional area lower than 6.6 mm^2) feature values of D_h that are 17% lower, with a value of the cross-sectional area which is 4.5% lower. For this reason, the definition of hydraulic diameter provided by Equation 7.8 is adopted for all the calculations treated in this chapter. The ratio of length (PT08-PT03) to hydraulic diameter is approximately 179:1.

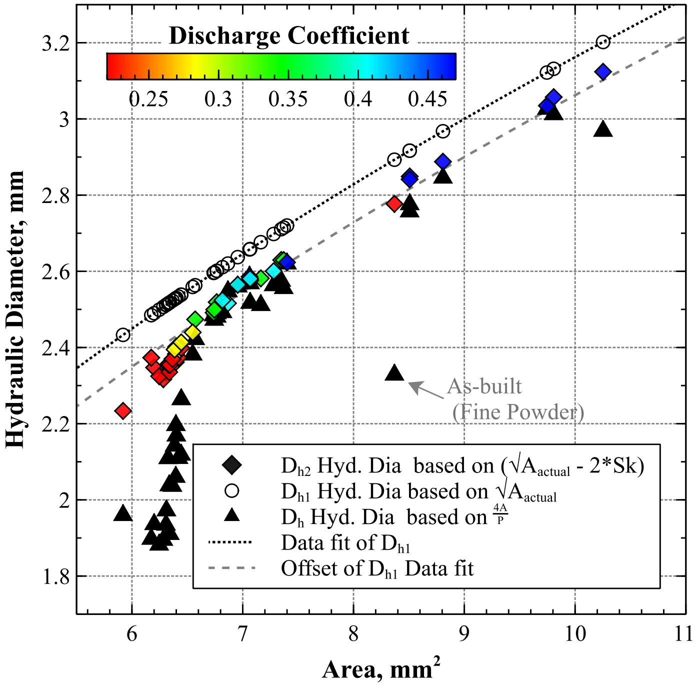

Figure 7.19. Hydraulic Diameter based on various definitions. D_{h2} is defined by equation 7.6, D_{h1} is defined by equation 7.7, and D_h is defined by equation 7.8. The D_{h2} symbols are colored according to the value of the *Cd*.

After an appropriate hydraulic diameter is calculated for the square channels, the Reynolds number is determined. The Reynolds number is defined as

$$Re = \frac{D_{h2} v \rho}{\mu}, \tag{7.9}$$

where D_{h2} is calculated according to equation 7.8, v is computed from equation 7.3, ρ is the fluid density, and μ is defined according to equation 7.1.

The values of *Re* for all test runs range from 17,011 to 122,818, thus the flow is fully turbulent. Figure 7.20 provides a plot of the values of the Reynolds number as a function of the mass flow rate with the symbols colored according to the velocity range. Values referring to samples treated with surface enhancements (polished) are plotted along with those referring to the as-built samples obtained with coarse powder and fine powder.

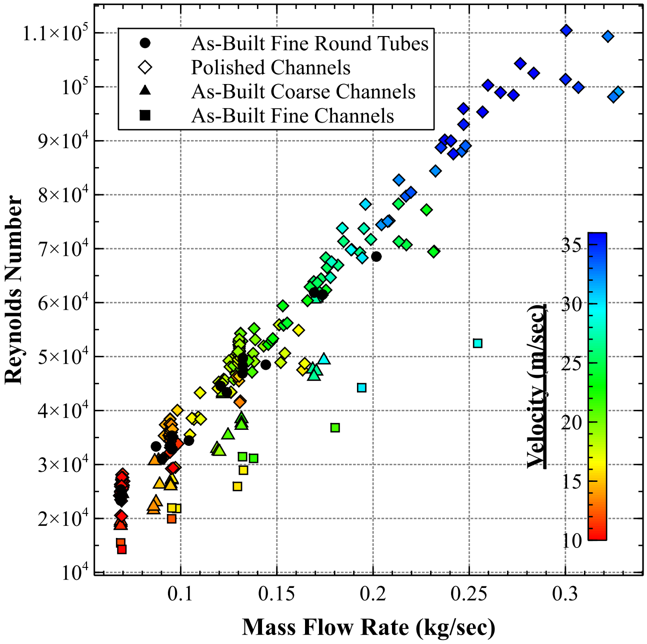

Figure 7.20. Reynolds number as a function of mass flow rate obtained from measurements on enhanced and as-built channels. The data is colored by velocity for samples processed with surface enhancements (polished) and as-built samples. The Reynolds number is calculated with the hydraulic diameter defined by Equation 7.6.

Figure 7.21 displays a chart of the pressure drop measured as the pressure difference between the values recorded by the PT08 and PT03 sensor as a function of the measured $\dot{m}$. The symbols are colored according to the processing method with which each channel was treated. As expected, differential pressure measured for the as-built channels are the highest for all mass flow rates. The AB-54L channel features a larger cross-sectional area, therefore the pressure drop measured for this channel is lower than that measured for the other as-built samples. The values of differential pressure at approximately constant mass flow rate equal to 0.069, 0.095, and 0.13 kg/sec were measured during test runs in which the venturi flow meter was employed. The value of $\dot{m}$ is the maximum due to the resistance in the channels and lower differential pressure.

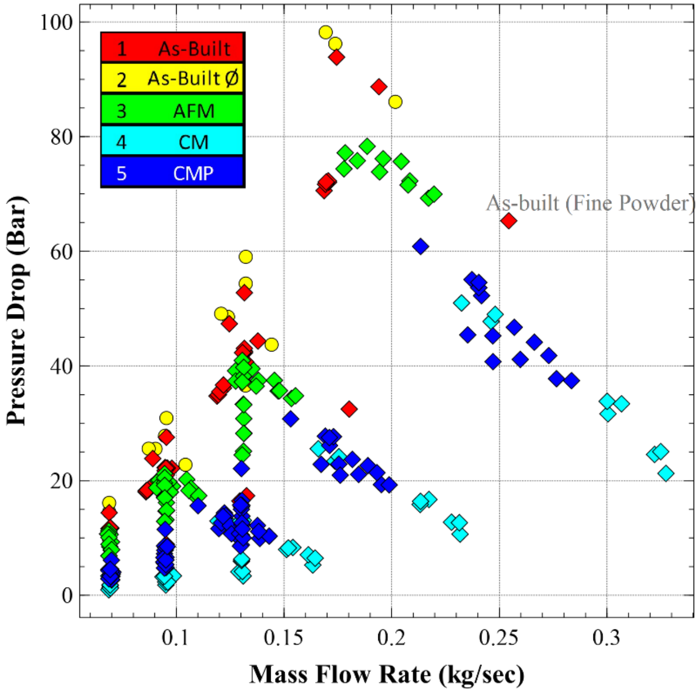

Figure 7.21. Pressure difference between the values recorded by the PT08 and PT03 sensors (Figure 7.8) as a function of the measured $\dot{m}$. The symbols are colored according to the processing method with which each channel was treated.

The same set of data used to obtain Figure 7.21 was used to obtain Figure 7.22, but in this plot the relation between pressure drop and mass flow rate is also displayed as a function of core surface texture, average directional waviness, and average directional roughness. Also, the results related to average texture, Sa, were analyzed, but the trends are similar to those valid for Sk, whereby the only difference is the range of values, namely from 11 to 32 µm. The trends visualized in Figure 7.22 for surface texture, waviness, and roughness are generally as expected. Values related to the surfaces with the highest roughness and waviness correlate with the highest pressure drop and vice versa. The core texture depth, Sk, is primary therefore it encompasses the effect of the waviness and roughness surface attributes. The plots indicate that both roughness and waviness affect the flow resistance, although the effect of roughness is much stronger. This observation is corroborated by the analysis of the *Cd* trends presented in Section 7.4.3.

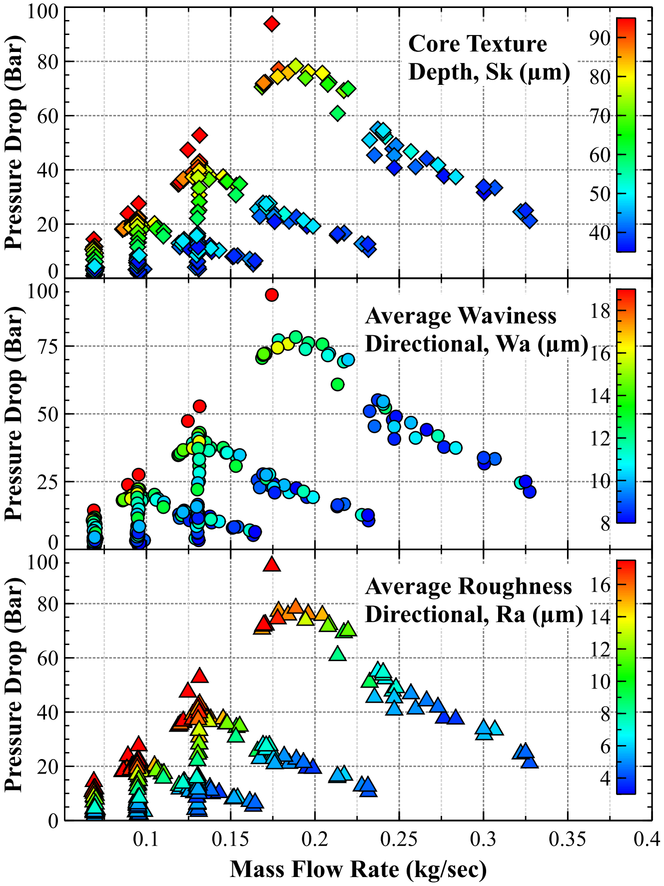

Figure 7.22. Pressure difference between the values recorded by the PT08 and PT03 sensors (Figure 7.8) as a function of the measured $\dot{m}$. The symbols are colored according to the values of three difference measured surface texture attributes, namely Sk, Wa, and Ra.

The correlation to determine pressure loss along the length of the channels and valid only in case of turbulent flow requires a correlation for the friction factor. The empirical Colebrook-White equation for the friction factor f_C [286,287] is

$$\frac{1}{\sqrt{f_C}} = -2log_{10}\left(\frac{2.51}{Re\sqrt{f_C}} + \frac{K_s}{3.7D_{h2}}\right) \qquad \textbf{7.10}$$

where Re is defined by Equation 7.12 and K_s is the equivalent sand grain roughness, sometimes referred to as ε. Equation 7.13 requires an implicit method to determine f_C.

Moody obtained a well-known diagram based on measurements performed by Darcy and Nikuradse showing the relationship between Reynolds number and friction factor depending on a relative pipe roughness [283]. The diagram was intended to provide designers with a graphic-based means to obtain values of friction factor for analysis. Several implicit and explicit equations to calculate the friction factor were developed, based on the Moody diagram and other experimental data sets. A commonly adopted explicit equation based on the Moody diagram for the calculation of the friction factor, defined here as f_M, is [298]

$$f_{\mathrm{M}} = 1.14 + 2\log_{10}\left(\frac{D_{h2}}{K_s}\right)^{-2} \qquad \mathbf{7.11}$$

The ratio K_S/D_h in equation 7.10 (and its inverse in 7.11) is commonly known as *relative pipe roughness* and it can be determined from the Moody diagram. The K_S/D_h ratio defines the sand grain roughness relative to the hydraulic diameter of the channel or pipe. Other researchers have proposed explicit expressions of the friction factor [298,305]. These expressions can vary depending on the range of Reynolds number, thus flow regime, and on the K_S/D_h ratio. The Swamee and Jain explicit friction factor expression [306] is recommended for values of $K_s/D \leq 0.05$ and is given by

$$f_{\mathrm{S}} = \frac{0.25}{\left[\log\left(\frac{\frac{K_s}{D_{h2}}}{3.7} + \frac{5.74}{Re^{0.9}}\right)\right]^2}, \qquad \mathbf{7.12}$$

where Re is defined from 7.12. Mileikovskyi and Tkachenko introduced another expression for the friction factor [307], valid for a wider range of K_S/D_h values, up to 0.65, and for Re up to 10^9. This expression for the friction factor, defined in this case as f_T, is

$$f_{\mathrm{T}} = \frac{1}{\left[0.8284\, ln\left(\frac{\frac{K_s}{D_{h2}}}{4.913} + \frac{10.31}{Re}\right)\right]^2} \qquad \mathbf{7.13}$$

The expression of Brkic and Cojbasic [308] is

$$f_{\mathrm{B}} = \left[-2log\left(\frac{2.18B}{Re} + \frac{\frac{K_s}{D_{h2}}}{3.71}\right)\right]^{-2}, \qquad \mathbf{7.14}$$

where B is

$$B = ln\frac{Re}{1.1816\ln\left(\frac{1.1Re}{\ln(1+1.1Re)}\right)}. \qquad \mathbf{7.15}$$

Finally, Avci and Kargoz [309] suggested to evaluate the friction factor, termed f_{A}, as

$$f_{\mathrm{A}} = \frac{6.4}{\left[ln(Re) - \ln\left(1 + .01Re\frac{K_s}{D_{h2}}\left(1 + 10\sqrt{\frac{K_s}{D_{h2}}}\right)\right)\right]^{2.4}}. \qquad \mathbf{7.16}$$

The validity of these friction factor definitions were experimentally evaluated with a general focus on round pipes [310,311]. One of the objectives of the experiments presented here is to characterize and determine an explicit friction factor expression for the analysis of additively manufactured square channels, with large variations in the surface texture.

All the expressions for the friction factor were compared regarding predictions of the differential pressure over the square-section channels, and the Darcy friction factor

$$f_{\mathrm{D}} = \frac{2\,\Delta P\,g_c\,D_{h2}}{\rho L v^2}. \qquad \mathbf{7.17}$$

In equation 7.17, ΔP is the pressure difference between two measuring ports, v is given by Equation 7.3, ρ is the fluid density, g_c is the gravitational constant (9.81 m/sec^2), and L is the length between the locations of the considered ports. Figure 7.23 depicts how the Darcy friction factor, determined by correlating all the measured the differential pressure data, varies with the mass flow rate. As expected, for low values of the mass flow rate f_{D} increases for a given of mass flow rate. f_{D} is larger for the AB channels and the AFM channels, for which a high density of powder particles are present on the surface. Figure 7.23 shows the constant mass flow rate tests conducted at 0.069, 0.095, and 0.13 kg/s, along with data sets where the flow rate is maximized. The friction factor remains relatively constant regardless of the flow rate. The values of f_{D} for selected channels is represented by a horizontal line, indicating minimal variation in friction factor with changes in flow rate (refer to Appendix, Figure 12.3).

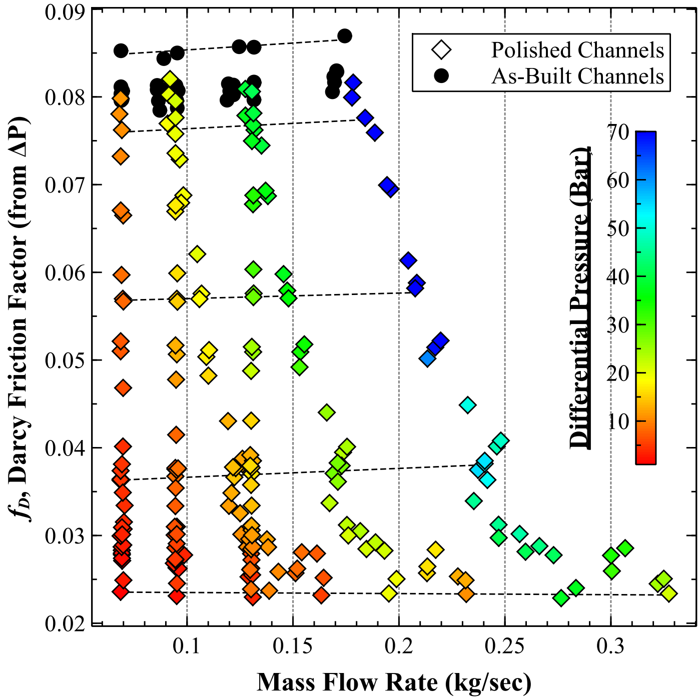

Figure 7.23. Darcy friction factor as a function of mass flow rate. The dotted horizontal lines represent the same channel across the six different test runs. The points are colored according to the measured value of the pressure difference between pressure ports.

The values of the Darcy friction factor obtained by correlating experimental results was evaluated against the values of friction factor calculated with the expressions based on the surface texture (*Re*, K_S, and D_{h2}) in relation to the discharge coefficient (Figure 7.24). These data are derived using the full-length channel value of the differential pressure (PT08-PT03) for each test condition. None of the friction factor correlations obtained with Equations 7.10 through 7.16 match the values of Darcy friction factor derived from measurements. The values obtained with Equations 7.10 to 7.16 show similar trends across the range of *Cd* with a maximum deviation between predictions of 10%. The value calculated with the Colebrook-White correlation falls within the median range of the values calculated with the other correlations. The plot also shows that there is discrepancy between values calculated with all the friction factor correlations and the Darcy friction factor, with the value calculated with surface-based friction factor correlations being lower for values of $Cd < 0.27$ and higher for $Cd > 0.3$. Based on these considerations, the Moody-derived friction factor expression (f_M) was selected for further analysis. At lower flow resistances, values calculated with f_M feature the least variance from those calculated with the f_D expression. At higher flow resistances, values calculated with the f_M

correlation are close to the mean of values computed with all other friction factor expressions.

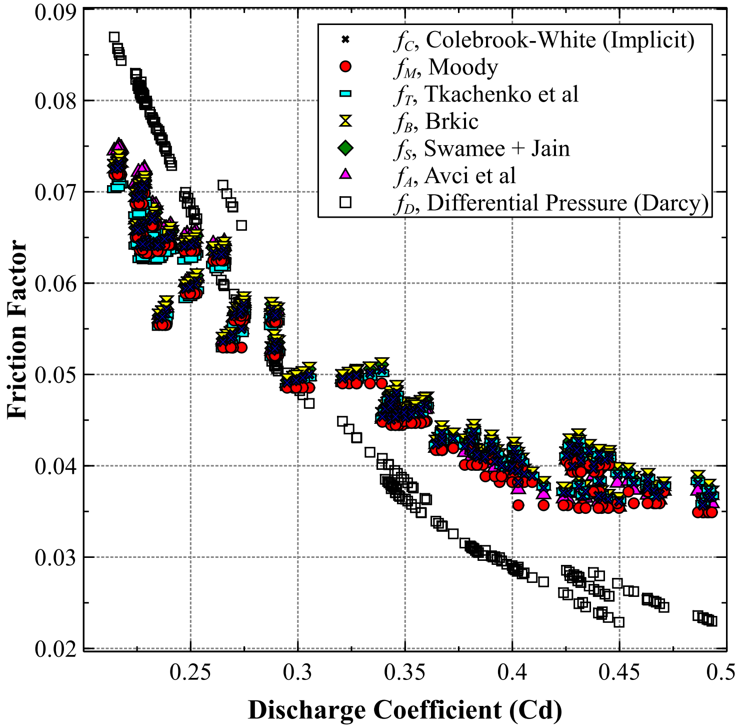

Figure 7.24. Comparison of the friction factor determined experimentally from differential pressure measurements along with friction factors calculated from various correlations (Equations 7.10–7.16).

The friction factor correlations 7.10 to 7.16 depend on the surface roughness and channel hydraulic diameter (K_S, D_{h2}) along with Re. K_S is not representative of surface roughness, or of surface texture, which can be directly measured. A possible assumption for the evaluation of surface roughness is that it is defined as the average directional roughness, Ra, since this is the most commonly measured. However, this parameter is insufficient to fully characterize texture, and other surface texture attributes are discussed in Section 7.4.5. Adams et al. [312] proposed a constant value of 5.863 for the K_S/Ra ratio. Similarly, Forster recommended a value of 7 for K_S/Ra [313], while Koch and Smith suggested a value of 6 [314]. The value of 5.863 was initially used to convert Ra to a K_S for the data presented in Figure 7.24. However, other authors have argued that a single K_S parameter is insufficient [305,315]. This deficiency is evident in Figure 7.24 where variations in surface texture led to changes in flow resistance and deviations in the friction factor correlations compared to the f_D correlation.

The correct characterization of the roughness of a surface is crucial for determining differential pressure along fully turbulent flow through a channel because the viscous sublayer and roughness sublayer are disturbed and deflected by the surface texture. The height and spacing of the roughness and waviness alters the contribution to the drag and pressure losses in addition go thickening the boundary layer further constricting the flow. Figure 7.25 shows that similar values of differential pressure may result from largely different Reynolds numbers and velocity values. This observation is consistent with that of Kadivar et al. [305] that the pressure drop is unaffected by fluid viscosity and velocity, if the peaks of the surface texture penetrate the roughness sublayer. The height of the roughness sublayer can be as much as 2 to 5 times the diameter of the sand grain roughness, K_S [316]. As presented in Chapter 6, the surface texture that results in the K_S is complex and comprises both micro roughness and macro waviness, therefore these surfaces must be fully characterized, and new correlations determined.

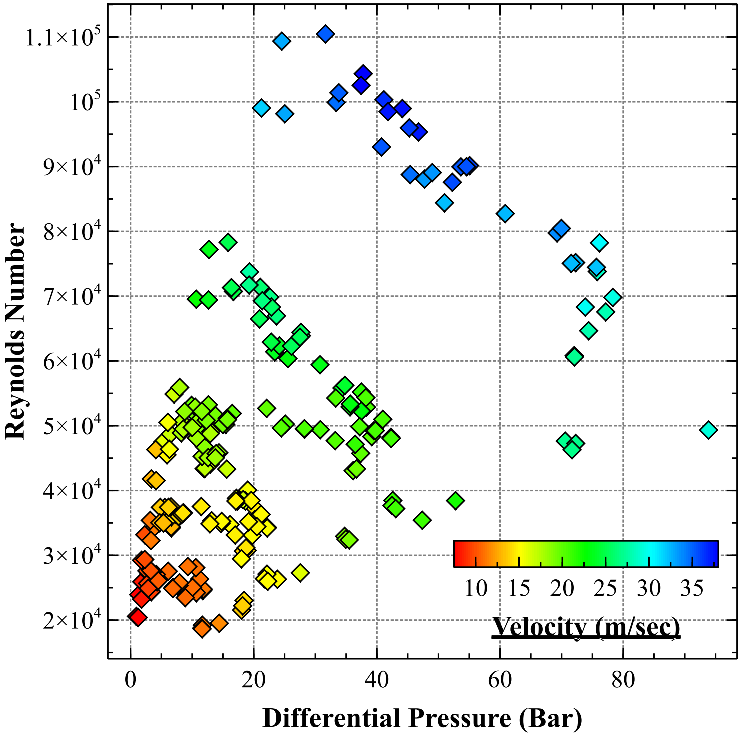

Figure 7.25. Reynolds number as a function of the differential pressure. The data points are colored by the mean velocity.

7.4.5 Sand Grain Roughness

The definition of sand grain roughness is related to the experiments of Darcy and Nikuradse: sand was bonded to internal pipes using an adhesive or lacquer in order to obtain a prescribed level of internal surface roughness [284,285]. The exact cross-sectional surface texture from these experiments is not known, but they are commonly represented as shown in Figure 7.26 (left). The surface roughness was obtained by measuring the diameter of a sand grain or evaluated by means of contact-type profilometers. Capillary action between the lacquer and sand grains applied to the pipe surface likely created small radii and captured the sand grains, so using the sand grain diameter is also an incorrect hypothesis. While sand grain roughness may appear similar to the roughness of a surface resulting from additive manufacturing, as in the case of a surface generated with the LP-DED process with its adhered powder particles, experimental data sets [305] indicate that the two surfaces are quite different, as evident from the images of Figure 7.26 (right). The microscopic shape of the surface resulting from the LP-DED process is made of both smooth and sharp irregularities due to waviness and roughness, and a combination of both. The resulting flow from these irregularities can result in trapped eddies at sharp transitions or pockets, vortex shedding, and crests that protrude into the boundary layer [317].

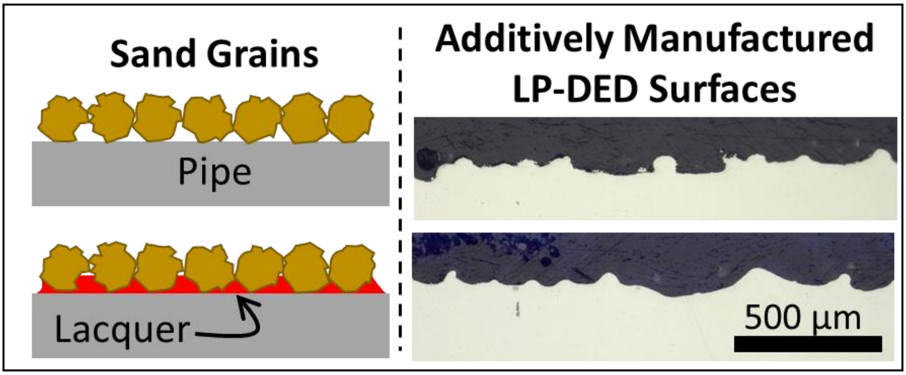

Figure 7.26. Left: schematic representation of sand grains attached to the pipe surface with and without glueing lacquer as in the experiments of Darcy and Nikuradse [284,285]. Microscopic image of the surface texture resulting from LP-DED manufacturing, showing both roughness and waviness.

The reason for the deviation between values of the friction factor computed with predictive equations and those based on measured differential pressures is further elucidated with the help of Figure 7.27, indicating the percent deviation in the friction factor (Δf) at three fixed flow rates. As the differential pressure increases due to the velocity rise from the increased mass flow, the experimental friction factor remains nearly constant across each channel. The maximum coefficient of variation (CV) of f_D at the three fixed flow rates is 5.8%. The average CV across all channel samples is 1.6%, with a median CV of 1.1%.

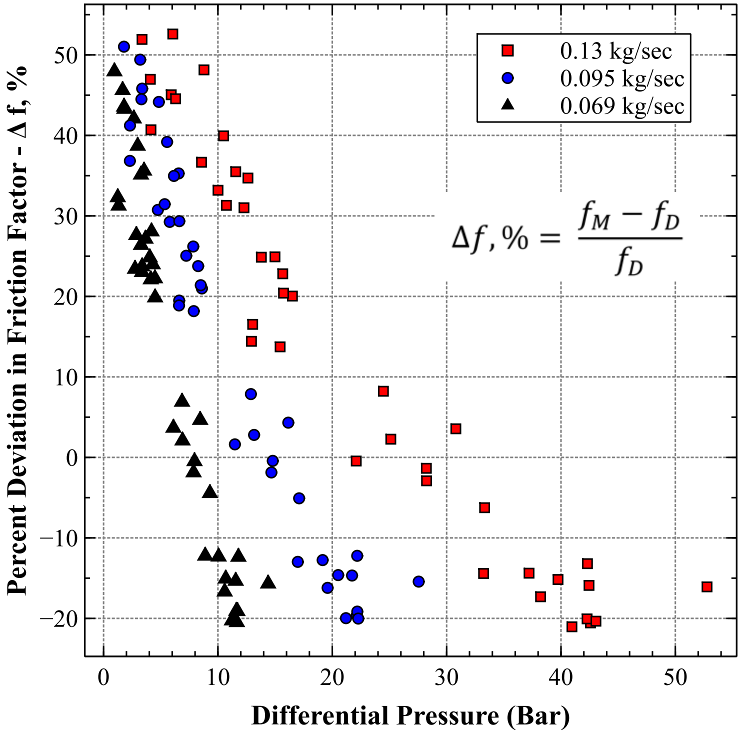

Figure 7.27. Percent deviation between the experimentally determined f_D and explicit f_M plotted with differential pressure. The points indicate the fixed mass flow rates when the venturi was installed.

To determine the appropriate conversion from the measured surface texture to sand grain roughness, an equation is solved iteratively for the sand grain roughness factor (K_F) as shown in Equation 7.18. This method uses the f_D from Equation 7.17, which is based on the measured pressure drop, as a known variable.

$$f_{\mathrm{D}} \approx f_{\mathrm{M1}} = 1.14 + 2log_{10}\left(\frac{D_{\mathrm{h2}}}{S_T \cdot K_{\mathrm{F}}}\right)^{-2} \qquad \mathbf{7.18}$$

where S_T is the measured surface texture/roughness (i.e., Ra, Pp, Sa, Sk), and K_F is the sand grain roughness factor. An iterative optimization was run for each data set that modified the K_F until the difference between f_{M1}, the new friction factor, and f_D was within 0.1%. The $S_T \cdot K_F$ value is then equal to K_S.

To incorporate K_s into friction factor correlations, Stimpson suggested using a parameter to normalize the value of the sand grain roughness with the hydraulic diameter (Ks/D_h) which allows for a comparison to the mean directional roughness (Ra/D_h) [108]. However, Stimpson only considered L-PBF as-built channels with rough texture variations, which did not include any partially or fully polished channel data. Wildgoose used a similar method to normalize additional data sets using Ks/Dh, but again with as-built L-PBF samples and no polishing [300]. Wildgoose omitted Ra/D_h values below 0.007, which is the ratio of interest for this current experiment using surface enhancements. Stimpson and Wildgoose employed micro-CT scanning to obtain the roughness parameters. While micro-CT could measure features as small as 30 µm, the uncertainty estimated for Ra was 4 µm.

Figure 7.28 presents the experimental data for various surface enhancement methods, showing the sand grain roughness (K_S/D_{h2}) and surface roughness/texture (S_T/D_{h2}) normalized with the hydraulic diameter. In each plot, K_S/D_{h2} remains constant, as it is directly calculated to equate f_{M1} with f_D in Equation 7.18. The normalized surface texture measurements (Ra/D_{h2}, Pp/D_{h2}, Sa/D_{h2}, Sk/D_{h2}) vary, filtering different surface features like roughness, waviness, and extreme peaks and valleys. Optimization based on mean filtered roughness (Ra) shows the least error with a linear fit, which is unexpected given its poor correlation to flow resistance as described in Section 6.5. The primary profile (Pp), a directional measurement including full texture, shows some linearity, but the slope plateaus at Pp/D_{h2} of 0.05. The average areal texture (Sa) and core texture depth (Sk) exhibit some linearity but with greater scatter.

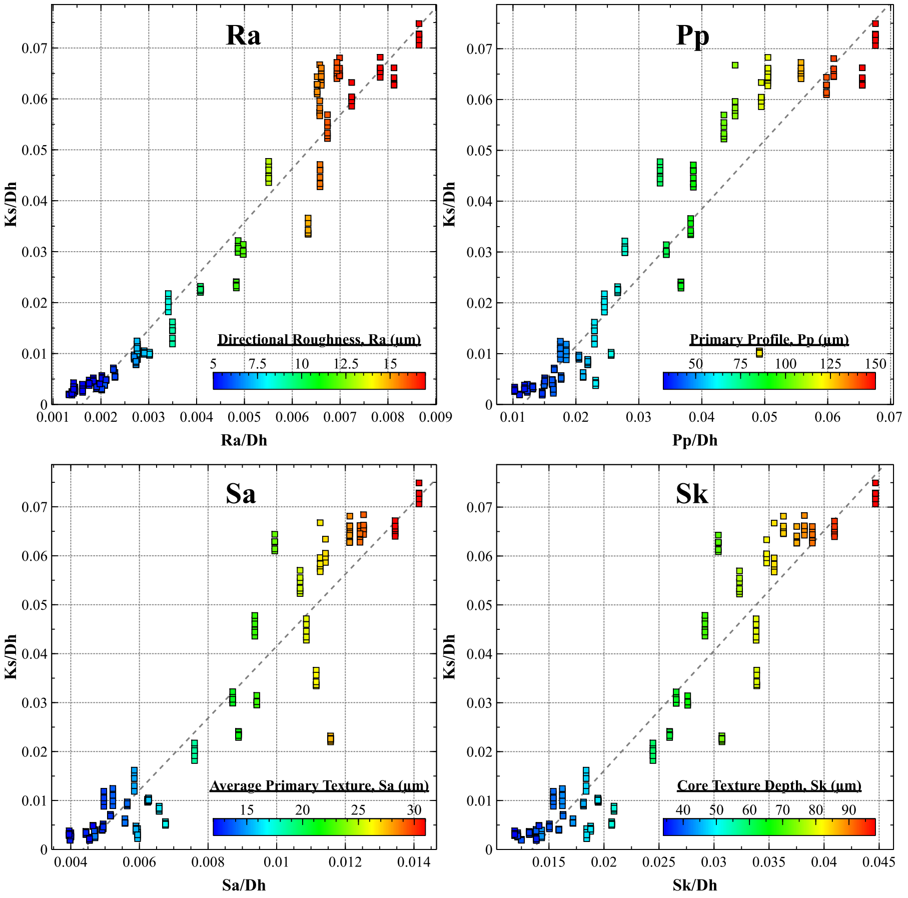

Figure 7.28. Sand grain roughness (K_S/D_{h2}) as a function of the surface roughness/texture parameters (S_T/D_{h2}) normalized by hydraulic diameter. The points are colored according to the measured roughness or texture values indicated for Ra, Pp, Sa, and Sk.

The correct prediction of the friction factor is essential for the design of heat exchanger channels; therefore the value of K_S must be determined, which in turn requires the value of K_F. Figure 7.29 displays a plot of the values of K_F as a function of the measured surface texture/roughness parameters. Regardless of the surface texture/roughness parameter, the absolute K_S value can be computed with the value of f_D. Based on the various surface texture/roughness parameters the range of K_S is 4.8 to 167 ±0.26 µm, corresponding to the enhanced samples and as-built, respectively. Ra and Sa, defined as average values, fail to capture the peak-to-valley range of the entire surface profile, leading to a broader range for K_F. Averaging all Ra values, as shown in Figure 7.29, yields a K_F value of 4.8. In comparison, the range suggested in section 7.4.4 is 5.863 to 7. Other researchers suggested a K_F of 0.2 to 0.4 for ground or machined surfaces [318], which aligns with Ra in the 3 to 5 µm range. Based on these observations and as made evident by Figure 7.29, the value of K_F is directly related to the roughness/texture and it cannot be assumed as a single constant.

The value of K_F for the Pp is much lower and its average value is 0.66. This is expected since it represents all profile features including roughness and waviness and is unfiltered. As Pp approaches as a value of 110 µm, indicative of as-built surfaces, the K_F approaches a value of 1. This observation provides some evidence that Pp could be used as a first-attempt approximation of the value of K_S when the surface is left in the as-built condition. The K_F related to Sa is lower than for Ra because the measured texture across the entire surface, with higher peaks and valleys, is captured. The average value of K_F is 0.84 related to Sk and indicates a linear trend with the absolute Sk. As-built roughness channels display a plateau in both Sa and Sk, but the friction factor remains relatively unchanged, suggesting the peak roughness sublayer may have been reached.

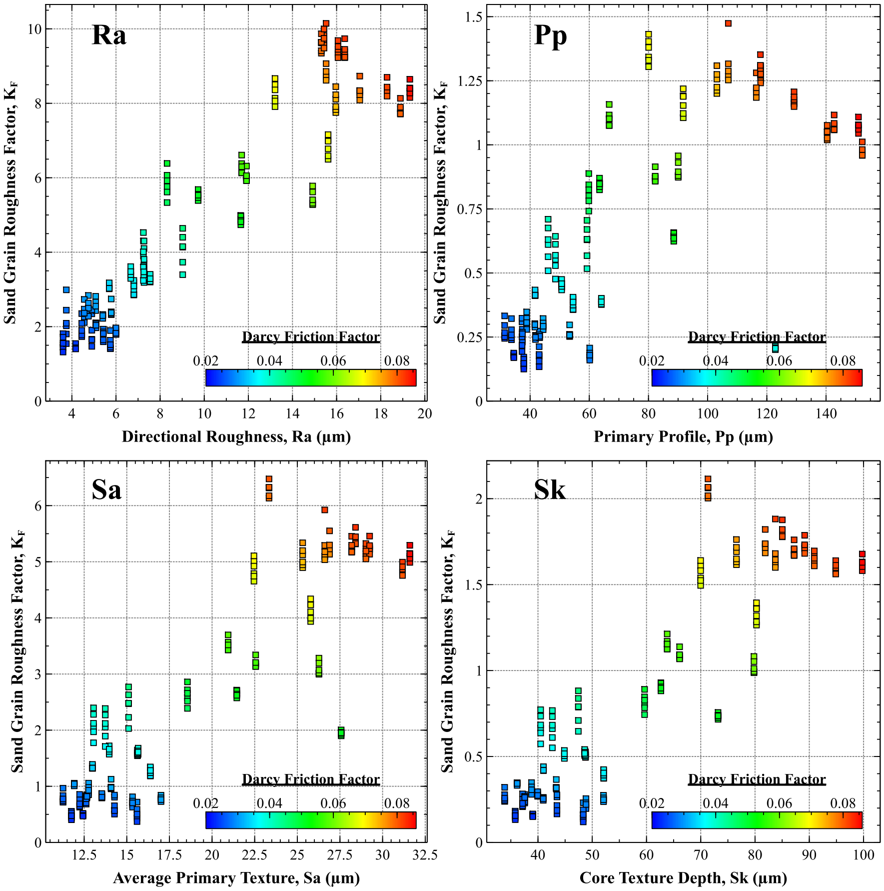

Figure 7.29. Values of sand grain roughness factor based on Equation 7.18 as a function of the measured surface texture/roughness values. The data sets are colored according to the value of f_D.

Table 7.7 provides the linear equations in terms of the K_S/D_{h2} ratio for the computation of the texture parameters resulting from the fitting of the experimental data. A linear fit of the K_S/D_{h2} *to the* Ra/D_{h2} parameter indicates a coefficient of determination of 95%. The primary profile (Pp) texture parameter revealed the highest proportional variance at 85.7%. The coefficient of determination for the Sa texture parameter was 88.2% and Sk at 90.1%.

Table 7.7. Summary of the linear fit of K_S/D_{h2} for texture parameters Ra, Pp, Sa, and Sk based on the data sets from Figure 7.28.

Texture Parameter	Linear Fit for K_S/D_{h2}
Ra	$\frac{K_S}{D_{h2}} = 10.535\frac{Ra}{D_{h2}} - 0.0169$
Pp	$\frac{K_S}{D_{h2}} = 1.3517\frac{Pp}{D_{h2}} - 0.0156$
Sa	$\frac{K_S}{D_{h2}} = 7.3534\frac{Sa}{D_{h2}} - 0.032$
Sk	$\frac{K_S}{D_{h2}} = 2.4545\frac{Sk}{D_{h2}} - 0.033$

7.4.6 Friction Factor Correlation and Mechanism

This section summarizes the data used to calculate the friction factor based on a new correlation (Equation 7.11 and Table 7.7) and hydraulic diameter expression (Equation 7.8). The surface profile characteristics and distinct texture types are presented in relation to their correlation with the experimental friction factor.

Using the linear fit of Ra from Table 7.7, a correlation for f_M was developed and results are presented in Figure 7.30. The values calculated with the new correlation (reported as circles), show improved accuracy by over 20% compared to the prior correlation (shown by triangles), which used a constant value of K_S. This new correlation also expands the applicable range of surface textures, as previous studies only considered fully rough, as-built tubes or channels. The new correlation becomes less accurate when the friction factor falls below 0.03, as surface roughness and waviness decrease. At this transition, calculating D_h (indicated by squares on Figure 7.30) using the traditional definition of hydraulic diameter ($4A/P$) may be more appropriate with the new linear fit model for K_S/D_{h2}. Several datasets at f <0.3, not shown in Figure 7.30, produced negative values for K_S when using D_{h2}. Switching to D_h corrects these negative values, but the predicted f may still be lower than the experimental values, as shown by the shift between D_{h2} and D_h predictions.

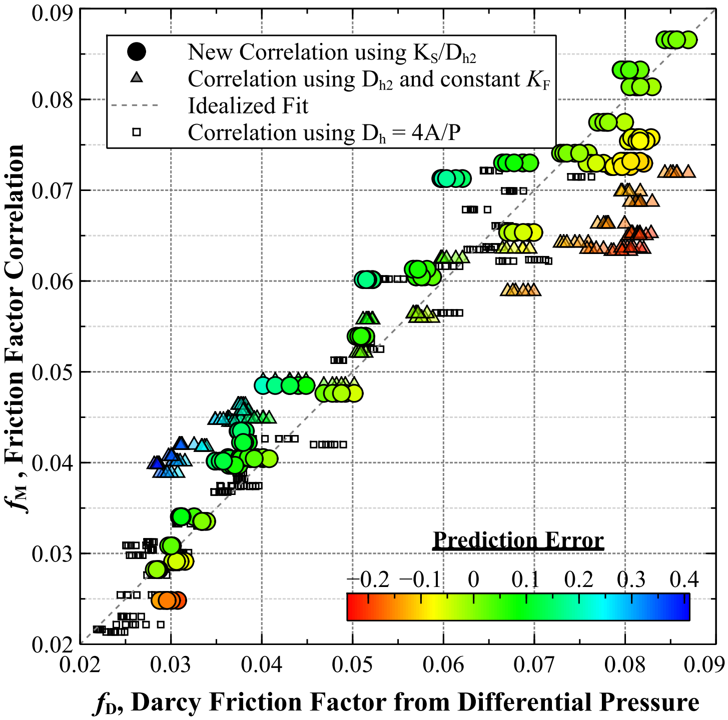

Figure 7.30. Correlation of f_M using the K_S/D_{h2} and Ra/D_{h2} linear fit method in relation to the f_D. The points are colored according to the prediction error from the idealized fit.

Previous chapters defined the surface texture is the result of randomly distributed adhered powder particles contributing to roughness, as well as of melt pool undulations and of build layers causing periodic and random macro waviness. The orientation of these surface features (treated in Chapter 4) relative to the flow direction affect the value of K_S. The channels utilized in the experiments described here were fabricated by depositing layers while moving the deposition nozzle in the vertical direction, therefore surface roughness is caused by randomly distributed particles and directionality is inconsequential. The direction in which the waviness is measured should be based on the direction of the flow and not the direction of the build. In this experiment, with the deposition in the vertical direction the macro-waves are perpendicular to the flow direction.

To establish the mathematical relationship between the surface texture parameters and the friction factor, as well as the pressure drop, the experimental data were limited to those related to channels having a mean flow areas of 6.64 mm^2 ±10%. Figure 7.31 presents a chart showing values of Darcy friction factor as a function of the measured maximum roughness peak height and maximum waviness height. The plot indicates that the roughness peaks, primarily due to the adhered powder particles, are the main cause of the variation of the friction factor. Adhered particles increase flow resistance by destroying the laminar sublayer within the boundary layer through the formation of eddies. However, Figure 7.31 also indicates the combined effect of the roughness peak height and maximum waviness height to achieve a friction factor lower than 0.05. As the powder-induced peaks are eliminated, the valleys resulting from the waviness cause flow recirculation that results in local velocity gradients.

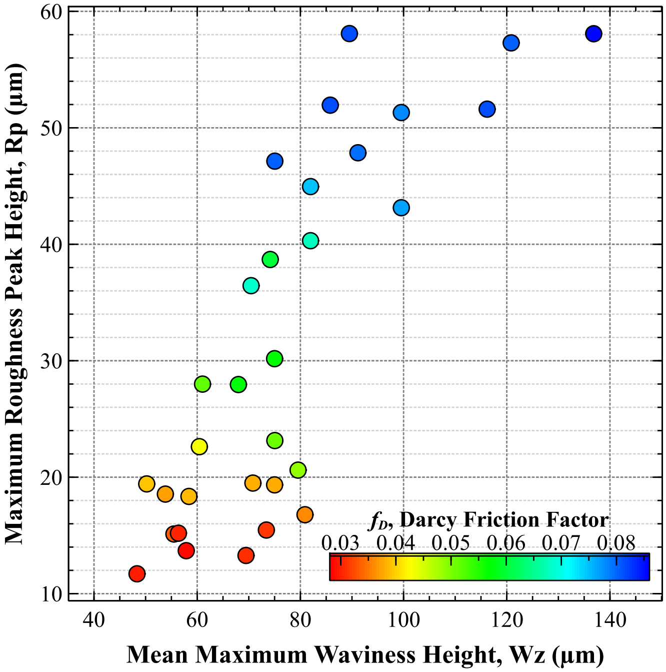

Figure 7.31. Maximum Peak Height (Rp) compared with maximum waviness height (Wz) for channel areas = 6.64 mm^2 ±10%, $\dot{m}$ = 0.13 kg/sec. The data sets are colored according to the f_D.

To assess the contributions of the valleys, a 3D functional texture parameter called void volume was evaluated for all channels. The void volume represents the space contained within surface texture that can trap fluid, defined as the volume between all peaks and valleys relative to an idealized flat plane fitted at the highest points of the surface (refer to Figure 7.14). This plane can then be offset in the Z-orientation (moving -Z towards the bottom of surface) to evaluate the peaks, core texture, and valleys. The void volume is normalized based on the volume per unit area, with units µm^3/µm^2.

Figure 7.32 displays the comparison of the roughness maximum profile peak height (Rp) with the dale void volume (Vvv). The Vvv of the as-built samples have a range of 2.7 to 4.6 µm^3/µm^2 due to heightened peaks and extreme valleys, often caused by adjacent particles; this is 61% of the total range shown on the plot. As surface enhancements reduce the roughness peaks and corresponding void volume, flow constriction and surface friction also decrease. The data suggest that an ideal void volume below ~2.3 µm^3/µm^2 is necessary to achieve a friction factor under 0.04. To approach a friction factor of 0.03, both peak removal nearing planarization and valley reduction are essential.

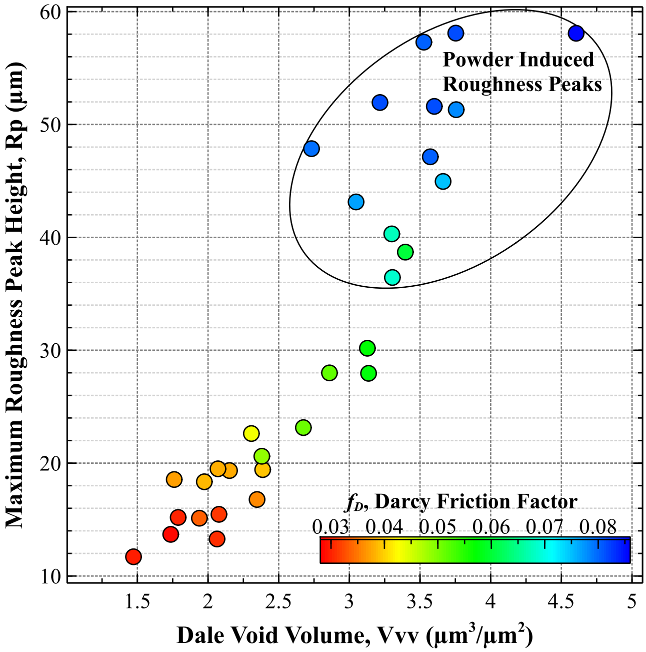

Figure 7.32. Maximum peak height (Rp) compared to the dale void volume (Vvv) indicating the remaining valleys; channel areas = 6.64 mm^2 ±10%, $\dot{m}$ = 0.13 kg/sec. The data sets are colored according to the f_D.

To reduce the friction factor, several surface texture attributes must be properly controlled during the channel processing, as indicated by the observed data. Figure 7.33 shows the comparison of the primary profile peak height (Pp) with the f_D. The primary profile incorporates both roughness and waviness surface attributes that affect the friction factor based on both roughness height and length scales. One of the values (CMP-B8) was identified as an outlier due to an erroneous Pp measurement and is not shown. The variation in the surface profile correlates to four distinct texture types and their corresponding reduction in the experimental friction factor: 1) roughness peaks, 2) peak smoothing/reduction, 3) minimized roughness and combined waviness and 4) valley reduction. These regions were selected arbitrarily based on the data set groupings observed in Figure 7.33 and their corresponding f_D.

The region labeled '*Roughness peaks*' is characterized by adhered powder particles that cause the highest friction factor. These peaks must be completely removed to reduce the friction factor. They significantly disrupt the roughness sublayer, increasing drag due to turbulent eddy structures [319], and causing flow recirculation in deep valleys. As a result, the flow area becomes constricted, with f_D

exceeding 0.07, likely due to the roughness sublayer extending into the outer layer. Perry et al. suggest that eddies can match the roughness height, extending into the core flow and further restricting the flow area [317]. The as-built channels and many AFM processed channels include roughness peak features. The Pp must be reduced by 36% by eliminating the powder induced roughness peaks before peak smoothing is present and the friction factor is reduced by 25%. The region labeled 'Peak Smoothing/Reduction' on Figure 7.33 indicates partially removed, rounded, and sometimes smeared peaks on the surface, resulting in an f_D of 0.06 ±0.01. SEM images in section 7.4.1 reveal remnants of adhered powder particles on the surface of the AFM-processed channels. The surface exhibits smeared or reduced peaks, where partial particles blend into the subsurface. These features correspond to a *'peak smoothing and reduction'* (as indicated in Figure 7.33), but residual particles are still present.

To further reduce surface friction, roughness peaks must be fully eliminated and macro waviness reduced, as indicated in the *'Minimized Roughness/Combined Waviness'* region in Figure 7.33. Achieving surface planarization requires the complete elimination of all powder particles resulting in a reduction of the peak profile by 30% to obtain a friction factor below 0.05. The depth of the roughness and waviness peaks and resulting flow micro-eddies, can exacerbate the flow constriction. These eddies are influenced by the height and spacing of the roughness and waviness peaks. Section 6.5 ascertained the combination of peaks and density contribution to flow resistance. This aligns with Coleman's research on discrete geometric ribs causing variations in flow disturbances based on the distance between ribs [320]. Therefore, the complete removal of powder particles and the reduction of the spatial waviness peaks are crucial.

Minimizing the surface peaks and reducing macro waviness leaves minor valleys present on the surface. At this surface condition, the minor peaks and associated valleys likely become submerged in the sublayer flow, exerting minimal influence on skin friction [318]. The primary profile shows an average reduction of 27% when transitioning from the 'minimized roughness/waviness' to the 'valley reduction' region. Figure 7.33 shows the primary profile reduction as an exponential curve, correlating with the friction factor reduction, where minimal material removal from waviness causes only slight changes in the friction factor.

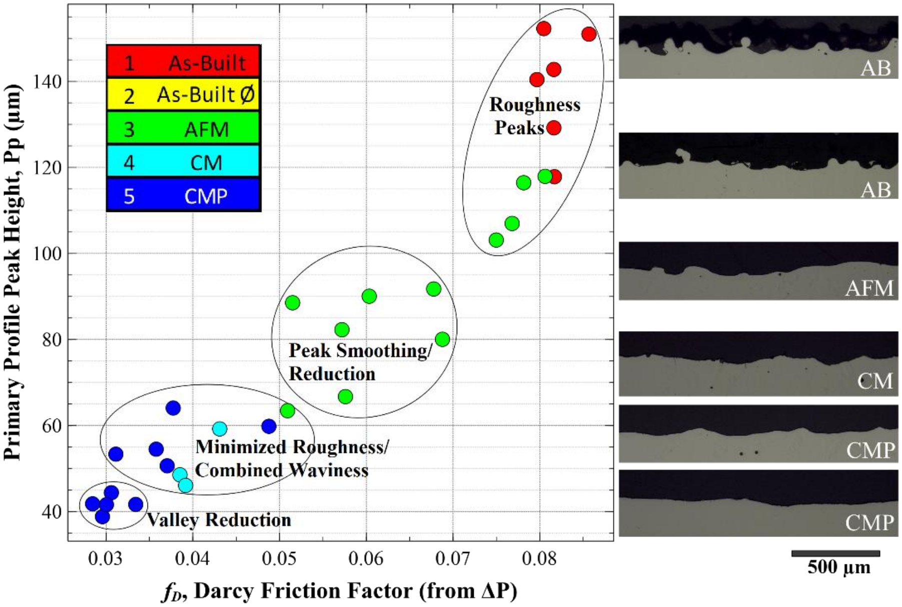

Figure 7.33. Surface attributes affecting reduction of the friction factor. The color of the symbols is associated to the surface enhancement process as listed in the legend. Right: The cross-section microscopic images are representative of the surfaces for each of the enhancement processes.

Modifying the surface through material removal is essential to achieve a planar surface to minimize flow friction. Heat exchangers are designed to meet performance targets based on mass flow rate, pressure drop, and heat transfer coefficient. This research focuses on specifying an as-built geometry, where surface alterations ensure the intended geometry and flow conditions are met. To achieve this, the required material removal must align with the heat exchanger's technical specifications and surface conditions (as shown in Figure 7.33). Technical merit should also include processing economics; excessive material removal leads to wasted powder feedstock, longer LP-DED build times, and extended post-processing, while insufficient removal results in high differential pressure, potentially missing performance targets.

Figure 7.34 illustrates the value of material removal per side as a function of the Dale void volume measurement. The CM process exhibits the highest material removal (over 90 µm), leading to the largest cross-sectional area but failing to achieve the lowest f_D. While CM is effective at removing powder particles and reducing partial waviness peaks, it does not fully planarize the surface by removing valleys. In contrast, CMP effectively reduces waviness peaks through abrasive media polishing, which also minimizes valleys, as shown by the reduction in Vvv (Figure 7.34). Removing 60 µm of material per side, combined with planarization, results in a friction factor of 0.03. Targeting material removal of 84 µm (a 40% increase) reduces the f_D by an additional 7%, bringing it down to 0.028.

The AFM process reduces surface friction with minimal material removal (less than 25 µm), but results in a f_D exceeding 0.05. Further reduction of the friction factor may be possible with increased slurry pressure, flow rate, resulting in more aggressive abrasive milling. While CM minimizes tooling and overall costs compared to AFM and CMP, all processes can be used to modify surfaces and adjust the friction factor based on end-use requirements. Future work may explore a combination of techniques to minimize material removal while effectively reducing surface roughness and waviness.

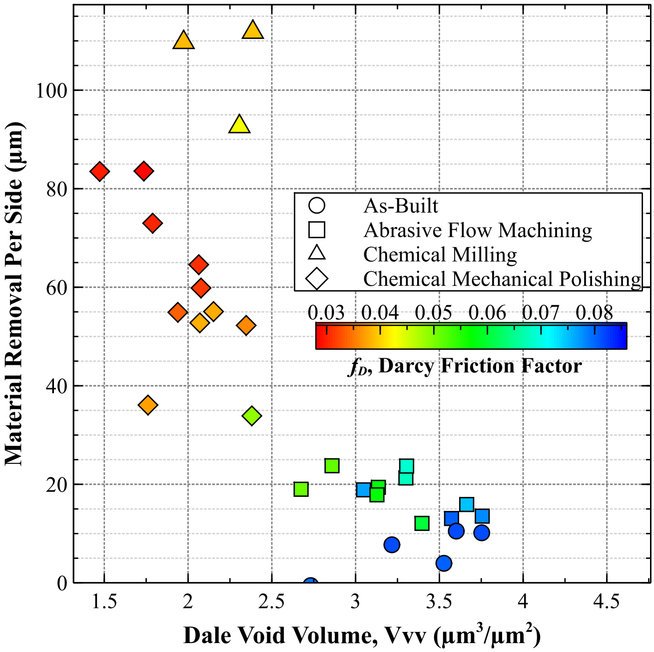

Figure 7.34. Material removal per side and dale void volume compared to the Darcy friction factor. The symbol markers indicate the surface enhancement process and data sets are colored according to the f_D.

7.5 CONCLUSIONS

This chapter presented the results of flow testing for 600 mm length channels, representative of LP-DED heat exchanger square channels. The effects of three surface enhancement methods—abrasive flow machining, chemical milling, and chemical mechanical polishing— on the fluid dynamic performance of heat exchanger channels were compared. As-built channels were used to determine the performance benchmark. All the built and tested channels feature square a cross section measuring 2.54 x 2.54 mm. The channels were fabricated from the NASA

HR-1 (Fe-Ni-Cr) alloy because the application is the cooling system of rocket nozzles, however results are applicable to heat exchangers realized with the LP-DED process in general.

Flow testing was conducted at various mass flow rates to characterize the pressure drop for each channel. Following experimental testing, the sample channels underwent destructive evaluation, whereby inner surfaces were characterized using SEM, optical microscopy, and optical surface texture analysis. Based on this detailed study, a friction factor correlation was developed. The correlation includes texture-dependent parameters which in turn relate to equivalent sand grain roughness. The sand grain roughness, originally based on the experiments of Darcy and Nikuradse, is commonly used for friction factor correlations. However, surfaces produced by the LP-DED process are more complex and cannot be characterized with sand grains values.

The following conclusions can be drawn:

- Surface enhancements significantly reduced boundary layer turbulence by eliminating adhered powder and planarizing the surface, resulting in a tenfold reduction in pressure drop.
- The surface enhancement techniques [abrasive flow machining (AFM), chemical milling (CM), and chemical mechanical polishing (CMP)] produce distinct surface attributes (peaks and valleys associated with roughness and waviness) due to differences in the way material is removed, thus surface flow drag is different.
- The surface texture was varied across the channels using enhancements applied to the as-built surfaces. The filtered Ra ranged from 3.6 to 19.3 µm, primary Sa ranged from 11.3 to 31.6 µm, primary Sk ranging from 33.9 to 99.8 µm, and Pp from 31.4 to 152.3 µm.
- A new definition of hydraulic diameter, dependent on the value of the characterized cross-sectional area and core surface texture (Sk), has been proposed and validated with experimental data. This definition reduces the error associated with traditional definitions of hydraulic diameter, which depend solely on cross-sectional area and perimeter. This new expression of the hydraulic diameter allows to overcome the large error due to the strong biases occurring in the case of highly textured surfaces. For example, the value of the actual perimeter of the cross-section of as-built channels is widely different from its design value, which assumes a perfect geometry, free from any irregularity.
- None of the friction factor correlations documented in the literature provide values that match those computed with the Darcy friction factor obtained from measured differential pressures, including the Colebrook-White correlation. A new friction factor correlation was obtained by modifying the sand grain roughness expression and that of the hydraulic diameter so as to take into account microscopic surface features. The predictive capabilities of the new correlation has been validated.
- The variation in the surface profile correlates to four distinct types of texture and relates to the reduction in the experimental friction factor: 1) roughness

peaks, 2) peak smoothing/reduction, 3) minimized roughness and combined waviness and 4) valley reduction.

- A method was developed to predict sand grain roughness based on variations in the surface texture and associated areal and directionally measured values.
- The proposed method for characterizing equivalent sand grain roughness calculates friction factor values with less than 20% deviation from the experimental data, whereas values calculated using other correlations in the literature deviate by approximately 50%.
- The primary profile, which considers surface roughness and waviness, provides a reasonable first-order approximation of equivalent sand grain roughness for as-built surfaces.
- The average directional roughness normalized by hydraulic diameter (Ra/Dh) provides the best fit for determining the equivalent sand grain roughness from experimental data.
- Optimal material removal is essential to eliminate roughness peaks and planarize waviness. Abrasive methods effectively achieve planarization, whereas chemical milling does not allow for waviness to be completely eliminated. A minimum removal thickness of 60 µm per side is necessary to achieve a friction factor below 0.03. Removing 84 µm of material (40% more than the minimum) resulted in a further 7% reduction in friction factor.

Chapter 8

Summary and Recommendations

8.1 MAIN FINDINGS AND CONCLUSIONS

The research documented in this thesis concerns the laser powder directed energy deposition (LP-DED) process for fabricating large-scale compact heat exchangers. With an upper limit for the build volume that is over 17 times larger than the largest possible with powder bed fusion machines (as of 2024), LP-DED enables the fabrication of large and highly complex parts, enhancing performance, part consolidation, and the ability to process novel alloys. This investigation encompassed comprehensive characterization and experimental testing of LP-DED-fabricated microchannels, as well as post-process surface enhancements, focusing on critical surface texture and its impact on fluid flow. The findings are essential to bring to widespread adoption of a manufacturing solution that addresses challenges related to consistent geometry, wall thickness, and high surface texture, establishing LP-DED as a viable technology for current and future heat exchanger fabrication. To summarize the main results, each key research question is addressed separately in the following.

RQ 1: How is the surface texture of heat exchanger microchannels affected by the LP-DED fabrication process?

The surface texture of LP-DED walls is influenced by the build process parameters and feedstock including input power, travel speed, layer height, powder feed rate, and powder size distribution. Chapter 3 and Chapter 4 address this research question by treating experiments and the destructive evaluations of samples which enabled the full characterization of the relationship between process parameters, geometric constraints, and the mechanisms causing the surface texture. The focus was on the reduction of the as-built surface texture, which is five to seven times rougher than that of traditionally machined surfaces. Fine powder was shown to reduce surface texture but resulted in larger variations of surface texture and bulk density compared to coarse powder. Geometrical studies revealed that wall angles exceeding 30° require stiffening or supports to prevent failure, with surface texture largely influenced by powder adherence and melt pool irregularities.

The characterization of the surface texture resulting from LP-DED requires the identification and measurement of key parameters. These include both those deriving from 3D areal surface measurements and 2D directional (legacy) measurements, filtered according to the necessary surface topography and ISO standards (ISO 4288-1996 and ISO 25178-2:2021) which provide information about primary texture, roughness, and waviness. The study evaluated: average texture (Sa), core roughness (Sk), peak height and valley depth (Spk, Svk), skewness (Ssk), kurtosis (Sku), and directional parameters including average, maximum height, and peak roughness (Ra, Rz, Rp, Rpk), primary, average, and maximum profile (Pp, Pa, Pz), and average and peak waviness (Wa, Wp). The assessment and analysis of these parameters led to the conclusion that while many standard height (amplitude) parameters were relevant for comparing deposition processes, a more detailed characterization, combining amplitude and functional parameters (Sk, Vvv), and material ratio (Spk, Spd), is necessary to fully evaluate surface topography and correlate it with flow performance.

The build process is significantly influenced by several key parameters. The study reported in Chapter 3 focused on the production of boxes with 1 mm wall thickness. The as-built inner and outer surfaces were characterized by varying machine parameters and powder sizes. Critical machine parameters included motion control, laser and optics, and powder feed and deposition. All build parameters were evaluated using a design of experiments (DOE) to understand contributions to surface texture and interactions. Key build parameters that were identified were input power, travel speed, layer height, powder feed rate, and powder size distribution. Fine powder (10-45 µm) and coarse powder (45-105 µm) feedstock made through rotary atomization were used. Destructive characterization of samples revealed that 3D areal and 2D profile surface texture correlate with twice the measured powder diameter or with the diameter of partially melted powder at the melt pool's trailing edge.

Several adjustments can be made to the LP-DED technique to enhance the build process and improve surface texture. Surface roughness stems from excess or partially melted powder adhered to the trailing edge of the melt pool in addition to melt pool irregularities. Fine powder (10-45 µm) reduces average surface texture by 23% compared to coarse powder (45-105 µm) but results in a higher degree of variability of the texture. Inner surfaces exhibit higher roughness due to ricochets and recirculation, particularly in thin-wall depositions where powder efficiency is reduced to 10-20% (i.e., only 10-20% of the blown powder is captured in the melt pool). Analysis of variance indicated that powder size, layer height, and their interaction accounts for 90% of inner surface roughness and 95% of outer surface roughness. Fine powder also resulted in lower overall porosity (0.03% ±0.01%) compared to coarse powder (0.13% ±0.07%).

To minimize waviness and achieve uniform surfaces, optimal parameters include a lower laser power (<333 W), higher layer height (<0.28 mm), increased travel speed (800 mm/min), and increased powder feed rate (24.2 g/min). Specific optimal parameters for minimizing surface roughness are fine powder, laser power of 350 W, powder feed rate of 23 g/min, travel speed of 762 mm/min, and a low layer height of 0.229 mm. Although these settings reduce surface roughness, process economics must also be considered. When the layer height is decreased by 10%, the build time increases by 17%, while the roughness only increases by 6% (+1 µm).

Chapter 4 describes a study devoted to examining how varying geometries, particularly angles and channel sizes, affect surface texture in case coarse NASA HR-1 powder is employed. Several enclosed vertical tracks with a target wall thickness of 1 mm and inclination angles up to 45° were fabricated and characterized. Evaluations focused on wall thickness, as-built microstructure (resulting from the melt pool), and surface texture, including waviness and roughness. Walls with angles up to 30° built successfully, but greater values of the angle may result in build failure, potentially requiring the stiffening of the adjacent wall for structural integrity. It was showed that wall thickness increases exponentially for values of the inclination angle above a 30°. Surface texture is primarily influenced by excess powder adherence, melt pool irregularities causing material droop, and excess material, which becomes excessive at angles above 30°. For downskin surfaces, the mean roughness decreases with increasing wall angle, while upskin roughness peaks at 20° and then gradually reduces as powder adheres within valleys. Both downskin and upskin textures are dominated by irregular waviness caused by the melt pool. The samples featured crack-free, low-porosity (<0.14%) material at all considered angles.

Primary areal surface texture (Sa) increases with wall angle due to surface irregularities caused by the melt pool and material droop, with peaks more dominant on the downskin surface. Waviness and wall thickness also increases with wall angle due to chaotic surface irregularities due to material droop on the downskin. Upskin waviness results from excess material deposition above the nominal melt pool, driven by direct particle impingement and remelted material flow. Proper filtering of texture measurements was essential to segregate roughness and waviness, as improper filtering could lead to incorrect conclusions about texture mechanisms. A λc of 0.8 mm is an appropriate cut-off filter for these thin-wall samples. As the angle increases, the filtered average areal and directional surface roughness (Sa, Ra) of the downskin surface significantly decreases, contrary to what was observed in relation to L-PBF processes. The upskin surface roughness increases with particle count, peaking at 20° and then decreases as adhered powder fills voids at higher angles.

A correlation for estimating wall thickness was developed using data obtained from measurements performed on angled samples. Results from single-pass angled walls indicated that the directional maximum profile height (Rz) could be estimated using the maximum particle size distribution, with only particles smaller than 85 µm adhering to the downskin surface at angles above 35° due to higher rebounds and recirculation. The stair-stepping typically observed in surfaces resulting from LP-DED was not detected with a layer height of 0.254 mm and remelting of 4-5 previously deposited layers.

RQ 2: What are the geometrical relationships and sensitivities affecting fluid flow performance if heat exchanger channels are manufactured with the LP-DED process?

The geometrical relationships and sensitivities affecting fluid flow performance include the cross-sectional area, perimeter, and surface texture characteristics including roughness and waviness. Surface characteristics result from roughness peaks and valleys, waviness peaks and valleys, and the frequency, or density, of these features. Fluid flow performance was evaluated experimentally by varying the flow rate and measuring the flow resistance (discharge coefficient) and pressure drop along the channel length. Various surface finishing techniques, such as abrasive flow machining (AFM), chemical milling (CM), chemical mechanical polishing (CMP), electrochemical machining (PECM), and thermal energy method (TEM) were applied to modify the internal surfaces. The microchannel samples used for these experiments were fabricated from the NASA HR-1 Fe-Ni-Cr alloy. The friction factor estimated from samples featuring as-built surfaces is 0.097±0.00028, while surface enhancement techniques reduce it to 0.023±0.00033. Destructive evaluation of channels following testing provides the opportunity to derive critical insights into surface texture and geometry if tools like optical microscopy, SEM, and CT scanning are used for detailed analysis.

Surface texture parameters, including areal and directional characteristics, are instrumental in identifying peaks, valleys, and their densities as they relate to microchannels. Directional measurements are sensitive to the location of the profile line along the sample length, which can result in variations in peaks or valleys. In contrast, areal measurements are affected by less error because the entire surface is involved in the measurement. Notably, Sp indicates high variation since it is based on a single peak value across the surface. This highlights the importance of using reduced peak height (Spk) and core roughness (Sk) to avoid bias toward the value of a single peak height.

Microchannels produced through LP-DED can be used in their as-fabricated condition, but they may not meet the pressure drop requirements of many heat exchangers depending on their applications. Surface texture variations, such as powder adherence, melt pool undulations, and polishing mechanisms, significantly affect fluid flow performance. The experimental flow test results presented in Chapter 6 and 7 indicate that as-built surfaces cause high flow resistance due to powder adherence, which diminishes with material removal. Adhered powder particles increase flow resistance and disrupt the flow boundary sublayer causing the formation of micro-scale eddies. The discharge coefficient analysis put into evidence that 65% of the flow resistance variations are due to area alterations, 8% to perimeter changes, and 25% to surface texture.

Surface enhancement processes aimed at improving the discharge coefficient must reduce surface roughness, waviness peaks, and their frequency. A minimum surface material removal of 50 µm is required to reduce the mean friction factor by more than 30% while removing 70 µm, equivalent to the mean powder diameter, can reduce the mean friction factor by more than 57%. Post-processing steps such as eliminating adhered powder and planarizing surface peaks and valleys are critical to reducing friction factors and flow resistance.

The differential pressure along the length of LP-DED microchannels is caused mainly by roughness peaks, but other surface characteristics play an important role in the reduction of the friction factor below 0.05. Therefore, peak smoothing/reduction, roughness minimization, and combined waviness/valley reduction are critical to reducing the friction factor. Effective heat exchanger microchannels rely on accurate predictions, and detailed characterization validates the assumptions. The ratios between roughness and waviness peaks and densities (Spk/Spd and Wp/WPc) are proposed therefore as one of the key parameters for surface characterization as they are directly correlated to flow resistance. Additionally, values of the dale void volume (Vvv) can be used to detect where fluid could be trapped inside the surface valleys. Moreover, Vvv correlates with the reduction of friction factor. The analysis of Vvv over the surface can be used to identify the location of the transition from roughness-dominated to waviness-dominated surface effects, thus it can guide the design of material removal processes aimed at optimizing flow resistance.

RQ 3: What improvements can be made to control the surface texture of thin-wall LP-DED internal microchannels?

The ability of controlling the surface texture of thin-wall internal microchannels allows to effectively design flow passages complying with a specified friction factor. These surface improvement processes must be controlled in terms of the detailed characteristics of the surface texture and repeatability. It is of paramount importance that associated predictive models for the estimation of the relevant surface parameters are available.

Several post-processing techniques were evaluated using 600 mm-long sample channels, namely abrasive flow machining (AFM), chemical milling (CM), and chemical mechanical polishing (CMP). These techniques reduce texture by eliminating partially and fully adhered powder, minimizing waviness, and achieving planarization. Detailed characterization of resulting surfaces, in relation to process parameters, revealed different characteristics, including remnant powder, jagged edges, crystals, scratches, pitting, and selective grain boundary attack. Material removal varied among the considered enhancement techniques, with CM and CMP being the most effective in this regard, allowing the elimination of a layer of up to 355 µm per side. The increased cross-sectional area considerably reduces the pressure drop over the length of the channel, which is also due to the decrease of boundary layer turbulence. However, material removal should be minimized to avoid the cost of excessive processing time. Maximum material removal does not result in the lowest friction factor.

It was further demonstrated that surface enhancements produce distinct surface attributes, affecting surface-induced drag differently in relation to the variations in material removal mechanisms (i.e., chemical and abrasive), which in turn result in different surface characteristics in terms of peaks and valleys. Channel surface conditions varied widely if comparing as-built surface to enhanced surfaces, with filtered Ra ranging from 3.6 to 19.3 µm, primary Sa from 11.3 to 31.6 µm, primary Sk ranging from 33.9 to 99.8 µm, and Pp from 31.4 to 152.3 µm. These variations in texture result in values of the friction factor ranging from 0.097 to 0.023. These large variations indicate that, while the techniques can be effective, the aspect of repeatability needs to be carefully addressed to ensure uniform results.

The coefficient of variation was used to evaluate the consistency of surface enhancement results along the length of the microchannels using data from three distinct cross-sections. Variation in perimeter and area was attributed to random error, with a maximum cross-sectional area error of 2.5%, the same for all considered post-processing techniques. Perimeter error varied more than cross-sectional area, driven by randomly adhered powder on the internal channel walls. AFM processed channels featured the highest perimeter variation, namely 6.2%; CM samples exhibited consistent perimeter variation, lower than 2.8%; the perimeter variation of CMP samples was within 1.9%. These values indicate significant improvement of surface texture, as the as-built samples featured a perimeter value that was 26% greater than the nominal value (the design specification).

Differences between hydraulic diameter values estimated with analytical methods and values determined by means of experimental flow data highlight the need for improved models, as those presented in this thesis. Traditional hydraulic diameter correlations do not account for the impact of surface texture of its value, leading to significant errors due to the much higher value of the actual perimeter. A new method for calculating the hydraulic diameter (D_h), which is made dependent also on the values of the as-fabricated area and of the core surface texture (Sk), has been proposed and validated. The correlation improves the accuracy of the friction factor prediction to within 20% of the value obtained with experimental data, compared to 50% of the previous methods.

None of the existing friction factor correlations, including the Colebrook-White correlation, can correctly predict the value of the Darcy friction factor obtained from experimental data. Using the newly proposed hydraulic diameter definition, a modified sand grain roughness correlation was developed in order to predict values associated with surfaces with different textures. This method, accounting for surface roughness and waviness, provides a more accurate prediction of the equivalent sand grain roughness (KS) and of the resulting friction factor. Experimental data showed that the average directional roughness normalized by the value of the hydraulic diameter (Ra/D_h) provided the best fit for determining equivalent sand grain roughness, in agreement with experimental observations. Additional linear fit methods incorporated surface texture parameters Pp, Sa, and Sk and normalized by

Dh. It was also observed that Pp, which accounts for the effects of surface roughness and waviness, provides a reasonable first-order approximation of the equivalent sand grain roughness for as-built surfaces.

In summary, being able to control the surface texture of thin-wall internal microchannels manufactured with LP-DED requires a combination of effective post-processing techniques and improved modeling correlations. The driving mechanisms of surface texture affecting friction factor reduction were identified, including roughness peaks, peak smoothing/reduction, minimized roughness and combined waviness, and valley reduction. Abrasive methods like CMP allow to achieve a high level of planarization, whereas chemical milling leaves macro waviness remnants. A minimum removal thickness of 60 µm per side is necessary to achieve a friction factor below 0.03, with diminishing returns observed below this threshold. Removing 84 µm of material (40% more than the minimum) resulted in a further 7% reduction in friction factor.

8.2 KEY INNOVATIONS

The research work has contributed to the body of knowledge on the general topic by providing a baseline understanding of the various aspects associated to surface texture and their relation to process parameters, geometry (such as channel sizes, angles, and surface orientation), key surface texture parameters, mechanisms that affect flow resistance and friction factors, and material removal targets using surface enhancement post-processing to achieve a required surface specification. Research results provide designers with a variety of options to properly tailor the surface to the flow requirements, like the specification of the pressure drop due to the flow through the microchannels in compact heat exchangers.

The main research innovations achieved with this research include:

1. Determination of the build factors and relationships associated with the surface texture of 1 mm thick NASA HR-1 alloy surfaces obtained with the LP-DED process (see Chapter 3 and Chapter 4).

    - Previous state-of-the-art research primarily examined the microstructural aspects and mechanical properties of samples produced using the LP-DED process, with wall thicknesses ranging from 1 to 3 mm. There was very limited research on the effect of process parameters and on surface texture (roughness, waviness) of 1 mm vertical walls. No information related to thin walls made with the NASA HR-1 alloy was available. Prior studies concentrated on roughness without considering waviness or distinguishing between these surface texture differences. Additionally, the impact of build parameters on surface texture was not extensively explored, especially for the NASA HR-1 alloy.

2. Characterization and identification of geometric constraints for repeatable LP-DED fabrication of heat exchangers (see Chapter 4 and Chapter 5).

    - To the best of the author's knowledge, no prior research on microchannels produced using the LP-DED process is documented in the open literature. Additionally, prior literature on the subject lacks' information on the geometric aspects, angled wall limitations, surface texture, and the process mechanisms causing these geometric variations. The characterization of geometry and surface texture of internal microchannels and of various enclosed boxes fabricated at different angles provides foundational information for heat exchanger designers.

3. Evaluation and characterization of surface enhancement techniques for 2.5 mm square internal microchannel features manufactured with the LP-DED process to tailor required flow characteristics (see Chapter 6 and Chapter 7).

    - Prior investigations on surface enhancement techniques focused exclusively on their application to additively manufactured laser powder bed fusion (L-PBF) samples. The geometric characterization of the process and channels allowed to conclude that the LP-DED process is fundamentally different from L-PBF. Conclusions from L-PBF research cannot be applied broadly to other AM processes, including LP-DED. This experimental study is the first concerning various surface enhancements applied to microchannels manufactured with the LP-DED process. For the first time, different surface texture mechanisms caused by distinct enhancement techniques were identified, including peak smoothing/reduction, minimized roughness, combined waviness, and valley reduction. Previous L-PBF samples were limited to less than 250 mm due to build constraints. This research develops and characterizes surface-enhanced samples that are 600 mm long, a 140% increase in length.

4. Development of an analytical model and correlation to estimate the pressure drop of high-roughness channels fabricated with LP-DED. The correlation is validated with experimental data (Chapter 7).

    - Friction factors and pressure drop associated with LP-DED made microchannels in both the as-built and surfaced enhanced state have been investigated for the first time. Considered surface treatments include abrasive flow machining, chemical milling, and chemical mechanical polishing. A wide range of surface conditions were obtained and allowed to develop a new correlation for the calculation of the hydraulic diameter of square channels. Additionally, based on experimental data resulting from flow tests, a new correlation to determine sand grain roughness, friction factors and pressure drop was developed. The correlation allows prediction of these values with a deviation of less than 20% with respect to experimental data.

8.3 FUTURE APPLICATIONS AND RESEARCH AREAS

8.3.1 Initial Application Cases

The research effort documented in this dissertation is integrated into a broader investigation concerning the use of the LP-DED process for the fabrication of components of liquid rocket engines. Although demonstrating and testing components were outside the scope of the work documented here, findings on channel characterization and build limitations from this research contributed to the design of nozzle and combustion chamber prototypes. Several channel-cooled nozzles made with the NASA HR-1 alloy were constructed and underwent hot-fire testing aimed at proving initial feasibility. These nozzles were tested using various propellant combinations including Liquid Oxygen/Liquid Hydrogen (LOX/LH2), LOX/Kerosene (LOX/RP-1), and LOX/Methane (LOX/CH4). The hot-fire testing campaigns took place at NASA Marshall Space Flight Center (MSFC) at thrust classes ranging from 8.9 to 178 kN. The testing demonstrated the suitability of the LP-DED process and of the alloy in a relevant environment, validated design assumptions, and allow to determine the heat transfer and pressure drop characteristics associated with various designs. A total of 488 starts were performed and the total duration of these tests was 16,291 seconds, whereby 12 nozzles were examined [13,321].

A single nozzle featuring a thrust of 8.9 kN accumulated 207 starts and 6,756 seconds of testing time with consistent performance between tests [254,321]. Figure 8.1 displays nozzles that were fabricated and successfully tested with as-built surface channels. While the NASA HR-1 alloy was demonstrated in the extreme environment, additional design and post-processing lessons were learned, like, for example, those related to more advanced polishing techniques. All this knowledge is essential to progress towards the use of these nozzles in actual missions. It can be argued that the results of the research documented here is essential to mature this manufacturing technology to the level that is needed for space flight and possibly other industrial applications.

In addition to the hot-fire demonstrations, large-scale manufacturing trials were also completed. A 1.52 m dia. and 1.78 m height integral channel nozzle made of NASA HR-1 alloy was built in 90 days. This is estimated to be four to six times faster than producing a traditionally manufactured unit for the first time. Additionally, a chamber was fabricated, also made of NASA HR-1, and used as a simulator for a nuclear thermal propulsion (NTP) engine. Examples of these large-scale manufacturing trials are shown in Figure 8.1. These manufacturing trials demonstrated a significant opportunity for schedule and cost reductions compared to traditional manufacturing technologies. The results have garnered active interest across the commercial space sector, highlighting the potential for manufacturing large-scale channel wall nozzles and combustion chambers using LP-DED.

Figure 8.1. Examples of LP-DED nozzles during hot-fire testing and fabrication. A) 178 kN integral channel on the test stand, B) Hot-fire testing of the 178 kN nozzle using LOX/LH2, C) 8.9 kN integral channel nozzle, D) NASA HR-1 nozzle accumulating 207 starts and 6,756 sec during test, E) Manufacturing trial of 1.52 m dia. and 1.78 m height integral channel nozzle, F) Manufacturing trial of NTP LP-DED chamber. (Courtesy: NASA) [254,321]

8.3.2 Future Applications

Several applications of the LP-DED process for the manufacturing of large compact heat exchangers for extreme environments can be envisaged for both terrestrial use and space exploration. Efficient and sustainable power generation will require novel high temperature compact heat exchangers. Examples are primary heat exchangers and recuperators of supercritical CO_2 cycle power plants, heat exchangers in hydrogen gas turbines, etc. Transitioning to hydrogen as a fuel source can significantly reduce carbon dioxide emissions, and compact novel suitable heat exchangers are key enablers of these new power technologies. Other potential uses in power generation include heat exchangers in solar thermal energy power plants. However, these heat exchangers will require the adoption of other materials and manufacturing processes, different from those treated in this dissertation.

The aviation industry is also exploring hydrogen as a more sustainable fuel. Future propulsion systems may include gas turbine engines, fuel cells, or hybrid systems that incorporate compact heat exchangers [322].The realization of supersonic commercial aircraft and hypersonic vehicles will require active cooling in leading edges and control surfaces, which can be obtained with microchannels integrated into large structures.

Future exploration missions will require in-space cryocooler storage for propellants with active cooling to prevent boil-off. The stored fuel can be used for propulsion systems, lunar or Martian power plants, resource extraction, and chemical or life support systems. Additionally, managing the extreme temperature fluctuations in space will require efficient spacecraft radiators. The complexity of these systems can be addressed through manufacturing methods like LP-DED and the use of hydrogen-resistant alloys.

8.4 RECOMMENDATIONS

8.4.1 Design and Analysis

Chapter 7 of this thesis describes the evaluation of various surface conditions and provides new correlations for determining the hydraulic diameter of square microchannels. Many numerical simulation methods do not take into account the complex effect of surface texture, and these new correlations should be integrated into flow models to enhance prediction accuracy. Additionally, the data sets from this research offer an opportunity to develop a new version of the Moody diagram, accounting for the intricacies of additively manufactured surfaces. Machine learning techniques could be employed to analyze the extensive data sets generated during this research. This approach could include not only the experimental test data but also the images, allowing for further improvement of the predictions of friction factors and flow resistances related to detailed surface topography.

The design and analysis of heat exchangers are highly interdisciplinary, involving both heat transfer and fluid dynamics. Future experiments should incorporate the investigation of heat transfer phenomena to determine Nusselt correlations depending on variations of the surface textures. These experiments should encompass varying channel sizes, materials, and fluids, including both liquids and gases, across a range of Reynolds numbers and surface conditions. Flow visualization on a micro-scale could also be included. Although the correlation between different types of roughness and waviness with respect to the variation in friction factors was established, visual confirmation of flow structures would enhance future modeling efforts. A challenge with this type of experiment is that using clear acrylic for visualization may diminish some of the three-dimensional flow effects.

8.4.2 Process Specific

If other materials will be studied in the future, factors such as build parameters, solidification rates, geometry (including channel sizes), powder efficiency, and heat treatment operations may alter the absolute values of surface texture. Evaluating other materials is essential to expand the database of alloys suitable for future compact high-temperature heat exchangers fabricated with LP-DED. Varying heat treatments of the NASA HR-1 alloy may slightly change the surface texture due to oxidation or the removal of partially adhered powder resulting from high thermal gradients.

Chapter 4 reports a study of surface texture with varying angles. Further research could investigate complex surfaces or variable channel geometries and the results would contribute to making available additional design solutions. These surfaces might include complex freeform surfaces or structures optimized through shape or topology optimization.

The post-processing surface modifications resulted in observations that included remnant powder, jagged edges and crystals, scratches, pitting or selective grain boundary attack. Some of these conditions merit an additional characterization effort since they could affect mechanical properties of the material. The jagged edges, scratches, pitting, and grain boundary attack might result in reduced fatigue life due the surface defects. Controlled mechanical testing should be conducted with the identical processing parameters to determine any debits to properties.

An important aspect related to this research in relation to the industrialization of the LP-DED is the tradeoff between the specification of the surface texture and the associated processing time and cost. This aspect was not addressed, and more specifically the lifecycle processing cost, specialty tooling, processing challenges, or processing timeline. The post-processing methods documented in Chapters 6 and 7 focused on more mature techniques, which are becoming accessible to the industry. Combining multiple techniques may provide an optimal solution that meets both technical and cost/programmatic specifications.

8.4.3 Production and Operation

As discussed in Chapter 2, the implications of surface texture on the production of system and components are often overlooked during the initial design phase. Bridging the gap between theoretical analysis and the practical challenges of manufacturing and achieving design specifications in the shortest possible time may require additional education or training for designers. Surface conditions can also change during operation due to factors such as erosion, wear, corrosion, oxidation, or other environmental influences. As AM processes become more common in industry, the long-term effects on surface texture during operation will need to be investigated. More data should be collected and publicly shared to identify performance shifts, determine their root causes, and assess their relation to potential changes in surface texture.

Early collection of surface texture data during the manufacturing process can help reduce uncertainty. The use of surface texture witness specimens is important as components using the LP-DED process enter production. An open channel, as proposed by Thiam [323], can be built alongside the part and measured to represent the closed internal microchannels. These data can then be used to reduce uncertainty in the analysis prior to actual testing, and early in the manufacturing phase. Based on the surface texture, the K_F value from this dissertation can be applied to improve predictions and reduce uncertainty.

8.5 REFLECTIONS

Designing components, such as compact heat exchangers, may seem "easy" if compared to the challenges encountered during their manufacturing. Manufacturing can yield non-conformances due to incorrect design assumptions, human error, integration or planning issues, or simply unforeseen circumstances. Similarly, planning might appear straightforward, but execution can falter. Research is no different—what seems like a simple path from A to B is rarely a straight line. This iterative process defines becoming an independent researcher. It involves methodically exploring every aspect to fully characterize the process using the scientific method, connecting previously unrelated topics, and constructing a comprehensive story.

I initially spent considerable time on literature searches regarding various heat exchanger topics, but felt overwhelmed by too many papers lacking focus and relevance. Although I thought I had scoped my topic, I did not grasp all the nuances until I started laboratory work and understood which questions needed to be asked. Developing a new process for manufacturing heat exchangers revealed many unknowns in the planning stage. I recommend maintaining flexibility in planning, as seemingly unimportant aspects might become crucial later. A schedule should be a living document, continuously updated. This approach proved true when characterizing the LP-DED samples at various angles, leading to insights that resulted in an unplanned but valuable journal article. Further characterization of surface enhancement techniques for LP-DED samples at varying angles is recommended to determine optimal processing parameters.

Challenging prior "facts" can be difficult, as I found when determining the hydraulic diameter. Using a known relationship did not match my assumptions, leading me to question my methods. Initially, I believed I had collected too many data, which caused me months of doubt. While it was ultimately beneficial for revealing challenges with the hydraulic diameter and evaluating various surface conditions, it was exhausting to measure, characterize, and evaluate dozens of measurements per tube (resulting in hundreds of channel sections to evaluate). In hindsight, a smaller data set might have led to similar results, if the importance of each measurement was correctly prioritized. Early test trials with one or two samples could help prioritize data sets, saving time in the end.

My current career trajectory has led me to the point where I contribute and lead research instead of solely “consuming” it. Throughout the years that led to this thesis, the term "independent researcher" resonated with me, a definition first mentioned by my supervisors. I noticed a gradual shift in how I reviewed and evaluated prior published research, often feeling frustrated by missing steps, incomplete data, or incorrect terminology. The term "roughness" is frequently misused in journal articles, defined incorrectly by data filtering. This realization led me to consult both experts and literature to ensure I used terms correctly. Accepted common terms might not always be accurate, and repeated incorrect references do not make them true.

My interactions with my supervisors, Dr. Angelo Cervone and Prof. Piero Colonna, were invaluable. These meetings often led to realizations, criticisms, and adjustments in planning and execution. While I sometimes sought confirmation that I had done something correctly, I did not always receive it. This was not negative; it made me realize that at a detailed research level, my supervisors might not have all the answers. Instead, they questioned my methodology and offered feedback, helping me to affirm or further probe my approach. From that process, I also learned how to guide others in their research, even if I am not the expert. A skill that an independent researcher is required to have. As undergraduates, we are taught that answers are in the back of the book. In the real world, we realize multiple answers exist. This research showed that we are developing new correlations, questioning prior assumptions and research, and adding to the overall body of knowledge as an independent researcher.

In the final six months of my analysis and writing, several questions arose, as outlined in section 8.4, but remained unanswered due to time and resource constraints. Developing and characterizing a new process for this application required substantial resources for maturation. Fully exploring every detail demanded more effort than initially anticipated, leading to a necessary rescoping of the research to a more achievable focus. I hope to collaborate with future researchers to expand this topic further. I look forward to the opportunity to incorporate heat transfer with pressure drop for different fluids, integrate this information into simulation codes, and conduct future experiments using flow visualization. Additionally, it will be critical to obtain mechanical properties (e.g., fatigue) with different surface enhancement methods and understand the processing economics to incorporate into actual applications. Although this dissertation concludes the research, my curiosity and desire to see it used by others is ultimately the highest compliment I strive for.

References

[1] J.E. Hesselgreaves, R. Law, D.A. Reay, Compact Heat Exchangers: Selection, Design and Operation, 2nd ed., Elsevier, 2016. https://www.sciencedirect.com/book/9780081003053/compact-heat-exchangers.

[2] S. Mahmoudinezhad, M. Sadi, H. Ghiasirad, A. Arabkoohsar, A comprehensive review on the current technologies and recent developments in high-temperature heat exchangers, Renew. Sustain. Energy Rev. 183 (2023) 113467. https://doi.org/10.1016/j.rser.2023.113467.

[3] K.A. Thole, S.P. Lynch, A.J. Wildgoose, Review of advances in convective heat transfer developed through additive manufacturing, 1st ed., Elsevier Inc., 2021. https://doi.org/10.1016/bs.aiht.2021.06.004.

[4] T. Teasley, B. Williams, A. Larkey, C. Protz, P. Gradl, A Review Towards the Design Optimization of High-Performance Additively Manufactured Rotating Detonation Rocket Engine Injectors, AIAA Propuls. Energy Forum, 2021. (2021). https://doi.org/10.2514/6.2021-3655.

[5] P. Gradl, A. Cervone, P. Colonna, Integral Channel Nozzles and Heat Exchangers using Additive Manufacturing Directed Energy Deposition NASA HR-1 Alloy, in: 73rd Int. Astronaut. Congr., Paris, France, 2022: p. IAC-22,C4,2,x73690.

[6] P. Gradl, O.R. Mireles, C. Katsarelis, T.M. Smith, J. Sowards, P. Chen, D. Tinker, C. Protz, T. Teasley, D.L. Ellis, C. Kantzos, Advancement of Extreme Environment Additively Manufactured Alloys for Next Generation Space Propulsion Applications, in: 73rd Int. Astronaut. Congr., International Astronautical Federation, Paris, France, 2022: pp. 18–22.

[7] T.M. Fedotowsky, B.B. Williams, P.R. Gradl, D.C. Tinker, J. Iten, A. Manerbino, A. Polizzi, Al6061-RAM2 Development and Hot-Fire Testing using Additive Manufacturing Laser Powder Directed Energy Deposition for Liquid Rocket Engine Channel-Cooled Nozzles, in: AIAA Scitech 2024, Orland, FL, 2024: pp. 8–12. https://doi.org/https://doi.org/10.2514/6.2024-0994.

[8] J.E. Bradford, A.C. Charania, B.S. Germain, REDTOP-2: Rocket engine design tool featuring engine performance, weight, cost, and reliability, 40th AIAA/ASME/SAE/ASEE Jt. Propuls. Conf. Exhib. (2004). https://doi.org/10.2514/6.2004-3514.

[9] J.L. Emdee, Liquid Propulsion: Systems Engineering, Design Trades, and Testing, Encycl. Aerosp. Eng. (2010). https://doi.org/10.1002/9780470686652.EAE111.

[10] J.B. Calvo, K. Hannemann, Analysis of the Heat Transfer in Liquid Rocket Engine Cooling Channels, New Results Numer. Exp. Fluid Mech. VII. Notes Numer. Fluid Mech. Multidiscip. Des. 112 (2010) 441–448. https://doi.org/10.1007/978-3-642-14243-7_54.

[11] G.P. Sutton, O. Biblarz, Rocket Propulsion Elements, 9th ed., Wiley, 2016. https://www.wiley.com/en-us/Rocket+Propulsion+Elements%2C+9th+Edition-p-9781118753910.

[12] D.K. Huzel, D.H. Huang, Modern Engineering for Design of Liquid-Propellant Rocket Engines, American Institute of Aeronautics and Astronautics, Reston, VA, 1992. https://doi.org/10.2514/4.866197.

[13] P.R. Gradl, C.S. Protz, Technology advancements for channel wall nozzle manufacturing in liquid rocket engines, Acta Astronaut. 174 (2020). https://doi.org/10.1016/j.actaastro.2020.04.067.

[14] A.B. Aminov, K.E. Dubrovsky, Influence of Brazing Process Parameters on the Strength of Liquid Rocket Engine Brazed Structures, IOP Conf. Ser. Mater. Sci. Eng. 491 (2018). https://iopscience.iop.org/article/10.1088/1757-899X/491/1/012034.

[15] P.R. Gradl, Rapid fabrication techniques for liquid rocket channel wall nozzles, in: 52nd AIAA/SAE/ASEE Jt. Propuls. Conf. 2016, American Institute of Aeronautics and Astronautics Inc, AIAA, 2016. https://doi.org/10.2514/6.2016-4771.

[16] P.R. Gradl, C.S. Protz, Channel wall nozzle manufacturing technology advancements for liquid rocket engines, in: Proc. Int. Astronaut. Congr. IAC, Washington, DC, 2019.

[17] H. Immich, J. Alting, J. Kretschmer, D. Preclik, Technologies for thrust chambers of future launch vehicle liquid rocket engines, 38th AIAA/ASME/SAE/ASEE Jt. Propuls. Conf. Exhib. (2002). https://doi.org/10.2514/6.2002-4143.

[18] P.G. Han, K.H. Kim, Y.C. Woo, Development of liquid rocket engines using liquefied natural gas in Hyundai MOBIS, 41st Aerosp. Sci. Meet. Exhib. (2003). https://doi.org/10.2514/6.2003-128.

[19] A. Boman, J. Häggander, J. Hass, Laser welded channel wall nozzle design, manufacturing and hot gas testing, 35th Jt. Propuls. Conf. Exhib. (1999) 1–8. https://doi.org/10.2514/6.1999-2750.

[20] R. Holmes, S. Elam, T. McKechenie, R. Hickman, Robust Low Cost Liquid Rocket Combustion Chamber By Advanced Vacuum Plasma Process, in: Sp. Congr. Proceedings. 8, 2002. https://commons.erau.edu/space-congress-proceedings/proceedings-2002-39th/april-30-2002/8 (accessed August 1, 2022).

[21] J. Fint, M.B. Hankins, M.L. Jew, D.G. Ulmer, B.L. Wherley, W.D. Romine, F.M. Kuck, D.S. Ades, Method of fabricating a rocket engine nozzle using pressure brazing, 8,127,443, 2012. https://patents.google.com/patent/US8127443B2/en.

[22] U. Högman, R. Rydén, The volvo aero laser welded sandwich nozzle, 40th AIAA/ASME/SAE/ASEE Jt. Propuls. Conf. Exhib. (2004) 1–9. https://doi.org/10.2514/6.2004-3677.

[23] P.R. Gradl, T.W. Teasley, C.S. Protz, M.B. Garcia, D. Ellis, C. Kantzos, Advancing GRCop-based Bimetallic Additive Manufacturing to Optimize Component Design and Applications for Liquid Rocket Engines, in: AIAA Propuls. Energy 2021, 2021: pp. 1–28. https://doi.org/10.2514/6.2021-3231.

[24] S. Contant, Design and Optimization of a Small Reusable Launch Vehicle Using Vertical Landing Techniques, Delft University of Technology, 2019. http://resolver.tudelft.nl/uuid:58cb0a6e-e9ac-4ce5-9051-5ddd863e98a8.

[25] H.W. Jones, The Future Impact of Much Lower Launch Cost, in: 48th Int. Conf. Environ. Syst., International Conference on Environmental Systems, Albuquerque, NM, 2018: pp. 1–11. https://ttu-ir.tdl.org/handle/2346/74068.

[26] F. Kerstens, A. Cervone, P. Gradl, End to end process evaluation for additively manufactured liquid rocket engine thrust chambers, Acta Astronaut. 182 (2021) 454–465. https://doi.org/10.1016/j.actaastro.2021.02.034.

[27] R.K. Leach, D. Bourell, S. Carmignato, A. Donmez, N. Senin, W. Dewulf, Geometrical metrology for metal additive manufacturing, CIRP Ann. 68 (2019) 677–700. https://doi.org/10.1016/j.cirp.2019.05.004.

[28] B. Lu, F. Mei, W.J. Meng, S. Guo, Fabrication of metal-based microchannel heat exchangers and quantification of their liquid flow and heat transfer characteristics, Heat Transf. Eng. 34 (2013) 15–28. https://doi.org/10.1080/01457632.2013.694733.

[29] W. Grzesik, B. Kruszynski, A. Ruszaj, Surface integrity of machined surfaces, Surf. Integr. Mach. (2010) 143–179. https://doi.org/10.1007/978-1-84882-874-2_5/COVER.

[30] G.J. Schiller, Additive manufacturing for Aerospace, IEEE Aerosp. Conf. Proc. 2015-June (2015). https://doi.org/10.1109/AERO.2015.7118958.

[31] J.R. McDonough, A perspective on the current and future roles of additive manufacturing in process engineering, with an emphasis on heat transfer, Therm. Sci. Eng. Prog. 19 (2020) 100594. https://doi.org/10.1016/j.tsep.2020.100594.

[32] A. Vafadar, F. Guzzomi, A. Rassau, K. Hayward, Advances in Metal Additive Manufacturing: A Review of Common Processes, Industrial Applications, and Current Challenges, Appl. Sci. 11 (2021) 1213. https://doi.org/10.3390/app11031213.

[33] H.R. Kotadia, G. Gibbons, A. Das, P.D. Howes, A review of Laser Powder Bed Fusion Additive Manufacturing of aluminium alloys: Microstructure and properties, Addit. Manuf. 46 (2021) 102155. https://doi.org/10.1016/j.addma.2021.102155.

[34] Z. Liu, B. He, T. Lyu, Y. Zou, A Review on Additive Manufacturing of Titanium Alloys for Aerospace Applications: Directed Energy Deposition and Beyond Ti-6Al-4V, Jom. (2021). https://doi.org/10.1007/s11837-021-04670-6.

[35] Y. Zhang, L. Wu, X. Guo, S. Kane, Y. Deng, Y.-G. Jung, J.-H. Lee, J. Zhang, Additive Manufacturing of Metallic Materials: A Review, J. Mater. Eng. Perform. 27 (2017) 1–13. https://doi.org/10.1007/s11665-017-2747-y.

[36] P. Gradl, D. Tinker, A. Park, O. Mireles, M. Garcia, R. Wilkerson, C. Mckinney, Robust Metal Additive Manufacturing Process Selection and Development for Aerospace Components, J. Mater. Eng. Performance, Springer. (2021). https://doi.org/10.1007/s11665-022-06850-0.

[37] B. Blakey-Milner, P. Gradl, G. Snedden, M. Brooks, J. Pitot, E. Lopez, M. Leary, F. Berto, A. du Plessis, Metal additive manufacturing in aerospace: A review, Mater. Des. 209 (2021) 110008. https://doi.org/10.1016/j.matdes.2021.110008.

[38] H. Bikas, S. Koutsoukos, P. Stavropoulos, A decision support method for evaluation and process selection of additive manufacturing, Procedia CIRP. 81 (2019) 1107–1112. https://doi.org/10.1016/j.procir.2019.03.261.

[39] V.C. Sobota, G. van de Kaa, T. Luomaranta, M. Martinsuo, J. Roland Ortt, Factors for metal additive manufacturing technology selection, J. Manuf. Technol. Manag. 32 (2021) 1741–1779. https://doi.org/10.1108/JMTM-12-2019-0448.

[40] M. Bhuvanesh Kumar, P. Sathiya, Methods and materials for additive manufacturing: A critical review on advancements and challenges, Thin-Walled Struct. 159 (2021) 107228. https://doi.org/10.1016/j.tws.2020.107228.

[41] A. du Plessis, N. Razavi, M. Benedetti, S. Murchio, M. Leary, M. Watson, D. Bhate, F. Berto, Properties and applications of additively manufactured metallic cellular materials: A review, Prog. Mater. Sci. 125 (2022) 100918. https://doi.org/10.1016/j.pmatsci.2021.100918.

[42] D. Herzog, K. Asami, C. Scholl, Design guidelines for laser powder bed fusion in Inconel 718, 012015 (2022). https://doi.org/10.2351/7.0000508.

[43] A. Ewald, J. Schlattmann, Design guidelines for laser metal deposition of lightweight structures, LIA Today. 26 (2018) 16–19. https://doi.org/10.2351/1.5040612.

[44] S. Gruber, C. Grunert, M. Riede, E. López, A. Marquardt, F. Brueckner, C. Leyens, Comparison of dimensional accuracy and tolerances of powder bed based and nozzle

based additive manufacturing processes, J. Laser Appl. 32 (2020) 032016. https://doi.org/10.2351/7.0000115.

[45] Z. Wu, S.P. Narra, A. Rollett, Exploring the fabrication limits of thin-wall structures in a laser powder bed fusion process, Int. J. Adv. Manuf. Technol. 110 (2020) 191–207. https://doi.org/10.1007/s00170-020-05827-4.

[46] J. Berez, M. Praniewicz, C. Saldana, Assessing laser powder bed fusion system geometric errors through artifact-based methods, Procedia Manuf. 53 (2021) 395–406. https://doi.org/10.1016/j.promfg.2021.06.042.

[47] B. Fotovvati, E. Asadi, Size effects on geometrical accuracy for additive manufacturing of Ti-6Al-4V ELI parts, Int. J. Adv. Manuf. Technol. 104 (2019) 2951–2959. https://doi.org/10.1007/s00170-019-04184-1.

[48] P.R. Gradl, D.C. Tinker, J. Ivester, S.W. Skinner, T. Teasley, J.L. Bili, Geometric Feature Reproducibility for Laser Powder Bed Fusion (L-PBF) Additive Manufacturing with Inconel 718, Addit. Manuf. 47 (2021) 102305. https://doi.org/10.1016/j.addma.2021.102305.

[49] P.R. Gradl, C.S. Protz, M. Le Corre, O.R. Mireles, F. Medina, M. Kottman, M. Norfolk, L. Ajdelsztajn, P. Allison, A. Elliott, Y. Bandari, Metal Additive Manufacturing Processes and Selection, in: P. Gradl, O.R. Mireles, C.S. Protz, C.P. Garcia (Eds.), Met. Addit. Manuf. Propuls. Appl., 1st ed., American Institute of Aeronautics and Astronautics, Inc., 2022: pp. 49–186. https://doi.org/10.2514/5.9781624106279.0049.0186.

[50] S.A. Niknam, M. Mortazavi, D. Li, Additively manufactured heat exchangers: a review on opportunities and challenges, Int. J. Adv. Manuf. Technol. 112 (2021) 601–618. https://doi.org/10.1007/s00170-020-06372-w.

[51] Paul R. Gradl, Omar R. Mireles, Christopher S. Protz, Chance P. Garcia, Metal Additive Manufacturing for Propulsion Applications, 1st ed., American Institute of Aeronautics and Astronautics, Inc., Reston, VA, 2022. https://doi.org/10.2514/4.106279.

[52] P.R. Gradl, S.E. Greene, C. Protz, B. Bullard, J. Buzzell, C. Garcia, J. Wood, K. Cooper, J. Hulka, R. Osborne, Additive manufacturing of liquid rocket engine combustion devices: A summary of process developments and hot-fire testing results, in: 2018 Jt. Propuls. Conf., American Institute of Aeronautics and Astronautics Inc, AIAA, 2018. https://doi.org/10.2514/6.2018-4625.

[53] T. Ghidini, M. Grasso, J. Gumpinger, A. Makaya, B.M. Colosimo, Additive manufacturing in the new space economy: Current achievements and future perspectives, Prog. Aerosp. Sci. 142 (2023) 100959. https://doi.org/10.1016/J.PAEROSCI.2023.100959.

[54] K.-O. Lee, B. Lim, D.-J. Kim, M. Hong, K. Lee, Technology Trends in Additively Manufactured Small Rocket Engines for Launcher Applications, J. Korean Soc. Propuls. Eng. 24 (2020) 73–82. https://doi.org/10.6108/KSPE.2020.24.2.073.

[55] P.R. Gradl, C.S. Protz, D.L. Ellis, S.E. Greene, Progress in additively manufactured copper-alloy GRCop-84, GRCop-42, and bimetallic combustion chambers for liquid rocket engines, in: Proc. Int. Astronaut. Congr. IAC 2019, 2019: pp. 21–25.

[56] P.R. Gradl, C. Protz, K. Cooper, C. Garcia, D. Ellis, L. Evans, GRCop-42 development and hot-fire testing using additive manufacturing powder bed fusion for channel-cooled combustion chambers, in: AIAA Propuls. Energy Forum Expo. 2019, American Institute of Aeronautics and Astronautics Inc, AIAA, 2019. https://doi.org/10.2514/6.2019-4228.

[57] T.W. Teasley, P.R. Gradl, M.B. Garcia, B.B. Williams, C.S. Protz, Extreme Environment Hot Fire Durability of Post Processed Additively Manufactured GRCop-Alloy Combustion Chambers, in: AIAA Propuls. Energy 2021, 2021: pp. 1–20. https://doi.org/10.2514/6.2021-3233.

[58] S. Tsopanos, M. Wong, I. Owen, C.J. Sutcliffe, Manufacturing Novel Heat Transfer Devices by Selective Laser Melting, Manufacturing. (2006). https://doi.org/10.1615/ihtc13.p13.40.

[59] X. Zhang, R. Tiwari, A.H. Shooshtari, M.M. Ohadi, An additively manufactured metallic manifold-microchannel heat exchanger for high temperature applications, Appl. Therm. Eng. 143 (2018) 899–908. https://doi.org/10.1016/j.applthermaleng.2018.08.032.

[60] B. Meng, M. Wan, R. Zhao, Z. Zou, H. Liu, Micromanufacturing technologies of compact heat exchangers for hypersonic precooled airbreathing propulsion: A review, Chinese J. Aeronaut. June 2020 (2020). https://doi.org/10.1016/j.cja.2020.03.028.

[61] S.M. Thompson, Z.S. Aspin, N. Shamsaei, A. Elwany, L. Bian, Additive manufacturing of heat exchangers: A case study on a multi-layered Ti–6Al–4V oscillating heat pipe, Addit. Manuf. 8 (2015) 163–174. https://doi.org/10.1016/j.addma.2015.09.003.

[62] C. Zhang, S. Wang, J. Li, Y. Zhu, T. Peng, H. Yang, Additive manufacturing of products with functional fluid channels: A review, Addit. Manuf. 36 (2020) 101490. https://doi.org/10.1016/j.addma.2020.101490.

[63] E. Klein, J. Ling, V. Aute, Y. Hwang, R. Radermacher, A Review of Recent Advances in Additively Manufactured Heat Exchangers, Int. Refrig. Air Cond. Conf. (2018) 1–10. https://docs.lib.purdue.edu/iracc%0Ahttps://docs.lib.purdue.edu/iracc/1983.

[64] X. Zhang, H. Keramati, M. Arie, F. Singer, R. Tiwari, A. Shooshtari, M. Ohadi, Recent Developments in High Temperature Heat Exchangers: A Review, Front. Heat Mass Transf. 11 (2018) 11–18. https://doi.org/10.5098/hmt.11.18.

[65] S. Zhang, W. Seiya, 3D Printing as an Alternative ManufacturingMethod for the Micro gas Turbine Heat Exchanger, DIVA. (2015). https://www.diva-portal.org/smash/record.jsf?pid=diva2%3A845180&dswid=-9954.

[66] E. Handler, A. Sterling, J. Pegues, H. Ozdes, M. Masoomi, N. Shamsaei, S. Thompson, Design and Process Considerations for Effective Additive Manufacturing of Heat Exchangers, 2019. https://sffsymposium.engr.utexas.edu/sites/default/files/2017/Manuscripts/DesignandProcessConsiderationsforEffectiveAd.pdf.

[67] F. Ascione, A. Conrozier, A. Sakly, P. Planquart, J.M. Hugo, D. Laboureur, Aerothermal Characterization of a Compact Heat Exchanger Element By Additive Manufacturing, (n.d.).

[68] T. DebRoy, H.L. Wei, J.S. Zuback, T. Mukherjee, J.W. Elmer, J.O. Milewski, A.M. Beese, A. Wilson-Heid, A. De, W. Zhang, Additive manufacturing of metallic components – Process, structure and properties, Prog. Mater. Sci. 92 (2018) 112–224. https://doi.org/10.1016/j.pmatsci.2017.10.001.

[69] M. Alsulami, M. Mortazavi, S.A. Niknam, D. Li, Design complexity and performance analysis in additively manufactured heat exchangers, Int. J. Adv. Manuf. Technol. 110 (2020) 865–873. https://doi.org/10.1007/s00170-020-05898-3.

[70] F. Careri, R.H.U. Khan, C. Todd, M.M. Attallah, Additive Manufacturing of Heat Exchangers in Aerospace Applications : A, Appl. Therm. Eng. (2023) 121387. https://doi.org/10.1016/j.applthermaleng.2023.121387.

[71] P.R. Gradl, C.S. Protz, C.P. Garcia, O.R. Mireles, M. Leary, Introduction to and Applications of Additive Manufacturing for Propulsion, Met. Addit. Manuf. Propuls. Appl. (2022) 1–48. https://doi.org/10.2514/5.9781624106279.0001.0048.

[72] C. Dordlofva, P. Törlind, Qualification challenges with additive manufacturing in space applications, Solid Free. Fabr. 2017 Proc. 28th Annu. Int. Solid Free. Fabr. Symp. - An Addit. Manuf. Conf. SFF 2017. (2020) 2699–2712.

[73] A. Dass, A. Moridi, State of the Art in Directed Energy Deposition: From Additive Manufacturing to Materials Design, Coatings. 9 (2019) 418. https://doi.org/10.3390/coatings9070418.

[74] D.G. Ahn, Directed Energy Deposition (DED) Process: State of the Art, Korean Society for Precision Engineering, 2021. https://doi.org/10.1007/s40684-020-00302-7.

[75] A. Singh, S. Kapil, M. Das, A comprehensive review of the methods and mechanisms for powder feedstock handling in directed energy deposition, Addit. Manuf. 35 (2020) 101388. https://doi.org/10.1016/J.ADDMA.2020.101388.

[76] T. Lehmann, D. Rose, E. Ranjbar, M. Ghasri-Khouzani, M. Tavakoli, H. Henein, T. Wolfe, A. Jawad Qureshi, Large-scale metal additive manufacturing: a holistic review of the state of the art and challenges, Int. Mater. Rev. 66 (2021). https://doi.org/10.1080/09506608.2021.1971427.

[77] P.R. Gradl, T.W. Teasley, C.S. Protz, C. Katsarelis, P. Chen, Process Development and Hot-fire Testing of Additively Manufactured NASA HR-1 for Liquid Rocket Engine Applications, in: AIAA Propuls. Energy 2021, 2021: pp. 1–23. https://doi.org/10.2514/6.2021-3236.

[78] P.R. Gradl, C. Protz, T. Wammen, Additive manufacturing development and hot-fire testing of liquid rocket channel wall nozzles using blown powder directed energy deposition inconel 625 and jbk-75 alloys, in: AIAA Propuls. Energy Forum Expo. 2019, American Institute of Aeronautics and Astronautics Inc, AIAA, 2019. https://doi.org/10.2514/6.2019-4362.

[79] C. Zhong, N. Pirch, A. Gasser, R. Poprawe, J.H. Schleifenbaum, The influence of the powder stream on high-deposition-rate laser metal deposition with inconel 718, Metals (Basel). 7 (2017). https://doi.org/10.3390/met7100443.

[80] K. Lin, L. Yuan, D. Gu, Influence of laser parameters and complex structural features on the bio-inspired complex thin-wall structures fabricated by selective laser melting, J. Mater. Process. Technol. 267 (2019) 34–43. https://doi.org/10.1016/j.jmatprotec.2018.12.004.

[81] G. Kasperovich, R. Becker, K. Artzt, P. Barriobero-Vila, G. Requena, J. Haubrich, The effect of build direction and geometric optimization in laser powder bed fusion of Inconel 718 structures with internal channels, Mater. Des. (2021) 109858. https://doi.org/10.1016/j.matdes.2021.109858.

[82] D. Jafari, W.W. Wits, The utilization of selective laser melting technology on heat transfer devices for thermal energy conversion applications: A review, Renew. Sustain. Energy Rev. 91 (2018) 420–442. https://doi.org/10.1016/j.rser.2018.03.109.

[83] M.C. Sow, T. De Terris, O. Castelnau, Z. Hamouche, F. Coste, R. Fabbro, P. Peyre, Influence of beam diameter on Laser Powder Bed Fusion (L-PBF) process, Addit. Manuf. 36 (2020) 101532. https://doi.org/10.1016/J.ADDMA.2020.101532.

[84] Z. Jardon, J. Ertveldt, M. Hinderdael, P. Guillaume, Process parameter study for enhancement of directed energy deposition powder efficiency based on single-track geometry evaluation Process parameter study for enhancement of directed energy deposition powder efficiency based on single-track geometry evalua, J. Laser Appl. 042023 (2021). https://doi.org/10.2351/7.0000516.

[85] J.C. Snyder, K.A. Thole, Understanding Laser Powder Bed Fusion Surface Roughness, J. Manuf. Sci. Eng. 142 (2020). https://doi.org/10.1115/1.4046504.

[86] J. Liu, L. Li, Effects of powder concentration distribution on fabrication of thin-wall parts in coaxial laser cladding, Opt. Laser Technol. 37 (2005) 287–292. https://doi.org/10.1016/j.optlastec.2004.04.009.

[87] P. Margerit, D. Weisz-Patrault, K. Ravi-Chandar, A. Constantinescu, Tensile and ductile fracture properties of as-printed 316L stainless steel thin walls obtained by directed energy deposition, Addit. Manuf. 37 (2021) 101664. https://doi.org/10.1016/j.addma.2020.101664.

[88] V. Errico, S.L. Campanelli, A. Angelastro, M. Dassisti, M. Mazzarisi, C. Bonserio, Coaxial monitoring of aisi 316l thin walls fabricated by direct metal laser deposition, Materials (Basel). 14 (2021) 1–17. https://doi.org/10.3390/ma14030673.

[89] Y. Balit, E. Charkaluk, A. Constantinescu, Digital image correlation for microstructural analysis of deformation pattern in additively manufactured 316L thin walls, Addit. Manuf. 31 (2020) 100862. https://doi.org/10.1016/j.addma.2019.100862.

[90] H. El Cheikh, B. Courant, S. Branchu, X. Huang, J.Y. Hascot, R. Guilln, Direct Laser Fabrication process with coaxial powder projection of 316L steel. Geometrical characteristics and microstructure characterization of wall structures, Opt. Lasers Eng. 50 (2012) 1779–1784. https://doi.org/10.1016/j.optlaseng.2012.07.002.

[91] Z. Mianji, A.A. Kholopov, I.I. Binkov, A. Kiani, Numerical Simulation of Thermal Behavior and Experimental Investigation of Thin Walls during Direct Metal Deposition of 316L Stainless Steel Powder, Lasers Manuf. Mater. Process. (2021). https://doi.org/10.1007/s40516-021-00155-1.

[92] S. Imbrogno, A. Alhuzaim, M.M. Attallah, Influence of the laser source pulsing frequency on the direct laser deposited Inconel 718 thin walls, J. Alloys Compd. 856 (2021) 158095. https://doi.org/10.1016/j.jallcom.2020.158095.

[93] L. Xu, Z. Chai, H. Chen, X. Zhang, J. Xie, X. Chen, Tailoring Laves phase and mechanical properties of directed energy deposited Inconel 718 thin-wall via a gradient laser power method, Mater. Sci. Eng. A. 824 (2021) 141822. https://doi.org/10.1016/j.msea.2021.141822.

[94] M.-N. Bold, J. Zielinski, S. Ziegler, Johannes Henrich Schleifenbaum, Study of laser metal deposition of IN718 on inclined planes: influences of inclination on height and width of deposited material, in: Met. Addit. Manuf. Conf., Orebro, Sweden, 2020.

[95] A.N. Jinoop, C.P. Paul, J. Denny, S.K. Nayak, V. Krishna, K.S. Bindra, Laser additive manufacturing (LAM) of Hastelloy-X thin walls using directed energy deposition (DED): Parametric investigation and multi-objective analysis, Lasers Eng. 46 (2020) 15–34.

[96] A.N. Jinoop, S.K. Nayak, S. Yadav, C.P. Paul, R. Singh, J.G. Kumar, K.S. Bindra, Effect of scan pattern on Hastelloy-X wall structures built by laser-directed energy deposition-based additive manufacturing, J. Micromanufacturing. (2021) 251659842110363. https://doi.org/10.1177/25165984211036312.

[97] H. Kalami, J. Urbanic, Process planning solution strategies for fabrication of thin-wall domes using directed energy deposition, Int. J. Comput. Integr. Manuf. 00 (2021) 1–17. https://doi.org/10.1080/0951192X.2021.1946851.

[98] J.I. Arrizubieta, S. Martínez, A. Lamikiz, E. Ukar, K. Arntz, F. Klocke, Instantaneous powder flux regulation system for Laser Metal Deposition, J. Manuf. Process. 29 (2017) 242–251. https://doi.org/10.1016/j.jmapro.2017.07.018.

[99] G. Barragan, F. Mariani, R. Coelho, Ti6Al4V Thin Walls Production using Laser Directed Energy Deposition (L-DED) Process, Int. J. Eng. Mater. Manuf. 6 (2021) 124–131. https://doi.org/10.26776/ijemm.06.03.2021.03.

[100] L. Yan, W. Cui, J.W. Newkirk, F. Liou, E.E. Thomas, A.H. Baker, J.B. Castle, Mechanical properties evaluation of a Ti-6Al-4V thin-wall structure produced by a hybrid manufacturing process, Solid Free. Fabr. 2018 Proc. 29th Annu. Int. Solid Free. Fabr. Symp. - An Addit. Manuf. Conf. SFF 2018. (2020) 291–301.

[101] M. Balichakra, S. Bontha, P. Krishna, V.K. Balla, Prediction and validation of residual stresses generated during laser metal deposition of γ titanium aluminide thin wall structures, Mater. Res. Express. 6 (2019) 106550. https://doi.org/10.1088/2053-1591/ab38ee.

[102] M.J. Kim, C. Saldana, Thin wall deposition of IN625 using directed energy deposition, J. Manuf. Process. 56 (2020) 1366–1373. https://doi.org/10.1016/j.jmapro.2020.04.032.

[103] P. Xue, L. Zhu, P. Xu, Y. Ren, B. Xin, S. Wang, Z. Yang, J. Ning, G. Meng, Z. Liu, CrCoNi medium-entropy alloy thin-walled parts manufactured by laser metal deposition: Microstructure evolution and mechanical anisotropy, Mater. Sci. Eng. A. 817 (2021) 141306. https://doi.org/10.1016/j.msea.2021.141306.

[104] R. Jardin, V. Tuninetti, J. Tchuindjang, N. Hashemi, R. Carrus, A. Mertens, L. Duch, H.S. Tran, A.M. Habraken, Sensitivity analysis in the modelling of a high speed steel thin-wall produced by directed energy deposition, Metals (Basel). 10 (2020) 1554.

[105] T. Zhao, W. Cai, M. Dahmen, J. Schaible, C. Hong, A. Gasser, A. Weisheit, T. Biermann, I. Kelbassa, H. Zhang, D. Gu, J.H. Schleifenbaum, Ageing response of an Al-Mg-Mn-Sc-Zr alloy processed by laser metal deposition in thin-wall structures, Vacuum. 158 (2018) 121–125. https://doi.org/10.1016/j.vacuum.2018.09.052.

[106] D. Rosen, S. Kim, Design and Manufacturing Implications of Additive Manufacturing, J. Mater. Eng. Perform. (2021). https://doi.org/10.1007/s11665-021-06030-6.

[107] T.D. Ngo, A. Kashani, G. Imbalzano, K.T.Q. Nguyen, D. Hui, Additive manufacturing (3D printing): A review of materials, methods, applications and challenges, Compos. Part B Eng. 143 (2018) 172–196. https://doi.org/10.1016/j.compositesb.2018.02.012.

[108] C.K. Stimpson, J.C. Snyder, K.A. Thole, D. Mongillo, Scaling Roughness Effects on Pressure Loss and Heat Transfer of Additively Manufactured Channels, J. Turbomach. 139 (2016) 1–10. https://doi.org/10.1115/1.4034555.

[109] A. Jones, M. Leary, S. Bateman, M. Easton, Effect of surface geometry on laser powder bed fusion defects, J. Mater. Process. Technol. 296 (2021) 117179. https://doi.org/10.1016/j.jmatprotec.2021.117179.

[110] A. Hemmasian Ettefagh, S. Guo, J. Raush, Corrosion performance of additively manufactured stainless steel parts: A review, Addit. Manuf. 37 (2020) 101689. https://doi.org/10.1016/j.addma.2020.101689.

[111] H.M. Khan, Y. Karabulut, O. Kitay, Y. Kaynak, I.S. Jawahir, Influence of the post-processing operations on surface integrity of metal components produced by laser powder bed fusion additive manufacturing: a review, Mach. Sci. Technol. 25 (2020) 118–176. https://doi.org/10.1080/10910344.2020.1855649.

[112] J.C. Fox, S.P. Moylan, B.M. Lane, Effect of Process Parameters on the Surface Roughness of Overhanging Structures in Laser Powder Bed Fusion Additive Manufacturing, Procedia CIRP. 45 (2016) 131–134. https://doi.org/10.1016/j.procir.2016.02.347.

[113] M. Jamshidinia, R. Kovacevic, The influence of heat accumulation on the surface roughness in powder-bed additive manufacturing, Surf. Topogr. Metrol. Prop. 3 (2015) 14003. https://doi.org/10.1088/2051-672X/3/1/014003.

[114] I. Gibson, D. Rosen, B. Stucker, Directed Energy Deposition Processes, Addit. Manuf. Technol. (2015) 245–268. https://doi.org/10.1007/978-1-4939-2113-3_10.

[115] A.N. Jinoop, C.P. Paul, S.K. Mishra, K.S. Bindra, Laser Additive Manufacturing using directed energy deposition of Inconel-718 wall structures with tailored characteristics, Vacuum. 166 (2019) 270–278. https://doi.org/10.1016/j.vacuum.2019.05.027.

[116] A. Azarniya, X.G. Colera, M.J. Mirzaali, S. Sovizi, F. Bartolomeu, M. k. St Weglowski, W.W. Wits, C.Y. Yap, J. Ahn, G. Miranda, F.S. Silva, H.R. Madaah Hosseini, S. Ramakrishna, A.A. Zadpoor, M. St Weglowski k, W.W. Wits, C.Y. Yap, J. Ahn, G. Miranda, F.S. Silva, H.R. Madaah Hosseini, S. Ramakrishna, A.A. Zadpoor, Additive manufacturing of Ti–6Al–4V parts through laser metal deposition (LMD): Process, microstructure, and mechanical properties, J. Alloys Compd. 804 (2019) 163–191. https://doi.org/10.1016/j.jallcom.2019.04.255.

[117] C. Li, Z.Y. Liu, X.Y. Fang, Y.B. Guo, Residual Stress in Metal Additive Manufacturing, Procedia CIRP. 71 (2018) 348–353. https://doi.org/10.1016/J.PROCIR.2018.05.039.

[118] J. Zhang, S. Shi, G. Fu, J. Shi, G. Zhu, D. Cheng, Analysis on surface finish of thin-wall parts by laser metal deposition with annular beam, Opt. Laser Technol. 119 (2019) 105605. https://doi.org/10.1016/j.optlastec.2019.105605.

[119] S. Morville, M. Carin, P. Peyre, M. Gharbi, D. Carron, P. Le Masson, R. Fabbro, 2D longitudinal modeling of heat transfer and fluid flow during multilayered direct laser metal deposition process, J. Laser Appl. 24 (2012) 032008. https://doi.org/10.2351/1.4726445.

[120] M. Gharbi, P. Peyre, C. Gorny, M. Carin, S. Morville, P. Le Masson, D. Carron, R. Fabbro, Influence of various process conditions on surface finishes induced by the direct metal deposition laser technique on a Ti-6Al-4V alloy, J. Mater. Process. Technol. 213 (2013) 791–800. https://doi.org/10.1016/j.jmatprotec.2012.11.015.

[121] S. Wang, L. Zhu, Y. Dun, Z. Yang, J.Y.H. Fuh, W. Yan, Multi-physics modeling of direct energy deposition process of thin-walled structures: defect analysis, Comput. Mech. 67 (2021) 1229–1242. https://doi.org/10.1007/s00466-021-01992-9.

[122] N. Nicolas, P. Rochus, J.P. Collette, J. Crahay, H. Jochem, M. Larnicol, J. Magnien, C. Masse, O. Rigo, J.F. Vanhumbeeck, L. Pambaguian, Surface engineering for parts made by additive manufacturing, Proc. Int. Astronaut. Congr. IAC. 9 (2015) 6669–6679.

[123] M.H. Nasab, D. Gastaldi, N.F. Lecis, M. Vedani, On morphological surface features of the parts printed by selective laser melting (SLM), Addit. Manuf. 24 (2018) 373–377. https://doi.org/10.1016/j.addma.2018.10.011.

[124] C.K. Chua, C.H. Wong, W.Y. Yeong, Standards, quality control and measurement sciences in 3D printing and additive manufacturing, London Academic Press, 2017. https://www.elsevier.com/books/standards-quality-control-and-measurement-sciences-in-3d-printing-and-additive-manufacturing/chua/978-0-12-813489-4.

[125] A.A. Zadpoor, Frontiers of Additively Manufactured Metallic Materials, Materials (Basel). 11 (2018) 1566. https://doi.org/10.3390/ma11091566.

[126] D. Obilanade, C. Dordlofva, P. Törlind, Surface roughness considerations in design for additive manufacturing - A literature review, Proc. Des. Soc. 1 (2021) 2841–2850. https://doi.org/10.1017/pds.2021.545.

[127] A. Diaz, Surface texture characterization and optimization of metal additive manufacturing-produced components for aerospace applications, Addit. Manuf. Aerosp. Ind. (2019) 341–374. https://doi.org/10.1016/B978-0-12-814062-8.00018-2.

[128] D.R. Hanson, S.T. McClain, J.C. Snyder, R.F. Kunz, K.A. Thole, Flow in a Scaled Turbine Coolant Channel With Roughness due to Additive Manufacturing, Vol. 5B Heat Transf. 5B-2019 (2019) 1–12. https://doi.org/10.1115/gt2019-90931.

[129] C. Tommila, Performance Losses In Additively Manufactured Low Thrust Nozzles, Air Force Institute of Technology, Masters Thesis, 2017. https://apps.dtic.mil/dtic/tr/fulltext/u2/1055372.pdf.

[130] C.K. Stimpson, J.C. Snyder, K.A. Thole, D. Mongillo, Roughness Effects on Flow and Heat Transfer for Additively Manufactured Channels, J. Turbomach. 138 (2016) 1–13. https://doi.org/10.1115/1.4032167.

[131] W. Demisse, J. Xu, L. Rice, P. Tyagi, Review of internal and external surface finishing technologies for additively manufactured metallic alloys components and new frontiers, Prog. Addit. Manuf. (2023). https://doi.org/10.1007/s40964-023-00412-z.

[132] A.W. Hashmi, H.S. Mali, A. Meena, K.K. Saxena, S. Ahmad, M.K. Agrawal, B. Sagbas, A.P. Valerga Puerta, M.I. Khan, A comprehensive review on surface post-treatments for freeform surfaces of bio-implants, J. Mater. Res. Technol. 23 (2023) 4866–4908. https://doi.org/10.1016/j.jmrt.2023.02.007.

[133] E. Manco, E. Cozzolino, A. Astarita, Laser polishing of additively manufactured metal parts: a review, Surf. Eng. 38 (2022) 217–233. https://doi.org/10.1080/02670844.2022.2072080.

[134] P. Tyagi, T. Goulet, C. Riso, F. Garcia-Moreno, Reducing surface roughness by chemical polishing of additively manufactured 3D printed 316 stainless steel components, Int. J. Adv. Manuf. Technol. 100 (2018) 2895–2900. https://doi.org/10.1007/s00170-018-2890-0.

[135] P. Tyagi, T. Goulet, C. Riso, R. Stephenson, N. Chuenprateep, J. Schlitzer, C. Benton, F. Garcia-Moreno, Reducing the roughness of internal surface of an additive manufacturing produced 316 steel component by chempolishing and electropolishing, Addit. Manuf. 25 (2019) 32–38. https://doi.org/10.1016/j.addma.2018.11.001.

[136] H. Yamaguchi, O. Fergani, P.-Y.Y. Wu, Modification using magnetic field-assisted finishing of the surface roughness and residual stress of additively manufactured components, CIRP Ann. 66 (2017) 305–308. https://doi.org/10.1016/j.cirp.2017.04.084.

[137] H. Hassanin, A. Elshaer, R. Benhadj-Djilali, F. Modica, I. Fassi, Surface Finish Improvement of Additive Manufactured Metal Parts, Micro Precis. Manuf. (2017) 145–164. https://doi.org/10.1007/978-3-319-68801-5_7.

[138] Z. Chaghazardi, R. Wüthrich, Review—Electropolishing of Additive Manufactured Metal Parts, J. Electrochem. Soc. 169 (2022) 043510. https://doi.org/10.1149/1945-7111/ac6450.

[139] J.C. Snyder, K.A. Thole, Performance of Public Film Cooling Geometries Produced Through Additive Manufacturing, Vol. 5B Heat Transf. (2019). https://doi.org/10.1115/gt2019-90877.

[140] J. Dávila, P.I. Neto, P.Y. Noritomi, R.T. Coelho, J. Vicente, L. da Silva, Hybrid manufacturing: a review of the synergy between directed energy deposition and subtractive processes, Int. J. Adv. Manuf. Technol. 110 (2020) 3377–3390. https://doi.org/10.1007/s00170-020-06062-7.

[141] M. Shen, F. Fang, Advances in polishing of internal structures on parts made by laser-based powder bed fusion, Front. Mech. Eng. 18 (2023). https://doi.org/10.1007/s11465-022-0724-0.

[142] H. Fayazfar, J. Sharifi, M.K. Keshavarz, M. Ansari, An overview of surface roughness enhancement of additively manufactured metal parts: a path towards removing the

post-print bottleneck for complex geometries, Springer London, 2023. https://doi.org/10.1007/s00170-023-10814-6.

[143] N.N. Kumbhar, A. V. Mulay, Post Processing Methods used to Improve Surface Finish of Products which are Manufactured by Additive Manufacturing Technologies: A Review, J. Inst. Eng. Ser. C. 99 (2016) 481–487. https://doi.org/10.1007/s40032-016-0340-z.

[144] J. Boban, A. Ahmed, E.K. Jithinraj, M.A. Rahman, M. Rahman, Polishing of additive manufactured metallic components: retrospect on existing methods and future prospects, Springer London, 2022. https://doi.org/10.1007/s00170-022-09382-y.

[145] A.W. Hashmi, H.S. Mali, A. Meena, V. Puerta, M.E. Kunkel, Surface characteristics improvement methods for metal additively manufactured parts: a review, Adv. Mater. Process. Technol. 00 (2022) 1–40. https://doi.org/10.1080/2374068X.2022.2077535.

[146] E. Maleki, S. Bagherifard, M. Bandini, M. Guagliano, Surface post-treatments for metal additive manufacturing: Progress, challenges, and opportunities, Addit. Manuf. 37 (2021) 101619. https://doi.org/10.1016/j.addma.2020.101619.

[147] J.Y. Lee, A.P. Nagalingam, S.H. Yeo, A review on the state-of-the-art of surface finishing processes and related ISO/ASTM standards for metal additive manufactured components, Virtual Phys. Prototyp. 0 (2020) 1–29. https://doi.org/10.1080/17452759.2020.1830346.

[148] D. De Oliveira, M.C. Gomes, A.G. Dos Santos, K.S.B. Ribeiro, I.J. Vasques, R.T. Coelho, M.B. Da Silva, N.W. Hung, Abrasive and non-conventional post-processing techniques to improve surface finish of additively manufactured metals: a review, Prog. Addit. Manuf. 8 (2023) 223–240. https://doi.org/10.1007/s40964-022-00325-3.

[149] J. Zhang, Y.J. Lee, H. Wang, A Brief Review on the Enhancement of Surface Finish for Metal Additive Manufacturing, (2021) 1–14.

[150] D. Syrlybayev, A. Seisekulova, D. Talamona, A. Perveen, The Post-Processing of Additive Manufactured Polymeric and Metallic Parts, J. Manuf. Mater. Process. 6 (2022). https://doi.org/10.3390/jmmp6050116.

[151] S. Yazdanparast, S. Raikar, M. Heilig, O.J. Hildreth, Iodine-Based Sensitization of Copper Alloys to Enable Self-Terminating Etching for Support Removal and Surface Improvements of Additively Manufactured Components, 3D Print. Addit. Manuf. 10 (2023) 619–630. https://doi.org/10.1089/3dp.2021.0242.

[152] A.P. Nagalingam, S.H. Yeo, Surface finishing of additively manufactured Inconel 625 complex internal channels: A case study using a multi-jet hydrodynamic approach, Addit. Manuf. 36 (2020) 101428. https://doi.org/10.1016/j.addma.2020.101428.

[153] A.P. Nagalingam, B.L. Toh, S.H. Yeo, Surface Polishing of Laser Powder Bed Fused Inconel 625 Surfaces Using Multi-jet Hydrodynamic Cavitation Abrasive Finishing: An Emerging Class of Cleaner Surface Enhancement Process, Int. J. Precis. Eng. Manuf. - Green Technol. 10 (2023) 637–657. https://doi.org/10.1007/s40684-022-00471-7.

[154] D. Lesyk, V. Dzhemelinskyi, B. Mordyuk, S. Martinez, O. Stamann, A. Lamikiz, Surface Polishing of Laser Powder Bed Fused Superalloy Components by Magnetic Post-treatment, Proc. 2020 IEEE 10th Int. Conf. "Nanomaterials Appl. Prop. N. 2020. (2020) 10–13. https://doi.org/10.1109/NAP51477.2020.9309600.

[155] J. Guo, K.H. Au, K. Liu, S.T. Ng, K.C.S. Shaw, A novel vibration-assisted magnetic abrasive polishing method for complex internal surface finishing, Proc. 17th Int. Conf. Eur. Soc. Precis. Eng. Nanotechnology, EUSPEN 2017. (2017) 161–162.

[156] L.E. dos Santos Paes, M. Pereira, F.A. Xavier, W.L. Weingaertner, A.S.C.M. D'Oliveira, E.C. Costa, L.O. Vilarinho, A. Scotti, Understanding the behavior of laser

surface remelting after directed energy deposition additive manufacturing through comparing the use of iron and Inconel powders, J. Manuf. Process. 70 (2021) 494–507. https://doi.org/10.1016/J.JMAPRO.2021.08.061.

[157] A.M. Souza, R. Ferreira, G. Barragán, J.G. Nuñez, F.E. Mariani, E.J. da Silva, R.T. Coelho, Effects of Laser Polishing on Surface Characteristics and Wettability of Directed Energy-Deposited 316L Stainless Steel, J. Mater. Eng. Perform. 30 (2021) 6752–6765. https://doi.org/10.1007/S11665-021-05991-Y/METRICS.

[158] A. Gisario, M. Barletta, F. Veniali, Laser polishing : a review of a constantly growing technology in the surface finishing of components made by additive manufacturing, Springer London, 2022. https://doi.org/10.1007/s00170-022-08840-x.

[159] A. Kumar, S. Saha, C.S. Kumar, A.K. Nath, Laser surface re-melting of additive manufactured samples with a line focused beam, Mater. Today Proc. 26 (2020) 1221–1225. https://doi.org/10.1016/J.MATPR.2020.02.245.

[160] C.P. Ma, Y.C. Guan, W. Zhou, Laser polishing of additive manufactured Ti alloys, Opt. Lasers Eng. 93 (2017) 171–177. https://doi.org/10.1016/j.optlaseng.2017.02.005.

[161] B. Rosa, P. Mognol, J. Hascoët, Laser polishing of additive laser manufacturing surfaces, J. Laser Appl. 27 (2015) S29102. https://doi.org/10.2351/1.4906385.

[162] J. Arrizubieta, M. Cortina, J. Ruiz, A. Lamikiz, Combination of Laser Material Deposition and Laser Surface Processes for the Holistic Manufacture of Inconel 718 Components, Materials (Basel). 11 (2018) 1247. https://doi.org/10.3390/ma11071247.

[163] J. Ghorbani, J. Li, A.K. Srivastava, Application of optimized laser surface re-melting process on selective laser melted 316L stainless steel inclined parts, J. Manuf. Process. 56 (2020) 726–734. https://doi.org/10.1016/j.jmapro.2020.05.025.

[164] M.M. Basha, S.M. Basha, V.K. Jain, M.R. Sankar, State of the art on chemical and electrochemical based finishing processes for additive manufactured features, Addit. Manuf. 58 (2022) 103028. https://doi.org/10.1016/j.addma.2022.103028.

[165] G. Favero, G. Berti, M. Bonesso, D. Morrone, S. Oriolo, P. Rebesan, R. Dima, P. Gregori, A. Pepato, A. Scanavini, S. Mancin, Experimental and numerical analyses of fluid flow inside additively manufactured and smoothed cooling channels, Int. Commun. Heat Mass Transf. 135 (2022) 106128. https://doi.org/10.1016/j.icheatmasstransfer.2022.106128.

[166] N. Mohammadian, S. Turenne, V. Brailovski, Surface finish control of additively-manufactured Inconel 625 components using combined chemical-abrasive flow polishing, J. Mater. Process. Technol. 252 (2018) 728–738. https://doi.org/10.1016/j.jmatprotec.2017.10.020.

[167] Y. Zhu, L. Zhou, S. Wang, C. Zhang, C. Zhao, L. Zhang, H. Yang, On friction factor of fluid channels fabricated using selective laser melting, Virtual Phys. Prototyp. 15 (2020) 496–509. https://doi.org/10.1080/17452759.2020.1823093.

[168] I. Kaur, P. Singh, State-of-the-art in heat exchanger additive manufacturing, Int. J. Heat Mass Transf. 178 (2021) 121600. https://doi.org/10.1016/j.ijheatmasstransfer.2021.121600.

[169] L. Zhou, Y. Zhu, H. Liu, T. He, C. Zhang, H. Yang, A comprehensive model to predict friction factors of fluid channels fabricated using laser powder bed fusion additive manufacturing, Addit. Manuf. 47 (2021) 102212. https://doi.org/10.1016/j.addma.2021.102212.

[170] C.İ. Çalışkan, M. Coşkun, G. Özer, E. Koç, T.A. Vurkır, G. Yöndem, Investigation of manufacturability and efficiency of micro channels with different geometries produced by direct metal laser sintering, Int. J. Adv. Manuf. Technol. 117 (2021) 3805–3817. https://doi.org/10.1007/s00170-021-07928-0.

[171] B.K.J. Evangelista, Laser Powder Bed Fusion-Induced Surface Roughness and Effects on Thermal Fluid Performance for Additively Manufactured Metals in Liquid Rocket Components, California State University, 2022.

[172] A.H. Seltzman, S.J. Wukitch, Surface roughness and finishing techniques in selective laser melted GRCop-84 copper for an additive manufactured lower hybrid current drive launcher, Fusion Eng. Des. 160 (2020) 111801. https://doi.org/10.1016/j.fusengdes.2020.111801.

[173] Z. Min, Y. Wu, K. Yang, J. Xu, S.N. Parbat, M.K. Chyu, Dimensional characterizations using scanning electron microscope and surface improvement with electrochemical polishing of additively manufactured microchannels, J. Eng. Gas Turbines Power. 143 (2021) 1–12. https://doi.org/10.1115/1.4049908.

[174] D. Jiang, Y. Tian, Y. Zhu, A. Huang, Investigation of surface roughness post-processing of additively manufactured nickel-based superalloy Hastelloy X using electropolishing, Surf. Coatings Technol. 441 (2022) 128529. https://doi.org/10.1016/j.surfcoat.2022.128529.

[175] L. An, D. Wang, D. Zhu, Combined electrochemical and mechanical polishing of interior channels in parts made by additive manufacturing, Addit. Manuf. 51 (2022) 102638. https://doi.org/10.1016/j.addma.2022.102638.

[176] J. Ferchow, H. Baumgartner, C. Klahn, M. Meboldt, Model of surface roughness and material removal using abrasive flow machining of selective laser melted channels, Rapid Prototyp. J. 26 (2020) 1165–1176. https://doi.org/10.1108/RPJ-09-2019-0241.

[177] M. Buchholz, S. Gruber, A. Selbmann, A. Marquardt, L. Meier, M. Müller, L. Seifert, C. Leyens, M. Tajmar, C. Bach, Flow rate improvements in additively manufactured flow channels suitable for rocket engine application, CEAS Sp. J. (2022). https://doi.org/10.1007/s12567-022-00476-7.

[178] S. Han, F. Salvatore, J. Rech, J. Bajolet, Abrasive flow machining (AFM) finishing of conformal cooling channels created by selective laser melting (SLM), Precis. Eng. 64 (2020) 20–33. https://doi.org/10.1016/j.precisioneng.2020.03.006.

[179] M.S. Duval-Chaneac, S. Han, C. Claudin, F. Salvatore, J. Bajolet, J. Rech, Experimental study on finishing of internal laser melting (SLM) surface with abrasive flow machining (AFM), Precis. Eng. 54 (2018) 1–6. https://doi.org/10.1016/j.precisioneng.2018.03.006.

[180] K. Dresia, E. Kurudzija, J. Deeken, G. Waxenegger-Wilfing, Improved Wall Temperature Prediction for the LUMEN Rocket Combustion Chamber with Neural Networks, Aerospace. 10 (2023) 1–15. https://doi.org/10.3390/aerospace10050450.

[181] F. Hötte, C. v. Sethe, T. Fiedler, M.C. Haupt, O.J. Haidn, M. Rohdenburg, Experimental lifetime study of regeneratively cooled rocket chamber walls, Int. J. Fatigue. 138 (2020) 105649. https://doi.org/10.1016/j.ijfatigue.2020.105649.

[182] J.R. Riccius, O.J. Haidn, E.B. Zametaev, Influence of time dependent effects on the estimated life time of liquid rocket combustion chamber walls, 40th AIAA/ASME/SAE/ASEE Jt. Propuls. Conf. Exhib. (2004). https://doi.org/10.2514/6.2004-3670.

[183] F. Kaji, A.N. Jinoop, M. Zimny, G. Frikel, K. Tam, E. Toyserkani, Process Planning for Additive Manufacturing of Geometries with Variable Overhang Angles using a Robotic Laser Directed Energy Deposition system, Addit. Manuf. Lett. 2 (2022) 100035. https://doi.org/10.1016/j.addlet.2022.100035.

[184] R. Cavillon, M.H. Naraghi, G. Chen, Comparison of Heat Transfer Characteristic of Rectangular and Oval Cooling Channels of Regeneratively Cooled Rocket Engines, (2015). https://doi.org/10.2514/6.2015-3759.

[185] B. Latini, M. Fiore, F. Nasuti, Modeling liquid rocket engine coolant flow and heat transfer in high roughness channels, Aerosp. Sci. Technol. 126 (2022) 107672. https://doi.org/10.1016/j.ast.2022.107672.

[186] T. Dixit, I. Ghosh, Review of micro- and mini-channel heat sinks and heat exchangers for single phase fluids, Renew. Sustain. Energy Rev. 41 (2015) 1298–1311. https://doi.org/10.1016/J.RSER.2014.09.024.

[187] J.P. Bons, R.P. Taylor, S.T. McClain, R.B. Rivir, The many faces of turbine surface roughness, J. Turbomach. 123 (2001) 739–748. https://doi.org/10.1115/1.1400115.

[188] J.R. Riccius, M.W. Böttcher, H. Duval, A first step into the blanching modelling of liquid rocket engines: Taking into account the roughness increase of the chamber wall, AIAA Propuls. Energy Forum Expo. 2019. (2019) 1–7. https://doi.org/10.2514/6.2019-3941.

[189] M. Riede, M. Knoll, C. Wilsnack, S. Gruber, A.A. Cubillo, C. Melzer, A. Brandão, L. Pambaguian, A. Seidel, E. Lopez, F. Brueckner, C. Leyens, Material characterization of AISI 316L flexure pivot bearings fabricated by additive manufacturing, Materials (Basel). 12 (2019). https://doi.org/10.3390/ma12152426.

[190] L. Lu, T. Shi, J. Zhang, Y. Mei, D. Cheng, G. Fu, S. Yu, Research on surface finish of thin-wall parts by laser with coaxial inside-beam powder feeding, J. Laser Appl. 33 (2021) 022003. https://doi.org/10.2351/7.0000206.

[191] R.M. Mahamood, E.T. Akinlabi, Effect of Laser Power on Surface Finish during Laser Metal Deposition Process, Proc. World Congr. Eng. Comput. Sci. Vol II (2014) 965–969. https://www.researchgate.net/publication/281928719_Effect_of_Laser_Power_on_Surface_Finish_during_Laser_Metal_Deposition_Process.

[192] M. Mazzarisi, S.L. Campanelli, A. Angelastro, M. Dassisti, Phenomenological modelling of direct laser metal deposition for single tracks, Int. J. Adv. Manuf. Technol. 111 (2020) 1955–1970. https://doi.org/10.1007/s00170-020-06204-x.

[193] R.M. Mahamood, E.T. Akinlabi, Effect of Powder Flow Rate on Surface Finish in Laser Additive Manufacturing Process, IOP Conf. Ser. Mater. Sci. Eng. 391 (2018) 12005. https://doi.org/10.1088/1757-899x/391/1/012005.

[194] M. Alimardani, V. Fallah, M. Iravani-Tabrizipour, A. Khajepour, Surface finish in laser solid freeform fabrication of an AISI 303L stainless steel thin wall, J. Mater. Process. Technol. 212 (2012) 113–119. https://doi.org/10.1016/j.jmatprotec.2011.08.012.

[195] G. Zhu, D. Li, A. Zhang, G. Pi, Y. Tang, The influence of laser and powder defocusing characteristics on the surface quality in laser direct metal deposition, Opt. Laser Technol. 44 (2012) 349–356. https://doi.org/10.1016/j.optlastec.2011.07.013.

[196] F. Careri, S. Imbrogno, D. Umbrello, M.M. Attallah, J. Outeiro, A.C. Batista, Machining and heat treatment as post-processing strategies for Ni-superalloys structures fabricated using direct energy deposition, J. Manuf. Process. 61 (2021) 236–244. https://doi.org/10.1016/j.jmapro.2020.11.024.

[197] P.A. Carroll, A.J. Pinkerton, J. Allen, W. Syed, H.K. Sezer, P. Brown, G.K.L. Ng, R. Scudamore, L. Li, The effect of powder recycling in direct metal laser deposition on powder and manufactured part characteristics, Eff. Manuf. via Net-Shape Process. (2006) 18-1 PP-Neuilly-sur-Seine, France. https://eprints.lancs.ac.uk/id/eprint/59645/1/MP_AVT_139_18.pdf.

[198] M.N. Ahsan, A.J. Pinkerton, R.J. Moat, J. Shackleton, A comparative study of laser direct metal deposition characteristics using gas and plasma-atomized Ti–6Al–4V

powders, Mater. Sci. Eng. A. 528 (2011) 7648–7657. https://doi.org/10.1016/j.msea.2011.06.074.

[199] B. Dutta, B. Jared, S. Babu, Science, technology and applications of metals in additive manufacturing, 1st Editio, Amsterdam Elsevier, 2019. https://www.elsevier.com/books/science-technology-and-applications-of-metals-in-additive-manufacturing/dutta/978-0-12-816634-5.

[200] Y. Li, J. Ma, Study on overlapping in the laser cladding process, Surf. Coatings Technol. 90 (1997) 1–5. https://doi.org/10.1016/S0257-8972(96)03022-8.

[201] C. Katsarelis, P. Chen, P.R. Gradl, C. Protz, Z. Jones, N. Marshall, S. Flight, D. Ellis, L. Evans, Additive Manufacturing of NASA HR-1 Material for Liquid Rocket Engine Component Applications, JANNAF Jt. Propuls. Conf. (2019) https://ntrs.nasa.gov/search.jsp?R=20200001007. https://ntrs.nasa.gov/search.jsp?R=20200001007.

[202] P.S. Chen, C.C. Katsarelis, W.M. Medders, P.R. Gradl, Segregation Evolution and Diffusion of Titanium in Directed Energy Deposited, 2021.

[203] A. Wang, H. Wang, Y. Wu, H. Wang, 3D printing of aluminum alloys using laser powder deposition: a review, Int. J. Adv. Manuf. Technol. 116 (2021). https://doi.org/10.1007/s00170-021-07440-5.

[204] K. Shah, A.J. Pinkerton, A. Salman, L. Li, Effects of melt pool variables and process parameters in laser direct metal deposition of aerospace alloys, Mater. Manuf. Process. 25 (2010) 1372–1380. https://doi.org/10.1080/10426914.2010.480999.

[205] P.-S. Chen, M. Mitchell, Aerospace Structural Metals Handbook ALLOY NASA-HR-1 Nickel Base Alloys-Ni, 2005.

[206] D.C. Montgomery, Design and analysis of experiments, 10th ed., Wiley, 2019. https://www.wiley.com/en-us/Design+and+Analysis+of+Experiments%2C+10th+Edition-p-9781119492443 (accessed November 22, 2021).

[207] American Society of Mechanical Engineers (ASME), Surface texture : surface roughness, waviness, and lay : ASME B46.1-2019, New York, N.Y, 2019. https://www.asme.org/codes-standards/find-codes-standards/b46-1-surface-texture (accessed December 29, 2021).

[208] H. Kalami, J. Urbanic, Exploration of surface roughness measurement solutions for additive manufactured components built by multi-axis tool paths, Addit. Manuf. 38 (2021) 101822. https://doi.org/10.1016/j.addma.2020.101822.

[209] N. Shamsaei, A. Yadollahi, L. Bian, S.M. Thompson, An overview of Direct Laser Deposition for additive manufacturing; Part II: Mechanical behavior, process parameter optimization and control, Addit. Manuf. 8 (2015) 12–35. https://doi.org/10.1016/j.addma.2015.07.002.

[210] A. Gamon, E. Arrieta, P.R. Gradl, C. Katsarelis, L.E. Murr, R.B. Wicker, F. Medina, Microstructure and hardness comparison of as-built Inconel 625 alloy following various additive manufacturing processes, Results Mater. 12 (2021). https://doi.org/10.1016/j.rinma.2021.100239.

[211] L. Bian, S.M. Thompson, N. Shamsaei, Mechanical Properties and Microstructural Features of Direct Laser-Deposited Ti-6Al-4V, JOM. 67 (2015) 629–638. https://doi.org/10.1007/s11837-015-1308-9.

[212] S.M. Thompson, L. Bian, N. Shamsaei, A. Yadollahi, An overview of Direct Laser Deposition for additive manufacturing; Part I: Transport phenomena, modeling and diagnostics, Addit. Manuf. 8 (2015) 36–62. https://doi.org/10.1016/j.addma.2015.07.001.

[213] N. Kladovasilakis, P. Charalampous, I. Kostavelis, D. Tzetzis, D. Tzovaras, Impact of metal additive manufacturing parameters on the powder bed fusion and direct energy deposition processes: a comprehensive review, Prog. Addit. Manuf. (2021). https://doi.org/10.1007/s40964-021-00180-8.

[214] C.Y. Kong, P.A. Carroll, P. Brown, R.J. Scudamore, The Effect of Average Powder Particle Size on Deposition Efficiency, Deposit Height and Surface Roughness in the Direct Metal Laser Deposition Process, in: 14th Int. Conf. Join. Mater., TWI Technology Centre, Helsingør, Denmark, 2007. https://www.twi-global.com/technical-knowledge/published-papers/the-effect-of-average-powder-particle-size-on-deposition-efficiency-deposit-height-and-surface-roughness-in-the-direct-metal-las.

[215] H. Tan, W. Fan, Y. Qian, Y. Chen, S. Liu, X. Lin, Influence of inclined substrate on process characteristics of directed energy deposition, Opt. Laser Technol. 129 (2020) 106288. https://doi.org/10.1016/j.optlastec.2020.106288.

[216] M.N. Ahsan, Modeling and analysis of laser direct metal deposition of Ti-6Al-4V alloy - ProQuest, Proquest.Com. (2011) 81–98. https://search.proquest.com/openview/b5882ed34c34857b895273c72bebab9a/1?pq-origsite=gscholar&cbl=51922&diss=y.

[217] S. Zekovic, R. Dwivedi, R. Kovacevic, Numerical simulation and experimental investigation of gas-powder flow from radially symmetrical nozzles in laser-based direct metal deposition, Int. J. Mach. Tools Manuf. 47 (2007) 112–123. https://doi.org/10.1016/j.ijmachtools.2006.02.004.

[218] H.S. Prasad, F. Brueckner, A.F.H. Kaplan, Powder catchment in laser metal deposition, J. Laser Appl. 31 (2019) 022308. https://doi.org/10.2351/1.5096130.

[219] I.E. Anderson, E.M.H. White, R. Dehoff, Feedstock powder processing research needs for additive manufacturing development, Curr. Opin. Solid State Mater. Sci. 22 (2018) 8–15. https://doi.org/10.1016/j.cossms.2018.01.002.

[220] A.D.D. Iams, M.Z.Z. Gao, A. Shetty, T.A.A. Palmer, Influence of particle size on powder rheology and effects on mass flow during directed energy deposition additive manufacturing, Powder Technol. 396 (2022) 316–326. https://doi.org/10.1016/j.powtec.2021.10.059.

[221] Y. Zhao, Y. Cui, Y. Hasebe, H. Bian, K. Yamanaka, K. Aoyagi, T. Hagisawa, A. Chiba, Controlling factors determining flowability of powders for additive manufacturing: A combined experimental and simulation study, Powder Technol. 393 (2021) 482–493. https://doi.org/10.1016/j.powtec.2021.08.006.

[222] A.B. Spierings, N. Herres, G. Levy, Influence of the particle size distribution on surface quality and mechanical properties in AM steel parts, Rapid Prototyp. J. 17 (2011) 195–202. https://doi.org/10.1108\/rpj.

[223] X. Gao, X.X. Yao, F.Y. Niu, Z. Zhang, The influence of nozzle geometry on powder flow behaviors in directed energy deposition additive manufacturing, Adv. Powder Technol. 33 (2022) 103487. https://doi.org/10.1016/j.apt.2022.103487.

[224] Y. Kakinuma, M. Mori, Y. Oda, T. Mori, M. Kashihara, A. Hansel, M. Fujishima, Influence of metal powder characteristics on product quality with directed energy deposition of Inconel 625, CIRP Ann. 65 (2016) 209–212. https://doi.org/10.1016/J.CIRP.2016.04.058.

[225] S. Takemura, R. Koike, Y. Kakinuma, Y. Sato, Y. Oda, Design of powder nozzle for high resource efficiency in directed energy deposition based on computational fluid dynamics simulation, Int. J. Adv. Manuf. Technol. 2019 10510. 105 (2019) 4107–4121. https://doi.org/10.1007/S00170-019-03552-1.

[226] C. Vundru, R. Singh, W. Yan, S. Karagadde, A comprehensive analytical-computational model of laser directed energy deposition to predict deposition geometry and integrity for sustainable repair, Int. J. Mech. Sci. 211 (2021) 106790. https://doi.org/10.1016/j.ijmecsci.2021.106790.

[227] A. Townsend, N. Senin, L. Blunt, R.K. Leach, J.S. Taylor, Surface texture metrology for metal additive manufacturing: a review, Precis. Eng. 46 (2016) 34–47. https://doi.org/10.1016/j.precisioneng.2016.06.001.

[228] A.N. Jinoop, C.P. Paul, K.S. Bindra, Laser-assisted directed energy deposition of nickel super alloys: A review, Proc. Inst. Mech. Eng. Part L J. Mater. Des. Appl. 233 (2019) 2376–2400. https://doi.org/10.1177/1464420719852658.

[229] F. Wirth, S. Arpagaus, K. Wegener, Analysis of melt pool dynamics in laser cladding and direct metal deposition by automated high-speed camera image evaluation, Addit. Manuf. 21 (2018) 369–382. https://doi.org/10.1016/J.ADDMA.2018.03.025.

[230] G.A. Barragan, D. Rojas, J.S. Grass, R.T. Coelho, Observations on laser additive manufacturing (lam) in terms of directed energy deposition (ded) with metal powder feedstock, Lasers Eng. 50 (2021) 117–141.

[231] A. Segerstark, J. Andersson, L.E. Svensson, Review of Laser Deposited Superalloys Using Powder as an Additive, 8th Int. Symp. Superalloy 718 Deriv. 2014. (2014) 391–408. https://doi.org/10.1002/9781119016854.CH31.

[232] A. Fathi, E. Toyserkani, A. Khajepour, M. Durali, Prediction of melt pool depth and dilution in laser powder deposition, J. Phys. D. Appl. Phys. 39 (2006) 2613–2623. https://doi.org/10.1088/0022-3727/39/12/022.

[233] D.S. Shim, G.Y. Baek, J.S. Seo, G.Y. Shin, K.P. Kim, K.Y. Lee, Effect of layer thickness setting on deposition characteristics in direct energy deposition (DED) process, Opt. Laser Technol. 86 (2016) 69–78. https://doi.org/10.1016/j.optlastec.2016.07.001.

[234] A.J. Pinkerton, L. Li, Effects of Powder Geometry and Composition in Coaxial Laser Deposition of 316L Steel for Rapid Prototyping, CIRP Ann. 52 (2003) 181–184. https://doi.org/10.1016/S0007-8506(07)60560-5.

[235] D. Svetlizky, B. Zheng, A. Vyatskikh, M. Das, S. Bose, A. Bandyopadhyay, J.M. Schoenung, E.J. Lavernia, N. Eliaz, Laser-based directed energy deposition (DED-LB) of advanced materials, Mater. Sci. Eng. A. 840 (2022) 142967. https://doi.org/10.1016/j.msea.2022.142967.

[236] X. Wang, Z. Liu, Z. Guo, Y. Hu, A fundamental investigation on three–dimensional laser material deposition of AISI316L stainless steel, Opt. Laser Technol. 126 (2020) 106107. https://doi.org/10.1016/j.optlastec.2020.106107.

[237] J.C. Pereira, H. Borovkov, F. Zubiri, M.C. Guerra, J. Caminos, Optimization of Thin Walls with Sharp Corners in SS316L and IN718 Alloys Manufactured with Laser Metal Deposition, J. Manuf. Mater. Process. 5 (2021) 5. https://doi.org/10.3390/jmmp5010005.

[238] A. Komodromos, F. Kolpak, A.E. Tekkaya, Manufacturing of Integrated Cooling Channels by Directed Energy Deposition for Hot Stamping Tools with Ball Burnished Surfaces, BHM Berg- Und Hüttenmännische Monatshefte. 167 (2022) 428–434. https://doi.org/10.1007/s00501-022-01264-w.

[239] A.C. Paul, A.N. Jinoop, C.P. Paul, P. Deogiri, K.S. Bindra, Investigating build geometry characteristics during laser directed energy deposition based additive manufacturing, J. Laser Appl. 32 (2020) 042002. https://doi.org/10.2351/7.0000004.

[240] M. Urb, J. Hodek, D. Melzer, M. Koukol, M. Br, P. Mart, S. Rzepa, J. Džugan, J. Vavˇ, Prediction of Behaviour of Thin-Walled DED-Processed, (2022).

[241] X. Wang, D. Deng, Y. Hu, F. Ning, H. Wang, W. Cong, H. Zhang, Overhang structure and accuracy in laser engineered net shaping of Fe-Cr steel, Opt. Laser Technol. 106 (2018) 357–365. https://doi.org/10.1016/j.optlastec.2018.04.015.

[242] M.A. Melia, J.G. Duran, J.R. Koepke, D.J. Saiz, B.H. Jared, E.J. Schindelholz, How build angle and post-processing impact roughness and corrosion of additively manufactured 316L stainless steel, Npj Mater. Degrad. 4 (2020) 1–11. https://doi.org/10.1038/s41529-020-00126-5.

[243] J. Boban, A. Ahmed, Improving the surface integrity and mechanical properties of additive manufactured stainless steel components by wire electrical discharge polishing, J. Mater. Process. Technol. 291 (2021) 117013. https://doi.org/10.1016/j.jmatprotec.2020.117013.

[244] A.J. Brooks, A. Dhakad, A. Diaz, D. Kowalik, Toward Understanding the Role of Surface Texture for Additively Manufactured Metal Parts, Struct. Integr. Addit. Manuf. Mater. Parts. ASTM Inter (2020) 61–87. https://doi.org/10.1520/stp163120190160.

[245] P. Pawlus, R. Reizer, M. Wieczorowski, Functional importance of surface texture parameters, Materials (Basel). 14 (2021) 1–29. https://doi.org/10.3390/ma14185326.

[246] S. Murchio, M. Dallago, F. Zanini, S. Carmignato, G. Zappini, F. Berto, D. Maniglio, M. Benedetti, Additively manufactured Ti–6Al–4V thin struts via laser powder bed fusion: Effect of building orientation on geometrical accuracy and mechanical properties, J. Mech. Behav. Biomed. Mater. 119 (2021) 104495. https://doi.org/10.1016/j.jmbbm.2021.104495.

[247] Y. Tian, D. Tomus, P. Rometsch, X. Wu, Influences of processing parameters on surface roughness of Hastelloy X produced by selective laser melting, Addit. Manuf. 13 (2017) 103–112. https://doi.org/10.1016/j.addma.2016.10.010.

[248] A. Charles, A. Elkaseer, U. Paggi, L. Thijs, V. Hagenmeyer, S. Scholz, Down-facing surfaces in laser powder bed fusion of Ti6Al4V: Effect of dross formation on dimensional accuracy and surface texture, Addit. Manuf. 46 (2021) 102148. https://doi.org/10.1016/j.addma.2021.102148.

[249] O. Abdulhameed, A. Al-Ahmari, W. Ameen, S.H. Mian, Additive manufacturing: Challenges, trends, and applications, Adv. Mech. Eng. 11 (2019) 168781401882288. https://doi.org/10.1177/1687814018822880.

[250] P. Stavropoulos, P. Foteinopoulos, Modelling of additive manufacturing processes: a review and classification, Manuf. Rev. 5 (2018) 2. https://doi.org/10.1051/mfreview/2017014.

[251] P.R. Gradl, A. Cervone, E. Gill, Surface texture characterization for thin-wall NASA HR-1 Fe – Ni – Cr alloy using laser powder directed energy deposition (LP-DED), Adv. Ind. Manuf. Eng. 4 (2022) 100084. https://doi.org/10.1016/j.aime.2022.100084.

[252] A. Soltani-tehrani, P. Chen, C. Katsarelis, P. Gradl, S. Shao, Thin-Walled Structures Mechanical properties of laser powder directed energy deposited NASA HR-1 superalloy : Effects of powder reuse and part orientation, Thin-Walled Struct. 185 (2023) 110636. https://doi.org/10.1016/j.tws.2023.110636.

[253] A. Soltani-tehrani, P. Chen, C. Katsarelis, P. Gradl, S. Shao, N. Shamsaei, Laser powder directed energy deposition (LP-DED) NASA HR-1 alloy : Laser power and heat treatment effects on microstructure and mechanical properties, Addit. Manuf. Lett. 3 (2022) 100097. https://doi.org/10.1016/j.addlet.2022.100097.

[254] P. Gradl, O.R. Mireles, C. Katsarelis, T.M. Smith, J. Sowards, P. Chen, D. Tinker, C. Protz, T. Teasley, D.L. Ellis, C. Kantzos, Advancement of Extreme Environment Additively Manufactured Alloys for Next Generation Space Propulsion Applications, Acta Astronaut. 211 (2023) 483–497. https://doi.org/10.1016/j.actaastro.2023.06.035.

[255] F. Marinello, A. Pezzuolo, Application of ISO 25178 standard for multiscale 3D parametric assessment of surface topographies, IOP Conf. Ser. Earth Environ. Sci. 275 (2019). https://doi.org/10.1088/1755-1315/275/1/012011.

[256] ISO, ISO 13565-2:1996: Geometrical Product Specifications (GPS) — Surface texture: Profile method; Surfaces having stratified functional properties — Part 2: Height characterization using the linear material ratio curve, 1996. https://www.iso.org/standard/22280.html.

[257] International Organization for Standardization, ISO 25178-2 Geometrical product specifications (GPS) — Surface texture: Areal — Part 2: Terms, definitions and surface texture parameters, Geneva, 2021. https://www.iso.org/standard/74591.html.

[258] J.C. Haley, J.M. Schoenung, E.J. Lavernia, Modelling particle impact on the melt pool and wettability effects in laser directed energy deposition additive manufacturing, Mater. Sci. Eng. A. 761 (2019) 138052. https://doi.org/10.1016/j.msea.2019.138052.

[259] B. Song, T. Yu, X. Jiang, W. Xi, X. Lin, Z. Ma, Z. Wang, Development of the molten pool and solidification characterization in single bead multilayer direct energy deposition, Addit. Manuf. 49 (2022) 102479. https://doi.org/10.1016/j.addma.2021.102479.

[260] B. Rosa, A. Brient, S. Samper, J.-Y. Hascoët, Operating parameters and multi-scale topography modeling of additive laser manufacturing process, 5th Int. Conf. Surf. Metrol. 4th. 4 (2016) 1–9. http://dx.doi.org/10.1088/2051-672X/4/4/045002.

[261] M. Heinl, M. Heinl, S. Greiner, K. Wudy, C. Pobel, M. Rasch, M. Rasch, F. Huber, F. Huber, T. Papke, M. Merklein, M. Schmidt, M. Schmidt, C. Körner, D. Drummer, T. Hausotte, Measuring procedures for surface evaluation of additively manufactured powder bed-based polymer and metal parts, Meas. Sci. Technol. 31 (2020). https://doi.org/10.1088/1361-6501/ab89e2.

[262] G. Piscopo, E. Atzeni, A. Saboori, An Overview of the Process Mechanisms in the Laser Powder Directed Energy Deposition, Appl. Sci. 13 (2023).

[263] L. Han, F.W. Liou, K.M. Phatak, Modeling of laser cladding with powder injection, Metall. Mater. Trans. B Process Metall. Mater. Process. Sci. 35 (2004) 1139–1150. https://doi.org/10.1007/s11663-004-0070-0.

[264] Z. Li, G. Yu, X. He, S. Li, Z. Shu, Surface Tension-Driven Flow and Its Correlation with Mass Transfer during L-DED of Co-Based Powders, Metals (Basel). 12 (2022). https://doi.org/10.3390/met12050842.

[265] Y.S. Lee, D.F. Farson, Surface tension-powered build dimension control in laser additive manufacturing process, Int. J. Adv. Manuf. Technol. 85 (2015) 1035–1044. https://doi.org/10.1007/s00170-015-7974-5.

[266] H. Liu, M. Wang, Y. Xu, X. Ge, J. Liang, Oxidation characterization of M2 powders exposed under humid atmosphere for a long time, IOP Conf. Ser. Mater. Sci. Eng. 677 (2019). https://doi.org/10.1088/1757-899X/677/2/022060.

[267] P.R. Gradl, C. Protz, J. Fikes, A. Clark, L. Evans, S. Miller, D. Ellis, T. Hudson, Lightweight thrust chamber assemblies using multi-alloy additive manufacturing and composite overwrap, in: AIAA Propuls. Energy 2020 Forum, American Institute of Aeronautics and Astronautics Inc, AIAA, 2020: pp. 1–25. https://doi.org/10.2514/6.2020-3787.

[268] C.A. Schneider, W.S. Rasband, K.W. Eliceiri, NIH Image to ImageJ: 25 years of image analysis, Nat. Methods. 9 (2012) 671–675. https://doi.org/doi:10.1038/nmeth.2089.

[269] P. Gradl, A. Cervone, P. Colonna, Influence of build angles on thin-wall geometry and surface texture in laser powder directed energy deposition, Mater. Des. 234 (2023) 112352. https://doi.org/10.1016/j.matdes.2023.112352.

[270] P.S. Chen, C.C. Katsarelis, W.M. Medders, P.R. Gradl, C.H. Su, Development of Directed Energy Deposited NASA HR-1 to Optimize Properties for Liquid Rocket Engine Applications, NASA Tech. Memo. NASA/TM–20 (2023).

[271] A. Wahab Hashmi, H. Singh Mali, A. Meena, Improving the surface characteristics of additively manufactured parts: A review, Mater. Today Proc. (2021). https://doi.org/10.1016/j.matpr.2021.04.223.

[272] M. Rauch, J. Hascoet, Improving additive manufactured surfaces properties with post processing techniques, (2021).

[273] K.L. Tan, S.-H.H. Yeo, C.H. Ong, Nontraditional finishing processes for internal surfaces and passages: A review, Proc. Inst. Mech. Eng. Part B J. Eng. Manuf. 231 (2016) 2302–2316. https://doi.org/10.1177/0954405415626087.

[274] S.K. Yadav, M.K. Singh, B.R. Singh, Effect of Unconventional Machining on Surface Roughness of Metal: Aluminum and Brass- A Case Study of Abrasive Flow, SAMRIDDHI A J. Phys. Sci. Eng. Technol. 2 (2015). https://doi.org/10.18090/samriddhi.v2i1.1598.

[275] M. Kulkarni, F. Gao, H. Liang, Chemical-mechanical polishing (CMP): a controlled tribocorrosion process, Tribocorrosion Passiv. Met. Coatings. (2011) 498-518e. https://doi.org/10.1533/9780857093738.3.498.

[276] U.S. Kim, J.W. Park, High-Quality Surface Finishing of Industrial Three-Dimensional Metal Additive Manufacturing Using Electrochemical Polishing, Int. J. Precis. Eng. Manuf. - Green Technol. 6 (2019) 11–21. https://doi.org/10.1007/s40684-019-00019-2.

[277] Sergiy Plankovskyy, V. Popov, O. Shypul, Y. Tsegelnyk, O. Tryfonov, D. Brega, Advanced thermal energy method for finishing precision parts, in: K. Gupta, A. Pramanik (Eds.), Adv. Mach. Finish., Elsevier, 2021: pp. 527–575. https://doi.org/https://doi.org/10.1016/C2018-0-00908-1.

[278] A. Fritz, L. Sekol, J. Koroskenyi, B. Walch, J. Minear, V. Fernandez, L. Liu, Experimental Analysis of Thermal Energy Deburring Process by Design of Experiment, in: American Society of Mechanical Engineers (ASME) (Ed.), ASME 2012 Int. Mech. Eng. Congr. Expo., Houston, TX USA, 2012: pp. 2035–2041. https://doi.org/10.1115/IMECE2012-88411.

[279] A. du Plessis, I. Yadroitsev, I. Yadroitsava, S.G. Le Roux, X-Ray Microcomputed Tomography in Additive Manufacturing: A Review of the Current Technology and Applications, 3D Print. Addit. Manuf. 5 (2018) 227–247. https://doi.org/10.1089/3DP.2018.0060.

[280] X. Wang, S. Li, Y. Fu, H. Gao, Finishing of additively manufactured metal parts by abrasive flow machining, Solid Free. Fabr. 2016 Proc. 27th Annu. Int. Solid Free. Fabr. Symp. - An Addit. Manuf. Conf. SFF 2016. (2016) 2470–2472.

[281] O. Maurer, F. Herter, D. Bähre, The impact of manufacturing parameters on corrosion resistance of additively manufactured AlSi10Mg-samples: A design of experiments approach, Manuf. Lett. 34 (2022) 29–33. https://doi.org/10.1016/j.mfglet.2022.08.006.

[282] L.A. Franco, A. Sinatora, 3D surface parameters (ISO 25178-2): Actual meaning of Spk and its relationship to Vmp, Precis. Eng. 40 (2015) 106–111. https://doi.org/10.1016/j.precisioneng.2014.10.011.

[283] L.F. Moody, Friction Factors for Pipe Flow, J. Fluids Eng. Trans. ASME. 66 (1944) 671–678. https://doi.org/10.1115/1.4018140.

[284] H. Darcy, Recherches Experimentales Relatives Au Mouvement De L'Eau Dans Les Tuyaux, Paris: Mallet- Bachelier- Bachelier., 1857.

[285] J. Nikuradse, Laws of flow in rough pipes [Stromungsgesetze in Rauen Rohren], VDI-Forschungsheft, Beilage Zu Forsch. Auf Dem Gebiete Des Ingenieurwesens, Ausgabe B Band 4 English Transl. NACA Tech. Memo 1292, 1950. 361 (1933) 315.

[286] C.F. Colebrook, Experiments with fluid friction in roughened pipes, Proc. Roy. Soc. Ser. Math. Phys. Sci. 161 (1937) 367–381.

[287] C.F. Colebrook, Turbulent flow in pipes with particular reference to the transition region between the smooth and rough pipe laws, J. Inst. Civil. Eng. Lond. 11 (1939) 133–156.

[288] J.B. Taylor, A.L. Carrano, S.G. Kandlikar, Characterization of the effect of surface roughness and texture on fluid flow - Past, present, and future, Proc. 3rd Int. Conf. Microchannels Minichannels, 2005. PART A (2005) 11–18. https://doi.org/10.1016/j.ijthermalsci.2006.01.004.

[289] S. Kandlikar, S. Garamella, Mi. King, Heat Transfer and Fluid Flow in Minichannels and Microchannels, 2nd ed., Elsevier, 2014. https://doi.org/10.1016/c2011-0-07521-x.

[290] T. Santese, A. Söndgerath, S. Soller, B. Latini, C. Manfletti, Experimental and Numerical Investigation of Frictional Behavior and Heat Transfer in 3D Printed Rocket Engine Cooling Channels, in: Sp. Propuls. Conf. 2024, Glasgow, 2024: p. 216.

[291] S.T. Mcclain, J.C. Snyder, D.R. Hanson, R.F. Kunz, K.A. Thole, Flow in a Simulated Turbine Blade Cooling Channel with Spatially Varying Roughness Caused by Additive Manufacturing Orientation, in: ASME Turbo Expo 2020, 2020: pp. 1–14.

[292] N. Richermoz, D. Gloriod, T. Baffie, Z. Anxionnaz-Minvielle, P. Coste, Roughness Effect on Thermal-Hydraulic Performances of Additively Manufactured Meandering Mini-Channels, Heat Transf. Eng. 0 (2023) 1–17. https://doi.org/10.1080/01457632.2023.2275234.

[293] J.C. Snyder, K.A. Thole, Effect of additive manufacturing process parameters on turbine cooling, J. Turbomach. 142 (2020). https://doi.org/10.1115/1.4046459/1074872.

[294] K.L. Kirsch, J.C. Snyder, C.K. Stimpson, K.A. Thole, D. Mongillo, Repeatability in performance of micro cooling geometries manufactured with laser powder bed fusion, 53rd AIAA/SAE/ASEE Jt. Propuls. Conf. 2017. (2017) 1–14. https://doi.org/10.2514/6.2017-4706.

[295] C.R. Hartsfield, T.E. Shelton, G.R. Cobb, R.A. Kemnitz, J. Weber, Understanding Flow Characteristics in Metal Additive Manufacturing, J. Aerosp. Eng. 34 (2021) 1–9. https://doi.org/10.1061/(asce)as.1943-5525.0001325.

[296] P. Gradl, A. Cervone, P. Colonna, Development and experimental evaluation of surface enhancement methods for laser powder directed energy deposition microchannels for laser powder directed energy deposition microchannels, Virtual Phys. Prototyp. 19 (2024) e2345389. https://doi.org/10.1080/17452759.2024.2345389.

[297] E. Lemmon, Thermophysical Properties of Fluids, National Institute of Standards and Technology (NIST), Gaithersburg, Maryland, 2009.

[298] D. Brkić, Review of explicit approximations to the Colebrook relation for flow friction, J. Pet. Sci. Eng. 77 (2011) 34–48. https://doi.org/10.1016/j.petrol.2011.02.006.

[299] Y.A. Cengel, J.M. Cimbala, Fluid Mechanics: Fundamentals and Applications, 3rd ed., McGraw-Hill, New York, N.Y, 2014.

[300] A.J. Wildgoose, K.A. Thole, E. Tuneskog, L. Wang, Roughness Related to Cooling Performance of Channels made through Additive Manufacturing, in: Proc. ASME Turbo Expo 2023, ASME Turbomachinery Technical Conference and Exposition, Boston, Massachusetts, 2023.

[301] K. Rehme, K. Nuclear, Simple Method of Predicting Friction Factors of Turbulent Flow in Non-Circular Channels, Int. J. Heat Mass Transf. 16 (1973) 933–950.

[302] G. Demeneghi, P. Gradl, J.R. Mayeur, K. Hazeli, Size Effect Characteristics and Influences on Fatigue Behavior of Laser Powder Bed Fusion of GRCop-42 Copper Alloy, Heliyon. 10 (2023) e28679. https://doi.org/10.1016/j.heliyon.2024.e28679.

[303] D. June, J.R. Mayeur, P. Gradl, A. Wessman, K. Hazeli, Effects of Size, Geometry, and Temperature on Additively Manufactured Ti-6Al-4V Titanium Alloy 1 2, Addit. Manuf. 80 (2024) 103970. https://doi.org/10.1016/j.addma.2024.103970.

[304] S.G. Kandlikar, D. Schmitt, A.L. Carrano, J.B. Taylor, Characterization of surface roughness effects on pressure drop in single-phase flow in minichannels, Phys. Fluids. 17 (2005) 100606. https://doi.org/10.1063/1.1896985.

[305] M. Kadivar, D. Tormey, G. Mcgranaghan, A review on turbulent flow over rough surfaces: fundamentals and theories, Int. J. Thermofluids. (2021) 100077. https://doi.org/10.1016/j.ijft.2021.100077.

[306] P.K. Swamee, A.K. Jain, Explicit Equations for Pipe-Flow Problems, J. Hydraul. Div. 102 (1976) 657–664. https://doi.org/10.1061/JYCEAJ.0004542.

[307] V. Mileikovskyi, T. Tkachenko, Precise Explicit Approximations of the Colebrook-White Equation for Engineering Systems, Lect. Notes Civ. Eng. 100 LNCE (2021) 303–310. https://doi.org/10.1007/978-3-030-57340-9_37.

[308] Ž. Ćojbašić, D. Brkić, Very accurate explicit approximations for calculation of the Colebrook friction factor, Int. J. Mech. Sci. 67 (2013) 10–13. https://doi.org/10.1016/J.IJMECSCI.2012.11.017.

[309] A. Avci, I. Karagoz, A novel explicit equation for friction factor in smooth and rough pipes, J. Fluids Eng. Trans. ASME. 131 (2009) 0612031–0612034. https://doi.org/10.1115/1.3129132/444690.

[310] G. Plascencia, L. Díaz–Damacillo, M. Robles-Agudo, On the estimation of the friction factor: a review of recent approaches, SN Appl. Sci. 2 (2020) 1–13. https://doi.org/10.1007/s42452-020-1938-6.

[311] M. Jaric, S. Genić, I. Arandjelović, P. Kolendić, M. Jarić, N. Budimir, V. Genić, A Review of Explicit Approximations of Colebrook's Equation, FME Trans. (2011) 39–67.

[312] T. Adams, C. Grant, H. Watson, A Simple Algorithm to Relate Measured Surface Roughness to Equivalent Sand-grain Roughness, Int. J. Mech. Eng. Mechatronics . 1 (2012) 66–71. https://ijmem.avestia.com/2012/008.html.

[313] V.T. Forster, Performance Loss of Modern Steam-Turbine Plant due to Surface Roughness, Proc. Inst. Mech. Eng. 181 (1966) 404–405. https://doi.org/10.1243/PIME_PROC_1966_181_038_02.

[314] C.C. Koch, L.H. Smith, Loss Sources and Magnitudes in Axial-Flow Compressors., Am. Soc. Mech. Eng. (1975) 411–424.

[315] M.N. Goodhand, K. Walton, L. Blunt, H.W. Lung, R.J. Miller, R. Marsden, The Limitations of using "ra" to describe surface roughness, J. Turbomach. 138 (2016). https://doi.org/10.1115/1.4032280.

[316] M.R. Raupach, R.A. Antonia, S. Rajagopalan, Rough-Wall Turbulent Boundary Layers, Appl. Mech. Rev. 44 (1991) 1–25. https://doi.org/10.1115/1.3119492.

[317] A.E. Perry, W.H. Schofield, P.N. Joubert, Rough wall turbulent boundary layers, J. Fluid Mech. 37 (1969) 383–413. https://doi.org/10.1017/S0022112069000619.

[318] K. Bammert, H. Sandstede, Influences of Manufacturing Tolerances and Surface Roughness of Blades on the Performance of Turbines., Am. Soc. Mech. Eng. (1975) 29–36.

[319] R.J. Volino, M.P. Schultz, K.A. Flack, Turbulence structure in rough- and smooth-wall boundary layers, J. Fluid Mech. 592 (2007) 263–293. https://doi.org/10.1017/S0022112007008518.

[320] S.E. Coleman, V.I. Nikora, S.R. Mclean, E. Schlicke, Spatially Averaged Turbulent Flow over Square Ribs, J. Eng. Mech. 133 (2007) 194–204. https://doi.org/10.1061/(ASCE)0733-9399(2007)133.

[321] D.C. Tinker, T.M. Fedotowsky, R.A. Bardsley, P.R. Gradl, Development of Large-Scale Thrust Chambers using Laser Powder Directed Energy Deposition, in: AIAA Scitech 2024, Orlando, FL, 2024: pp. 8–12. https://doi.org/https://doi.org/10.2514/6.2024-0995.

[322] S. Manigandan, T.R. Praveenkumar, J. Ir Ryu, T. Nath Verma, A. Pugazhendhi, Role of hydrogen on aviation sector: A review on hydrogen storage, fuel flexibility, flame stability, and emissions reduction on gas turbines engines, Fuel. 352 (2023) 129064. https://doi.org/10.1016/j.fuel.2023.129064.

[323] A. Thiam, Experimental Study of L-PBF Micro-channel Surface Roughness An Experimental Study on the Effects of Build by, Delft University of Technology, 2024. https://repository.tudelft.nl/record/uuid:23093bde-4438-46a0-ad48-3b12f7c6ea01.

Acknowledgements

In exploring the world around us, I have come to appreciate the diverse surfaces that define our lives. From meticulously polished playground bars to the undulating textures of natural elements like trees and mountains, surfaces are omnipresent. They influence the wind, control motion and fluids, create beauty in children's toys, and reflect our own images in the mirror. My reflection is not just about surfaces, but about the unique skills and support contributed by my family, friends, and colleagues. This thesis integrates the profound understanding of the world, artistic prowess, perfectionism, planning, organization, drive, passion, and leadership instilled by each of you.

Dax, your insightful observations of the world consistently astound me. Your ability to articulate complex concepts, such as the physics behind a straw resisting the wind and the defects in a glass car window, reflects a curiosity that is truly inspiring. The anecdote of our windy walk after playing hockey, where you confidently explained the principles at play on the straw, stands as a testament to your intellectual depth and curiosity. I drew upon your curiosity to spark my own within my research.

Tess, your exceptional artistic flair never ceases to amaze me. Your meticulous planning and relentless pursuit of perfection in translating ideas onto paper showcase an unwavering commitment to your craft. Your ability to come up with artistic ideas and solutions through Legos, yarn, paper, and crafts is amazing. I drew upon your perfectionism and creativeness to devise unique and artistic solutions to problems.

Leah, my life partner, epitomizes qualities of drive, visionary thinking, a love of life, supportiveness of everyone around you, effective communication, compassionate and servant leadership, and organizational prowess. Your unwavering support throughout this journey fueled my inspiration. I am immensely grateful for the shared moments and eagerly anticipate the future we will navigate together. I drew upon many of your skills, support, and compassion, but I certainly cannot compete with your amazing qualities. Love u!

To my parents and family, I extend heartfelt gratitude for instilling in me the values of hard work, motivation, and boundless love. Your enduring guidance has been a guiding light in my pursuit. To my family, I appreciate your support and for challenging me over the years. I drew upon all of these values that each of you instilled in me throughout my life.

Angelo and Piero, I deeply appreciate the time we spent together as friends and colleagues throughout this challenging and rewarding journey. Your critical input, discussions, challenges, advice, support, and friendship have been invaluable. I thoroughly enjoyed each of our conversations, whether in the office or over meals, and I learned so much from both of you on the path to becoming an independent researcher. Thank you for welcoming me into your research groups. I know that lifelong friendships were formed, and I hope to continue working with you and making you proud.

To my NASA, industry, and academic colleagues, I express sincere appreciation for your invaluable contributions—whether through engaging

discussions, criticism, answering queries, or providing general support. I want to particularly acknowledge Dr. Agustin Diaz, Dr. Bill Scott, Sara Rengifo, Tyler Blumenthal, Dr. Darren Tinker, Tom Teasley, Dr. Joe Sims, Dr. Hallie Collopy, John Fikes, Matt Marsh, Dr. Bhaskar Dutta, Joe Ruf, Colton Katsarelis, Po Chen, Dr. Gabe Demeneghi, and many others who provided valuable inputs and support. Lynn Machamer – thank you for your help with various imaging edits. Thank you to (Dr.) Michelle Rudd for the numerous conversations about Delft life and sharing our research woes. I would also like to thank the various companies and organizations involved in this study and industry experts at these organizations including RPM Innovations, REM Surface Engineering, Extrude Hone, TechMet, Voxel, HMI, Laser Tech Associates, and MSFC Component Development Area.

I extend my deepest gratitude to everyone who has played a role in shaping this endeavor, turning it into a rich tapestry influenced by your individual support, insights, and expertise.

Published Research Related to this Dissertation

Gradl, P., Cervone, A., Colonna, P., Enhancement of friction factors for microchannels fabricated using laser powder directed energy deposition, Materials & Design 251 (2025) 113673. https://doi.org/10.1016/j.matdes.2025.113673

Gradl, P., Cervone, A., Colonna, P., 2024. Development and experimental evaluation of surface enhancement methods for laser powder directed energy deposition microchannels. Virtual Phys. Prototyp. 19:1. e2345389. https://doi.org/10.1080/17452759.2024.2345389

Gradl, P., Cervone, A., Colonna, P., 2023. Influence of build angles on thin-wall geometry and surface texture in laser powder directed energy deposition. Materials & Design 234, 112352. https://doi.org/10.1016/j.matdes.2023.112352

Gradl, P., Mireles, O.R., Katsarelis, C., Smith, T.M., Sowards, J., Chen, P., Tinker, D., Protz, C., Teasley, T., Ellis, D.L., Kantzos, C., 2023. Advancement of Extreme Environment Additively Manufactured Alloys for Next Generation Space Propulsion Applications. Acta Astronautica 211, 483–497. https://doi.org/10.1016/j.actaastro.2023.06.035

Gradl, P., Cervone, A., Colonna, P., 2022. Integral Channel Nozzles and Heat Exchangers using Additive Manufacturing Directed Energy Deposition NASA HR-1 Alloy. 73rd International Astronautical Congress. Paris, France, IAC-22,C4,2,x73690.

Gradl, P.R., Cervone, A., Gill, E., 2022. Surface texture characterization for thin-wall NASA HR-1 Fe – Ni – Cr alloy using laser powder directed energy deposition (LP-DED). Advances in Industrial and Manufacturing Engineering 4, 100084. https://doi.org/10.1016/j.aime.2022.100084

Gradl, P., Tinker, D., Park, A., Mireles, O., Garcia, M., Wilkerson, R., Mckinney, C., 2022. Robust Metal Additive Manufacturing Process Selection and Development for Aerospace Components. Journal of Materials Engineering and Performance, Springer. 31. 6013-6044. https://doi.org/10.1007/s11665-022-06850-0

Kerstens, F., Cervone, A., Gradl, P., 2021. End to end process evaluation for additively manufactured liquid rocket engine thrust chambers. Acta Astronautica 182, 454–465. https://doi.org/10.1016/j.actaastro.2021.02.034

Gradl, P.R., 2022. Application of optical measurement techniques during various stages of pregnancy. Measurement: Sensors 24, 100453. https://doi.org/10.1016/j.measen.2022.100453

Books and Book Chapters:

R. Pederson, J. Anderson, S. Joshi. Additive Manufacturing of High-Performance Metallic Materials: Superalloys and Titanium Alloys. (2024). Contributing author for chapter 8 titled “Surface Post-Treatment of Additively Manufactured Components”. Elsevier. ISBN: 9780323918855

Volume: Paul R. Gradl, Omar R. Mireles, Christopher S. Protz, Chance P. Garcia, 2022. Metal Additive Manufacturing for Propulsion Applications, 1st ed, Metal Additive Manufacturing for Propulsion Applications. American Institute of Aeronautics and Astronautics, Inc., Reston, VA. https://doi.org/10.2514/4.106279

Gradl, P.R., Protz, C.S., Garcia, C.P., Mireles, O.R., Leary, M., 2022. Introduction to and Applications of Additive Manufacturing for Propulsion. Metal Additive Manufacturing for Propulsion Applications 1–48. https://doi.org/10.2514/5.9781624106279.0001.0048

Gradl, P.R., Protz, C.S., Le Corre, M., Mireles, O.R., Medina, F., Kottman, M., Norfolk, M., Ajdelsztajn, L., Allison, P., Elliott, A., Bandari, Y., 2022. Metal Additive Manufacturing Processes and Selection. In: Gradl, P., Mireles, O.R., Protz, C.S., Garcia, C.P. (Eds.), Metal Additive Manufacturing for Propulsion Applications. American Institute of Aeronautics and Astronautics, Inc., 49–186. https://doi.org/10.2514/5.9781624106279.0049.0186

Gradl, P.R., Mireles, O.R., Katsarelis, C., Protz, C.S., Chen, P.-S., Dennies, D.P., Tylka, J., Hemmasian-Ettefagh, A., Guo, S., 2022. Selection and Overview of Additive Manufactured Metals and Metal Alloys. Metal Additive Manufacturing for Propulsion Applications 187–236. https://doi.org/10.2514/5.9781624106279.0187.0236

Mireles, O.R., Gradl, P.R., Lanigan, E., Evans, W., Plessis, A. du, 2022. Post-Processing of Metal Additively Manufactured Components. Metal Additive Manufacturing for Propulsion Applications 307–404. https://doi.org/10.2514/5.9781624106279.0307.0404

Appendix

Raw data files for the Chapter 7 experiment and measurements is located at:
https://surfdrive.surf.nl/files/index.php/s/Fsb7aS7KPJIlwOW

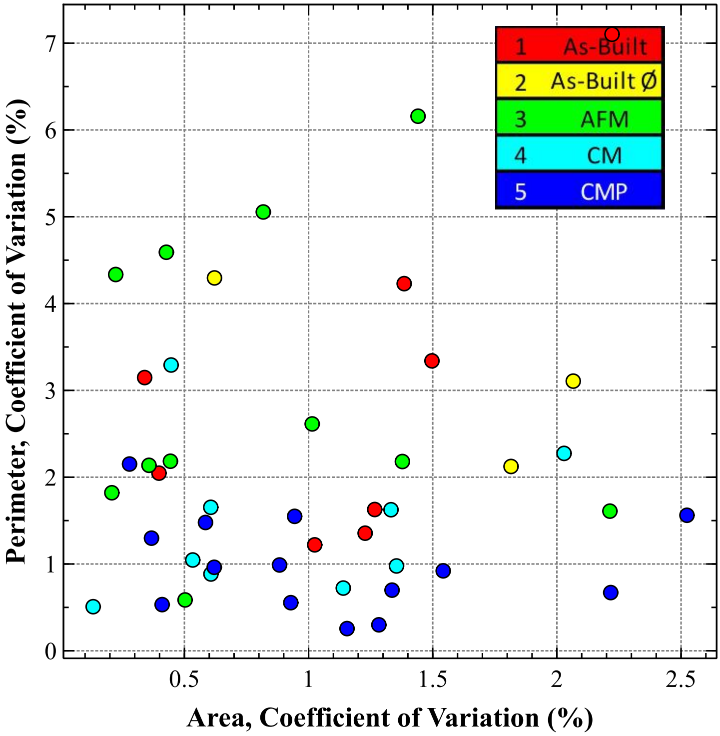

Figure 12.1. Relationship of perimeter to cross-sectional area coefficient of variation for 600 mm length channel samples.

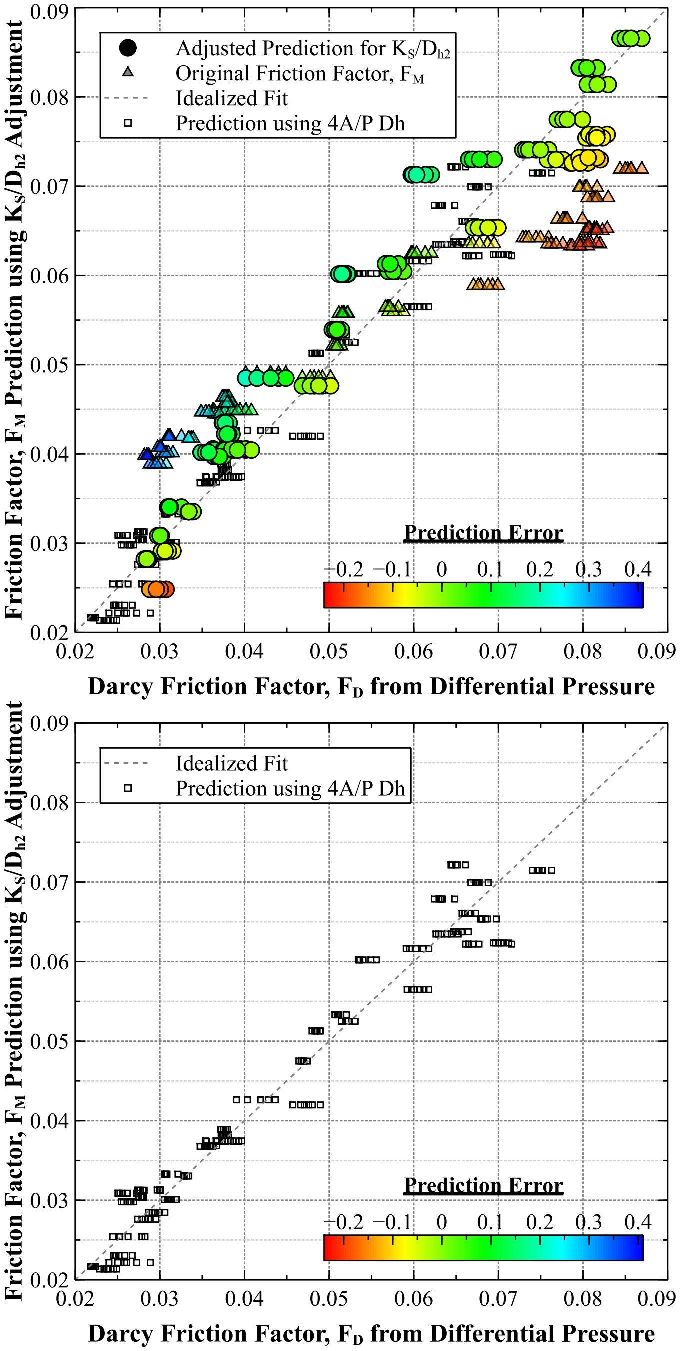

Figure 12.2. Prediction of f_M using the K_S/D_{h2} and Ra/D_{h2} method compared to the experimental f_D. Prediction using 4A/P for D_h.

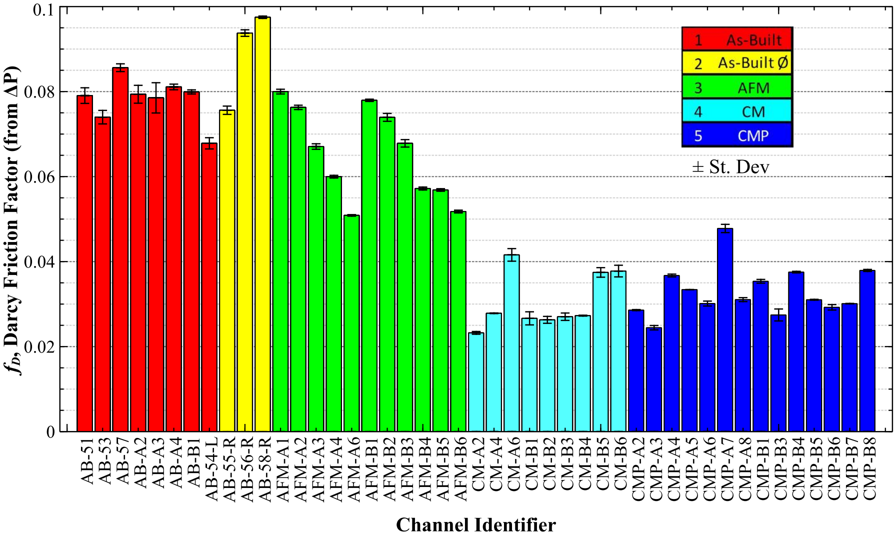

Figure 12.3. Average Darcy friction factor and standard deviation based on three fixed mass flow rate from venturi.

	Tube AB-55-R	Tube AB-56-R	Tube AB-58-R
Powder	Fine	Coarse	Coarse
Avg Diameter (mm)	2.777 ±0.056	2.682 ±0.066	2.646 ±0.084
Perimeter (mm)	11.727 ±0.364	11.848 ±0.509	10.848 ±0.230
Area (mm^2)	6.052 ±0.125	5.617 ±0.035	5.504 ±0.099
Circularity (%)	55.3% ±0.023	50.4% ±0.040	58.8% ±0.021
Roundness (%)	95.2% ±0.017	94.6% ±0.011	92% ±0.014

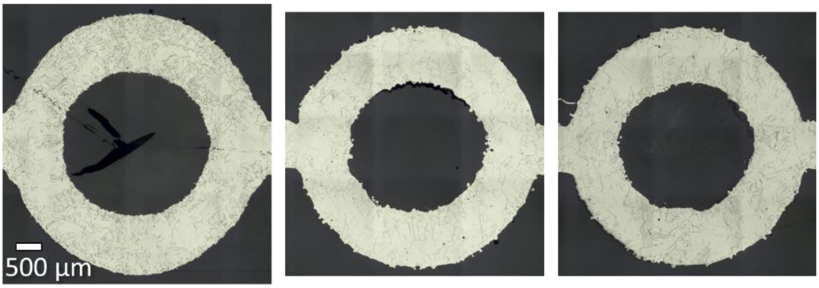

Figure 12.4. Etched micrographs of the mid-section of round tubes (AB-55-R, AB-56-R, AB-58-R). The table lists the measured diameter, perimeter, area, circularity, and roundness obtained from the micrographs of the cross-sections (average of three cross-sections).

TU Delft